

Sheffield Hallam University

Advanced quartz crystal microbalance techniques applied to calixarene sensing membranes.

HOLLOWAY, Alan Franciszek.

Available from the Sheffield Hallam University Research Archive (SHURA) at:

<http://shura.shu.ac.uk/19817/>

A Sheffield Hallam University thesis

This thesis is protected by copyright which belongs to the author.

The content must not be changed in any way or sold commercially in any format or medium without the formal permission of the author.

When referring to this work, full bibliographic details including the author, title, awarding institution and date of the thesis must be given.

Please visit <http://shura.shu.ac.uk/19817/> and <http://shura.shu.ac.uk/information.html> for further details about copyright and re-use permissions.

Assets Centre City Campus
Sheffield S1 1WB

101 807 120 2



on to Learning Centre o
are charged at 50p per

'07

TUL

d

8

REFERENCE

ProQuest Number: 10697123

All rights reserved

INFORMATION TO ALL USERS

The quality of this reproduction is dependent upon the quality of the copy submitted.

In the unlikely event that the author did not send a complete manuscript and there are missing pages, these will be noted. Also, if material had to be removed, a note will indicate the deletion.



ProQuest 10697123

Published by ProQuest LLC (2017). Copyright of the Dissertation is held by the Author.

All rights reserved.

This work is protected against unauthorized copying under Title 17, United States Code
Microform Edition © ProQuest LLC.

ProQuest LLC.
789 East Eisenhower Parkway
P.O. Box 1346
Ann Arbor, MI 48106 – 1346

**ADVANCED QUARTZ CRYSTAL
MICROBALANCE TECHNIQUES APPLIED
TO CALIXARENE SENSING MEMBRANES**

ALAN FRANCISZEK HOLLOWAY

**A thesis submitted in partial fulfilment of the requirements of
Sheffield Hallam University
for the degree of Doctor of Philosophy**



September 2005

Declaration

I hereby declare that this thesis submitted for the degree of PhD is the result of my own research and that this thesis has not been submitted for a higher degree to any other university or institution.

Signed

Alan Franciszek Holloway

ABSTRACT

Several Quartz Crystal Microbalance (QCM) measurement techniques in conjunction with a series of calix[4]resorcinarene sensing membranes have been successfully exploited for the detection of volatile organic solvents at vapour concentrations below their lower explosive level.

The impedance analysis technique involves the measurement of the electrical properties of the QCM around the resonant frequencies of crystal. Subsequent fitting of the measured spectra to an equivalent circuit allows parameters directly related to mass loading and the mechanical properties (viscosity) of the film to be obtained. An experimental setup which allows the real time in situ extraction of these parameters has been developed.

It has been shown that unique changes in mass loading and the films viscoelastic properties caused by the adsorption of target vapours into a calix[4]resorcinarene $C_{15}H_{31}$ sensing membrane can be detected. In some cases this facilitates both the detection and discrimination of target vapours using a single QCM sensing element. The changes in the films mechanical properties are believed to be caused by capillary condensation of vapours at values below saturated vapour pressure inside the nanoporous calix[4]resorcinarene film matrix.

The work is extended by the use of the sensor array technique. In the first instance frequency only measurements are used. Four QCM have been coated with calix[4]resorcinarene compounds with different hydrocarbon chain lengths and exposed to range of organic vapours. The variation in chain length produces selectivity between the sensing membranes, and leads to the classification of all the tested organic vapours using a feed forward multilayer Artificial Neural Network. The trained network successfully classified over 98% of the test data.

The additional measurement of film dissipation using impedance analysis/QCMD shows interesting phenomena. An unexpected increase in mechanical stiffness of the film is observed for small chain length C[4]RA compounds (CH_3) on vapour sorption. A speculative model has been proposed relating the chain length and effective cavity size to the observed phenomena.

An alternative low cost multi parameter measurement set up has also been developed using the QCMD principle. The crystal is driven from an external oscillatory source and subsequently disconnected. The resonant frequency and dissipation factor can be extracted from the decaying sinusoid signal. This approach eliminates the need for expensive network analysers. An additional multiplexing circuit has been combined with the QCMD technique and allows both the frequency and dissipation factor of several crystals to be measured in pseudo real time. This makes the system ideally suited for multi parameter array measurements.

The basis for a discriminative explosive vapour sensor based on calix[4]resorcinarene membranes has been investigated and promising results for future development have been obtained. The exact adsorption mechanisms are however complex and although

speculative models have been proposed, further research is suggested to fully characterize the complete adsorption process and the mechanical changes taking place within the film.

ACKNOWLEDGEMENTS

Without the guidance and knowledge of my director of studies, supervisors and colleagues this work would not have been possible. I would therefore like to thank them individually.

Firstly, my director of studies Dr Alexei Nabok, who provided excellent support and expert knowledge throughout the work. My supervisory team Prof Asim Ray, Prof Jawed Siddiqi and Dr David Crowther and prominently Dr M Thompson.

Special thanks also go to Dr Aseel Hassan and Dr Thomas Wilkop for many words of advice, Ken Duty for the design and fabrication of several PCB's, Prof Valerie Bliznyuk and Dr Frank Davis for the supply and synthesis of several sensing membranes, and Bryan Didsbury and Roger Tingle for the machining of the gas chambers.

I would also like to thank my PhD colleagues and friends Alistair, Anna, Saharudin Malik and Abbas for making life interesting during many hours underground in the laboratory.

Sincere thanks to my parents who encouraged and supported me throughout the work and finally my girlfriend Nicola for her encouragement, support and taking on household responsibilities leaving me free to write this thesis.

Contents

1. Introduction	1
1.1 Aims and Objectives of the Research	6
References	7
2. Literature review and theoretical background	10
2.0 Introduction	10
2.1 Piezoelectric effect	10
2.2 Acoustic Waves	11
2.3 The Quartz Crystal Microbalance (QCM)	13
2.3.1 The QCM as a gravimetric sensor	13
2.3.2 Z match technique	17
2.3.3 The Transmission Line Model	18
2.4 Surface Loading	27
2.4.1 The acoustic Load concept	29
2.4.2 The Viscoelastic Film	29
2.4.3 Special case of the Sauerbrey relationship	31
2.5 Modelling QCM loading using the Modified BVD equivalent circuit	32
2.6 Modelling a viscoelastic film	34
2.7 Organic vapour sensing using the QCM	39
2.8 QCM sensor arrays	40
2.9 Advanced QCM sensor signal interpretation	42
2.10 Sensing membranes	44
2.11 Target Analytes (VOC's)	46
References	48

3. Experimental Methodology

3.0 Introduction	54
3.1 Deposition of QCM sensing membranes	54
3.11 Surface preparation	55
3.12 Spin coating	55
3.13 Langmuir Blodgett deposition	56
3.2 Exposure methods and techniques	57
3.2.1 Gas cell/ chamber	57
3.2.2 Vapour injection method	58
3.2.3 Vapour flow method	60
3.2.4 Vapour concentrations	61
3.2.5 Saturated vapour pressures	61
3.3 QCM measurement techniques and equipment	62
3.3.1 Resonant oscillator circuits	63
3.3.2 QCMD (Dissipation)	63
3.3.3 Impedance/Network analysis	67
3.3.4 Experimental errors	68
3.3.5 Increasing measurement accuracy	72
3.3.6 Real time analysis	74
3.4 Array measurements and techniques	76
3.4.1 Resonant oscillator array	76
3.4.2 QCMD Array	77
3.5 Data acquisition and analysis	79
3.5.1 Curve fitting	79

3.5.2 Simulated Annealing technique	80
3.5.3 Levenberg Marquadt	81
3.5.4 Parameter minimization	83
3.5.5 Feature extraction	84
3.6 Film characterisation techniques	87
3.6.1 Atomic Force Microscopy (AFM)	88
3.6.2 Ellipsometry	88
3.7 Conclusions	90
References	91
 4. Result and discussion - QCM characterisation and coating properties	
4.0 Introduction	95
4.1 Experimental setup validation and performance	96
4.1.1 Frequency based measurements	96
4.1.2 Impedance analysis	97
4.1.3 QCMD	103
4.2 Effects of temperature on the QCM and sensing membranes	104
4.3 Crystal properties and selection	108
4.4 Results of crystal coating	110
4.5 Film properties/structure	116
4.5.1 AFM measurements	116
4.5.2 Ellipsometry measurements	122
4.6 Conclusions	123
References	125

5. Results and discussion - vapour exposure

5.0 Introduction	126
5.1 Vapour exposure frequency based measurements	127
5.2 Analysis of the QCM array using ANN techniques	134
5.3 QCM impedance measurement results	149
5.4 QCMD measurement results	151
5.5 Vapour sensing – impedance analysis/QCMD measurements for an array based sensor	154
5.6 Coating stability	166
5.7 Summary	169
References	171

6. Conclusion and recommendations

6.0 Conclusions	174
6.1 Recommendations for future work	178
References	180

APPENDIX

Appendix[A]- MATLAB programs:

1. Program to calculate and produce 3D plot the acoustic load
2. Program to generate admittance spectra from TLM model
3. Implementation of fast three step method
4. Calculate Δf and ΔR for known film parameters

Appendix[B]- Oscillator circuit and multiplexer schematic

Appendix[C]- QCMD circuit and PIC controller schematic

Appendix[D]- Impedance analysis capture software

Appendix[E]- Polynomial admittance fitting software

Appendix[F]- Approximations used for the fast three step method and MATLAB implementation.

List of publications

1. "Impedance analysis of the thickness shear mode resonator for organic vapour sensing." *Sensors and Actuators B*, 99 (2004), pages 355-360.
2. "New Method of Vapour Discrimination Using the Thickness Shear Mode (TSM) Resonator." *Sensors* 3, 2003, pages 187-191.
3. "Discriminative Sensing of Volatile Organic Solvents. Comparative Analysis Using Different QCM Techniques." *IEEE sensors 2004 conference proceedings*, Vienna Austria, pages 1500-1503.
4. "Registration of Low Molecular Weight Environmental Toxins with Total Internal Reflection Ellipsometry". *IEEE sensors 2004 conference proceedings*, Vienna Austria, pages 1195-1198.

Chapter 1

Introduction

The detection of hazardous substances causing harm to health, the environment and causing risk of explosion is a major concern in many industrial, commercial, and laboratory environments. Of particular interest in this thesis is the class of volatile organic compounds (VOC), many of which display both toxic and carcinogenic properties [1]. VOC's are found in common items, such as paints, adhesives, cleaning solvents and are major constituents of petrol and other hydrogen based fuels.

The key property of VOC's is that their high saturated vapour pressure allows them to easily vaporise at room temperature. This fact leads to the importance of the Lower and Upper Explosion Limits (LEL and UEL), defining the lower and upper concentrations of vapour in the air at which ignition may occur (see figure 1.1). Between these limits the risk of explosion is significant. The typical LEL for most organic solvents is in the region of 1% of the total air volume (10,000ppm), small solvent spillages/leaks may rapidly give rise to concentrations above this value in the atmosphere within close proximity of the spillage. A minute spark from an electrical machine could be the trigger for a catastrophic explosion. Such a scenario is relevant and of great concern in the petrochemical industry; where the transport and storage of liquid petroleum in large pipes and tankers is common. The ability to detect a leaking VOC is of substantial benefit both in terms of safety and reducing waste.

The requirement of such sensors with increased accuracy, smaller size, high versatility and predominantly low cost are therefore always in demand, for both commercial and scientific gain.

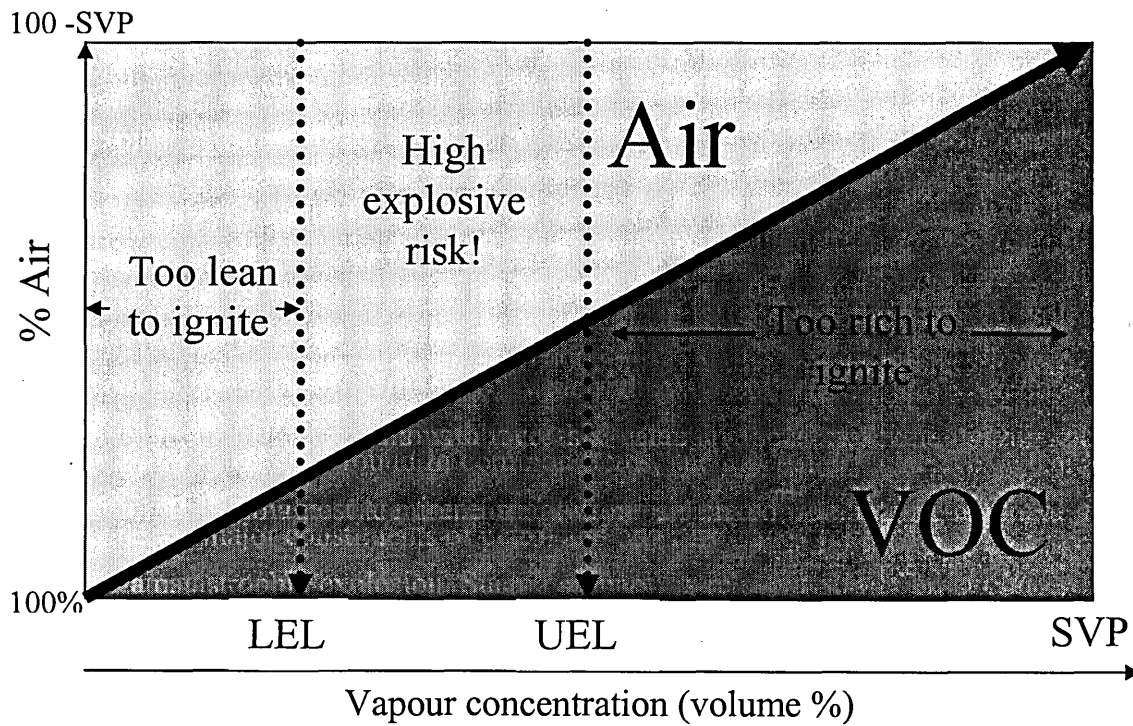


Figure 1.1. Graphical representation showing the flammable properties of a typical organic solvent.

Vapour	LEL-UEL (ppm) $\times 10^3$
Hexane	12 - 77
Benzene	13 - 80
Toluene	10 - 70
xylene	11 - 70
cyclohexane	13 - 84
m xylene	11 - 70

Also check

Table 1.1. Concentration in parts per million (ppm) for the lower and upper explosion limits of a range of VOC's.

A conventional sensor can be defined as a device which produces a measurable output signal in response to some input quantity i.e. a certain quantity of analyte molecules [2]. In nearly all cases this output quantity is in the form of an electrical signal which carries information about the measured parameter(s). The sensor itself is a combination of several components usually comprising of the sensitive membrane where the molecular recognition or chemical reactions occur, transducer which transforms the chemical reaction into a physical measurable parameter and signal processing system as shown in figure 1.2. It is also acknowledged that sensor technology is an interdisciplinary field combining fields of physics, chemistry, biology, computing and engineering.

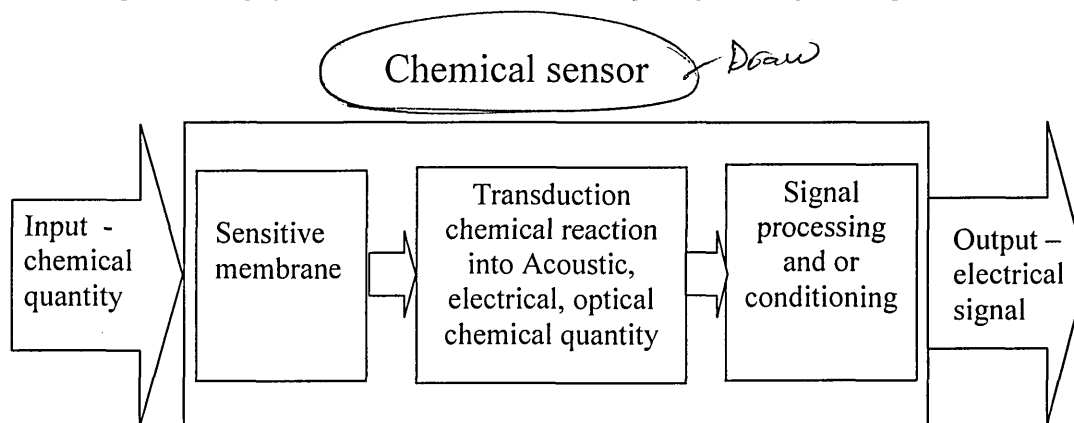


Figure 1.2. Chemical sensor block diagram showing a typical arrangement of input, sensitive membrane, transduction, signal processing and output.

A range of different transduction mechanisms have been employed for vapour detection. Common examples include metal oxide sensors (MOS) [3,4], conducting polymers [5-8] and the acoustic wave based sensor [9-15] used for the work in this thesis.

The Acoustic Wave Sensor (AWS) operates on the principle that the input quantity produces a change in the path over which the acoustic wave travels. In the case of the Thickness Shear mode (TSM) resonator, changes in the path are related to an additional effective thickness of the crystal which results in the decrease in resonant frequency of the

device. Sauerbrey was the first to utilize the TSM resonator as a mass sensing device. He discovered the frequency of the device is directly proportional to the deposited mass on the surface of the crystal and hence the TSM resonator is often referred to as the Quartz Crystal Microbalance [16]. The Sauerbrey relation is however based on several assumptions defined in Chapter 2. In this work a simple gravimetric regime defined by Sauerbrey can not be used, and more complex analysis is required to fully characterise the TSM resonator and contacting media.

To obtain additional information on the mechanical properties of the film, the impedance analysis technique has been exploited. The impedance spectrum of the QCM is measured over a range of frequencies around resonance. Subsequent fitting of the spectra to an equivalent circuit model allows the extraction of parameters which are directly related to the mass loading and changes in the mechanical properties of the film. Vapour adsorption causing unique changes in the properties of the film can therefore be detected, allowing the discriminative detection of the target vapours.

This approach has been applied to several calix[4]resorcinarene based sensing membranes on exposure to a range of VOC's. The results show the additional information obtained in some cases allows a single QCM to discriminate between a number of volatile organic solvents.

Further improvements on vapour identification can be achieved with the sensor array (electronic nose) approach. The generally accepted definition of the electronic nose is defined by Gardner and Bartlett. "An electronic nose is an instrument which comprises chemical sensors with partial specificity and an appropriate pattern recognition system capable of recognising simple or complex odours" [17]. The aim of this work is the

development of such a system for the detection of Volatile Organic Compounds using the TSM resonator as the transduction mechanism. While many QCM based systems have been reported [9,13,18-30], the focus of the research is to combine multiple parameter measurements from a single crystal with the sensor array technique. The resultant sensor should have a decreased array size while still providing both the detection and discrimination capabilities found in large QCM sensor arrays.

1.1 Aims and objectives of the research

The aim of this research is to develop chemical sensing devices, intended to detect various organic solvents and evaluate their concentration. The system is based on the monitoring of changes in the electrical characteristics of the Thickness Shear Mode (TSM) resonator to allow the analysis and furthermore recognition of contacting chemical compounds and calculation of their relative concentrations. Measurement of both the mass loading and dissipation which occur in the film is used in conjunction with sensor array techniques to aid classification and quantification of the target vapours.

Objectives:

1. The development of an experimental set-up for QCM impedance measurements.
2. Development of software to allow the extraction of equivalent circuit parameters from the obtained impedance spectra.
3. Deposition of organic sensitive membranes onto the QCM.
4. The study of the impedance characteristics of sensitive membranes on exposure to different gaseous analytes (organic vapours, toxic gases). Evaluation of the parameters of the equivalent circuit and their correlation to visco-elastic properties of the coating.
5. The development of a circuit board for the QCM sensor array and writing the software for Artificial Neural Network (ANN) analysis of the sensor array response.
6. Investigation of different analytes using ANN. Accumulation of data, building a database of responses for the training of the ANN. Recognition and quantitative analysis of unknown mixtures of analytes.
7. The development of QCM as a cost effective alternative to the impedance analysis method.
8. Development of the prototype sensor, interfacing both software and hardware elements.

REFERENCES

- [1] Health and Safety Executive, "Control of Substances Hazardous to Health - COSHH," 2002.
- [2] D. S. Ballatine, R. M. White, S. J. Martin, A. J. Ricco, G. C. Fryre, E. T. Zellers, and H. Wohltjen, , "Acoustic Wave Sensors Theory, Design and Physico chemical applications," Academic press, New York, 1997,
- [3] G. Sberveglieri, "Gas sensors principles operations and developments"; Kluwer Academic Publishers Group, 1992.
- [4] M. Morvan, T. Talou, and J. F. Beziau, "MOS-MOSFET gas sensors array measurements versus sensory and chemical characterisation of VOC's emissions from car seat foams," *Sensors and Actuators B: Chemical*, vol. 95,pp. 212-223, Oct. 2003.
- [5] C. P. de Melo, B. B. Neto, E. G. de Lima, L. F. B. de Lira, and J. E. G. de Souza, "Use of conducting polypyrrole blends as gas sensors," *Sensors and Actuators B: Chemical*, vol. 109,pp. 348-354, Sept. 2005.
- [6] M. E. H. Amrani, R. M. Dowdeswell, P. A. Payne, and K. C. Persaud, "An intelligent gas sensing system," *Sensors and Actuators B: Chemical*, vol. 44,pp. 512-516, Oct. 1997.
- [7] K. C. Persaud, S. M. Khaffaf, J. S. Payne, A. M. Pisanelli, D. H. Lee, and H. G. Byun, "Sensor array techniques for mimicking the mammalian olfactory system," *Sensors and Actuators B: Chemical*, vol. 36,pp. 267-273, Oct. 1996.
- [8] M. E. Hassan Amrani, P. A. Payne, and K. C. Persaud, "Multi-frequency measurements of organic conducting polymers for sensing of gases and vapours," *Sensors and Actuators B: Chemical*, vol. 33,pp. 137-141, July 1996.
- [9] J. Auge, P. Hauptmann, J. Hartmann, S. Rosler, and R. Lucklum, "Versatile microcontrolled gas sensor array system using the quartz microbalance principle and pattern recognition methods," *Sensors and Actuators B: Chemical*, vol. 26,pp. 181-186, May 1995.
- [10] Z. K. Chen, S. C. Ng, S. F. Y. Li, L. Zhong, L. Xu, and H. S. O. Chan, "The fabrication and evaluation of a vapour sensor based on quartz crystal microbalance coated with poly(o-anisidine) langmuir-blodgett layers," *Synthetic Metals*, vol. 87,pp. 201-204, Apr. 1997.
- [11] A. Hierlemann, U. Weimar, G. Kraus, M. Schweizer-Berberich, and W. Gopel, "Polymer-based sensor arrays and multicomponent analysis for the detection of hazardous organic vapours in the environment," *Sensors and Actuators B: Chemical*, vol. 26,pp. 126-134, May 1995.
- [12] A. F. Holloway, A. Nabok, M. Thompson, A. K. Ray, and T. Wilkop, "Impedance analysis of the thickness shear mode resonator for organic vapour sensing," *Sensors and Actuators B: Chemical*, vol. 99,pp. 355-360, Feb. 2004.

- [13] V. I. Kalchenko, I. A. Koshets, E. P Matsas, O. N Kopylov, A Solovyov, and Z. I. Shirshov Yu. M. Kazantseva, "Calixarene-based QCM Sensors Array and Its Response to Volatile Organic Vapours," *Materials Science*, vol. 20, pp. 73-87, 2003.
- [14] P. Nelli, E. Dalcanale, G. Faglia, G. Sberveglieri, and P. Soncini, "Cavitands as selective materials for QMB sensors for nitrobenzene and other aromatic vapours," *Sensors and Actuators B: Chemical*, vol. 13, pp. 302-304, May 1993.
- [15] X. C. Zhou, L. Zhong, S. F. Y. Li, S. C. Ng, and H. S. O. Chan, "Organic vapour sensors based on quartz crystal microbalance coated with self-assembled monolayers," *Sensors and Actuators B: Chemical*, vol. 42, pp. 59-65, July 1997.
- [16] G. Sauerbrey, "Verwendung von Schwingquarzen zur Wägung dünner Schichten und zur Mikrowägung," *Zeitschrift für Physik*, vol. 155, pp. 206, 1959.
- [17] J. W. Gardner and P. N. Bartlett, "Electronic Noses Principles and Applications," pages 245, Oxford University Press, New York, 1999.
- [18] J. Auge, K. Dierks, F. Eichelbaum, and P. Hauptmann, "High-speed multi-parameter data acquisition and web-based remote access to resonant sensors and sensor arrays," *Sensors and Actuators B: Chemical*, vol. 95, pp. 32-38, Oct. 2003.
- [19] G. Barko, J. Abonyi, and J. Hlavay, "Application of fuzzy clustering and piezoelectric chemical sensor array for investigation on organic compounds," *Analytica Chimica Acta*, vol. 398, pp. 219-226, Oct. 1999.
- [20] J. M. Beeley, C. Mills, P. A. Hammond, A. Glidle, J. M. Cooper, L. Wang, and D. R. S. Cumming, "All-digital interface ASIC for a QCM-based electronic nose," *Sensors and Actuators B-Chemical*, vol. 103, pp. 31-36, 2004.
- [21] V. Ferrari, D. Marioli, A. Taroni, and E. Ranucci, "Multisensor array of mass microbalances for chemical detection based on resonant piezo-layers of screen-printed PZT," *Sensors and Actuators B: Chemical*, vol. 68, pp. 81-87, Aug. 2000.
- [22] J. Ito, T. Nakamoto, and H. Uematsu, "Discrimination of halitosis substance using QCM sensor array and a preconcentrator," *Sensors and Actuators B: Chemical*, vol. 99, pp. 431-436, May 2004.
- [23] T. Nakamoto, S. Hanaki, and T. Moriizumi, "Artificial odor-recognition system using neural network for estimating sensory quantities of blended fragrance," *Sensors and Actuators A: Physical*, vol. 57, pp. 65-71, Oct. 1996.
- [24] T. Nakamoto, K. Sukegawa, and E. Sumitomo, "Higher -Order Sensing Using QCM Sensor Array and Preconcentrator with Variable Temperature," *IEEE*, pp. 366-371, 2002.
- [25] T. Nakamoto, Y. Nakahira, H. Hiramatsu, and T. Moriizumi, "Odor recorder using active odor sensing system," *Sensors and Actuators B: Chemical*, vol. 76, pp. 465-469, June 2001.
- [26] K. Nakamura, T. Nakamoto, and T. Moriizumi, "Prediction of QCM gas sensor responses and calculation of electrostatic contribution to sensor responses using a

computational chemistry method," *Materials Science and Engineering: C*, vol. 12, pp. 3-7, Aug. 2000.

- [27] R. Polikar, R. Shinar, L. Udpa, and M. D. Porter, "Artificial intelligence methods for selection of an optimized sensor array for identification of volatile organic compounds," *Sensors and Actuators B: Chemical*, vol. 80, pp. 243-254, Dec. 2001.
- [28] V.I. Kalchenko, I.A. Koshets, E.P. Matsas, O.N. Kopylov, A. Solovyov, Z.I. Kazantseva, and Y.M. Shirshov, "Calixarene-based QCM sensors array and its response to volatile organic vapours," *Materials Science*, vol. 20, 2002.
- [29] T. Yamanaka, K. Yoshikawa, and T. Nakamoto, "Improvement of odor-recorder capability for recording dynamical change in odor," *Sensors and Actuators B: Chemical*, vol. 99, pp. 367-372, May 2004.
- [30] T. Yamanaka, R. Matsumoto, and T. Nakamoto, "Odor recorder for multi-component odor using two-level quantization method," *Sensors and Actuators B: Chemical*, vol. 89, pp. 120-125, Mar. 2003.

Chapter 2

Literature review and theoretical background

2.0 Introduction

This chapter gives a background of the thickness shear mode resonator both theoretically and historically. A description of the transduction mechanism through the quartz and contacting film(s) are given and of how various loading conditions affect quartz parameters. The latter sections give a review of the current state of the art in the area including advanced QCM measurement techniques and QCM based sensor arrays.

2.1 Piezoelectric effect

In 1880 the Curie brothers first reported that when certain crystalline minerals were subjected to a mechanical force an electrical polarization is created [1], this is known as the piezoelectric effect. The opposite effect was first proved theoretically by Lipmann in 1881 and subsequently confirmed experimentally by the Curies [2]. All crystals exhibiting piezoelectric behaviour also show a mechanical deformation on the application of an electric field known as the converse piezoelectric effect. Figure 2.1 shows a schematic of the relationship between the mechanical and electrical variables.

This property is not however common to all crystals. The crystal structure must lack a centre of inversion symmetry; this is only evident in 21 of the 32 crystallographic point groups [3]. Out of these 21 groups only the quartz structure has the combination of

suitable mechanical, electrical, chemical, and thermal parameters to be used significantly in commercial applications [1].

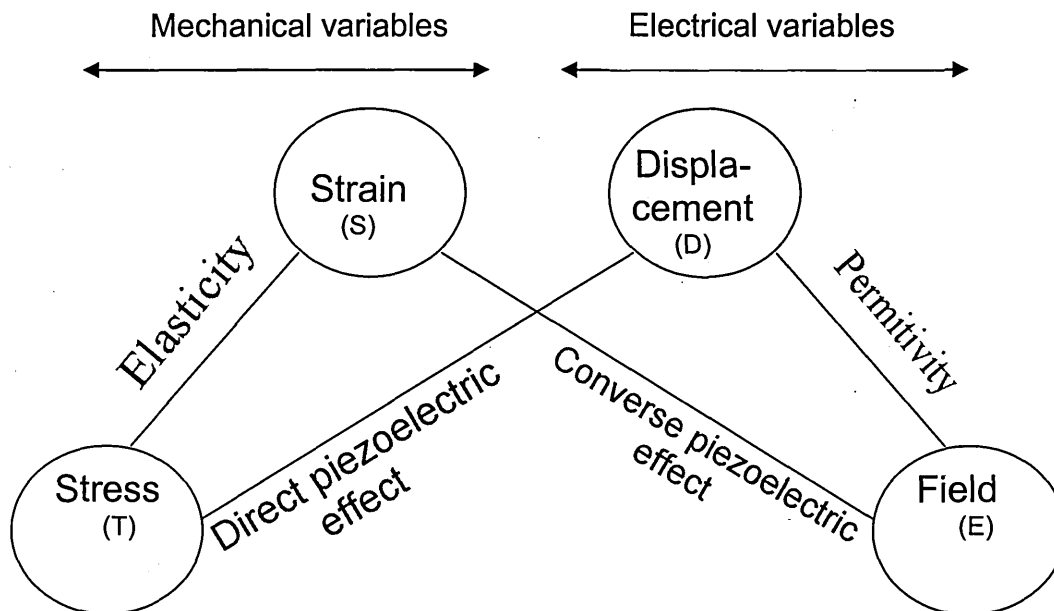


Figure 2.1. The relationship between mechanical and electrical variables.

By application of an alternating electrical field to a crystal it may be excited into mechanical resonance with a standing acoustic wave travelling across the quartz.

2.2 Acoustic waves

The frequencies covered by acoustic waves span from approximately 0.01Hz to several terahertz, with the bulk of sensing applications in the range of a few hundred Hz up to hundreds of MHz. Figure 2.2 shows a small selection of phenomena and devices which operate within the acoustic wave spectrum. Several acoustic wave sensing devices are highlighted [3].

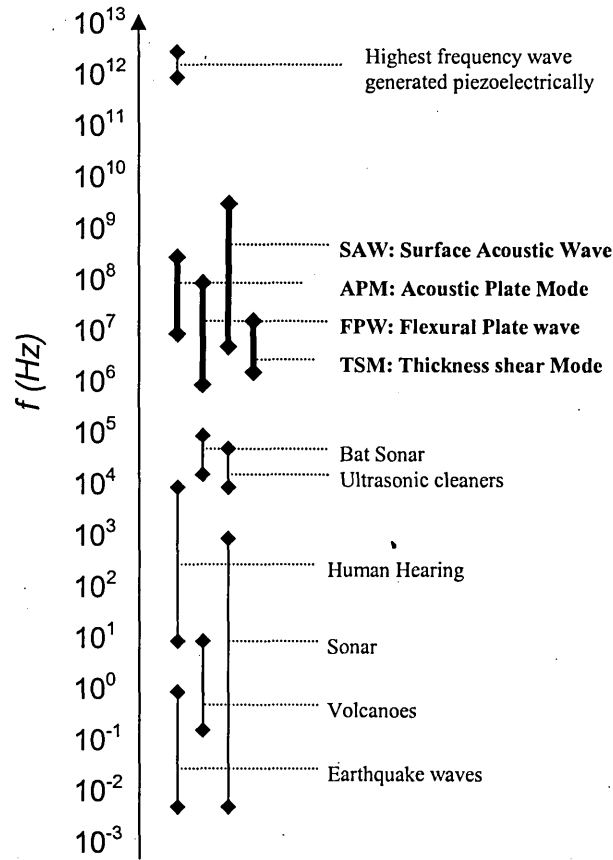


Figure 2.2 The acoustic wave spectrum covers approximately 14 orders of magnitude, the most common acoustic wave sensors are shown and highlighted.

Acoustic wave sensing is based on the principle that the input quantity into the sensing device produces change in the path over which the acoustic wave propagates. Several acoustic wave based devices are now common in studying interactions with thin films and liquids. Typical examples include, Surface Acoustic Waves (SAW), Flexural Plate Wave (FPW), Acoustic plate mode (APM) and the Thickness Shear Mode (TSM) resonator used within this work. To fully characterise the TSM resonator it is essential to understand both how the acoustic wave travels through the quartz and how it interacts with contacting layers and or media.

2.3 The Quartz Crystal Microbalance

The QCM system consists of a thin disk of AT-cut quartz crystal coated with electrodes on each side as shown in figure 2.3. An a.c. signal is applied between the electrodes resulting in a shear deformation wave across the crystal. Due to the piezoelectric properties of the quartz, it can be electrically excited into a number of resonant modes with maximum displacement occurring at the crystal faces (see figure 2.4). The property of maximum displacement at the crystal faces in the Thickness Shear Mode (TSM) makes this mode of excitation extremely sensitive to surface mass accumulation [3].

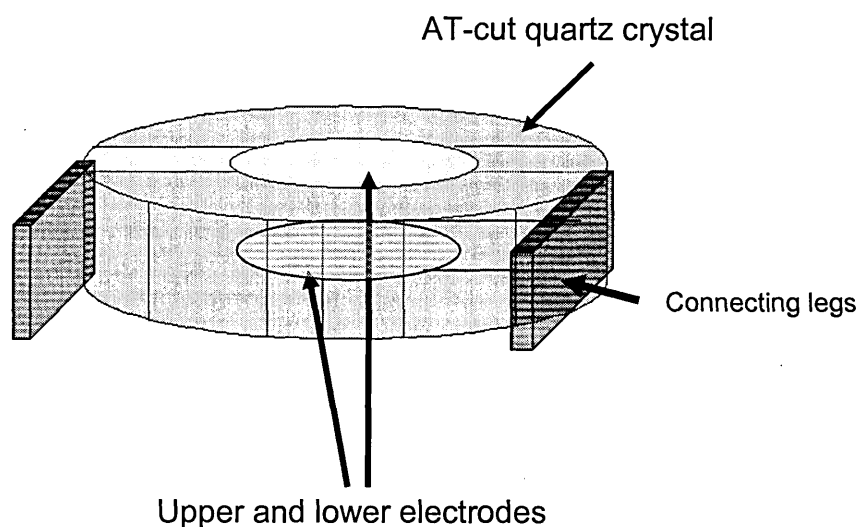


Figure 2.3. Cross sectional schematic of a TSM resonator.

2.3.1 QCM as a gravimetric sensor

In 1959 Sauerbrey [4] first showed that the shift in resonant frequency of a Thickness Shear Mode (TSM) resonator was proportional to the deposited mass on the surface of the crystal. It was originally used for the measurement of metal deposition rates but has since successfully been used in many applications with the sensitivity now reaching sub nanogram levels [5]. In most instances the TSM resonator is configured as a gravimetric

mass sensor often referred to as a Quartz Crystal Microbalance (QCM), where the crystal works as the frequency-determining element in an electrical oscillator circuit.

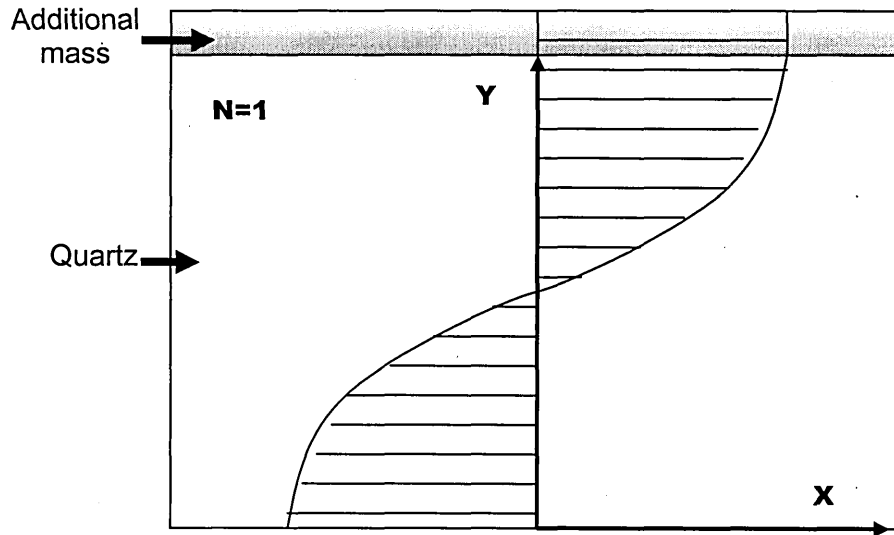


Figure 2.4. Displacement profile showing the fundamental resonant frequency ($N=1$) with maximum displacement at the crystal surfaces.

Additional mass is seen as an extension of the quartz.

For resonance to occur in a quartz crystal the total phase shift of the standing wave propagating through the crystal must be an integer of 2π , producing constructive interference between the incident and the return waves. When resonance occurs the following criteria described by equations (2.1-2.3) must apply.

$$h_q = N \left(\frac{\lambda}{2} \right) \quad (2.1)$$

where λ is the acoustic wavelength, h_q is the crystal thickness and N is the resonator harmonic number representing the resonant mode.

$$f_0 = N \frac{v_q}{2h_q} \quad (2.2)$$

where f_0 is the fundamental resonant frequency and v_q is the shear wave velocity given by equation 2.3.

$$v_q = \left(\frac{\mu_q}{\rho_q} \right)^{1/2} \quad (2.3)$$

where ρ_q is the quartz density (2.65g/cm³), and μ_q is the shear stiffness (2.95×10¹¹ dyne/cm²). Sauerbrey demonstrated that a small increase in mass is proportional to a change in thickness and resonant frequency as shown by equation (2.4) [4].

$$\frac{\Delta f_0}{f_0} = -\frac{\Delta h_q}{h_q} = -\frac{\Delta M_q}{M_q} \quad (2.4)$$

where $M_q = \rho_q h_q$ is the mass density. Substituting in equations (2.2) and (2.3) equation (2.5) can be obtained directly relating the change in mass to the change in resonant frequency often referred to as the Sauerbrey relationship.

$$\Delta f = -\frac{2f_0^2 \Delta M_q}{\sqrt{\mu_q \rho_q}} \quad (2.5a)$$

Equation (2.5a) can be presented in the form:

$$\Delta M_q (\text{g}) / \text{cm}^2 = \frac{\Delta f}{2.26 \times 10^{-6} f_0^2} \quad (2.5b)$$

Equation (2.5) is only valid on the condition that the acoustic phase shift ϕ across the film (equation 2.6) is small.

$$\phi = \omega h \left(\frac{\rho}{G} \right)^{1/2} \quad (2.6)$$

where ρ is the film density h is the film thickness $\omega = 2\pi f_0$ and G is the shear modulus (assumed real).

The relation described by Sauerbrey is however a limited case and conditions of the additional layer/mass must be acoustically thin, rigidly coupled to the surface of the QCM, moving synchronously with quartz itself. Sauerbrey assumes the additional mass may be treated as an extension of the quartz itself, in essence just adding to the thickness of the quartz as shown in figure 2.4. The range of which the Sauerbrey's equation is considered suitable is $\frac{\Delta m_f}{m_q} < 2\%$ [6]. Where Δm_f is the areal mass density of the foreign layer and m_q areal mass density of the quartz.

An increase in the working range of the standard QCM was extended by improvements in both crystal design and oscillator driving circuits [6,7]. In 1971 Behrndt proposed that the period τ of the crystal oscillation is proportional to the mass loading as described in equation (2.7) :

$$\frac{m_f}{m_q} = \frac{\tau - \tau_q}{\tau_q} = -\frac{f - f_q}{f} \quad (2.7)$$

where τ is the oscillation period unloaded quartz and τ_q is the oscillation period of the loaded quartz. Using equation (2.7) the operating range of the QCM is increased to $\frac{\Delta m_f}{m_q} < 10\%$.

Benes [6,7] argues that equation (2.7) makes more sense theoretically as compared to equation (2.4) because it is based on direct proportionality between the crystal thickness h_q and the period of oscillation at resonance $\tau_q = \frac{1}{f_q}$.

2.3.2. Z match technique

Miller and Bolef [8,9] were the first to treat the quartz crystal/film as a composite resonator, taking into account the acoustic properties of the film. Their long and complex expression was later simplified and reduced by Lu and Lewis [10] to equation (2.8).

$$Z_q \tan\left(\frac{f_c}{f_q}\right)\pi + Z_f \tan\left(\frac{f_c}{f_f}\right)\pi = 0 \quad (2.8)$$

where Z_q is the acoustic impedance of the quartz, Z_f is the acoustic impedance of the film, f_c is the composite resonant frequency and f_q and f_f are the mechanical resonant frequencies of the quartz and film respectively.

The relationship between the mass load and frequency is therefore given by equation (2.9).

$$\frac{m_f}{m_q} = -\frac{Z_f f_q}{Z_q \pi f} \arctan\left(\frac{Z_q}{Z_f} \tan \frac{\pi f}{f_q}\right) \quad (2.9)$$

Using the following substitutions.

$$f_q = \frac{1}{2h_q} \sqrt{\frac{c_q}{\rho_q}} \quad (2.10) \text{ for the mechanical resonance frequency of quartz.}$$

$$f_f = \frac{1}{2h_f} \sqrt{\frac{c_f}{\rho_f}} \quad (2.11) \text{ for the mechanical resonance frequency of film.}$$

$$Z_q = \rho_q v_q = \sqrt{\rho_q c_q} \quad (2.12) \quad Z_f = \rho_f v_f = \sqrt{\rho_f c_f} \quad (2.13)$$

where v_q is the shear wave velocity in quartz, c_q is the shear stiffness constant for quartz, v_f is the shear wave velocity in the film and c_f is the shear stiffness constant for the film.

The operating mass range from equation (2.9) is $\frac{\Delta m_f}{m_q} < 70\%$ [6]. The method is generally referred to as the ‘z match’ technique and is now used in commercial mass deposition monitors. The values of density and acoustic impedance for the deposited material must be known for successful implementation of the technique.

2.3.3 Transmission Line Model

The QCM is often modelled as a piezoelectric layer (the quartz) and a number of connected non piezoelectric layers into which the acoustic wave spreads [11,12] (see figure 2.5). The behaviour of a quartz resonator may be derived from the one dimensional wave equation and a number of boundary conditions. When an alternating voltage is applied to the quartz electrodes two acoustic waves (A and B) are generated travelling in opposite directions. The displacement in the crystal is given by a superposition of these waves and must satisfy the acoustic boundary conditions on each face of the crystal and all external interfaces equations (2.17a-f) [13]. The acoustic voltage $u(z)$ and current $i(z)$ can therefore be defined by equations (2.14a and b) [14].

$$u_i(z) = (A_i e^{jk_i z} + B_i e^{-jk_i z}) e^{j\omega T} \quad (2.14a)$$

$$i_i(z) = \frac{1}{Z} (A_i e^{jk_i z} - B_i e^{-jk_i z}) e^{j\omega T} \quad (2.14b)$$

where $\gamma_q = jk = j \frac{\omega}{(G/\rho)^{1/2}}$ (2.15) is the complex wave propagation constant and

$Z = (\rho G)^{1/2}$ (2.16) is the complex impedance where G is the complex shear modulus.

1. Continuous displacement at the crystal coating interface

$$u_i(z = h_i) = u_{i+1}(z = h_i) \quad (2.17a)$$

2. Continuous shear stress at the crystal coating interface

$$T_i(z = h_i) = T_{i+1}(z = h_i) \quad (2.17b)$$

3. Vanishing shear stress at free crystal surface

$$T(z = 0) = 0 \quad (2.17c)$$

4. Vanishing shear stress at free coating surface

$$T(z = \sum h_i) = 0 \quad (2.17d)$$

5. The driving electrical potential at the upper electrode

$$\phi(z = hq) = -\phi_0 e^{j\omega t} \quad (2.17e)$$

6. The driving electrical potential at the lower electrode

$$\phi(z = 0) = \phi_0 e^{j\omega t} \quad (2.17f)$$

The analogy between electromagnetic and acoustic fields can easily be made. Table 2.1 shows the equivalent relationships between acoustic and electrical wave propagation.

Mechanical stress	T	↔	U	Electrical Voltage
Particle speed	\dot{u}	↔	I	Electric current
Acoustic impedance	$Z_a = T/\dot{u}$	↔	$Z_{\text{elect}} = U/I$	Electrical impedance

Table 2.1. Equivalent relationship between acoustic and electrical wave propagation

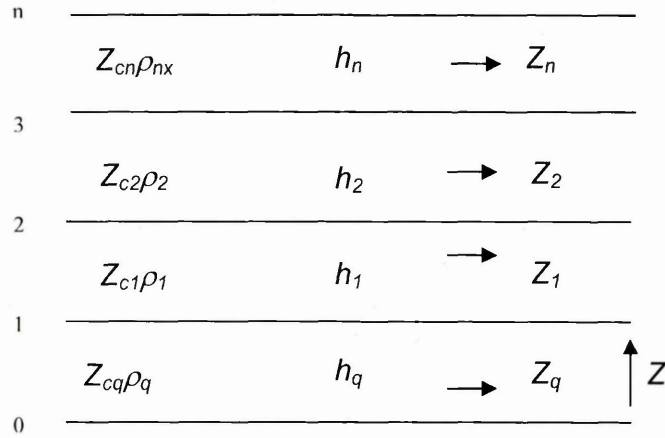


Figure 2.5. Generally accepted arrangement of a QCM with a multilayer number of coatings (n).

It is common to treat the propagation of acoustic waves as analogous to the transmission of electrical waves. Piezoelectric layers such as quartz can be defined by a three port model with two acoustic ports representing the top and bottom quartz surfaces, and the third port coupled via a transformer representing the piezoelectric connection [3,11,13,15]. This arrangement is widely known as a transmission line shown in figure 2.6. An additional deposited layer on one side of the quartz is shown by an extension of the transmission line shown in figure 2.6. The Transmission Line Model (TLM) describes the piezoelectric transformation between electrical and mechanical vibration and the propagation of acoustic waves in the system.

The transmission line concept is implemented using a chain matrix technique [13,16].

The propagation matrix \mathbf{P} (2.18a) and transfer matrix \mathbf{T} (2.18b) are used in order to determine the transformation matrix \mathbf{M} as shown in equation (2.19).

$$P_q = \begin{pmatrix} e^{-\gamma_q \frac{h_q}{2}} & 0 \\ 0 & e^{\gamma_q \frac{h_q}{2}} \end{pmatrix} \quad (2.18a)$$

$$T_q = \begin{pmatrix} \frac{1}{Z_q} & 1 \\ \frac{1}{Z_q} & -1 \end{pmatrix} \quad (2.18b)$$

$$M_q = T_q^{-1} P_q^{-1} T_q = \begin{pmatrix} \cos(\gamma_q \frac{h_q}{2}) & Z_q \sin(\gamma_q \frac{h_q}{2}) \\ \frac{1}{Z_q} \sin(\gamma_q \frac{h_q}{2}) & \cos(\gamma_q \frac{h_q}{2}) \end{pmatrix} \quad (2.19)$$

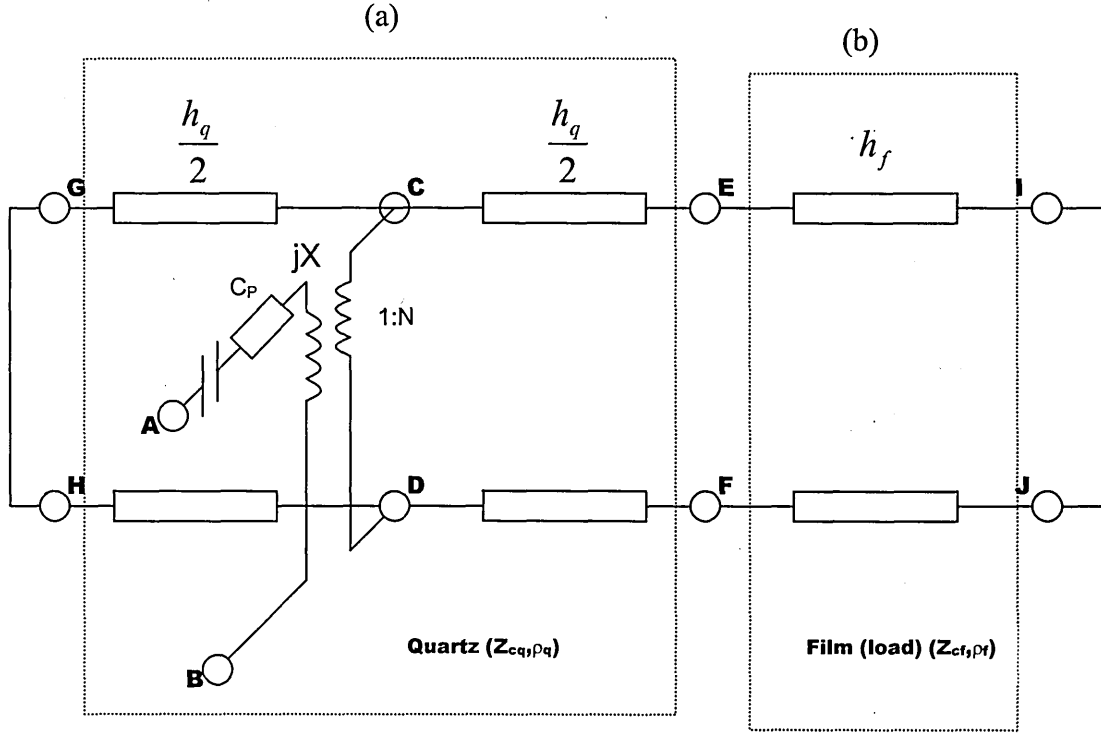


Figure 2.6. The transmission line Model (TLM). Section (a) identifies the uncoated quartz crystal with two acoustic ports and one electrical port representing the piezoelectric properties of the quartz. Section (b) identifies the additional non piezoelectric layer.

The acoustic impedance at CD can be realised as electrical impedance at port AB using the following equations.

$$Z = Z_{AB} = \frac{1}{j\omega C_p} + jX + \frac{1}{N^2} Z_{CD} \quad (2.20)$$

where jX represents the piezoelectric transformer with turns ratio 1:N given by equations 2.21 and 2.22 respectively.

$$jX = \frac{1}{j\omega C_p} \frac{K^2}{\alpha} \sin \alpha \quad (2.21)$$

$$\frac{1}{N^2} = \frac{1}{\omega C_p} \frac{4K^2}{\alpha} \frac{1}{Z_{cq}} \sin^2 \frac{\alpha}{2} \quad (2.22)$$

The final solution to the one dimensional problem is given in equation (2.23).

$$Z = \frac{1}{j\omega C_p} \left[1 - \frac{K^2}{\alpha} \frac{2 \tan \frac{\alpha}{2} - j \frac{Z_L}{Z_{cq}}}{1 - j \frac{Z_L}{Z_{cq}} \cot \alpha} \right] \quad (2.23)$$

Using

$K^2 = \frac{e_q^2}{\varepsilon_q c_q}$ is the electromechanical coupling coefficient of quartz.

$\alpha = \omega h_q \sqrt{\frac{\rho_q}{c_q}}$ is the acoustic phase shift inside the quartz crystal.

$Z_{cq} = \sqrt{\rho_q c_q}$ is the characteristic acoustic impedance of quartz.

$C_p = \varepsilon_q \frac{A}{h_q}$ is the static quartz crystal capacitance.

where e_q is the piezoelectric constant, ε_q is the permittivity, and c_q is the piezoelectric stiffened elastic constant (q designates properties for quartz). Z_L is the acoustic load impedance acting at the surface of the quartz crystal and η_q is the phenomenological quartz viscosity.

It is often helpful to split the electrical impedance in equation (2.23) into a parallel circuit consisting of the static capacitance C_p and a motional impedance of the quartz (Z_m). The motional impedance may be split further into two parts Z_{mq} and Z_{mL} representing the unloaded quartz ($Z_{mL}=0$) and the acoustic load respectively.

$$Z_m = Z_{mq} + Z_{mL}$$

$$Z_{mq} = \frac{1}{j\omega C_p} \left[\frac{\frac{\alpha}{K^2}}{2 \tan \frac{\alpha}{2}} - 1 \right] \quad (2.24)$$

$$Z_{mL} = \frac{1}{\omega C_p} \frac{\alpha}{4K^2} \frac{Z_L}{Z_{cq}} \frac{1}{1 - \left(j \frac{Z_L}{Z_{cq}} / 2 \tan \frac{\alpha}{2} \right)} \quad (2.25)$$

Close to the resonant frequency of the unloaded quartz crystal the following approximation (2.26) may be used.

$$\tan \frac{\alpha_q}{2} \approx \frac{4\alpha_q}{(N\pi)^2 - \alpha^2} \quad (2.26)$$

where N is the resonator harmonic number (odd integer). Substituting equation (2.26) into equation (2.24) gives

$$Z_{mq} = \frac{1}{j\omega C_p} \left[\frac{(N\pi)^2 - \alpha^2}{8K^2} - 1 \right] \quad (2.27)$$

where the phase shift across the quartz is $\alpha = \omega h_q (\rho_q / \mu_q)^{\frac{1}{2}}$. To account for losses in the quartz $\mu_q = \mu_{qo} + j\omega \eta_q \cdot \mu_{qo}$ is the shear stiffness and η_q is the effective quartz viscosity. Substituting these into equation (2.27) gives equation (2.28)

$$Z_{mq} = \left(\frac{\omega^2 h_q^2 \rho_q \eta_q}{8K^2 C_p |\mu_q|^2} \right) + j\omega \left(\frac{h_q^2 \rho_q \mu_{qo}}{8K^2 C_p |\mu_q|^2} \right) + \frac{1}{j\omega} \left(\frac{(N\pi)^2 - 8K^2}{8K^2 C_p} \right) \quad (2.28)$$

$$R_q + j\omega L_q + \frac{1}{j\omega C_q} \quad (2.29)$$

Equations (2.29) can be evaluated to the simple RLC circuit if one assumes that $\omega = \omega_s = 2\pi f_s$, where the series resonant frequency is f_s . Figure 2.7 shows the series RLC network often referred to as the motional branch. By aligning equation (2.28) and equation (2.29) the circuit elements may be identified (2.30-2.32). Assuming quartz losses are small the following may be applied.

$\omega\eta_q \ll \mu_{qo}$, therefore $|\mu_q| \cong \mu_{qo}$ and let $\omega = \omega_s$

$$R = \left(\frac{\omega^2 h_q^2 \rho_q \eta_q}{8K^2 C_p |\mu_q|^2} \right) \quad (2.30)$$

$$L = \left(\frac{h_q^2 \rho_q}{8K^2 C_p \mu_q} \right) \quad (2.31)$$

$$C = \left(\frac{8K^2 C_p}{(N\pi)^2 - 8K^2 C_p} \right) \quad (2.32)$$

Equations (2.30-2.32) can be transformed into the motional branch of the commonly used Butterworth Van dyke (BVD) equivalent circuit shown in figure 2.7

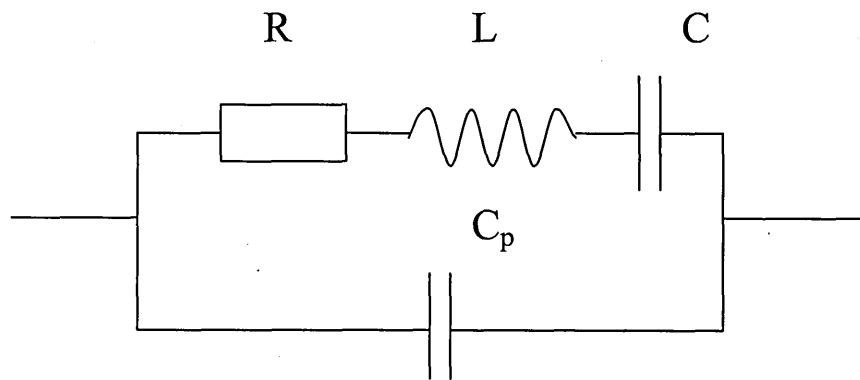


Figure 2.7. The lumped element Butterworth Van-Dyke equivalent circuit model for an uncoated QCM near resonance.

The lumped element BVD equivalent model may be used instead of the transmission line model with negligible deviation when modelling the unperturbed resonator [17].

The Butterworth-Van-Dyke (BVD) model consists of four variable parameters: Resistance (R), Inductance (L) and Capacitance (C) in series representing the motional branch, and a parallel capacitance (C_p) representing the static capacitance of the quartz resonator.

crystal compose the motional arm, while Parallel Capacitance (C_p) represents the static arm of the unperturbed crystal as shown in figure 2.7. Each element in the model represents a physical property of the crystal. The resistance 'R' represents the energy loss arising from the effects of the viscous medium, internal friction and damping induced by the crystal holder, inductance 'L', the initial mass/motional inertia of the system, capacitance C the mechanical elasticity of the quartz and parallel capacitance ' C_p ', which consists of the capacitance of the quartz between the electrodes and the parasitic capacitance of the crystal fixture. The parallel capacitance C_p dominates the admittance spectra away from quartz resonance.

$$C_p = \epsilon_q \frac{A}{h_q} \quad (2.33)$$

Where A is the active area of the quartz. The BVD model may be conveniently used to model the unloaded quartz and allows quick and effective simulation and calculation of the quartz resonances. From the equivalent circuit model the circuit admittance ($Y=G+JB$) can be determined.

$$Y(\omega) = j\omega C_p + \frac{1}{Z_m} \quad (2.34)$$

$$\text{where } Z_m(\omega) = R + j\omega L + \frac{1}{j\omega C} \quad (2.35)$$

When $R \rightarrow 0$, two distinct resonant frequencies are apparent as shown in figure 2.8. (i) The series resonant frequency f_s , where the motional reactance is zero; and (ii) the parallel resonant frequency f_p where the total reactance is equal to zero. These correspond to the frequencies of maximum and minimum admittance and can be defined as:

$$f_s = \frac{1}{2\pi\sqrt{LC}} \quad (2.36)$$

$$f_p = \frac{1}{2\pi} \sqrt{\left[\frac{1}{L} \left(\frac{1}{C} + \frac{1}{C_p} \right) \right]} \quad (2.37)$$

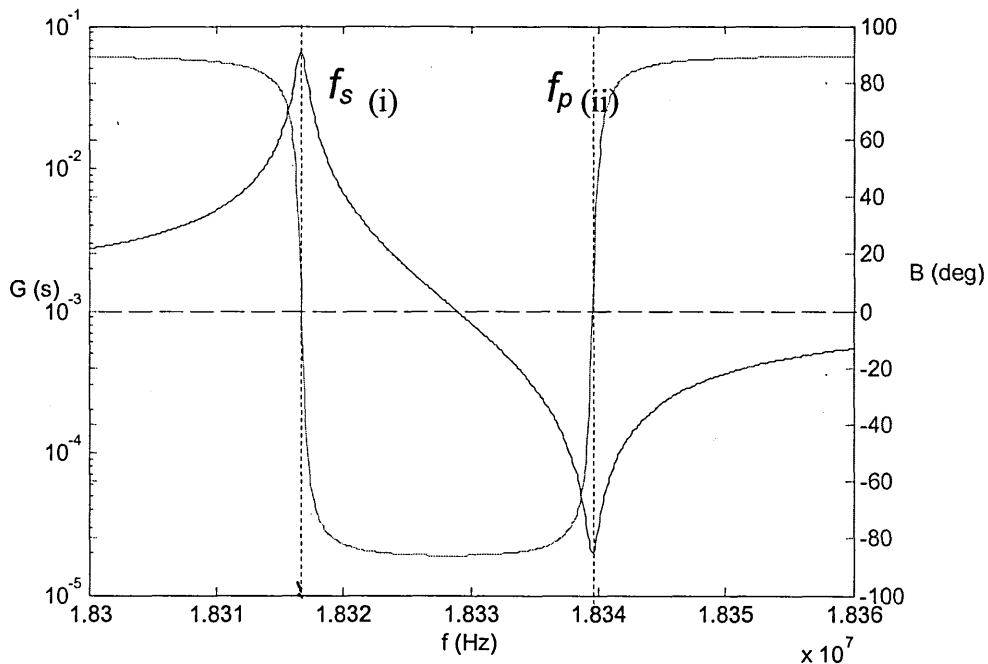


Figure. 2.8. Admittance magnitude and phase as a function of frequency with the series (f_s) and parallel (f_p) resonant frequencies indicated.

In all practical applications where energy dissipation occurs ($R > 0$), frequencies of f_s , f_p and zero phase differ from those at the max /min admittance shown in figure 2.9. In the case of series resonance f_s , the frequencies are defined below. Where $f_{(G_{max})}$ is the frequency at maximum admittance magnitude and $f_{(B=0)_{lower}}$ the lower frequency of zero phase crossing illustrated in figure 2.9.

$$f_{(G_{max})} = \frac{1}{2\pi\sqrt{LC}} \left(1 - \frac{C_p R^2}{2L} \right) \quad (2.38)$$

$$f_{(B=0)_{lower}} = \frac{1}{2\pi\sqrt{LC}} \left(1 + \frac{C_p R^2}{2L} \right) \quad (2.39)$$

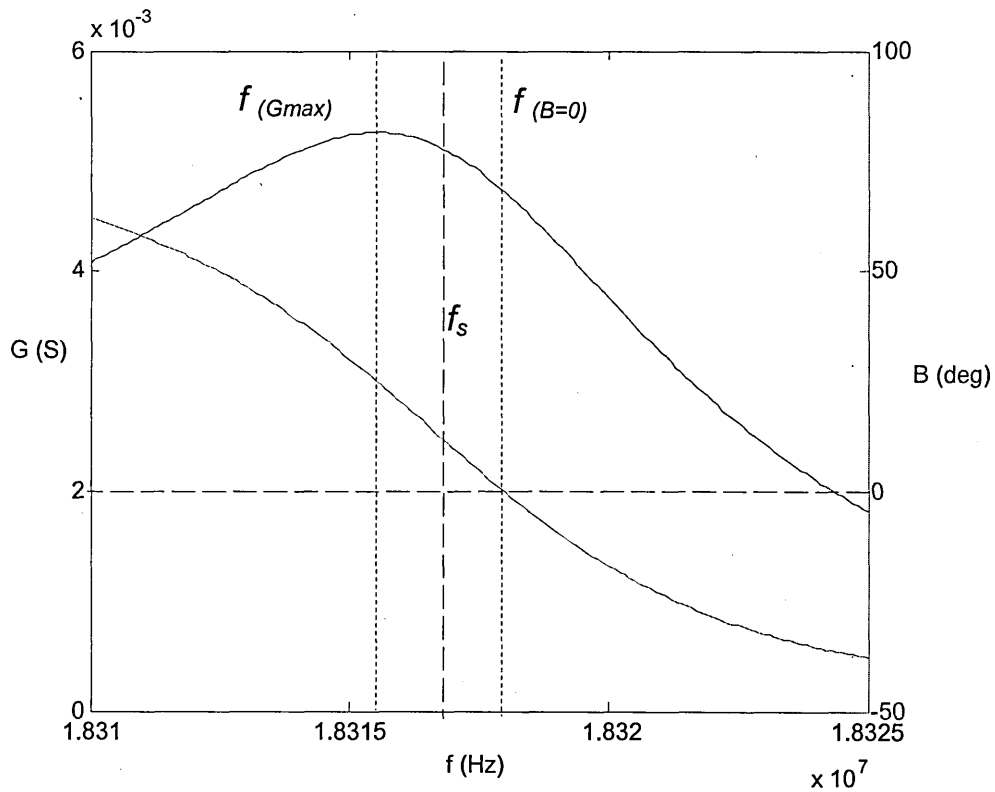


Figure. 2.9 Admittance magnitude and phase as a function of frequency with frequencies at admittance maximum $f_{(Gmax)}$, zero phase $f_{(B=0)}$ and series resonance f_s indicated.

2.4 Surface loading

From equation (2.25) the surface load acting on the quartz may be represented by

$$Z_{mL} = \frac{1}{\omega C_p} \frac{\alpha}{4K^2} \frac{Z_L}{Z_{cq}} \frac{1}{1 - \left(j \frac{Z_L}{Z_{cq}} / 2 \tan \frac{\alpha}{2} \right)} \quad (2.25 \text{ repeated})$$

For small loads the approximation shown in equation (2.40) may be used. In this case the last term in equation (2.25) can be simplified to equation (2.41) [17].

$$\frac{Z_L}{Z_{cq}} \ll \tan \frac{\alpha_q}{2} \quad (2.40)$$

$$= \frac{1}{\omega C_p} \frac{\alpha}{4K^2} \frac{Z_L}{Z_{cq}} = R_l + jX_l \quad (2.41)$$

The motional impedance is now directly related to the acoustic load Z_L . With Z_{mL} a complex resistance where R_l and X_l are the real and imaginary components in series with the motional resistance and defines the surface load on the quartz.

Equation (2.35) can be modified to incorporate these two additional elements in the motional branch equation (2.42) and shown schematically in a modified Butterworth Van Dyke circuit shown in figure 2.10.

$$Z_m(\omega) = (R + R_l) + j\omega(L + L_l) + \frac{1}{j\omega C} \quad (2.42)$$

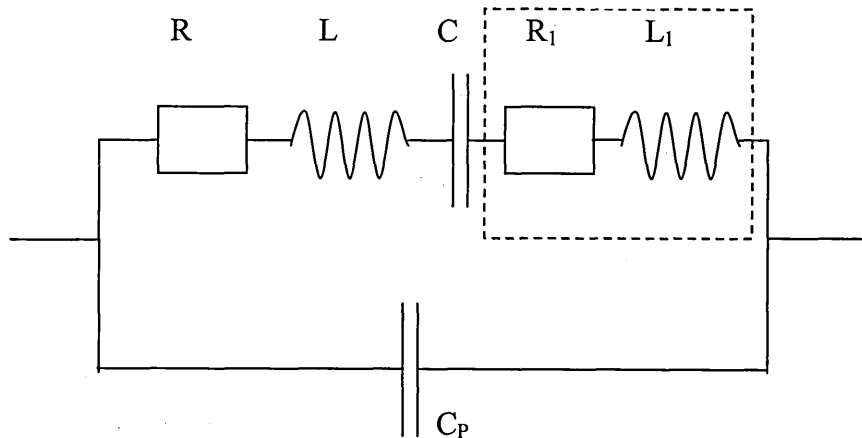


Figure 2.10. Modified Butterworth Van-Dyke Equivalent circuit Model for an uncoated QCM near resonance with additional elements R_l and L_l accounting for the surface load.

2.4.1 The Acoustic Load Concept (ALC)

Lucklum and co-workers [11,18-20] have recently introduced the Acoustic Load concept (ALC). This offers a direct relationship between the complex acoustic impedance Z_L and two parameters which may be measured using several experimental techniques described in Chapter 3. These approximations may be applied to all typical coatings used in chemical or biochemical sensing [11,21]. Values of L and f_0 are physical properties specific to a particular quartz resonator and may be obtained from a separate measurement of the bare quartz. The imaginary part of Z_L is related to the frequency at the phase admittance maximum ($f_{(Gmax)}$) which corresponds to resonance of the motional arm according to equation (2.43a) (see figure 2.9). The real part of Z_L is related to acoustic energy dissipation/resistance equation (2.43b).

$$\frac{\Delta f_s}{f_0} = -\frac{\text{Im}(Z_L)}{\pi Z_{cq}} \quad (2.43a) \qquad \frac{\Delta R}{2\omega_0 L} = \frac{\text{Re}(Z_L)}{\pi Z_{cq}} \quad (2.43b)$$

2.4.2 The Viscoelastic film

Of considerable importance to the sensor world is the vapour-sensitive film. These coatings combine properties of viscous and rigid materials. Many polymers exhibiting viscoelastic properties are now used as chemically sensitive films in sensing applications. Under sinusoidal deformation the properties of the viscoelastic material are described by a complex shear modulus.

$$G = G' + jG''$$

Where, the real part G' is the stress component in phase with the strain which leads to energy storage. The imaginary component G'' is the stress component 90° out of phase with the strain, and is a measure of energy dissipation. The two terms of the shear modulus $G' + jG''$ are often known as the storage and loss moduli respectively. When

resonance occurs the part of the film in contact with the crystal oscillates synchronously with it, however the outer sections may lag behind the inner regions in contact with the oscillating crystal. This is known as the acoustic phase shift φ .

The acoustic load of a viscoelastic film with finite thickness can be calculated from equation (2.44), which may be rearranged separating the mass and acoustic factor M (2.46a) and V (2.46b) respectively [11,21].

$$Z_L = j(\rho_f G_f)^{1/2} \tan \left(\omega \left(\frac{\rho_f}{G_f} \right)^{1/2} h_f \right) \quad (2.44)$$

where $G_f = G' + jG''$ which may be transformed into

$$Z_L = j\omega\rho_f h_f \frac{\tan \varphi}{\varphi} = jMV \quad (2.45)$$

where $\varphi = h_f \omega \left(\frac{\rho_f}{G_f} \right)^{1/2}$ is the phase difference between crystal surface and outer surface

of the coating, $M = \omega\rho_f h_f$ (2.46a) is the mass factor and $V = \frac{\tan \varphi}{\varphi}$ (2.46b) is the

acoustic factor. For a small but perceptible phase shift φ , the following approximation

may be applied. $\tan \varphi \approx \frac{\varphi + \varphi^3/3}{\varphi}$. The acoustic factor may be rewritten as shown in

equation (2.47).

$$V = \frac{\tan \varphi}{\varphi} \approx \frac{\varphi + \varphi^3/3}{\varphi} = 1 + \frac{\varphi^2}{3} = 1 + \frac{M^2}{3Z_{cf}^2} \quad (2.47)$$

where Z_{cf} is the acoustic impedance of the film. The acoustic load for a sufficiently thin film becomes

$$Z_L = jM \left(1 + \frac{M^2}{3Z_{cf}^2} \right) \quad (2.48)$$

Using equations (2.43a) and (2.43b) the frequency shift Δf and resistance change ΔR caused by a viscoelastic film are approximated by equations (2.49a) and (2.49b) respectively.

$$\Delta f \propto M \left(1 + \frac{1}{3} \frac{G'}{\rho |G|^2} M^2 \right) \quad (2.49a)$$

$$\Delta R \propto M \left(1 + \frac{1}{3} \frac{G''}{\rho |G|^2} M^2 \right) \quad (2.49b)$$

The resultant frequency shift due to the viscoelastic coating has the effect of an additional erroneous mass. This extra perceived frequency shift leads to an over estimation of the mass accumulation unless viscoelastic contributions are considered. The viscoelastic film also causes an increase in the resistance, this is created by the introduction of the loss moduli G'' associated with a viscoelastic film.

2.4.3 Special case for Sauerbrey relationship

As stated in section 2.31 the Sauerbrey equation is based on a thin rigid film . This is a special case of equation (2.44) where h_f is small and G a real number only (i.e. the film is thin and sufficiently rigid). Equations (2.44) may then be simplified if one assumes $\gamma_f h_f \rightarrow 0$ and $\tanh(\gamma_f h_f) \rightarrow \gamma_f h_f$ and therefore the load $Z_L = j\omega\rho_f h_f$. Substituting in equation (2.43a) the change in frequency Δf can be written as equation (2.50), which is equivalent to the Sauerbrey relation [13].

$$\Delta f = -\frac{2f_0^2 \rho_f h_f}{\sqrt{c_q \rho_q}} \quad (2.50)$$

2.5 Modelling QCM loading using the Modified BVD equivalent circuit

The effects of each parameter of the BVD equivalent circuit on the admittance spectra are shown in figures 2.11 a-d produced by MATLAB version 6.0 simulations. Figure 2.11 shows the direct effects of mass loading through an additional inductance L_1 in the BVD model; the whole spectrum is translated to a lower frequency without any change in peak or half width. Figure 2.11b shows an increase in the motional resistance R_1 directly related to damping effects and primarily caused by changes in the film viscosity or by contacting liquid medium. Figures 2.11c shows changes in the capacitance C , which represents the mechanical elasticity of the quartz. Figures 2.11d shows changes in the parallel capacitance C_p , which determines the admittance away from resonance, and consists of the capacitance of the quartz between the electrodes and the parasitic capacitance of the crystal fixture. Both C and C_p remain constant throughout coating and analyte exposure as they are intrinsic properties of the crystal.

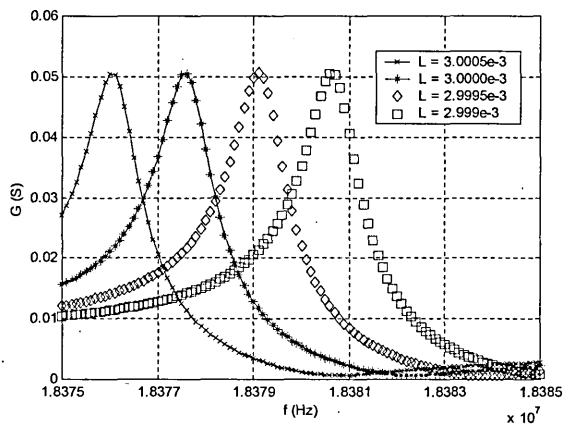


Figure 2.11a. The effects of pure mass loading leading to an increase in L (L_1) associated with a decrease in resonant frequency.

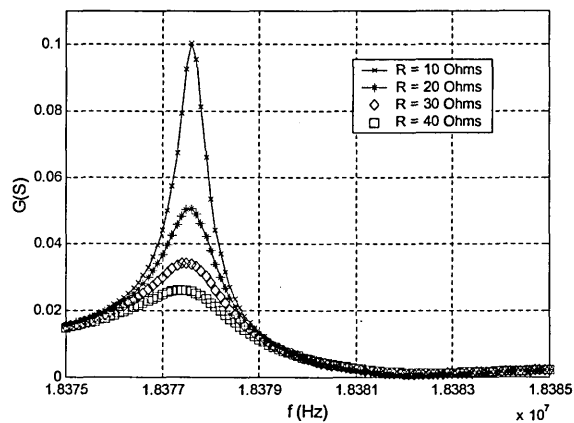


Figure 2.11b. Changes in viscoelastic film properties shown through changes in R (R_1).

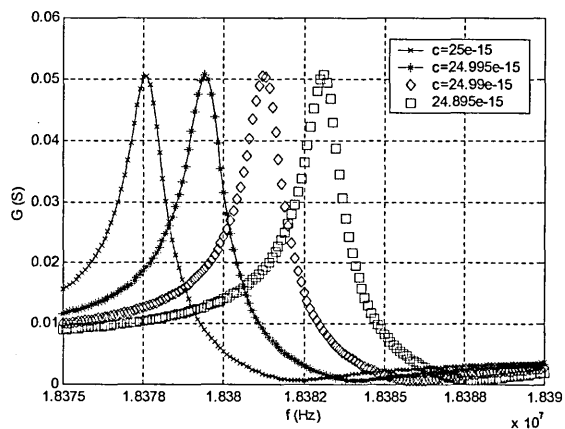


Figure 2.11c Several values of C representing various values of quartz elasticity.

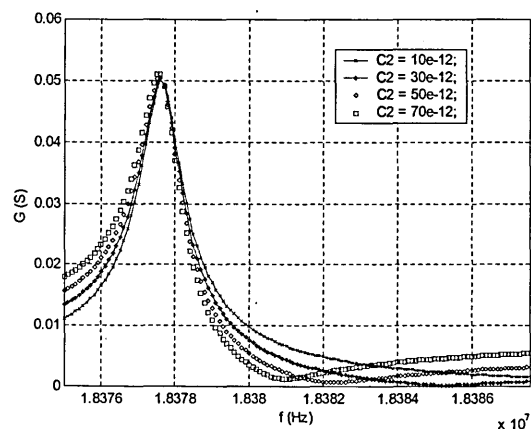


Figure 2.11d Increases in parasitic capacitance C_p .

2.6 Modelling a viscoelastic film

The acoustic load (Z_L) representing a viscoelastic film described in equation (2.44) may be modelled three dimensionally as shown in figures 2.12a&b through 2.13a&b, showing the imaginary and real parts of the acoustic load respectively. Both figures show two distinct regions, one principally plain region with slight incline and the second region showing large maxima/minima. These two regions correspond to acoustically thin and acoustically thick films [11,22]. The right hand corner of figures 2.12a and 2.13a show the film in its glassy state (acoustically thin films). In this region the changes in the film shear parameters have a relatively small effect on both the imaginary and real parts of the load (hence a small Δf and ΔR). An enlarged scale of this region is shown in figures 2.12b and 2.13b for the imaginary and real values of Z_L respectively. Although changes in either parameter are relatively small in comparison to figures 2.12a and 2.13a, a distinguishable variation is still present in the glassy state region. In the glassy region the film moves synchronously with the surface of the quartz. The lower left hand section of figures 2.12a and 2.13a show the film in its rubbery state (approx $G' = 10^6$ and $G'' < G'$). The imaginary value shown in figure 2.12a shows a large groove and high peak, a corresponding large peak is shown in the real part of Z_L at approximately the same values of shear moduli (see figure 2.13a). This section is related to acoustically thick films where the upper surface of the film appreciably lags the oscillating quartz creating a large phase shift between the polymer surface and quartz surface. Here the tangent function dominates the acoustic load [11]. Table 2.1 gives typical values of shear modulus (G' and G'') for glass, rubbery and transition states.

The contribution to frequency shift and film dissipation caused by the acoustic load shown in figures 2.12a and 2.13a can be calculated using equations (2.43 a & b). The

corresponding Δf and ΔR are shown on right hand side of figures 2.12 and 2.13 respectively. The large changes in both Δf and ΔR show the dramatic effect which an acoustic load may cause on quartz crystal properties.

	G' (Pa)	G'' (Pa)
Glassy state	$\approx 10^9$	$G' \gg G''$
Transition region	$\approx 10^7$	$G' \approx G''$
Rubbery	10^6	$G' > G''$

Table 2.2. Typical values of shear modulus for the three different states.

The effects of an acoustic load on the electrical admittance of the QCM is shown in figure 2.14(a&b). Curves 'B', 'C' and 'D' represent different loads corresponding to the points indicated in figure 2.13a while 'A' represents the uncoated quartz. For a glassy rigid film (acoustically thin) the admittance curve is simply translated to a lower frequency with no change in the shape or magnitude (curve 'B'). In contrast curve 'C' is heavily damped to the extent that the phase plot does not cross the zero line. As most crystal oscillators operate at the phase angle of zero degrees [13], under these heavy loading conditions, typically found with liquid loading and thick viscoelastic films, oscillation would fail. At these conditions advanced techniques, such as network analysis or QCMD are required (see Chapter 3). Curve 'D' shows the film at acoustic resonance, in this case the oscillation may jump to a higher frequency, in

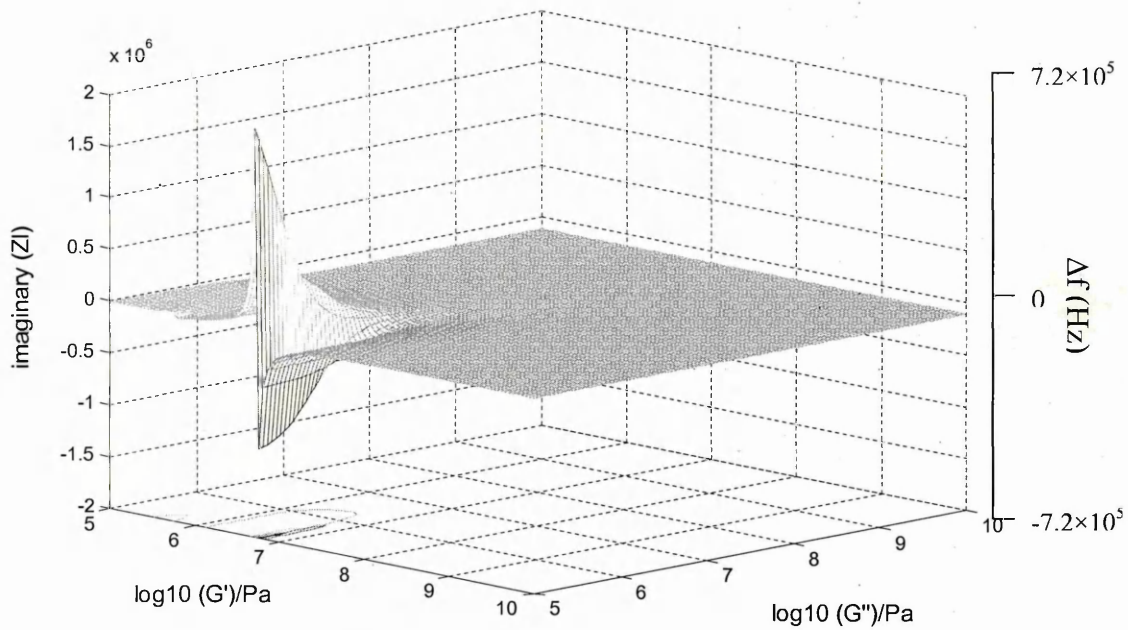


Figure 2.12a. Imaginary part of an acoustic load based on a single layer film with thickness $1\mu\text{m}$ with a density of 1000kg m^{-3} ; this value was taken from literature. An excitation frequency of 18MHz was chosen to give a realistic comparison to the experimental section.

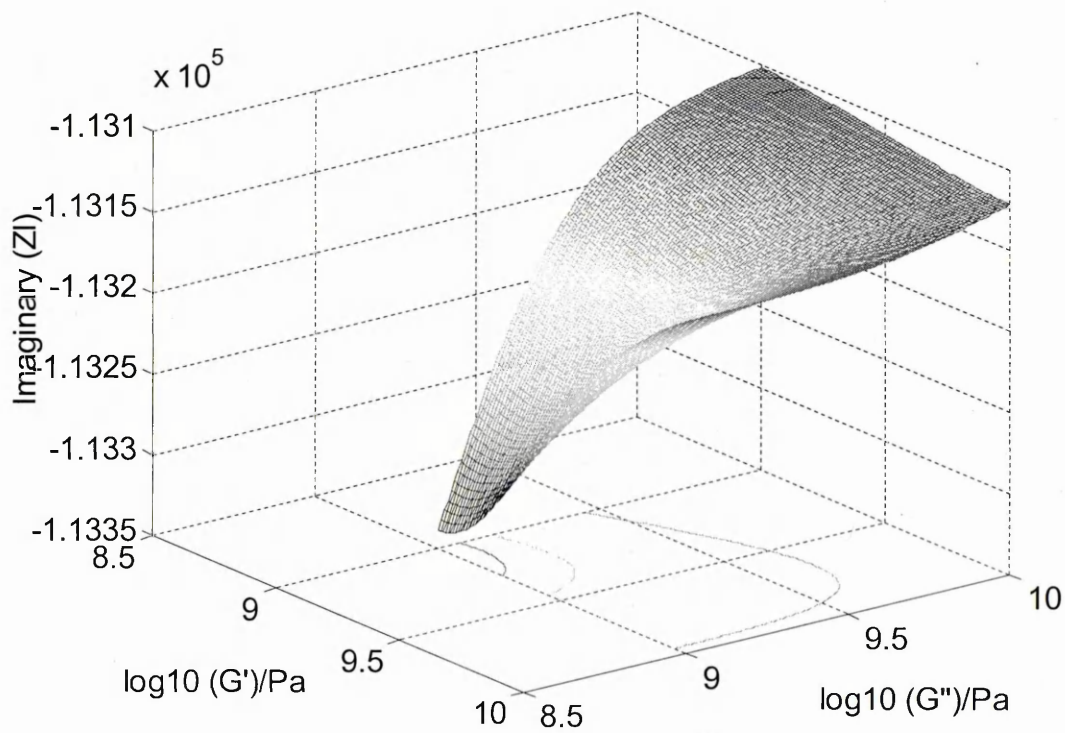


Figure 2.12b. Enlarged section of figure 2.21a.

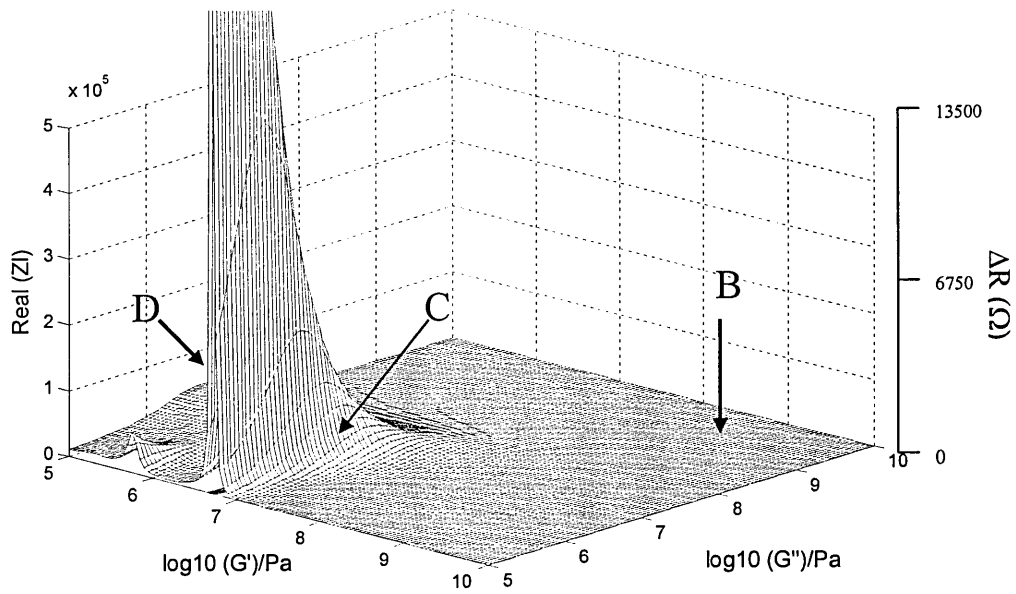


Figure 2.13a. Real part of an acoustic load based on a single layer film with thickness $1\mu\text{m}$ with a density of 1000kg m^{-3} and excitation frequency of 18MHz .

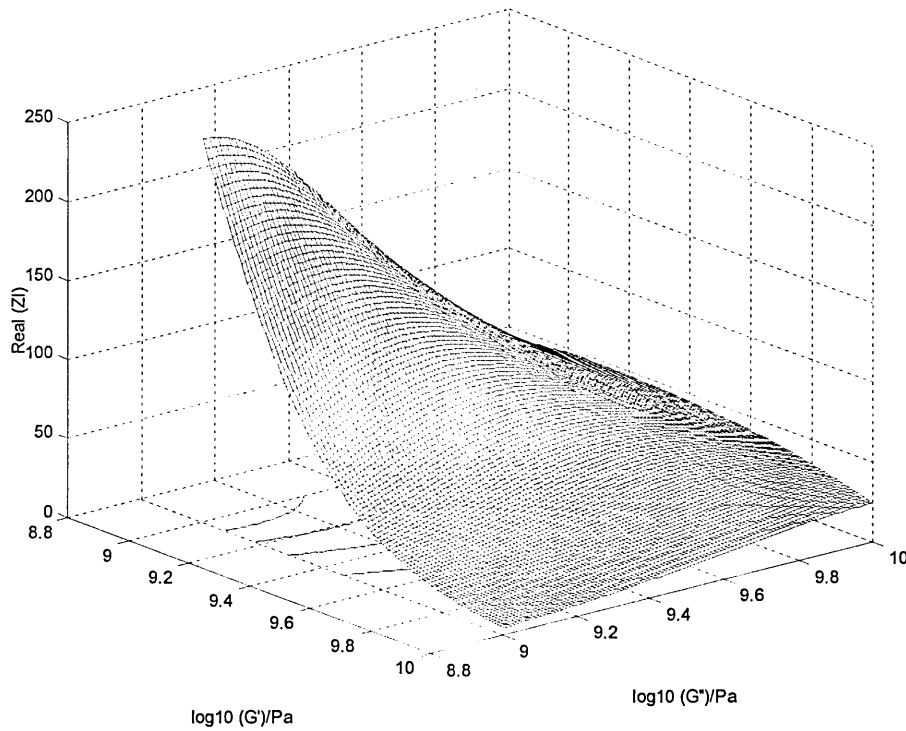


Figure 2.13b. Enlarged section of figure 2.13a.

some cases above the original frequency of the uncoated quartz (curve 'A'). This leads to a misleading observation of zero mass increase. Details of the MATLAB simulations used to produce figures 2.12 through 1.14 can be found in appendix [A].

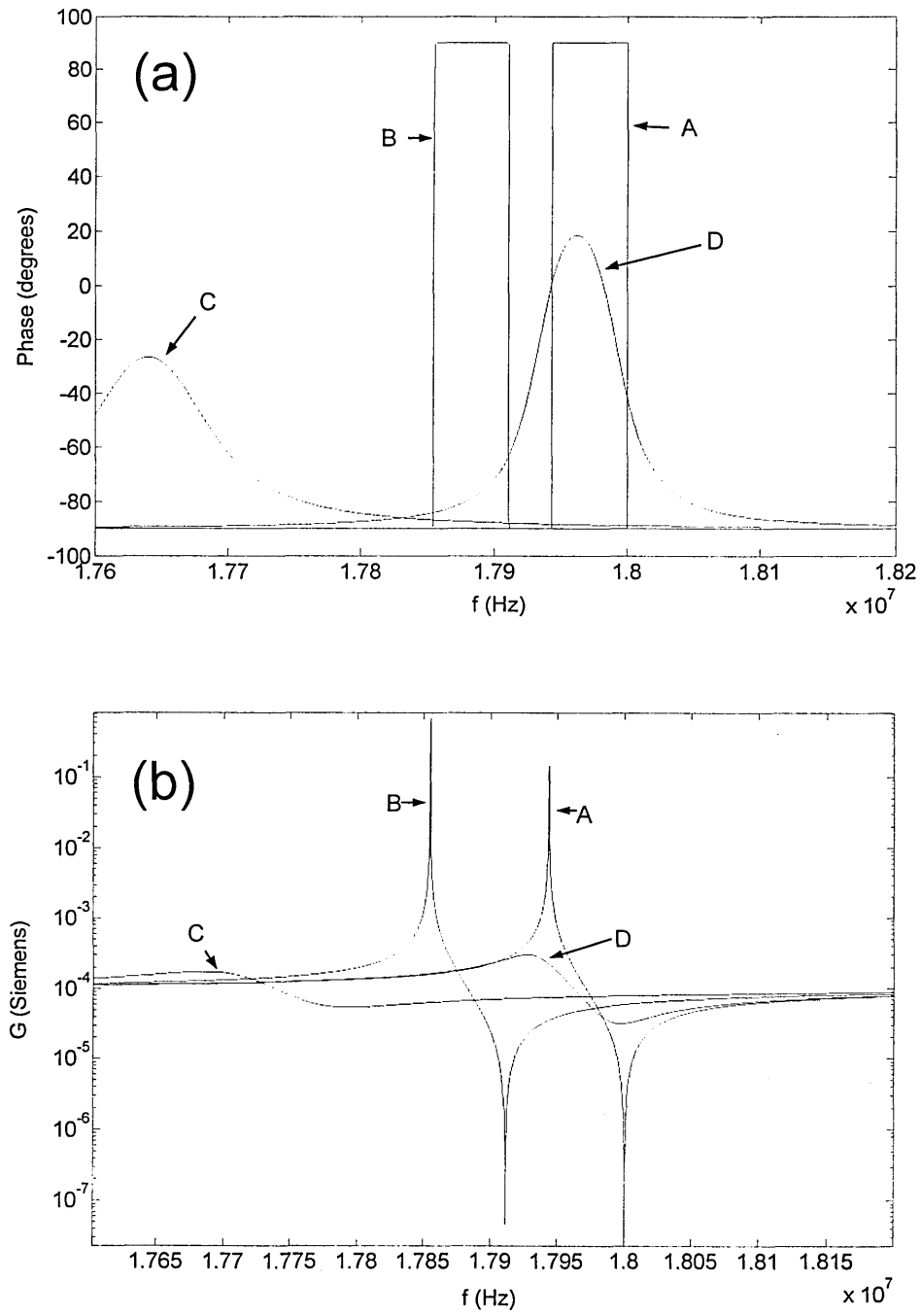


Figure 2.14. a) Simulated admittance phase and b) magnitude under different loading conditions.

2.7 Organic vapour sensing using the QCM

To exploit the TSM resonator in gas sensing applications a sorbent coating/membrane must be applied to the surface of the device. The range of compounds for sensing membranes is vast and choosing a suitable material for the intended target vapour has been the subject of many research works [23-28]. Polymer films are the most common of all sensing membranes, in particular compounds with soft rubbery characteristics, as penetration of vapours into glassy and or crystalline structures is slow [29]. Hence, polymers with low glass transition temperatures producing faster responses are widely used. The adsorption mechanism and interactions between the target molecules and sensing membranes have been of much interest. Interaction between vapour molecules and sensing membranes are normally non-covalent and may include dispersion forces, dipole/dipole interactions, dipole/dipole induced interactions, and hydrogen bonding [29]. Many researchers have reported host-guest interactions between the cavitand and the molecules [30-35].

Adsorption in the bulk of the applied sensing membrane is characterised by the partition coefficient K , defined in equation (2.51). The partition coefficient relates the distribution of vapour molecules between the gas phase (concentration C_v) and the sorbent phase (concentration C_s) [36]. The sensor is therefore in reality measuring the number of molecules in C_s and does not directly give a measure of the concentration of molecules in the gas phase. In order to determine C_v the partition coefficient K must be known for the sensing compound.

$$K = C_s / C_v. \quad (2.51)$$

The frequency shift may be related to the partition coefficient by equation (2.52) [36,37].

$$\Delta f(mass) = \Delta f_s C_v K / \rho_s \quad (2.52)$$

Where Δf_s represents the frequency shift seen when the sensing membrane is applied, ρ_s is the density of the polymer material/sensing membrane.

The phenomena of film swelling has been observed by many researchers during the adsorption of vapours into a sensing membrane and is often accompanied by changes in the physical properties of the film [37].

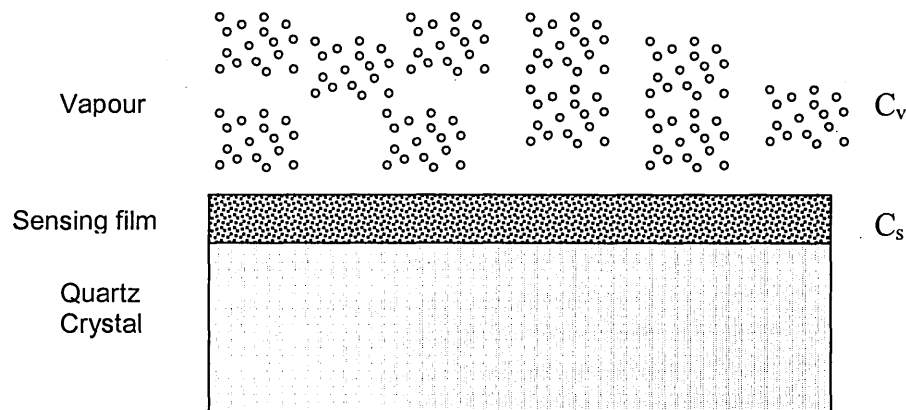


Figure 2.15. Equilibrium partitioning of solute vapour molecules between the gas phase and a sorbent sensing film.

2.8 QCM sensor arrays

The sensor array principle can be applied to QCM having different sorbent coatings with only partial specificity to the target analytes. Analysis of the sensor response pattern is then performed, often allowing both the classification and quantification of the target analytes. The fundamental requirement for the sensor array is that it generates

a pattern of responses and that these patterns are discernibly different from each sample [29]. The inherent disadvantage of the sensor array approach, is however, the increased system complexity often referred to as "the curse of high dimensionality" [38], and additional analysis techniques must be applied to the data obtained. Several multivariate techniques have been utilized for the analysis of QCM sensor arrays, these include Artificial Neural Networks (ANN) [39-49], fuzzy logic [40,43,50], Principal Component Analysis (PCA), cluster analysis and many more. A detailed description, examples and applications of these techniques can be found in [29].

Currently most useful of the data processing techniques for sensor arrays are Principle Component Analysis and Artificial Neural Networks [29]. In this work the ANN was selected primarily because of its ability to handle non linear signals from the sensor array [38,51]. A schematic of a typical QCM sensor array is shown in figure 2.16.

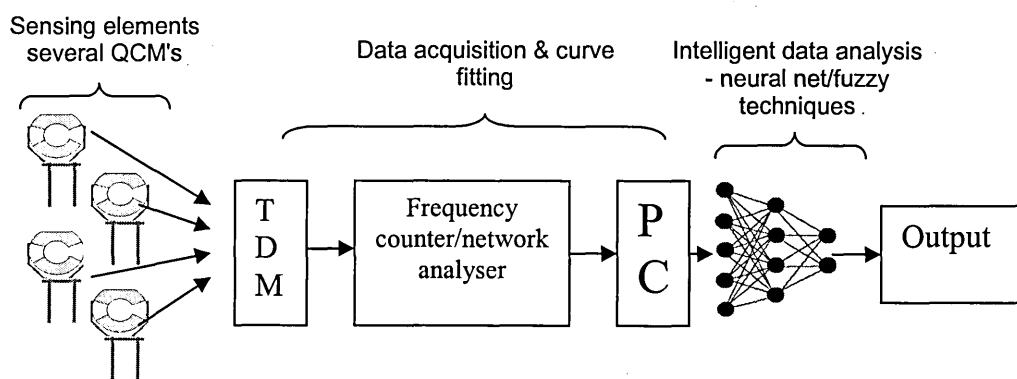


Figure 2.16. Block diagram of QCM array sensing system

With the sensor array approach, both the discrimination and quantification of a range of aromatic compounds has been successfully accomplished by many researchers. Table 2.3 summarises the analysis methods, the number of sensing elements in the array and the target odours tested from a selected number of researchers in this area.

Target odours	Analysis method	Number of QCM	Reference
Organic solvents	ANN, PCA	16	Kalchenko et al 2002[52]
Organic compounds	Fuzzy clustering	4	Barko et al 1999[50]
Volatile sulfur compounds (Halitosis)	PCA	8	Ito et al 2004[53]
Blended fragrance	ANN Fuzzy logic	8	Nakamoto et al 1996[43]
Apple flavor	Unknown	8	Nakamoto et al 2001[54]
Food products	PCA	7	Pardo et al [55]
Organic compounds	ANN Decision tree classification and hill climb search	6	Polikar et al 2001[45]

Table 2.3. Summary of the research works using QCM sensor arrays.

2.9 Advanced QCM sensor signal interpretation - the Δf - ΔR technique

It has been stated by Gardner and Bartlett [29] that “One emerging way forward in sensor technology is in the use of multidimensional measurements from the same sensor”. Increasing the amount of information available from a single sensor leads to a decrease in array size and hence a decrease in the system complexity.

It has been discovered by several researchers that the adsorption of an analyte into a viscoelastic coating may cause changes in both the mass and the shear properties (i.e. a hardening or softening of the film) [3,5,56,57]. As demonstrated in this chapter, changes

in the properties of the surface load are translated into changes in the equivalent circuit parameters (equation 2.42). Hence additional information on the film may be obtained by the measurements of the resonant frequency and energy losses; the latter is related to the equivalent circuit resistance, R in the BVD model.

This work uses the additional information obtained from the resistance parameter (energy dissipation) observed on analyte absorption to produce sensor discrimination using a single QCM, and or to reduce the number of QCM required in a sensor array. Although many researchers have used the additional dissipation parameter technique (usually through measuring the BVD equivalent circuit resistance R), little work has been done using the additional information to aid discrimination and classification of contacting target vapours using viscoelastic sensing membranes.

In the field of biosensing in particular where measurements in liquid phase are utilized, the QCM dissipation techniques have been used extensively. Hook & Rodahl et al 1998 exploited the QCMD technique to measure structural changes in haemoglobin. Marxer et al [58] use the dissipation technique to measure adsorption and viscoelastic properties of proteins. While Lucklum [5,11,13,16,56,59-65] and co-workers have extensively used multiple parameters from QCM measurements for material characterisation, extraction of film parameters and monitoring changes in film properties with gases and in liquids.

2.10 Sensing membranes

The selection of a suitable coating for the QCM is of paramount importance for sensor design. The sensitive coating/membrane must ideally have the following properties:

- (i) Fast response to the contacting analyte, (ideally a few seconds). The response time of the sensor (t_{on}) defined as the time taken for the device to reach a predetermined fraction of its final response following a step change in concentration [29].
- (ii) Sensor membrane recovery after exposure, the sensor signal should return to its original baseline. In the case of sensor poisoning the analyte irreversibly binds to the sensing material often leading to a reduction or complete loss of sensitivity. The recovery time should be as fast as possible (in the order of minutes).
- (iii) ✓ High sensitivity: the sensing material should show a high sensitivity to the target analyte. Where the sensitivity is defined as a measure of the magnitude of the output signal produced in response to a certain input quantity of specified magnitude [3].
- (iv) ✓ High resolution: with the resolution defined as the minimum quantity to which the sensor can respond [3].
- (v) ✓ High selectivity: the ability to distinguish one input quantity from another [3].
- (vi) ✓ A low limit of detection, the detection limit defined as a concentration which produces a response above $2 \times$ the standard deviation of the baseline noise [29].
- (vii) ✓ High reproducibility: this property becomes of increasing importance in a sensor array configuration as the sensor head may be replaced without the need for retraining of the ANN [29].

The problem of selectivity of sensing membranes has recently been advanced with the use of synthetic molecules as receptors. The design of synthetic receptors allowed tuning of the selectivity towards different classes of compounds/analytes [31,66].

Cavitand compounds have been defined as synthetic organic compounds with enforced concave cavities of molecular dimensions [30,31,33]. In the last few years cavitand based synthetic coatings have been increasingly used as sensing membranes for the detection of organic solvents [30-35,67]. The series of calix[4]resorcinarene derivatives was of particular interest throughout this work. It has been shown that the calixarene cavitand structure is suitable for the formation of inclusion complexes with several organic guest molecules [34]. Several groups have reported how the shape and dimensions of the cavity can influence the selectivity of organic solvents through specific host guest interactions [30,33,34,68-70]. While Dalcanale [30] has shown that the selectivity of the material is due to the presence of pre organised cavities, Grate [67] suggests alternatively that the selectivity is produced from general dispersion interactions.

In this work several calix[4]resorcinarene based compounds have been used with the principal difference between them being the size of the hydrocarbon chain length and hence the resultant cavity size. Previous work utilizing the Surface Plasmon Resonance (SPR) technique has shown the suitability of calixarene compounds for sensing of several organic solvent vapours and produces fast reversible responses ideally suited to a sensor array [34,70,71]. The basic calix[4]resorcinarene structure is shown in figure 2.17, and calix[4]resorcinarene derivatives used in this thesis are listed in table 2.4.

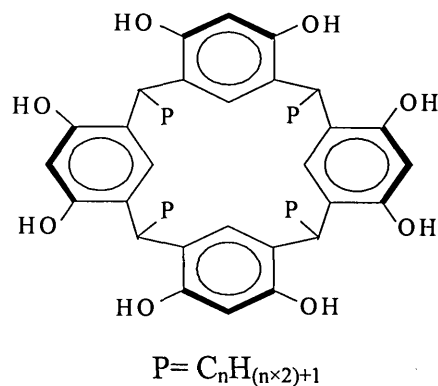


Figure 2.17. Calix(4)resorcinarene with 'P' representing the hydrocarbon tail composition.

	Substituting hydrocarbon tail	Molecular weight (Da)
Calix[4]resorcinarene	C ₁ H ₃	540.5599
	C ₃ H ₇	652.7726
	C ₅ H ₁₁	764.9852
	C ₁₁ H ₂₃	1101.623
	C ₁₅ H ₃₁	1326.048
	C ₁₇ H ₃₅	1438.261

Table 2.4. Sensing membranes used for VOC detection.

2.1.1 Target Analytes - Volatile Organic Compounds (VOC)

The detection of volatile organic compounds in the gaseous phase is of vital environmental importance. The presence of VOC's such as benzene, toluene or m-xylene in small quantities in the atmosphere are hazardous to human health, with benzene for example classed as a human carcinogen. Such VOC's are frequently found in vehicle exhaust fumes, spillage in fuel stations and leaks in fuel pipes, these all contribute to the excessive amount of aromatic hydrocarbons in the atmosphere [34].

The VOC's tested in this thesis are listed in Chapter 5 table 5.4.

The calixarenes used in this work are predominantly suited for the registration of relatively large concentrations of vapour. In previously published works by Nabok et al it was shown that organic vapour adsorption is fast and fully recoverable [34,69-72]. However the concentrations are in the range of 100ppm and above (a few percent of saturated vapour pressure). Although such levels are above typical health and safety exposure levels they are still an order of magnitude below the lower explosion limits for the tested solvent vapours. This makes the calixarene films ideally suited for the application as a pre explosive vapour alarm/sensor. With typical installations within oil ships, petrol stations and oil refineries, where the detection of leaking solvent from pipes or tanks is required.

REFERENCES

- [1] A. Janshoff, H. Galla, and C. Steinman, "Piezoelectric Mass Sensing devices as Biosensors - An alternative to optical Biosensors?," *Angew.Chem.Int.Ed.*, vol. 39, pp. 4004-4032, 2000.
- [2] M. Trainer, "Kelvin and piezoelectricity," *European Journal of Physics*, vol. 24, pp. 535-542, 2003.
- [3] D. S. Ballatine, R. M. White, S. J. Martin, A. J. Ricco, G. C. Fryre, E. T. Zellers, and H. Wohltjen, "Acoustic Wave Sensors Theory, Design and Physico chemical applications," Academic press, New York, 1997.
- [4] G Sauerbrey, "Verwendung von Schwingquarzen zur Wägung dünner Schichten und zur Mikrowägung," *Zeitschrift für Physik*, vol. 155, pp. 206, 1959.
- [5] R. Lucklum and P. Hauptmann, "The $[\Delta]f$ - $[\Delta]R$ QCM technique: an approach to an advanced sensor signal interpretation," *Electrochimica Acta*, vol. 45, pp. 3907-3916, July 2000.
- [6] E. Benes, "Improved quartz crystal microbalance technique," *Journal of Applied Physics*, vol. 56, pp. 608-626, Aug. 1984.
- [7] E. Benes, M. Groschl, W. Burger, and M. Schmid, "Sensors based on piezoelectric resonators," *Sensors and Actuators A: Physical*, vol. 48, pp. 1-21, May 1995.
- [8] J. G. Miller and D. I. Bolef, "Sensitivity Enhancement by the use of acoustic resonators in cw ultrasonic spectroscopy," *Journal of Applied Physics*, vol. 39, pp. 4589-4593, Sept. 1968.
- [9] J. G. Miller and D. I. Bolef, "Acoustic Wave Analysis of the Operation of Quartz-Crystal Film-Thickness Monitors," *Journal of Applied Physics*, vol. 39, pp. 5815-5816, Nov. 1968.
- [10] C. S. Lu and O. Lewis, "Investigation of film-thickness determination by oscillating quartz resonators with large mass load," *Journal of Applied Physics*, vol. 43, pp. 4385-4390, Nov. 1972.
- [11] R. Lucklum and P. Hauptmann, "Transduction mechanism of acoustic-wave based chemical and biochemical sensors," *Measurement Science and Technology*, vol. 14, pp. 1854-1864, 2003.
- [12] S. J. Martin, "Interactions of acoustic waves with thin films and interfaces - Closing remarks," *Faraday Discussions*, vol. 107, pp. 463-476, 1997.
- [13] R. Lucklum and P. Hauptmann, "Determination of polymer shear modulus with quartz crystal resonators," *Faraday Discussions*, vol. 107, pp. 123-140, 1997.

- [14] R. Lucklum, C. Behling, R. W. Cernosek, and S. J. Martin, "Determination of complex shear modulus with thickness shear mode resonators," *Journal of Physics D: Applied Physics*, vol. 30, pp. 346-356, 1997.
- [15] S. J. Martin, H. L. Bandey, R. W. Cernosek, A. R. Hillman, and M. J. Brown, "Equivalent-circuit model for the thickness-shear mode resonator with a viscoelastic film near film resonance," *Analytical Chemistry*, vol. 72, pp. 141-149, Jan. 2000.
- [16] R. Lucklum, S. Schranz, C. Behling, F. Eichelbaum, and P. Hauptmann, "Analysis of compressional-wave influence on thickness-shear-mode resonators in liquids," *Sensors and Actuators A: Physical*, vol. 60, pp. 40-48, May 1997.
- [17] H. L. Bandey, S. J. Martin, R. W. Cernosek, and A. R. Hillman, "modelling the responses of thickness-shear mode resonators under various loading conditions," *Analytical Chemistry*, vol. 71, pp. 2205-2214, Mar. 1999.
- [18] R. Lucklum and G. McHale, "Treatment of slip in a generalised acoustic load concept," 2000 IEEE/EIA Int. frequency control symposium & exhibition, pp. 40-45, 2000.
- [19] R. Lucklum, P. Hauptmann, and R. W. Cernosek, "Thin film material properties analysis with quartz crystal resonators," 2001 IEEE Int. frequency control symposium & PDA exhibition, pp. 542-550, 2001.
- [20] R. Lucklum and P. Hauptmann, "Generalized acoustic parameters of non homogeneous thin films," 2002 frequency control symposium & PDA exhibition, pp. 234-241, 2002.
- [21] C. Behling, R. Lucklum, and P. Hauptmann, "The non-gravimetric quartz crystal resonator response and its application for determination of polymer shear modulus," *Measurement Science and Technology*, vol. 9, pp. 1886-1893, 1998.
- [22] S. J. Martin, C Gregory, G. C Fryre, and S Senturia, "Dynamics and Response of Polymer-Coated Surface Acoustic Wave Devices: Effect of Viscoelastic Properties and Film Resonance," *Analytical Chemistry*, vol. 66, pp. 2201-2219, 1994.
- [23] M. Gomes, A.C. Duarte, and J. A. B. P. Oliveira, "Critical assessment of the parameters that affect the selection of coating compounds for piezoelectric quartz crystal microbalances," *Talanta*, vol. 48, pp. 81-89, Jan. 1999.
- [24] A. Hierlemann, K. Bodenhofer, M. Fluck, V. Schurig, and W. Gopel, "Selective detection of nitrogen and oxygen containing volatile organic compounds: use of metal-modified polysiloxanes as sensor coatings," *Analytica Chimica Acta*, vol. 346, pp. 327-339, July 1997.
- [25] I. A. Koshets, Z. I. Kazantseva, Yu Shirshov, S. A. Cherenok, and V. I. Kalchenko, "Calixarene films as sensitive coatings for QCM-based gas sensors," *Sensors and Actuators B: Chemical*, vol. 106, April 2005.

- [26] S. P. Sakti, S. Rosler, R. Lucklum, P. Hauptmann, F. Buhling, and S. Ansorge, "Thick polystyrene-coated quartz crystal microbalance as a basis of a cost effective immunosensor," *Sensors and Actuators A: Physical*, vol. 76, pp. 98-102, Aug. 1999.
- [27] J. Zhang, J. Hu, Z. Q. Zhu, H. Gong, and S. J. O'Shea, "Quartz crystal microbalance coated with sol-gel-derived indium-tin oxide thin films as gas sensor for NO detection," *Colloids and Surfaces A: Physicochemical and Engineering Aspects*, vol. 236, pp. 23-30, Apr. 2004.
- [28] X. C. Zhou, L. Zhong, S. F. Y. Li, S. C. Ng, and H. S. O. Chan, "Organic vapour sensors based on quartz crystal microbalance coated with self-assembled monolayers," *Sensors and Actuators B: Chemical*, vol. 42, pp. 59-65, July 1997.
- [29] J. W. Gardner and P. N. Bartlett, "Electronic Noses Principles and Applications," Oxford University Press, New York, 1999.
- [30] E. Dalcanale and J. Hartmann, "Selective detection of organic compounds by means of cavitand-coated QCM transducers," *Sensors and Actuators B: Chemical*, vol. 24, pp. 39-42, Mar. 1995.
- [31] E. B. Feresenbet, E. Dalcanale, C. Dulcey, and D. K. Shenoy, "Optical sensing of the selective interaction of aromatic vapors with cavitands," *Sensors and Actuators B: Chemical*, vol. 97, pp. 211-220, Feb. 2004.
- [32] M. Ferrari, V. Ferrari, D. Marioli, A. Taroni, M. Suman, and E. Dalcanale, "Cavitand-coated PZT resonant piezo-layer sensors: properties, structure, and comparison with QCM sensors at different temperatures under exposure to organic vapors," *Sensors and Actuators B: Chemical*, vol. 103, pp. 240-246, Sept. 2004.
- [33] J. Hartmann, P. Hauptmann, S. Levi, and E. Dalcanale, "Chemical sensing with cavitands: influence of cavity shape and dimensions on the detection of solvent vapors," *Sensors and Actuators B: Chemical*, vol. 35, pp. 154-157, Sept. 1996.
- [34] A. K. Hassan, A. K. Ray, A. V. Nabok, and T. Wilkop, "Kinetic studies of BTEX vapour adsorption onto surfaces of calix-4-resorcinarene films," *Applied Surface Science*, vol. 182, pp. 49-54, Oct. 2001.
- [35] P. Nelli, E. Dalcanale, G. Faglia, G. Sberveglieri, and P. Soncini, "Cavitands as selective materials for QMB sensors for nitrobenzene and other aromatic vapours," *Sensors and Actuators B: Chemical*, vol. 13, pp. 302-304, May 1993.
- [36] J. W. Grate, S. N. Kaganove, and V. R. Bhethanabotla, "Examination of mass and modulus contributions to thickness shear mode and surface acoustic wave vapour sensor responses using partition coefficients," *Faraday Discussions*, vol. 107, pp. 259-283, 1997.
- [37] J. W. Grate, M. Klusty, R. A. McGill, M. H. Abraham, G. Whiting, and J. Andonianhaftvan, "The predominant role of swelling-induced modulus changes of the sorbent phase in determining the responses of polymer-coated

surface acoustic-wave vapor sensors," *Analytical Chemistry*, vol. 64, pp. 610-624, 1992.

- [38] J. W. Gardner, P. Boilot, and E. L. Hines, "Enhancing electronic nose performance by sensor selection using a new integer-based genetic algorithm approach," *Sensors and Actuators B: Chemical*, vol. 106, pp. 114-121, 2005.
- [39] J. Auge, P. Hauptmann, J. Hartmann, S. Rosler, and R. Lucklum, "Versatile microcontrolled gas sensor array system using the quartz microbalance principle and pattern recognition methods," *Sensors and Actuators B: Chemical*, vol. 26, pp. 181-186, May 1995.
- [40] R. Dutta, E. L. Hines, J. W. Gardner, K. R. Kashwan, and M. Bhuyan, "Tea quality prediction using a tin oxide-based electronic nose: an artificial intelligence approach," *Sensors and Actuators B: Chemical*, vol. 94, pp. 228-237, Sept. 2003.
- [41] J. W. Gardner, E. L. Hines, and H. C. Tang, "Detection of vapours and odours from a multisensor array using pattern-recognition techniques Part 2. Artificial neural networks," *Sensors and Actuators B: Chemical*, vol. 9, pp. 9-15, July 1992.
- [42] M. Holmberg, F. Winquist, I. Lundstrom, J. W. Gardner, and E. L. Hines, "Identification of paper quality using a hybrid electronic nose," *Sensors and Actuators B: Chemical*, vol. 27, pp. 246-249, June 1995.
- [43] T. Nakamoto, S. Hanaki, and T. Moriizumi, "Artificial odor-recognition system using neural network for estimating sensory quantities of blended fragrance," *Sensors and Actuators A: Physical*, vol. 57, pp. 65-71, Oct. 1996.
- [44] T. Nakamoto and H. Hiramatsu, "Study of odor recorder for dynamical change of odor using QCM sensors and neural network," *Sensors and Actuators B: Chemical*, vol. 85, pp. 263-269, July 2002.
- [45] R. Polikar, R. Shinar, L. Udpa, and M. D. Porter, "Artificial intelligence methods for selection of an optimized sensor array for identification of volatile organic compounds," *Sensors and Actuators B: Chemical*, vol. 80, pp. 243-254, Dec. 2001.
- [46] A. M. Reznik, A. A. Galinskaya, O. K. Dekhtyarenko, and D. W. Nowicki, "Preprocessing of matrix QCM sensors data for the classification by means of neural network," *Sensors and Actuators B: Chemical*, vol. 106, pp. 158-63, 2005.
- [47] H. Shinichi, T. Nakamoto, and M. Toyosaka, "Artificial odor-recognition system using neural network for estimating sensory quantities of blended fragrance," *Sensors and Actuators A: Physical*, vol. 57, pp. 65-71, Oct. 1996.
- [48] L. X. Sun and T. Okada, "Simultaneous determination of the concentration of methanol and relative humidity based on a single Nafion(Ag)-coated quartz crystal microbalance," *Analytica Chimica Acta*, vol. 421, pp. 83-92, Sept. 2000.

- [49] T. Nakamoto and H. Hiramatsu, "Study of odor recorder for dynamical change of odor using QCM sensors and neural network," *Sensors and Actuators B: Chemical*, vol. 85, pp. 263-269, July 2002.
- [50] G. Barko, J. Abonyi, and J. Hlavay, "Application of fuzzy clustering and piezoelectric chemical sensor array for investigation on organic compounds," *Analytica Chimica Acta*, vol. 398, pp. 219-226, Oct. 1999.
- [51] M. A. Craven, J. W. Gardner, and P. N. Bartlett, "Electronic noses -- development and future prospects," *TrAC Trends in Analytical Chemistry*, vol. 15, pp. 486-493, Oct. 1996.
- [52] V. I. Kalchenko, I. A. Koshets, E. P. Matsas, O. N. Kopylov, A. Solovyov, and Z. I. Shirshov Yu. M. Kazantseva, "Calixarene-based QCM sensors array and its response to volatile organic vapours," *Materials Science*, vol. 20, pp. 73-87, 2003.
- [53] J. Ito, T. Nakamoto, and H. Uematsu, "Discrimination of halitosis substance using QCM sensor array and a preconcentrator," *Sensors and Actuators B: Chemical*, vol. 99, pp. 431-436, May 2004.
- [54] T. Nakamoto, Y. Nakahira, H. Hiramatsu, and T. Moriizumi, "Odor recorder using active odor sensing system," *Sensors and Actuators B: Chemical*, vol. 76, pp. 465-469, June 2001.
- [55] M. Pardo, L. G. Kwong, G. Sberveglieri, K. Brubaker, J. F. Schneider, W. R. Penrose, and J. R. Stetter, "Data analysis for a hybrid sensor array," *Sensors and Actuators B: Chemical*, vol. 106, pp. 136-143, 2005.
- [56] R. Lucklum, C. Behling, and P. Hauptmann, "Gravimetric and non-gravimetric chemical quartz crystal resonators," *Sensors and Actuators B: Chemical*, vol. 65, pp. 277-283, June 2000.
- [57] C. Behling, R. Lucklum, and P. Hauptmann, "Response of quartz-crystal resonators to gas and liquid analyte exposure," *Sensors and Actuators A: Physical*, vol. 68, pp. 388-398, June 1998.
- [58] C. Galli Marxer, M. Collaud Coen, and L. Schlapbach, "Study of adsorption and viscoelastic properties of proteins with a quartz crystal microbalance by measuring the oscillation amplitude," *Journal of Colloid and Interface Science*, vol. 261, pp. 291-298, May 2003.
- [59] F. Hook, M. Rodahl, C. Kellwe, K. Glasmaster, C. Fredriksson, P. Dahlqvist, and B. Kasemo, "The Dissipative QCM-D Technique: Interfacial Phenomena and Sensor Applications for Proteins Biomembranes, Living Cells and Polymers," 1999 Joint Meeting EFTF - IEEE IFCS, pp. 966-972, 1999.
- [60] R. Lucklum, B. Henning, P. Hauptmann, K. D. Schierbaum, S. Vaihinger, and W. Gopel, "Quartz microbalance sensors for gas detection," *Sensors and Actuators A: Physical*, vol. 27, pp. 717-722, May 1991.
- [61] R. Lucklum, S. Rosler, P. Hauptmann, and J. Hartmann, "On-line detection of organic pollutants in water by thickness shear mode resonators," *Sensors and Actuators B: Chemical*, vol. 35, pp. 103-111, Sept. 1996.

- [62] R. Lucklum and P. Hauptmann, "Determination of polymer shear modulus with quartz crystal resonators," *Faraday Discussions*, vol. 107 pp. 123-140, 1997.
- [63] R. Lucklum, C. Behling, P. Hauptmann, S. J. Martin, and R. W. Cernosek, "Error analysis of material parameter determination with quartz-crystal resonators," *Sensors and Actuators A: Physical*, vol. 66, pp. 184-192, Apr. 1998.
- [64] R. Lucklum, C. Behling, and P. Hauptmann, "Signal amplification with multilayer arrangements on chemical quartz crystal resonators," 1999 Joint Meeting EFTF - IEEE IFCS, pp. 987-990, 1999.
- [65] R. Lucklum and P. Hauptmann, "The quartz crystal microbalance: mass sensitivity, viscoelasticity and acoustic amplification," *Sensors and Actuators B: Chemical*, vol. 70, pp. 30-36, Nov. 2000.
- [66] F. L. Dickert and R. Sikorski, "Supramolecular strategies in chemical sensing," *Materials Science and Engineering: C*, vol. 10, pp. 39-46, Dec. 1999.
- [67] J. W. Grate, S. J. Patra, M. H. Abraham, and C. M. Du, "Selective vapor sorption by polymers and cavitands on acoustic wave sensors: Is this molecular recognition?," *Analytical Chemistry*, vol. 68, pp. 913-917, 1996.
- [68] A. K. Hassan, A. K. Ray, A. V. Nabok, and F. Davis, "Spun films of novel calix[4]resorcinarene derivatives for benzene vapour sensing," *Sensors and Actuators B: Chemical*, vol. 77, pp. 638-641, July 2001.
- [69] A. V. Nabok, A. K. Hassan, A. K. Ray, O. Omar, and V. I. Kalchenko, "Study of adsorption of some organic molecules in calix[4]resorcinolarene LB films by surface plasmon resonance," *Sensors and Actuators B: Chemical*, vol. 45, pp. 115-121, Dec. 1997.
- [70] A. V. Nabok, A. K. Hassan, and A. K. Ray, "Condensation of organic vapours within nanoporous calixarene thin films," *Journal of materials chemistry*, vol. 10, pp. 189-194, June 1999.
- [71] A. K. Hassan, A. V. Nabok, A. K. Ray, A. Lucke, K. Smith, C. J. M. Stirling, and F. Davis, "Thin films of calix-4-resorcinarene deposited by spin coating and Langmuir-Blodgett techniques: determination of film parameters by surface plasmon resonance," *Materials Science and Engineering: C*, vol. 8-9, pp. 251-255, Dec. 1999.
- [72] A. V. Nabok, N. V. Lavrik, Z. I. Kazantseva, B. A. Nesterenko, L. N. Markovskiy, V. I. Kalchenko, and A. N. Shivaniuk, "Complexing properties of calix[4]resorcinolarene LB films," *Thin Solid Films*, vol. 259, pp. 244-247, Apr. 1995.

Chapter 3

Experimental methodology

3.0 Introduction

This chapter is divided into four sections. The first describes how the sensing membranes are deposited onto the QCM and gives a brief discussion on the techniques used. Section two covers the delivery of the target solvent to the sensing element including the design of the apparatus used and calculation of vapour concentrations. Section three gives a detailed account of several techniques and equipment which may be used to measure QCM devices. Section four gives information on how the sensing membranes may be measured and characterized using two different techniques Atomic Force Microscopy (AFM) and ellipsometry.

3.1 QCM sensing membranes film deposition

For the QCM to operate as a chemical sensor, it must first be coated with a sensing membrane suitable for the target analyte for which it is intended. Several methods are available including dip coating, spray coating [1,2], spin coating [3] and Langmuir Blodgett (LB) [4-7]. Throughout this work only the spin coating and LB deposition techniques were used, this choice was primarily based on the large amount of experience within the group of using the two techniques and suitable equipment/apparatus being available. Much work on making films with a suitable thickness and consistent homogeneity has been carried out by the group previously, with the results confirmed using Surface Plasmon Resonance (SPR), UV Spectroscopy and ellipsometry [4,5,7-9].

3.1.1 Surface preparation

Prior to the deposition of a film onto any substrate it is vital to have a clean surface free from any defects. In the case of the QCM major defects, such as poor contact between the quartz and the electrodes, can easily be seen from a visual inspection of the QCM. All crystals were rinsed thoroughly using acetone and dried with a stream of pure nitrogen before the initial measurement of the uncoated QCM was taken. All preparation and coating of the crystals was all undertaken inside a grade 100 clean room. Handling of the crystals was performed using fine tweezers and latex were gloves worn throughout to avoid contamination. All chemicals used for the cleaning and preparation process were of scientific grade and purchased from Fisher Scientific.

3.1.2 Spin coating

The spin coating technique is fast, cheap and relatively simple to perform. To achieve suitable film properties using spin coating a number of parameters were optimized, namely the concentration of sensing compound, type of solvent, the spinning regime (acceleration, spin speed, and the duration) and the amount of solution deposited on the crystal surface.

Several solvents were tested and ethanol was found to give the best results. It was also noted that a non linear relationship between the solvent concentration and film thickness is evident; a plateau of thickness was reached at approximately 25mg/ml. To obtain a homogeneous cluster-free spinning solution the coating compound is dissolved in ethanol, and placed in the ultrasonic bath for approximately fives minutes. Table 3.1 gives a summary of the parameters used to achieve the desired film coating. The numbers in brackets relates to the particular program number on the spin coating instrument used, which in this instance was the electronic micro systems model 4000.

	Solvent	Compound concentration	Ramp	Spin speed	Spin duration
Spin coating	ethanol	25mg/ml	2	2000rpm (1085)	30 sec

Table 3.1. Summary of parameters used for the spin coating process.

3.1.3 Langmuir Blodgett (LB) deposition

Compared to the spin coating technique, the LB method inherently has several disadvantages, in particular the complexity of preparation of the LB trough and the long time required to produce suitably thick films. A typical time period to attain a suitable number of layers would be over twenty four hours, and although the system is semi-automated and computer controlled, the material would need to be re-spread approximately four to six times during the process. This must be done manually on this particular system, although more advanced systems are available where this process can also be automated.

The dipping process must also be optimized to each particular compound to gain the best transfer ratio. These parameters include the surface pressure and dipping speed on both up and down strokes. In some cases a negative transfer ratio (corresponding to the film peeling off) has been observed if these parameters are not set correctly. A summary of typical parameters used for the LB process is given in table 3.2.

LB Deposition	
Solution concentration	1mg/ml
Initial spreading	65 μ l
Subsequent spread	40 μ l
Dipper speed down-stroke	10mm/min
Dipper speed up-stroke	60mm/min

Table 3.2. Summary of parameters used for the spin coating process.

3.2 Exposure methods and techniques

To deliver the target vapour to the QCM two techniques were investigated, the injection of the liquid solvent with a micro syringe and constant vapour flow technique. To realize the safe, consistent and accurate delivery of the vapours two gas cells (chambers) were purposely designed and manufactured in the university workshop.

3.2.1 Gas cell/chamber

The two chambers were designed with similar specifications only altering in size. One was designed to hold a single QCM, and the other one contained up to seven QCM's allowing the array measurements. The cells were designed to have the minimum volume possible, this was intended to allow the domination of the kinetics of vapour adsorption rather than the time required to fill a large cell with target vapour. The total volume of the single QCM chamber was 7.5cm^3 . To avoid the condensation of vapours on the walls of the chamber, all internal surfaces were fabricated from PTFE (Teflon®), with all other major components machined from stainless steel. Nitrile O-rings were also used to seal between the lid of the chamber; these were recessed into the bottom part of the chamber to allow consistent positioning and relocating of the two mating parts. For easy mounting of QCM inside the chamber, two brass pins were inserted through the base. The pins were machined to a specific size in order accommodate a standard electronic terminal block. The cell complete with terminal block and connectors is shown in figure 3.1. The terminal block connection was incorporated to allow a simple and quick mounting of QCM inside the chamber. Inlet and outlet pipes were located on the top of the chamber with the outlet connected to a vapour extraction system via a simple airtight valve positioned just outside the chamber. This system allowed a safe and convenient method of sealing the chamber and flushing with air after each

exposure. No special temperature stabilization measures were undertaken; however the temperature was monitored to be constant within $\pm 0.5^{\circ}\text{C}$ during experiments. A schematic of the chamber is shown in figure 3.2.

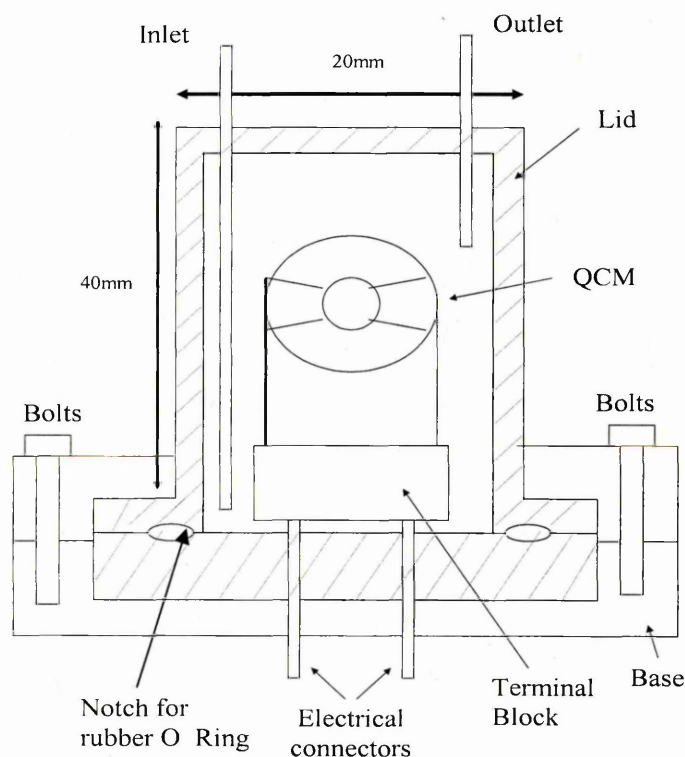


Figure 3.1. Cross sectional diagram of the small vapour exposure cell. Cross hatched areas show the PTFE fabricated cell walls total cell volume 0.0075 litres.

3.2.2 Vapour injection method

The simplest and most convenient form of vapour delivery was the vapour injection method. Micro syringes in the volume range of 1μ to $50\mu\text{l}$ were purchased specifically for this purpose. The target solvents were placed in sealed test tubes with a needle inserted through the top plastic sealing plug, this allowed the minimization of loss and evaporation of the solvent.

A certain amount of solvent was injected into the chamber by piercing nescofilm® which covers the inlet (a) on the chamber. The solvent then evaporates inside the chamber. To flush the chamber the air valve (c) has to be opened (see figure 3.2).

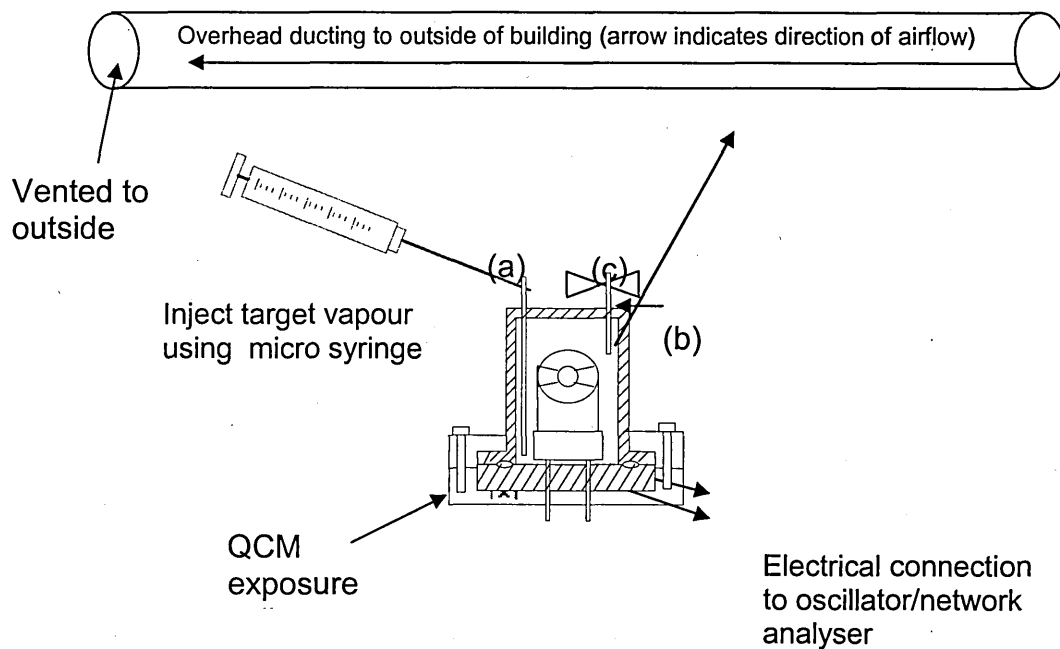


Figure 3.2. Schematic of the exposure chamber and ducting system used when performing vapour exposure. On injecting the vapour through inlet (a) valve (c) connected to outlet (b) would be closed creating an airtight chamber. After each exposure the chamber is flushed with air by opening valve (c) creating a vacuum and sucking air through the chamber.

3.2.3 Vapour flow method

The vapour flow method is based on the diffusion tube principle and allowed a supply of constant flow of known low concentration of vapours in the carrier gas (air/nitrogen). The system provides highly accurate and reliable low vapour concentrations as long as the following criteria are met: the diffusion tube is held at a constant temperature ($\pm 0.1^\circ\text{C}$) and the gas flow rate is accurate down to $\pm 1\%$ [10]. A schematic of the setup is shown in Figure 3.3. The system does however require a quite elaborate calibration procedure. At constant temperature, the weight of diffusion gas permeating and the weight of diffusion gas evaporating will both be set at constant levels. The gas concentrations are determined from the dynamic weight loss obtained from several measurements taken at set time periods. The process is described in detail in [10].

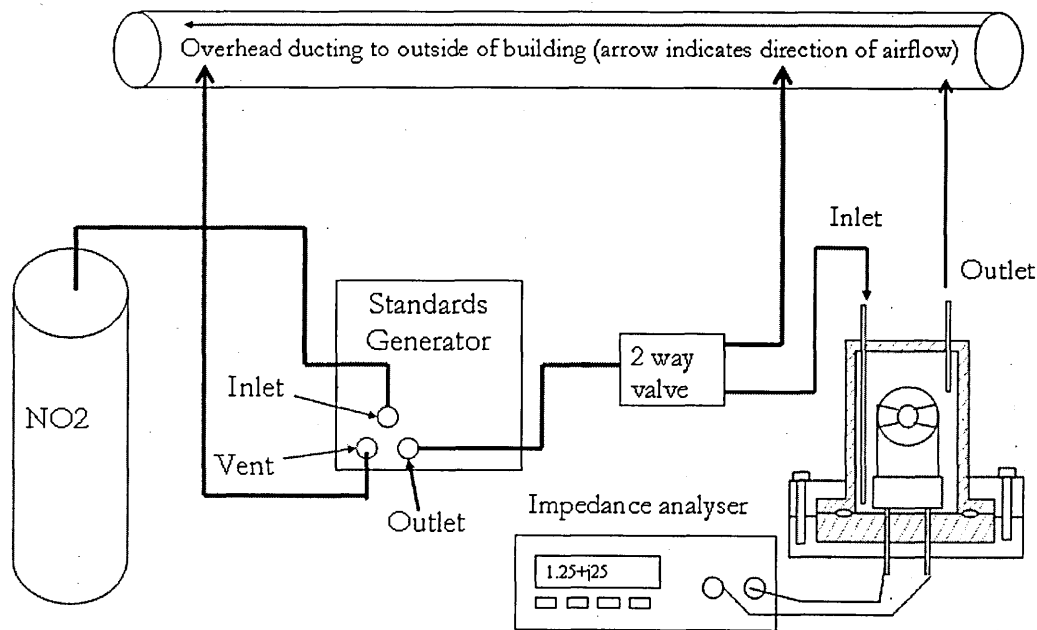


Figure 3.3. Schematic of vapour exposure using the standards generator.

3.2.4 Vapour Concentration and Saturated vapor pressure

To calculate the concentration of injected liquid solvent inside the chamber the equation (3.1) was used. A list of typical vapours used and the amount of liquid solvent needed to achieve a concentration of 10000ppm is listed in table 3.3.

$$\text{Concentration(ppm)} = \frac{D \times Q_s \times 22.4 \times 1000}{m.w \times C_{vol}} \quad (3.1)$$

where D is the density, Q_s is the quantity of liquid solvent in micro litres, $m.w$ is the molecular weight of solvent, C_{vol} is the volume of the exposure cell and 22.4 is the molar gas volume constant.

Assuming a chamber size of 0.0075l		
	Liquid Solvent μ l at 10000ppm	% of SVP
Benzene	0.2977	10.1325
Hexane	0.4406	5.9603
M-Xylene	0.4095	126.6561
Cyclohexane	0.3619	7.9783
Toluene	0.3558	34.9406

Table 3.3. Liquid solvent required to achieve 10000ppm and its respective percentage of saturated vapour pressure.

3.2.5 Saturated vapour pressure

The analysis of the results also required the saturated pressure of the solvents to be known. These were calculated using equation (3.2). Table 3.4 lists all the vapour pressure for the solvents used.

$$w(g/l) = \frac{(P \times m.w \times V)}{(R \times (T + 273.15))} \quad (3.2)$$

where P (Vapour pressure in atm) = $\frac{kPa}{101.325}$ (3.3). To convert from g/l units to ppm to

equation (3.4) was used.

$$ppm = \frac{w(mg/m^3) \times R_g \times (T + 273.15)}{m.w} \quad (3.4)$$

where w is concentration in grammes per litre, $m.w$ is the molecular weight of the solvent in grammes, V is the volume (1 litre), P is the vapour pressure in atmospheres at specified temperature, T is Temperature in degrees Celsius and R_g is the Gas Constant ($8.206 \times 10^{-2} \text{ L atm K}^{-1} \text{ mol}^{-1}$).

Compound	molecular weight	Vapour pressure (kPa)	pressure atm	concentration mg/m ³	concentration ppm
Benzene	78.11	10	0.0986923	320456.152	98692.326
Hexane	86.2	17	0.1677769	601198.881	167776.955
Toluene	92.1	2.9	0.0286207	109577.050	28620.774
M-xylene	106.2	0.8	0.0078953	34855.914	7895.386
acetone	58.1	24	0.2368615	572070.233	236861.584
p xylene	106.2	0.9	0.0088823	39212.904	8882.309
aniline	93.1	0.04	0.0003947	1527.818	394.770
Cyclohexane	84.1608	12.7	0.1253392	438506.013	125339.255

Table 3.4. List of solvents, their molecular weights, vapour pressures and respective concentrations in ppm at saturated vapour pressures.

3.3 QCM Measurements techniques and equipment

Since the first report by Sauerbrey in 1959 of using a QCM to measure the thickness of vacuum deposited metals [11], both QCM measurement techniques and understanding of the device itself have advanced significantly. With the realization that the measurements of the resonant frequency alone is inadequate to fully characterize the TSM resonator, several advanced techniques have been established which allow both the frequency shift and the damping (dissipation) to be measured. The following

sections describe several measurement techniques and their implementation in this work for the characterization of the TSM resonators and/or contacting media.

3.3.1 Resonant oscillator circuits

The simplest measurement of the QCM is by the means of the resonant oscillator circuit. The QCM acts as the frequency determining element in an electrical oscillator circuit, the properties of the crystal itself inherently provide high frequency stability and low thermal drift [12]. With the discovery that the QCM may also operate in the heavily damped environments (i.e. liquid phase) [13] a range of new oscillator have been developed. Several oscillator circuits for gaseous and liquid phase can be found in the following references [14,15] and some liquid phase specific designs may be found in [16,17].

Some recent oscillator designs also allow measurement of Q factor (dissipation) [18-23], these however often need complex and time consuming calibration to obtain true values for frequency and resistance (dissipation), and often lack high resolution which can only be achieved with the network analyzer instruments.

The oscillator circuits exploited in this work were based on previous achievements of the group [24] in the development of pre explosive vapour sensor alarm devices. The original concept for the design was sourced from Hwang et al [25]. A circuit diagram of the oscillator can be found in appendix [B].

3.3.2 QCMD (Dissipation)

The QCMD method is based on the measurements of the decay properties of the oscillating quartz. For full details and in-depth information on the QCMD technique see references [26,27]. The crystal is driven by an external frequency generator at

approximately resonant frequency, subsequently disconnected from the driving oscillatory force, and the exponentially decayed sinusoid was measured. Both the resonant frequency of the crystal and the dissipation factor are obtained from fitting the decay curve to equation (3.5). The parameter τ (decay time constant) is a function of the QCM dissipation factor described in equation (3.6), and the resonant frequency f is extracted directly from equation (3.5). The QCMD method is relatively simple and can be implemented at a fairly low cost with the basic requirements of function generator and a Digital Storage Oscilloscope (DSO) interfaced to a PC via GPIB interface. A high degree of accuracy can also be easily obtained. A schematic of the QCMD setup is illustrated in figure 3.4. The dissipation factor D is related to the BVD equivalent circuit model resistance by equation (3.7).

$$U(t) = A_0 e^{-t/\tau} \sin(2\pi ft + \phi) \quad (3.5)$$

where ϕ is the phase, τ is the decay time constant and A_0 the amplitude of the a.c. signal.

$$D = \frac{1}{\pi f \tau} \quad (3.6)$$

$$D = \frac{R}{\omega L} \quad (3.7)$$

The setup does however require computer control and automation. The timing of the relay and triggering of the scope must be precisely defined to obtain the decaying sinusoid. The function generator must also be automated to track the resonant frequency of the QCM, hence after each measurement the function generator is set to the extracted resonant frequency measurement obtained from fitting the previous decay curve. If the excitation frequency does not match the QCM resonant frequency, the amplitude of oscillations is reduced increasing noise within the system and if the frequencies are too

far apart, the crystal may fail to oscillate. To facilitate the tracking of the resonant frequency a Stanford Research model DS345 programmable function generator controlled via GPIB bus was used. The signal was captured using a Tektronix 500MHz digital storage oscilloscope once again utilizing the GPIB interface for transfer of the captured decay curve to the PC. The block diagram in figure 3.4 was realized on printed circuit board. Details of the circuit design, and components can be found in appendix [B].

Measurements start by closing the computer controlled relay (Clare MSS-2), a period of approximately 20ms is then given allowing the crystal oscillations to stabilize. The computer then opens the relay and triggers the scope to capture the decay curve. The data are then transferred from the oscilloscope to PC and data fit performed. The Levenberg Marquadt algorithm from the Labview® analysis toolbox was used for the data fitting. Due to malfunction of the Tektronix oscilloscope it was replaced with a Gould 1604, the triggering using GPIB was found to be inaccurate so a PIC 16F84 microcontroller was used to close the relay and to trigger the oscilloscope using the external trigger. Details of the Labview® software and 'C' program for the PIC microcontroller can be found in appendix [C].

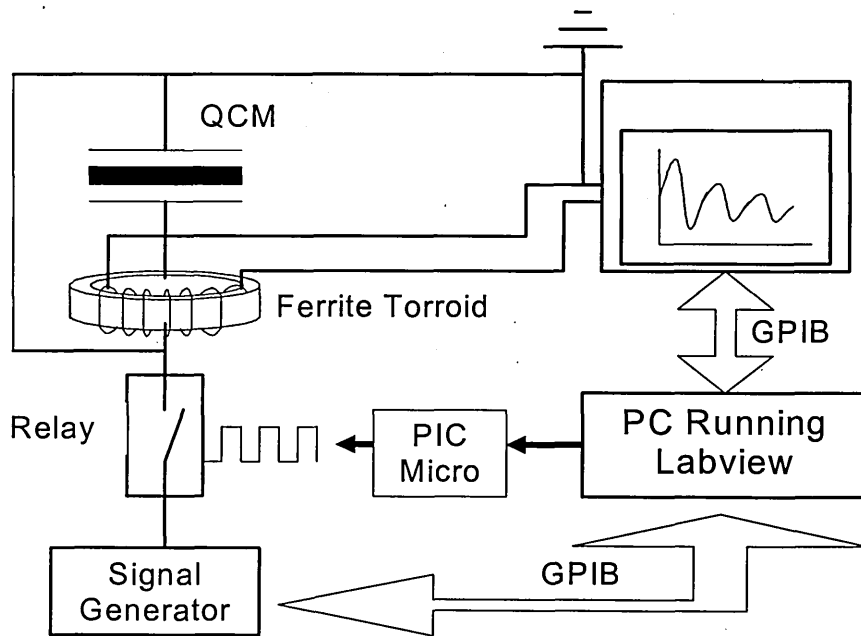


Figure 3.4. Block diagram of the QCMD setup, the PIC microcontroller being used to accurately trigger the oscilloscope using the external trigger.

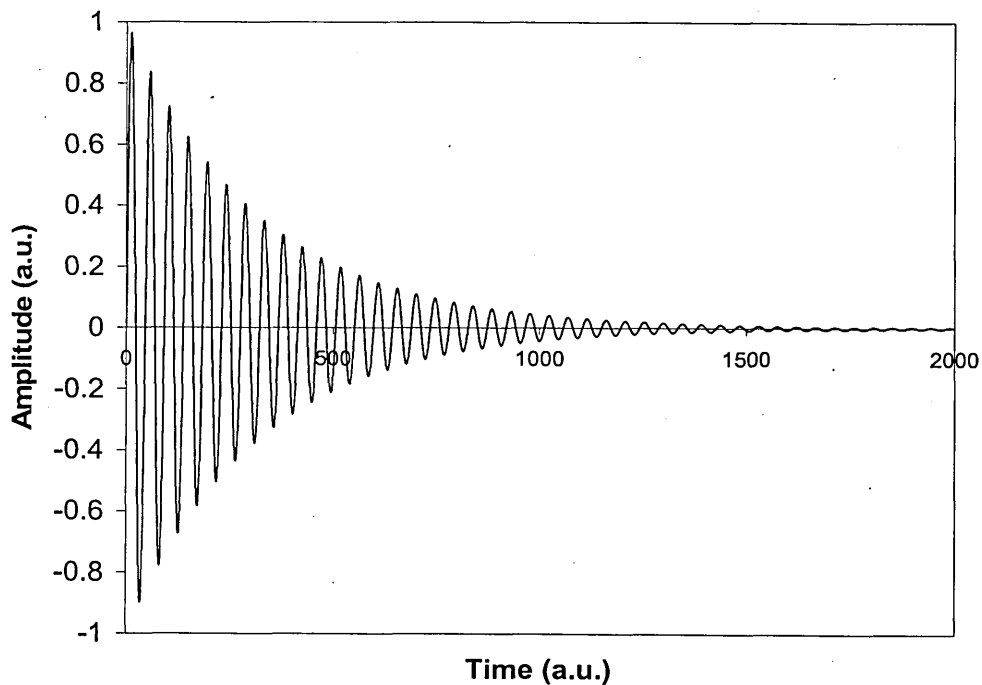


Figure 3.5. Typical decay curve obtained from equation (3.5).

3.3.3 Impedance/Network Analysis

The most comprehensive analysis of the QCM is achieved from the measurements of Impedance/Admittance over a range of frequencies around crystal resonance [28]. This method allows all crystal resonances to be observed (see chapter 2).

The impedance of a device can be defined as the total opposition a device or circuit offers to the flow of alternating current at a given frequency [29]. Impedance is represented by a complex quantity consisting of a real part (resistance R) and an imaginary part (reactance X). It can be expressed in the rectangular coordinates form $R+jX$ or in polar form as a magnitude and phase $|Z| \angle \theta$. In many cases it is however more convenient to use the reciprocal of the impedance $\frac{1}{R+jX}$ known as the admittance Y , which is represented by the complex quantity $Y=G+jB$, where G is the conductance and B is the susceptance.

The main drawback of the network analysis method is high instrument cost, with a typical purchase price of over £20 000 limiting the use of such method to the analytical laboratory. Several research groups have however recently implemented low cost designs performing the same function of the network analyzer [30-32].

For all the experiments in this thesis, a Solartron SI 1260 impedance analyzer was used. Control and interface software was written in Labview®, details of which can be found in appendix [D]. An initial crystal measurement consisted of setting the start and stop frequencies at approximately 10kHz above and below the parallel and series resonant frequencies of the QCM respectively. A measurement at a sampling step of 1kHz would be taken to check if the full spectra is obtained. If successful, the start and stop frequencies are adjusted to 2000Hz above the parallel and 2000Hz below the serial resonant frequency, a further sweep is then taken at 100Hz sampling frequency to give

an accurate representation of the impedance spectra. A typical sweep is shown in figure 3.6 showing both the admittance magnitude and phase.

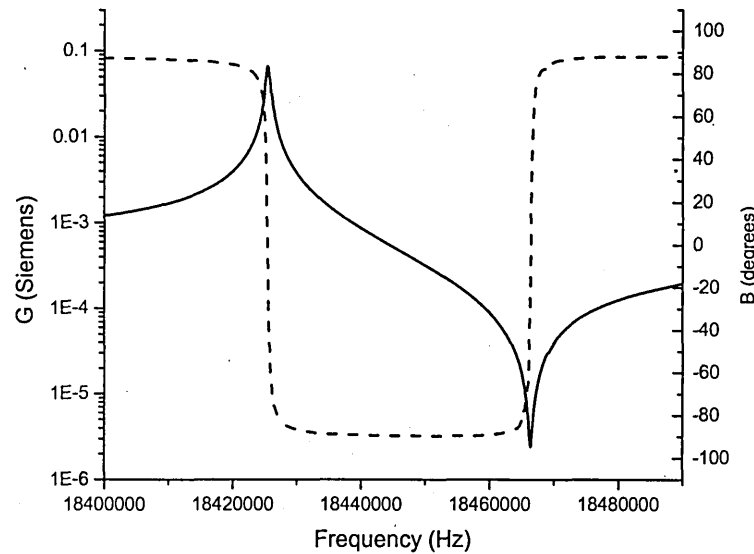


Figure 3.6. Experimental measured admittance spectra showing both serial and parallel resonances (note nulling procedure described in section 3.7 has been applied to this spectrum).

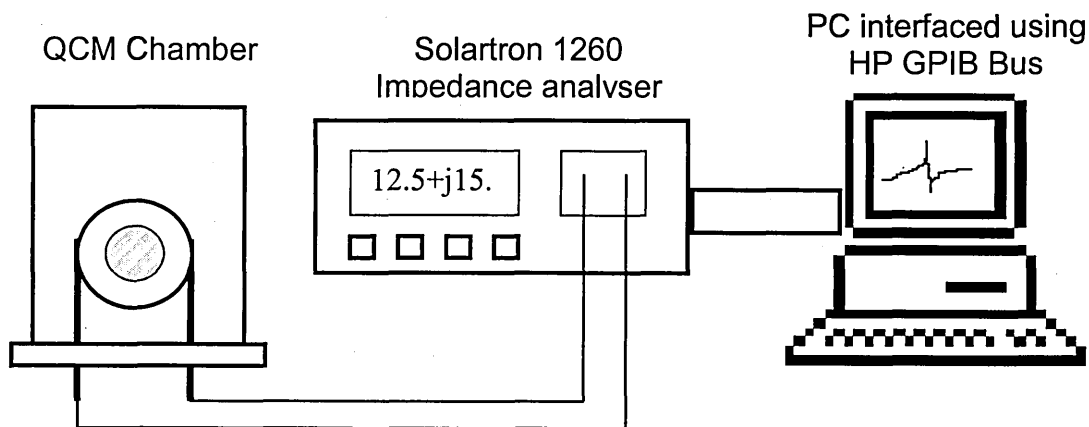


Figure 3.7. Diagram of the Basic Experimental set-up.

3.3.4 Experimental errors

From preliminary crystal measurements it was found that errors were also being introduced from parasitic stray impedances associated with the test leads, mounting fixtures, and crystal connectors. This can clearly be seen on the admittance phase

diagram in figure 3.8. As the phase approaches the parallel resonant frequency large spikes in the spectra are evident.

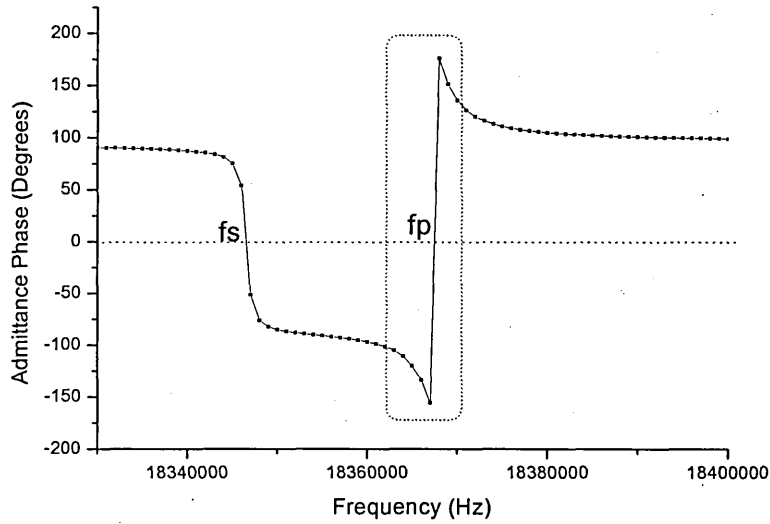


Figure 3.8. The admittance phase with series and parallel resonant frequencies indicated; the large spikes in admittance phase are also highlighted.

The following procedure was therefore completed before each set of measurements to compensate for the additional capacitance/inductance introduced by the test setup. The basis of the approach is to carry out short circuit and open circuit tests to find the parasitic series and parallel impedances (figures 3.9b and 3.9c respectively) and then subtract these values from the experimental data at each measured frequency. The procedure is outlined in figures 3.10a-c.

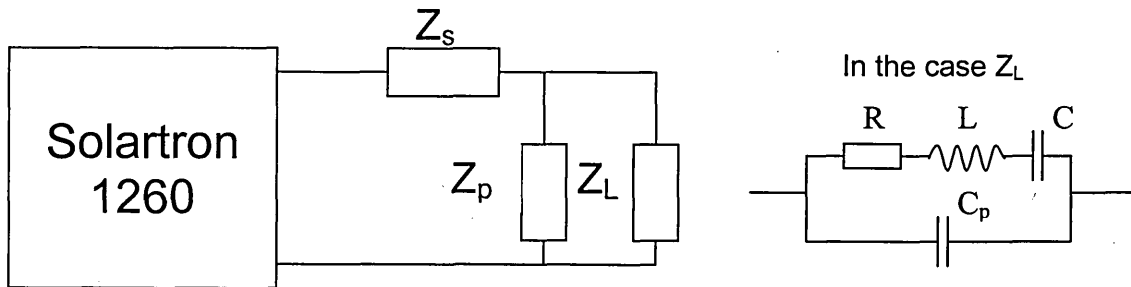


Figure 3.9a. The experimental setup may be represented by the above circuit where Z_L is the object under test.

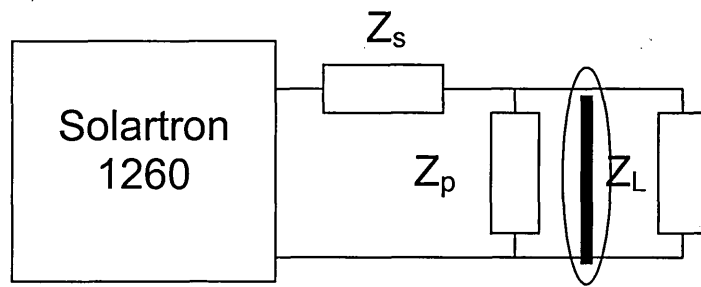


Figure 3.9b. Perform Short Circuit (s/c) test to give Z_s .

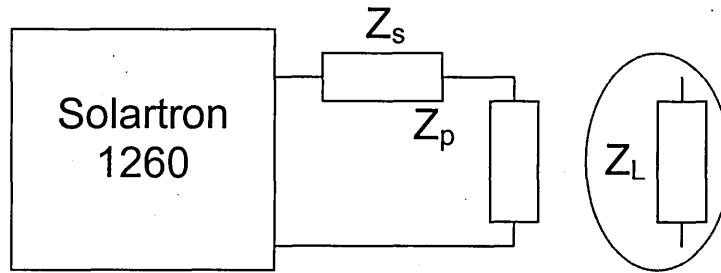


Figure 3.9c. Perform Open Circuit (o/c) test to give $Z_s + Z_p$.

$$Z_T = Z_s + \frac{1}{\left(\frac{1}{Z_L} + \frac{1}{Z_p}\right)} \quad (3.8)$$

which after rearrangement for Z_L Gives

$$Z_L = \frac{1}{\left(\frac{1}{Z_T - Z_s}\right) - \frac{1}{Z_p}} \quad (3.9)$$

Examples of the spectra before and after compensation (nulling) are shown in figure 3.10 a-d. The results show a significant decrease in both the resonant frequency and admittance magnitude, as well as pseudo stretching of the spectra. Most noticeably, no spikes appeared in the admittance phase.

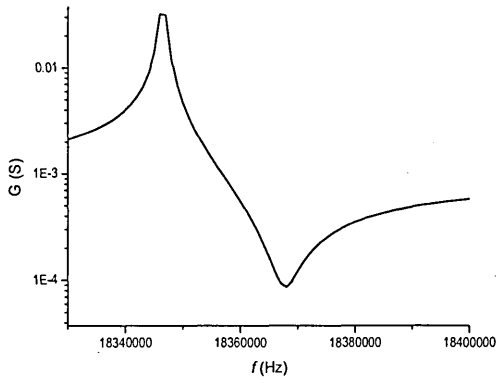


Figure 3.10a Admittance magnitude before nulling.

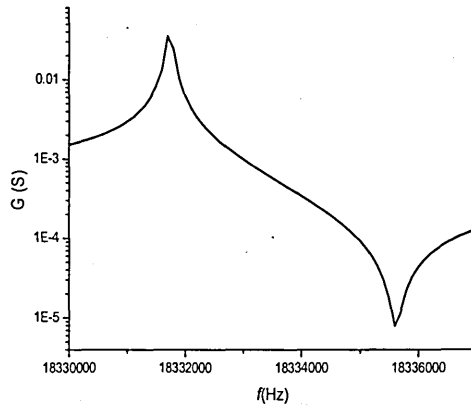


Figure 3.10b Admittance magnitude after nulling.

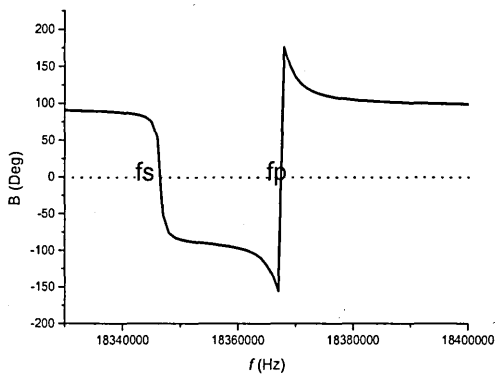


Figure 3.10c. Admittance phase before nulling.

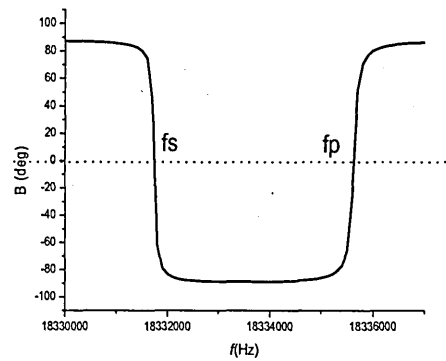


Figure 3.10d Admittance phase after nulling.

3.3.5 Increasing measurement accuracy

In an ideal case the measurement setup should have the resolution of less than one hertz and allow recording of a full spectrum (range of 100kHz), in under one second. While modern network analyzers quote specifications close to these parameters the Solartron 1260 is limited to approximately 1pt/0.8s. A typical spectrum is shown in figure 3.6 sampled at a frequency of 100Hz over a 100kHz range, and therefore required approximately eight minutes.

An increase in accuracy was obtained by interpolating extra data points above the sampling frequency. This was implemented by additional data fitting. The peak of the admittance magnitude (G) (figure 3.10a) is fitted to a polynomial curve, as shown in (figure 3.10b) and the zero crossing of the admittance phase (B) (figure 3.10c) is fitted to a linear equation. For the polynomial fit nine data points would be taken centred on the measured frequency of maximum admittance $G_{(max)}$, as shown in (fig 3.10b). A polynomial fit was then performed on the selected nine data points and the best fit coefficients obtained were saved. The order of the polynomial was determined by an iterative process, and a 4th order polynomial was found to give the most accurate results. Polynomials of lower orders give a poor fit to the data, while higher polynomials follow errors in the experimental data. The saved best fit coefficients were then used to re-plot the admittance peak at an increased sampling frequency of 1 Hz (see figure 3.10b). The new frequency of $G_{(max)}$ was then taken from the peak of the interpolated data. Similarly, seven points were taken about the zero phase crossing and fitted to a linear equation with additional points interpolated at a 1Hz frequency. The verification was performed using simulated data and the results show that the frequencies $G_{(max)}$ and $B_{(=0)}$ could be obtained with the accuracy better than $\pm 3\text{Hz}$ using a sampling frequency of 100Hz for the initial data. The technique described gives rise to a significant increase in

accuracy and also reduces the overall noise of the setup. Documentation for the program can be found in the appendix [E].

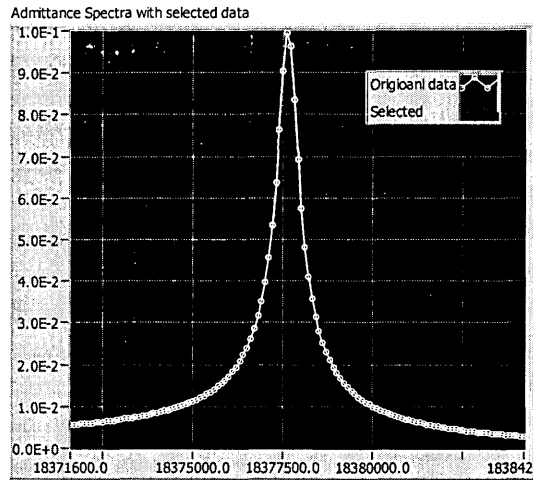


Figure 3.11(a). Admittance spectra at series resonance showing selected points for the polynomial fit.

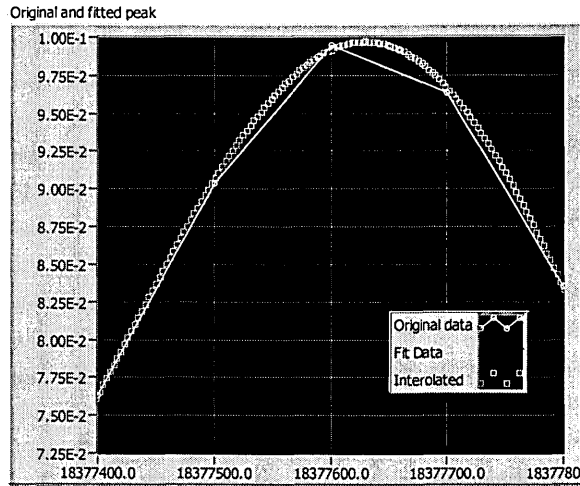


Figure 3.11(b). Original data, fitted 4th order polynomial to the resonance peak and interpolated data points.

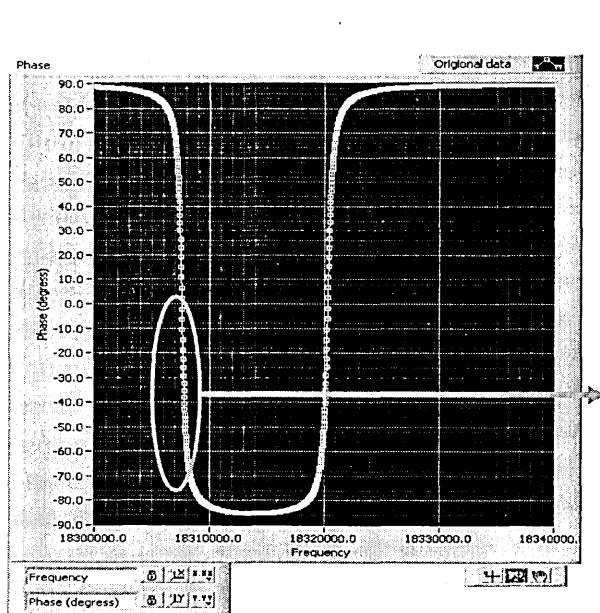


Figure 3.11(c). Admittance phase with zero phase crossing at series resonance selected.

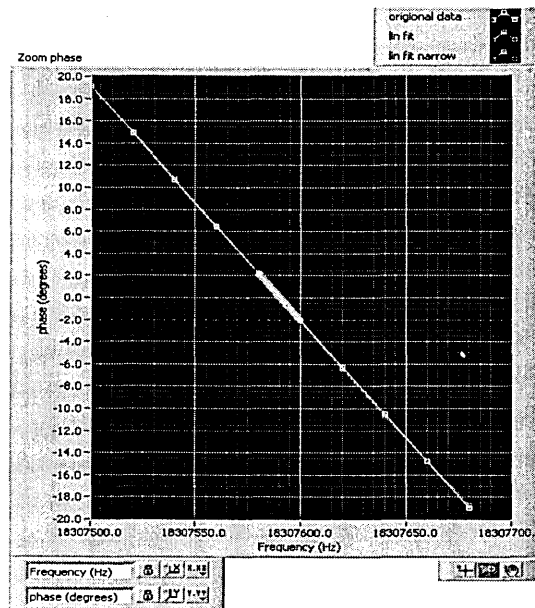


Figure 3.11(d). Linearly fitted admittance phase centered on the zero phase crossing.

Figure 3.11 a-d. Screen capture of Labview® data interpolation software.

3.3.6 Real time analysis

A specific goal for the experimental setup was to allow the real time analysis of QCM parameters. From literature and early experimental results using oscillator only measurements, the response time of a QCM on vapour exposure was found to be extremely quick; typically being under five seconds [3,4,7,9]. With frequency only measurements the sampling time was not a problem as the only limitation imposed was the gating time of the frequency counter. However, with the Solartron analyzer taking over eight minutes to obtain a full spectrum, real time analysis was not a realistic option without modification of both the software and setup. The following approach was therefore devised to allow a pseudo real time response. For all initial QCM measurements the full spectra would be undertaken, fitted to the BVD equivalent circuit, and values of R, L, C and C_p obtained for the uncoated quartz. For all further measurements a narrow frequency range of 1800Hz centered on the frequency at maximum admittance magnitude (G_{max}) was used. With the fixed parameters of the quartz R, L, C and C_p established, further fitting were applied to L_1 and R_1 related to the additional mass and dissipation respectively. These two parameters can be obtained from the narrow frequency scans as discussed previously.

Measurements of 18 points took approximately 23 seconds; this includes setting the frequency range of the analyzer, download of the measured spectra to PC and all data fitting (analysis). The Labview® software was programmed to track the frequency of (G_{max}) after each measurement, the start and end points for the next measurement would be set to ± 900 Hz centred on the $G_{(max)}$ frequency.

A major disadvantage of slow measurement speed is that a false spectrum would be obtained if the evaporation of the vapour is not complete, or leakage occurs during the measurement. In this case, the vapour concentration is not constant during the complete

measurement of the spectra, and the spectra are therefore stretched towards lower frequency due to evaporation and to a higher frequency due to leakage (see figure 3.12a). Figure 3.12b shows a true representation of the admittance spectra if a quick acquisition time is available, and a number of spectra are measured during the 8 minute period.

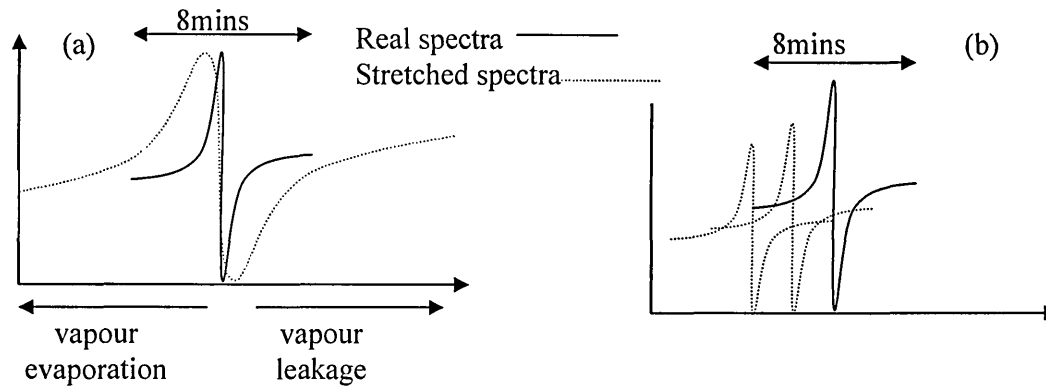


Figure 3.12 a). The result of slow acquisition time when the properties of the QCM change during a spectra measurement. The spectrum is stretched to higher or lower frequency depending on adsorption or desorption of the vapour. b) Several spectra recorded in the same 8 minute period.

To obtain a true admittance measurement over an 8 minute period it must also be assumed that the sorption of vapour and changes in viscoelastic properties of the sensing membrane are not time dependant and remain constant throughout. From previous work by Nabok, Hassan et al [3,4,9] this assumption cannot be made, and the measurement of the kinetics during vapour adsorption yields more realistic results. The narrow frequency range 23 second measurement period was found to be acceptable, giving realistic response kinetics on vapour exposure without any major loss in characteristics of the admittance curves.

3.4 Array measurements and techniques

To measure several QCM in real time, two additional circuits were developed allowing several QCM to be multiplexed into a single measurement device. With the rapid sampling times achievable using resonant oscillator circuits and the QCMD technique, it was possible to obtain the measurement of up to five QCM in under four seconds. This gives a realistic pseudo real time response of the kinetics during vapour adsorption.

3.4.1 Resonant oscillator array

The measurement of several QCM was performed by using the time division multiplexing technique. In several commercial multiplexer integrated circuits that were tested the cross talk between the channels was too high. The final design was therefore based around a relay approach, each oscillator connected to the frequency counter by an individual relay. At sampling of a channel, the corresponding relay would be closed by a signal triggered from the IEEE 1284 bus, creating a physical connection to the frequency counter. The measurement would then be taken, data transferred and logged on PC, then the next channel would be sampled and so on. To achieve stable operation the oscillator must be given a suitable warm up period, ruling out the possibility of multiplexing all the QCM into a single oscillator circuit. A separate oscillator circuit is required for each crystal in the array. Again all control and data logging were performed using Labview® software, full details of circuit designs and components can be found in appendix [B,C]. A block diagram of the test setup is shown in figure 3.13.

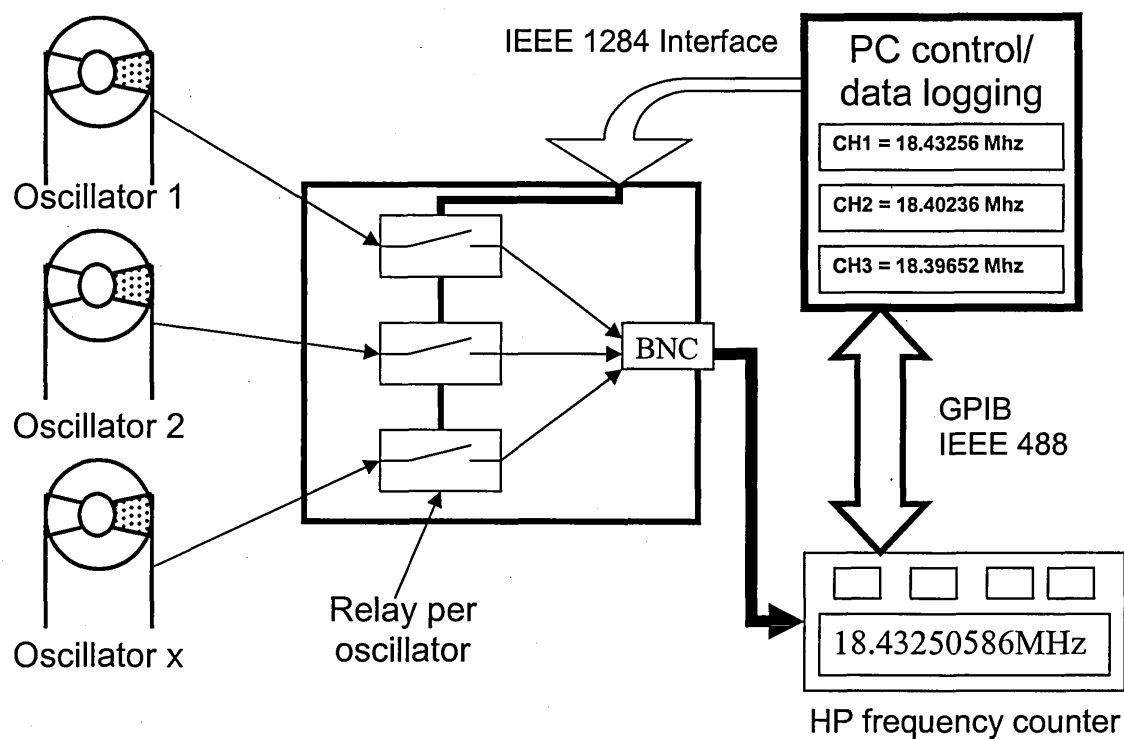


Figure 3.13. Block diagram of resonant oscillator QCM array, all the relays IEEE 1284 connectors and associated electronics were mounted onto a single PCB.

3.4.2 QCMD Array

For multiple sensor QCMD measurements, the same relay based multiplexing approach was implemented. The major difference being only a single measurement circuit was used (see figure 3.14), whereas in the oscillator array each QCM was driven by an individual oscillator circuit. A sampling time of approximately one second per QCM was achieved. Details of circuit designs, components, can be found in appendix [C].

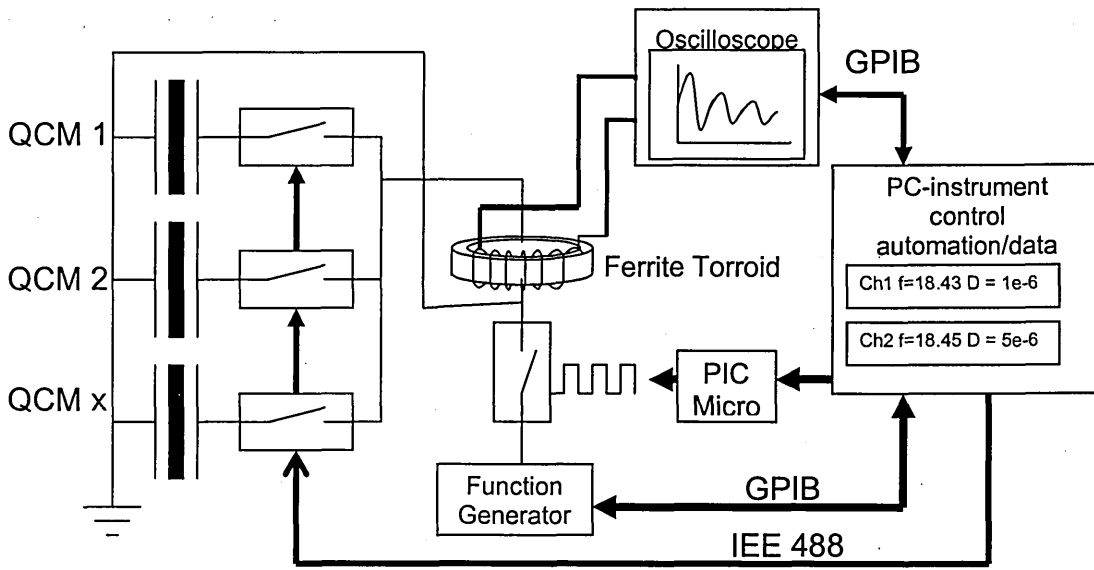


Figure 3.14. Schematic of QCMD array. Each QCM is connected through individual relay to the driving circuitry with the relay switching controlled using IEE 488 bus.

3.5 Data acquisition and analysis

After either an impedance spectra or QCMD decay curve is obtained a suitable fitting procedure was performed to extract the relevant parameters related to the mass accumulation and/or changes in the film viscosity. Several fitting algorithms were tested with the main performance criteria being the accuracy and fitting speed. As real time analysis was required, a fitting time of less than one second was seen as acceptable.

3.5.1 Curve fitting

Several curve fitting techniques based around the least square error principle were tested ranging from an iterative approach of testing every possible combination of the equivalent circuit parameters within a specified search space, Genetic Algorithms, simulated annealing and Levenberg Marquadt technique.

If good estimate coefficients for the fit were available the Levenberg Marquadt (LM) technique gave the best performance regarding both the speed and the fit accuracy. However, if the initial guess coefficients were not close enough to the actual values the LM technique proved to be ineffective often giving erroneous values. In this case the simulated annealing (SA) approach proved to be effective. The SA minimization technique has been proven to be successful for circuit tuning applications [33-35], and was therefore applied to fitting experimental data of the TSM resonator to the BVD equivalent circuit model.

3.5.2 Simulated Annealing (SA) technique

A basic overview of the SA algorithm used and how it was applied in this application is shown below.

- Select the initial system configuration R,L,C and C_p -(datum point 'p₁')
 - Let the variables move from this datum point by a small quantity R±Δ, L±Δ, C±Δ, C_p±Δ. generating a new point 'p₂'.
- The probability of this new point becoming the old datum point 'p₁' is determined using the metropolis criterion.

$$\text{if } f_2 < f_1 \quad \text{probability} = e^{-\frac{(f_1 - f_2)}{T}} \quad (3.10)$$

$$\text{else probability} = 1$$

where f_i is the sum of the squared errors between the experimental or generated spectra and the spectra generated using the parameters of datum point 'p₁'.

$$f_1 = \frac{1}{n} \sum_{i=0}^{n-1} (p1_i - y_i)^2 \quad (3.11)$$

Where n is the number of data points, $p1_i$ is the admittance value generated from equations (2.34) and (2.35) using parameters of 'p₁' (values of R, L, C and C_p), and y_i are the values of experimental admittance spectra.

In the same way f_2 can be found as the sum of the squared errors between the experimental or generated spectra and the spectra generated using the parameters of point 'p₂'. $p2_i$ is the admittance value generated from equations (2.34) and (2.35) using parameters of datum point 'p₂'.

$$f_2 = \frac{1}{n} \sum_{i=0}^{n-1} (p2_i - y_i)^2 \quad (3.12)$$

- A random number is generated between 0 – 1; if this number is greater than or equal to the calculated probability, f_2 becomes the new datum point, else f_1 remains the datum point.
- T is a control parameter often referred to as '*temperature*'. This dictates the willingness of the algorithm to accept points with higher errors.
- A number of iterations are made at each value of T . At high values of T the probability of a new point being selected as the datum points is high as the value of T decreases the algorithm is increasingly selective only selecting points with a smaller error.

The algorithm was implemented in MATLAB 6.0 and tested using simulated data. The program proved successful at fitting equivalent circuit parameters when poor initial guess coefficients are used. Its major disadvantage was however the lengthy fitting time (up to 30s) and was therefore not feasible for real time analysis.

3.5.3 Levenberg Marquadt

If a spectrum containing both f_s and f_p is obtained, realistic initial parameters can be calculated using a non linear Levenberg Marquardt [36,37] least squares fitting algorithm. The initial implementation was to manually adjust equivalent circuit parameters until a reasonable visible fit obtained. These parameters are then used as the guess coefficients. To obtain initial parameters from the spectra the following method was applied.

At small values of R , the series resonant frequency f_s defined by equation (2.4) can be estimated from G_{max} . However as R increases the correlation between G_{max} and f_s starts to diminish and the approximation is no longer feasible. A more accurate estimation of f_s is found from the mid point between the frequency $f(G_{max})$ and the frequency $f(B_{low}=0)$

(the lower frequency of zero phase crossing) see figure 3.15. Table 3.5 shows examples of resonance characteristics for four different values R .

R	f_s	$f_{(Gmax)}$	$f_{(B_{low}=0)}$	$f_s - f_{(Gmax)}$	$f_s - (B_{low}=0)$
10	18316675.68	18316672.7	18316678.8	2.9833004	-3.1167
20	18316675.68	18316663.6	18316687.9	12.0833	-12.2167
100	18316675.68	18316376.4	18316983.1	299.2833	-307.4167
200	18316675.68	18315521.2	18317961	1154.4833	-1285.317

Table 3.5. Simulated resonance properties for different values of R .

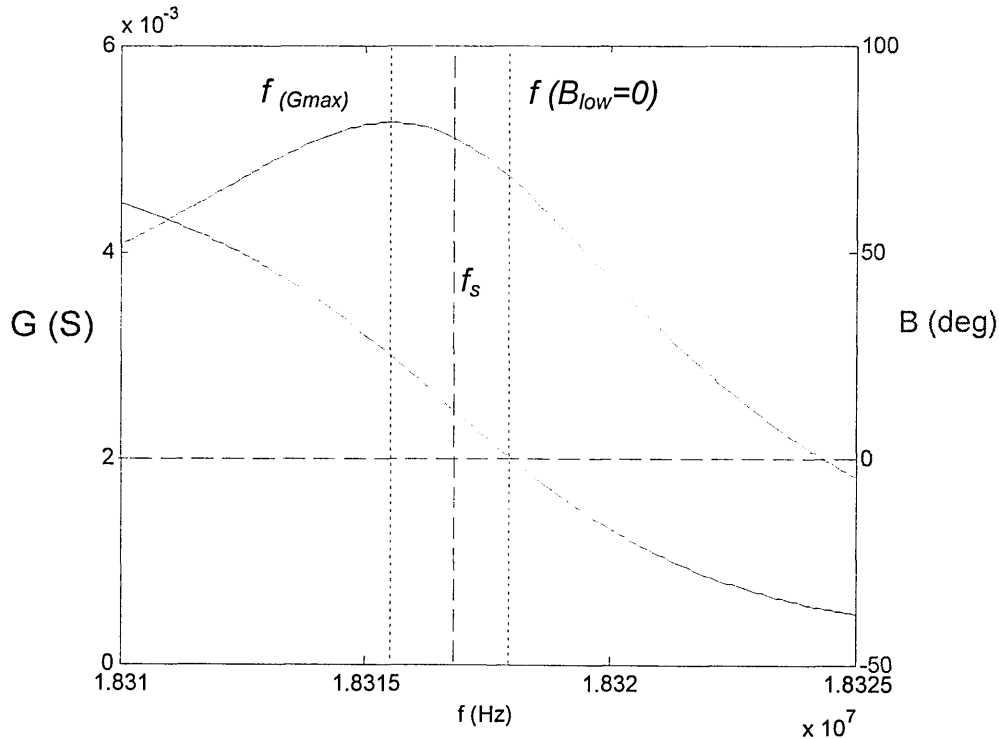


Figure 3.15. Simulation of admittance spectra around series resonance using the following parameters $R = 200\Omega$, $L=3.02\text{mH}$, $C=25\text{fF}$ and $C_p= 12\text{pF}$. A clear separation between the series resonance f_s , maximum admittance $f_{(Gmax)}$ and zero phase crossing $f_{(B_{low} = 0)}$ can be observed.

The parallel capacitance C_p can be estimated from equation (3.13), with $G_{(min)}$ taken as the parallel resonant frequency. Additional data points were again interpolated through polynomial fitting of the series/parallel resonance curves as described in section 3.35 to

increase the sampling frequency measurements up to $\pm 3\text{Hz}$. Guess coefficients for L and C are found from equations (3.14) and (3.15) respectively [12].

$$C_p = \sqrt{\frac{G_{(\min)}}{(2\pi f)^2 R}} \quad (3.13)$$

$$L = \frac{1}{8\pi^2 f C_p \Delta f_{sp}} \quad (3.14)$$

$$C = \frac{2\Delta f_{sp} C_p}{f} \quad (3.15)$$

where $\Delta f_{sp} = f_p \cdot f_s$

The complete fitting process described was implemented using Labview® software, which incorporates both the data acquisition and curve fitting programs with all calculations/fitting being performed autonomously. The complete post acquisition analysis requires less than 50ms on an IBM PC running at 1700 MHz. Fitting accuracy was tested on generated spectra; and the results presented in Table 3.6 show the error of less than 0.1%.

	R (Ω)	L (mH)	C (Ff)	C _p (Pf)
Actual	18.000000	3.022000	25.000000	10.000000
fitted	17.999998	3.022002	24.999983	10.000026

Table 3.6. Example of fitted values produced from simulated data to test the curve fitting software.

3.5.4 Parameter minimization

From the equation for the series resonant frequency (is clearly evident that f_s is a function of equivalent circuit parameters L and C). If f_s is accurately extracted from the spectra the fitting equation can be minimized to three parameters. The value of f_s was estimated as the frequency half-way between $f_{(G_{max})}$ and $f_{(Blower=0)}$ (as shown previously

in figure 3.15). The software was modified to include the calculation of L or C from the series resonant frequency, and therefore to reduce the problem to three variables.

3.5.5 Feature extraction

With typical experimental vapour exposure lasting several hours the amount of data collected is vast. This becomes increasingly problematic as the number of crystals is measured. An example of an array containing 5 QCM over a period of 2 hours would give: $5(\text{number of QCM}) \times 2(\text{number of parameters } f \text{ and } D \text{ or } R) \times 12(\text{number of measurements per minute}) \times 120(\text{Total time}) = 14400$ measured data points. A typical measurement for a single QCM is shown in figure 3.16a & b

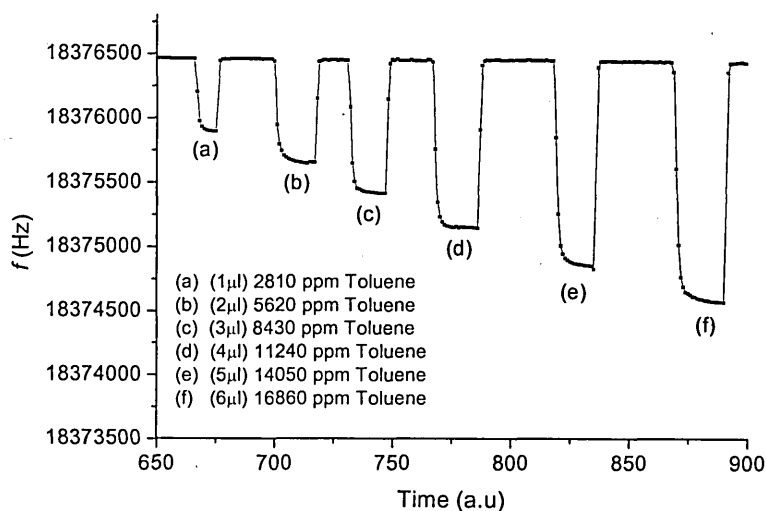


Figure 3.16a. Typical measurement of frequency during a sequence of exposures to an organic solvent.

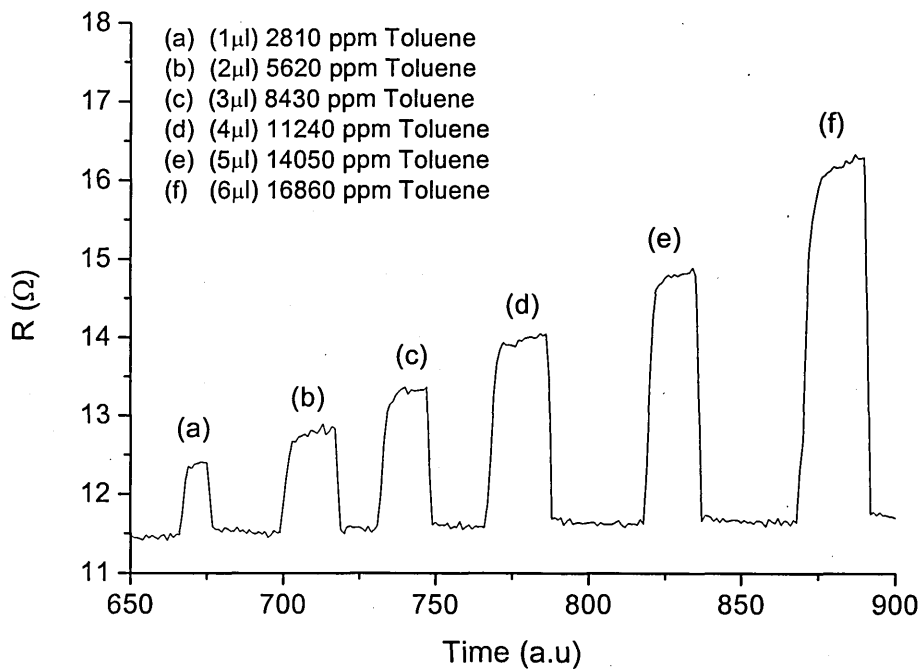


Figure 3.16b. Typical measurement of resistance during a sequence of exposures to an organic solvent.

From this set of data shown in figure 3.16a & b, it is apparent that only specific features are of prominent interest, principally the segments corresponding to vapour exposure. From these segments a single precise value must be obtained to represent the Δf and ΔR at a specific concentration as shown in figure 3.17.

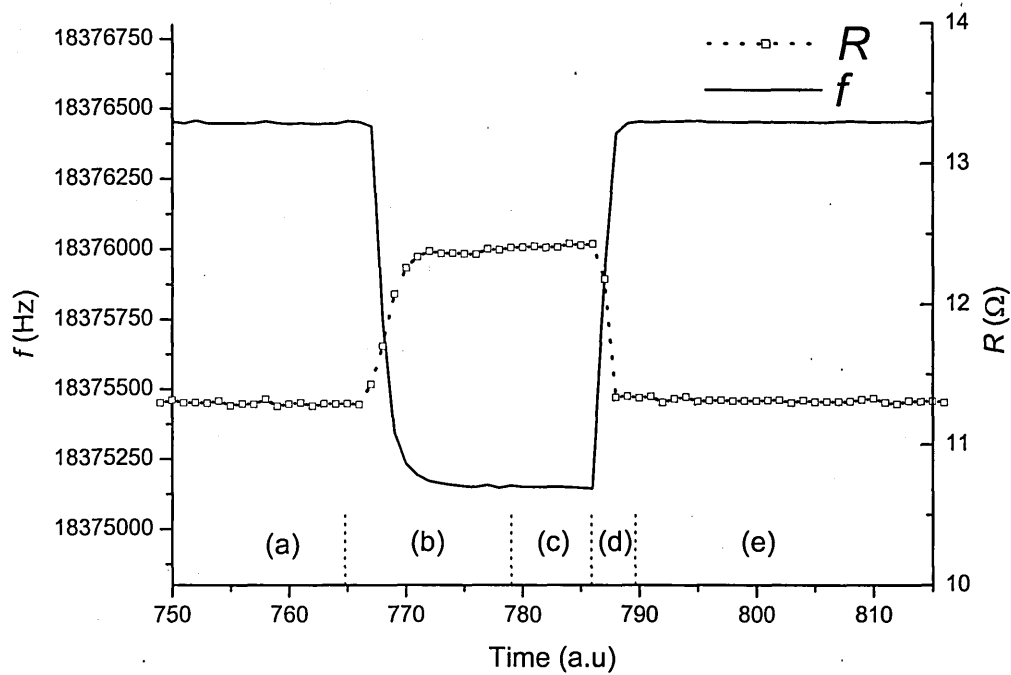


Figure 3.17 Typical responses of f and R on vapour exposure. 5 distinctive regions are apparent: a) In air b) injection of vapour c) steady state d) flushing of chamber e) recovered.

The key parameters which must be obtained are the values of f and R before exposure section (a) figure 3.17 and the settled response during exposure (section (c) in figure 3.17). To extract these points the Labview® software was programmed to perform the following.

- Differentiate the frequency data to find the injection and vapour release points which are shown by large spikes, which correspond to sections (b) and (d) of figure 3.17 respectively.
- Find the 3 values with the smallest differential in the preceding 20 data points before section (b), take the mean of these three to obtain values frequency (f_b) and resistance (R_b) before exposure.

- Find the three points between sections figure 3.17 (b) and (d) having the smallest differential. Take the average of the three values to obtain the exposed frequency and resistance values f_e and R_e respectively.

$$\Delta f = f_b - f_e$$

$$\Delta R = R_b - R_e$$

The software implementation of the above allowed the fast, accurate, and repeatable extraction of the Δf and ΔR parameters.

3.6 Film characterization techniques

Many aspects of the QCM theory presented in Chapter 2 are based on the assumption that the coating (sensing membrane) covers the full surface area of the QCM electrodes and has a consistent thickness and homogeneity. Many researchers have found the surface roughness plays a major role in the TSM resonator response, and becomes increasingly important in the liquid phase where “trapping” of liquid inside the film matrix may occur [38-41]. Textured and smooth surfaces also show different behaviour, with the textured surfaces giving an increased motional resistance [38].

It is also anticipated that the calixarene films are not acting purely according to the Sauerbrey equation and therefore a simple linear relation between the frequency shift may not be applicable. A major contribution from viscoelastic properties may be evident in the frequency shift. Hence the confirmation of the film thickness by an independent method is required. Therefore, to determine surface roughness, homogeneity and film thickness the techniques of Atomic Force Microscopy (AFM) and ellipsometry were employed.

3.6.1 Atomic Force Microscopy (AFM)

The principles of AFM operation are relatively simple. An atomically sharp tip is scanned over the surface of the object with a feedback mechanism that allows the piezo-electric scanners to maintain the tip at a constant force, therefore obtaining height information. The inverse may be applied maintaining constant height to obtain force information above the sample surface. Tips are normally made from Si_3N_4 or Si, and extended down from the end of a cantilever. The nanoscope AFM head employs an optical detection system, in which the tip is attached to the underside of a reflective cantilever. A laser diode is focused onto the back of a reflective cantilever. As the tip scans the surface of the sample, moving up and down with the contour of the surface, the laser beam is deflected from the attached cantilever into a quadrupole element photodiode. The photodetector measures the difference in light intensities between the upper/lower and left/right sections of the photodetectors, and then converts to voltage. Feedback from the photodiode difference signal, through software control from the computer, enables the tip to maintain either a constant force or constant height above the sample. In the constant force mode the piezo-electric transducer monitors real time height deviation. In the constant height mode the deflection force on the sample is recorded. The latter mode of operation requires calibration parameters of the scanning tip to be inserted in the sensitivity of the AFM head during force calibration of the microscope [42,43].

3.6.2 Ellipsometry

Ellipsometry measures the change in polarization state of light reflected from the surface of a sample. The measured values are expressed as Ψ and Δ , standing for the ratio of amplitudes of p and s components of polarized light (3.17) and their phase difference (3.18).

$$\Psi = \tan^{-1} \frac{\Delta_p}{\Delta_s} \quad (3.17) \quad \Delta = \Psi_p - \Psi_s \quad (3.18)$$

These values are related to the ratio of Fresnel reflection coefficients, R_p and R_s for p and s -polarized light, respectively.

$$\tan(\Psi)e^{i\Delta} = \frac{R_p}{R_s}$$

Parameters (i.e. thickness, refractive index) of thin films deposited on silicon wafers can be found by fitting the experimental data (Ψ and Δ spectra) to Fresnel's formula.

The science of ellipsometry is vast and out of the scope of this thesis, more information can be found from the following references [44,45]. The Instrument used in this work was the JA Woolam and co M-2000V.

3.7 Conclusions

This chapter introduces several techniques which are used for QCM measurements. Three primary methods have been described; oscillator circuits, QCMD and impedance analysis. The latter two techniques show a distinct advantage as dissipation which occurs in the film can also be measured. Additional fitting and feature extraction is also required to obtain the necessary information from the measured data. The techniques used include Simulated Annealing, Levenberg Marquadt, polynomial and linear fitting. Details of the experimental procedures have been given, the Langmuir Blodgett and spin coating techniques used to apply sorbent coatings to the QCM are shown. The experimental setup and exposure methods have also been described. Lastly a brief summary of AFM and ellipsometry techniques has been given which are used to characterize the sorbent coatings used in this work.

REFERENCES

- [1] M. Ferrari, V. Ferrari, D. Marioli, A. Taroni, M. Suman, and E. Dalcanale, "Cavitation-coated PZT resonant piezo-layer sensors: properties, structure, and comparison with QCM sensors at different temperatures under exposure to organic vapors," *Sensors and Actuators B: Chemical*, vol. 103, pp. 240-246, Sept. 2004.
- [2] P. Hauptmann, "Editorial: Incoming Honorary Editor," *Measurement Science and Technology*, vol. 13, pp. 2002.
- [3] A. K. Hassan, A. K. Ray, A. V. Nabok, and F. Davis, "Spun films of novel calix[4]resorcinarene derivatives for benzene vapour sensing," *Sensors and Actuators B: Chemical*, vol. 77, pp. 638-641, July 2001.
- [4] A. K. Hassan, A. K. Ray, A. V. Nabok, and T. Wilkop, "Kinetic studies of BTEX vapour adsorption onto surfaces of calix-4-resorcinarene films," *Applied Surface Science*, vol. 182, pp. 49-54, Oct. 2001.
- [5] A. K. Hassan, A. V. Nabok, A. K. Ray, A. Lucke, K. Smith, C. J. M. Stirling, and F. Davis, "Thin films of calix-4-resorcinarene deposited by spin coating and Langmuir-Blodgett techniques: determination of film parameters by surface plasmon resonance," *Materials Science and Engineering: C*, vol. 8-9, pp. 251-255, Dec. 1999.
- [6] A. V. Nabok, N. V. Lavrik, Z. I. Kazantseva, B. A. Nesterenko, L. N. Markovskiy, V. I. Kalchenko, and A. N. Shivaniuk, "Complexing properties of calix[4]resorcinolarene LB films," *Thin Solid Films*, vol. 259, pp. 244-247, Apr. 1995.
- [7] A. V. Nabok, A. K. Hassan, A. K. Ray, O. Omar, and V. I. Kalchenko, "Study of adsorption of some organic molecules in calix[4]resorcinolarene LB films by surface plasmon resonance," *Sensors and Actuators B: Chemical*, vol. 45, pp. 115-121, Dec. 1997.
- [8] T. Wilkop, "Thin film calixresorcinarene membranes for chemical sensing," PhD Thesis, Sheffield Hallam University UK, 2001.
- [9] A. V. Nabok, A. K. Hassan, and A. K. Ray, "Condensation of organic vapours within nanoporous calixarene thin films," *Journal of Materials Chemistry*, vol. 10, pp. 189-194, June 1999.
- [10] Analytical Instrument Development, "Instruction manual A.I.D model 350 standards generator," 2005.
- [11] G. Sauerbrey, "Verwendung von Schwingquarzen zur Wägung dünner Schichten und zur Mikrowägung," *Zeitschrift für Physik*, vol. 155, pp. 206, 1959.
- [12] V. Bottom, "Introduction to Quartz Crystal Unit Design," New York: Van Nostrand Reinhold, 1982, pp. 82-83.
- [13] K. K. Kanazawa and J. Gordon, "Frequency of a quartz microbalance in contact with liquid," *Analytical Chemistry*, vol. 57, pp. 1770-1771, 1985.

- [14] F. Eichelbaum, R. Borngraber, J. Schroder, R. Lucklum, and P. Hauptmann, "Interface circuits for quartz-crystal-microbalance sensors," *Review of Scientific Instruments*, vol. 70, pp. 2537-2545, May 1999.
- [15] J. M. Beeley, C. Mills, P. A. Hammond, A. Glidle, J. M. Cooper, L. Wang, and D. R. S. Cumming, "All-digital interface ASIC for a QCM-based electronic nose," *Sensors and Actuators B-Chemical*, vol. 103, pp. 31-36, 2004.
- [16] J. Auge, P. Hauptmann, J. Hartmann, S. Rosler, and R. Lucklum, "New design for QCM sensors in liquids," *Sensors and Actuators B: Chemical*, vol. 24, pp. 43-48, Mar. 1995.
- [17] K. O. Wessendorf, "The active -bridge oscillator for use with liquid loaded QCM sensors," 2001 IEEE Int. frequency control symposium & PDA exhibition, pp. 400-407, 2001.
- [18] A. Arnau, T. Sogorb, and Y. Jimenez, "A continuous motional series resonant frequency monitoring circuit and a new method of determining Butterworth-Van Dyke parameters of a quartz crystal microbalance in fluid media," *Review of Scientific Instruments*, vol. 71, pp. 2563-2571, 2000.
- [19] A. Arnau, T. Sogorb, and Y. Jimenez, "A new method for continuous monitoring of series resonance frequency and simple determination of motional impedance parameters for loaded quartz-crystal resonators," *IEEE Transactions on Ultrasonics Ferroelectrics and Frequency Control*, vol. 48, pp. 617-623, 2001.
- [20] A. Arnau, T. Sogorb, and Y. Jimenez, "Circuit for continuous motional series resonant frequency and motional resistance monitoring of quartz crystal resonators by parallel capacitance compensation," *Review of Scientific Instruments*, vol. 73, pp. 2724-2737, 2002.
- [21] A. Arnau, Y. Jimenez, and T. Sogorb, "Circuit for continuous monitoring of quartz-crystal resonators in sensor applications," *Electronics Letters*, vol. 38, pp. 365-367, 2002.
- [22] T. Nakamoto and Takeharu Kobayashi, "Development of Circuit for Measuring both Q Variation and Resonant frequency Shift of Quartz Crystal Microbalance," *Ieee Transactions on Ultrasonics Ferroelectrics and Frequency Control*, vol. 41, pp. 806-811, Nov. 1994.
- [23] J. Schröder, R. Borngraber, F. Eichelbaum, and P. Hauptmann, "Advanced interface electronics and methods for QCM," *Sensors and Actuators A: Physical*, vol. 97-98, pp. 543-547, Apr. 2002.
- [24] T. Wilkop, "RECRAFT A35 Report," Evaluation of sensing membranes for VOC's using the QCM, Sheffield Hallam University UK, 2002.
- [25] E. Hwang and Y. Lim, "Construction of Low Noise Electrochemical Quartz Crystal Microbalance," *The Bulletin of the Korean Chemical Society*, vol. 17, pp. 39-42, 2005.
- [26] M. Rodahl, F. Hook, A. Krozer, P. Bzezinski, and B. Kasemo, "Quartz crystal microbalance setup for frequency and Q-factor measurements in gaseous and

- liquid environments," *Review of Scientific Instruments*, vol. 66, pp. 3924-3930, June 1995.
- [27] M. Rodahl and B. Kasemo, "A simple setup to simultaneously measure the resonant frequency and the absolute dissipation factor of a quartz crystal microbalance," *Review of Scientific Instruments*, vol. 67, pp. 3238-3241, Aug. 1996.
- [28] A. Kipling and M. Thompson, "Network analysis method applied to liquid-phase acoustic wave sensors," *Analytical Chemistry*, vol. 62, pp. 1514-1519, 2005.
- [29] Agilent Technologies, "Agilent Technologies Impedance Measurement Handbook," 2003.
- [30] M. Schmid, E. Benes, and R. Sedlaczek, "A computer -controlled system for the measurement of complete admittance spectra of piezoelectric resonators," *Measurement Science & Technology*, vol. 1, pp. 970-975, 1990.
- [31] J. Schroder, R. Borngraber, R. Lucklum, and P. Hauptmann, "Network analysis based interface electronics for quartz crystal microbalance," *Review of Scientific Instruments*, vol. 72, pp. 2750-2755, June 2001.
- [32] J. Schroder, S. Doerner, T. Schneider, and P. Hauptmann, "Analogue and digital sensor interfaces for impedance spectroscopy," *Measurement Science & Technology*, vol. 15, pp. 1271-1278, Apr. 2004.
- [33] M. Thompson, "Application of multi objective genetic algorithm and simulated annealing to filter design," *First International Conference, Evolutionary Multi-Criterion Optimization, 2001 Lecture Notes in Computer Science*, vol. 1, pp. 546-559, 1993.
- [34] M. Thompson and J. K. Fidler, "Tuning the pi-network using the genetic algorithm and simulated annealing," *Proc. of the 1997 European Conference on Circuit Theory and Design, Budapest, Hungary*, pp. 949-954, 1997.
- [35] M. Thompson and J. K. Fidler, "A novel approach for fast antenna tuning using transputer based simulated annealing," *Electronics Letters*, vol. 36, pp. 603-304, 2000.
- [36] K. Levenberg, "A Method for the Solution of Certain Problems in Least Squares," *Appl. Math*, vol. 2, pp. 164-168, 1944.
- [37] D. Marquardt, "An Algorithm for Least-Squares Estimation of Nonlinear Parameters," *Appl. Math.*, pp. 431-441, 1963.
- [38] D. S. Ballatine, R. M. White, S. J. Martin, A. J. Ricco, G. C. Fryre, E. T. Zellers, and H. Wohltjen, "Acoustic Wave Sensors Theory, Design and Physico chemical applications," Academic press, New York, 1997.
- [39] L. Daikhin and M. Urbakh, "Influence of surface roughness on the quartz crystal microbalance response in a solution - new configuration for QCM studies," *Faraday Discussions*, vol. 107, pp. 27-38, 1997.

- [40] L. Daikhin, E Gileadi, G Katz, V Tsionsky, M. Urbakh, and D Zagidulim, "Influence of Roughness on the Admittance of the Quartz Crystal Microbalance Immersed in Liquids," *Analytical Chemistry*, vol. 74, pp. 554-561, 2002.
- [41] S. J. Martin, C Gregory, G. C Fryre, and A. J Ricco, "Effect of Surface Roughness on the Response of Thickness-Shear Mode Resonators in Liquids," *Analytical Chemistry*, vol. 65, pp. 2910-2922, 1993.
- [42] A. Round, "Atomic Force Microscopy," H.H.Wills Physics Laboratory, University of Bristol, Bristol, BS8 1TL, UK. <http://spm.phy.bris.ac.uk/techniques/AFM/>
- [43] D. Baselt, "General concept and defining characteristics of AFM ," California Institute of Technology. <http://stm2.nrl.navy.mil/how-afm/how-afm.html#General%20concept>
- [44] H. G. Tompkins and E. Irene, "Handbook of Ellipsometry", pages 875, William Andrew Publishing, Norwich, New York, 2004.
- [45] H. G. Tompkins and W. A. McGahan, "Spectroscopic Ellipsometry and Reflectometry: A User's Guide", pages 248, John Wiley & Sons, New York, 1999.

Chapter 4

Results and discussion – QCM characterisation and coating properties

4.0 Introduction

This chapter reports the results from measurements taken using QCM sensor, coating processes and film characterisation techniques described in chapter 3. The chapter is divided into several sections; firstly the validation and performance of the experimental setups/techniques are measured and compared. Section 4.2 records the effects of temperature on the parameters of the QCM. Although the uncoated AT cut quartz has a temperature coefficient of approximately zero [1], the properties of the soft polymer coatings are affected considerably by the temperature. Section 4.3 shows the variation in quartz crystals and how they are selected for coating. The results obtained from the crystal coating process are given in section 4.4 and comparisons between experimental and simulated calculations are given. The latter sections give details taken from AFM and ellipsometry measurements. Film properties such as thickness, morphology and homogeneity are characterised.

4.1 Experimental setup validation and performance

The experimental test setups and techniques described in Chapter 3 have been evaluated and compared in performance; the properties of sensitivity, stability and reproducibility were selected as measurement criteria.

4.1.1 Frequency based measurements

The simplest and most common of all the QCM techniques is the oscillator circuit. The setup described in Chapter 3.4.1 was tested with an uncoated quartz crystal over a period of 1 hour. The measured resonant frequency of the crystal is shown in figure 4.1. Before the hour measurement was taken the oscillator was left on for an additional hour period to allow full 'warm up'. The temperature was checked periodically and remained constant at 23°C throughout the experiment. The sampling frequency was set to approximately 0.5 seconds. Although a faster sampling period is easily achieved, the selected value was established as a suitable period to obtain accurate transient information without creating colossal amounts of data. From the obtained measurements the mean frequency and the standard deviation are calculated, (see table 4.1). The Limit of Detection (LOD) defined as concentration which produces a response ($2 \times$ standard deviation) of the baseline noise [2], is also calculated. It must however be noted that the stability observed does not remain constant over longer periods, with spikes of approximately 5-10Hz being observed periodically and a drift of 5-20Hz over a 24 hour period. Within the typical experiment time used in this work the results given in table 4.1 are however applicable.

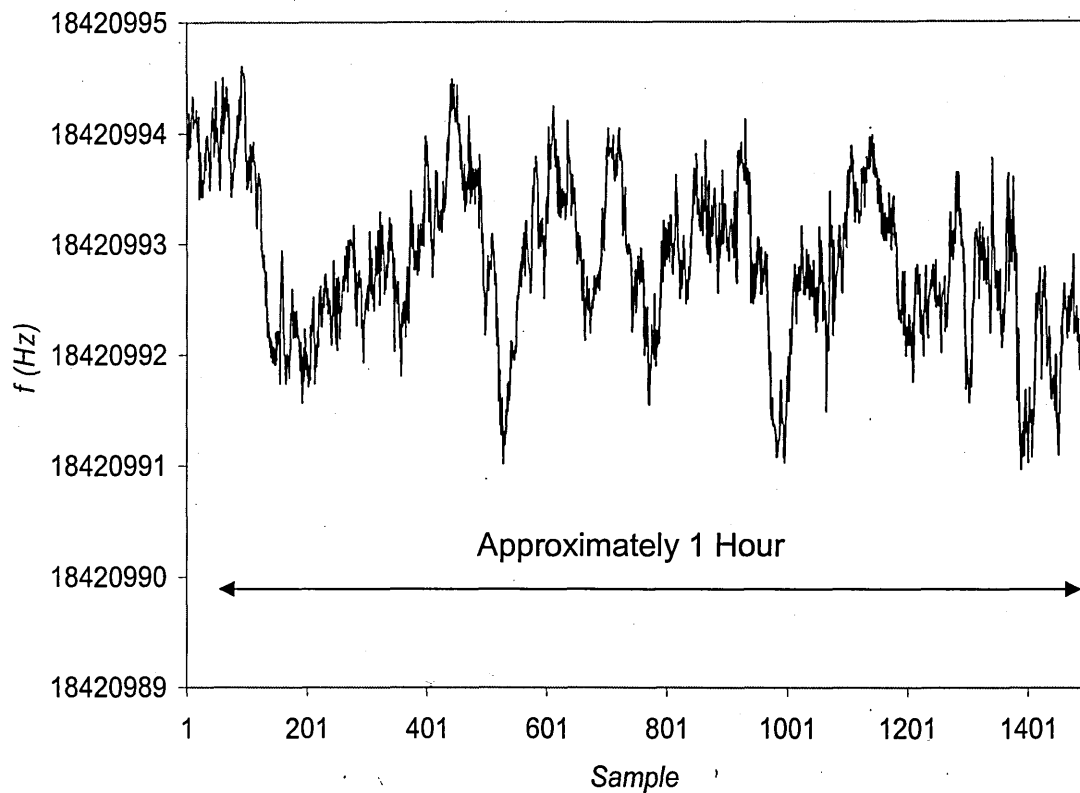


Figure 4.1. Direct frequency measurement of a coated QCM using oscillator circuits described in Chapter 3.3.1.

	Mean	Standard Deviation (SD)	2×SD
Frequency (Hz)	18420992.85	0.2922	0.5844

Table 4.1 Statistics obtained from frequency based measurements.

4.1.2 Impedance analysis

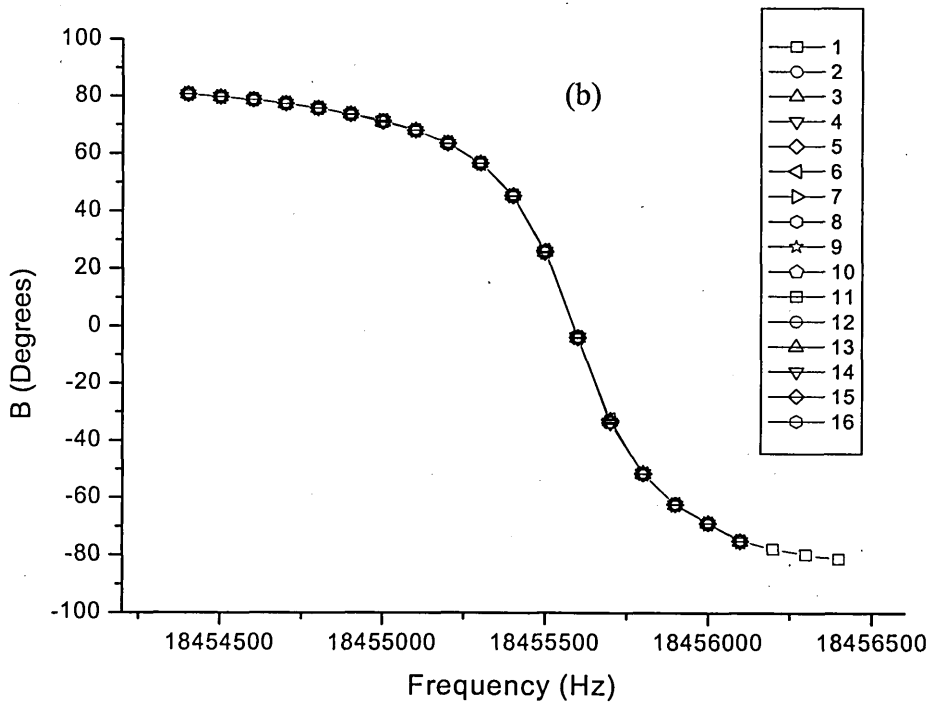
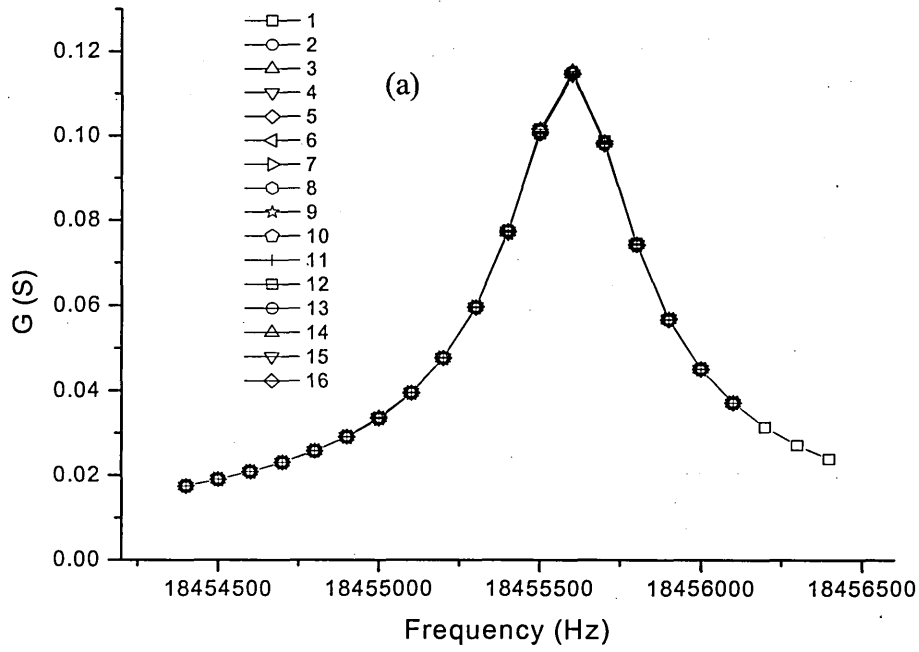
The impedance analysis setup described in Chapter 3.3.3 was tested using the following procedure. 18 points were taken during each sweep centred on the frequency of the maximum admittance as shown in figure 4.2a. Over a one hour period 156 spectra were measured equating to approximately 23.1 seconds per sweep. The spectra were fitted to the BVD equivalent circuit as described in Chapter 3, and parameters f and R were extracted. Figure 4.2 a&b shows the admittance spectra magnitude and phase

respectively over a one hour period, for clarity only every tenth spectra is shown. The stability and reproducibility of the technique is clear with virtually indistinguishable changes in spectra over the period of one hour. The impedance measurement technique inherently has several advantages over oscillator circuits; primarily all oscillators suffer from warm up time, drift, and they are often affected by temperature.

Figure 4.3 shows the extracted values of f and R over a one hour period, the statistical data from the measurements are given in table 4.2. With the additional fitting described in chapter 3.3.5 the extraction of f is considerably improved above the value of $\pm 50\text{Hz}$ achieved with the 100Hz sampling frequency. Fitting the resonance peak to the polynomial has been justified from the measurement of the admittance spectra at an increased sampling frequency around the resonance peak. Figure 4.4 shows the admittance spectra sampled at 4Hz and 100Hz intervals. The 4Hz data have been fitted to a 4th order polynomial with excellent agreement, validating the polynomial fitting procedure described in Chapter 3.3.5, which was used to improve the measurement accuracy.

	Mean	Standard Deviation (SD)	LOD = 2 × SD
Frequency (Hz)	18455593.03	1.5903	3.1806
Resistance (Ω)	8.7350	0.0248	0.0497

Table 4.2. Statistics of the extracted f and R parameters using the impedance analysis technique.



Figures 4.2 a&b. Impedance spectra measured over a 1 hour period with every tenth measured spectra shown.

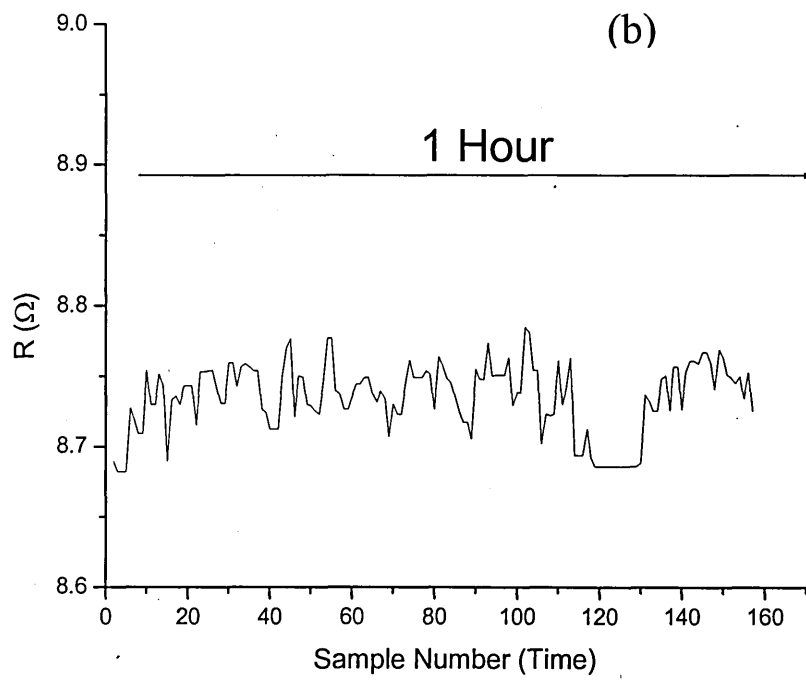
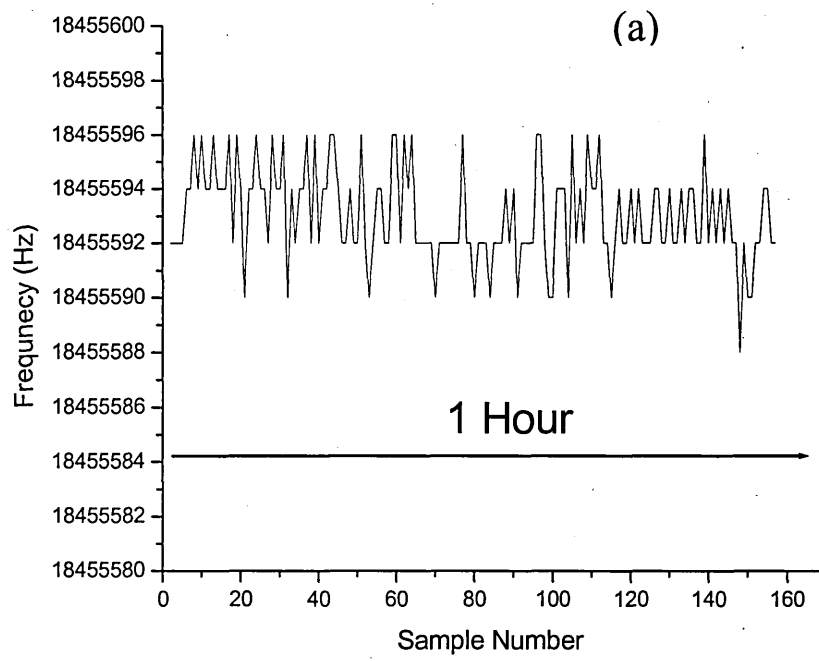


Figure 4.3 a&b. Extracted values of f and R over a 1 hour period, obtained from fitting the admittance spectra to the BVD equivalent circuit model.

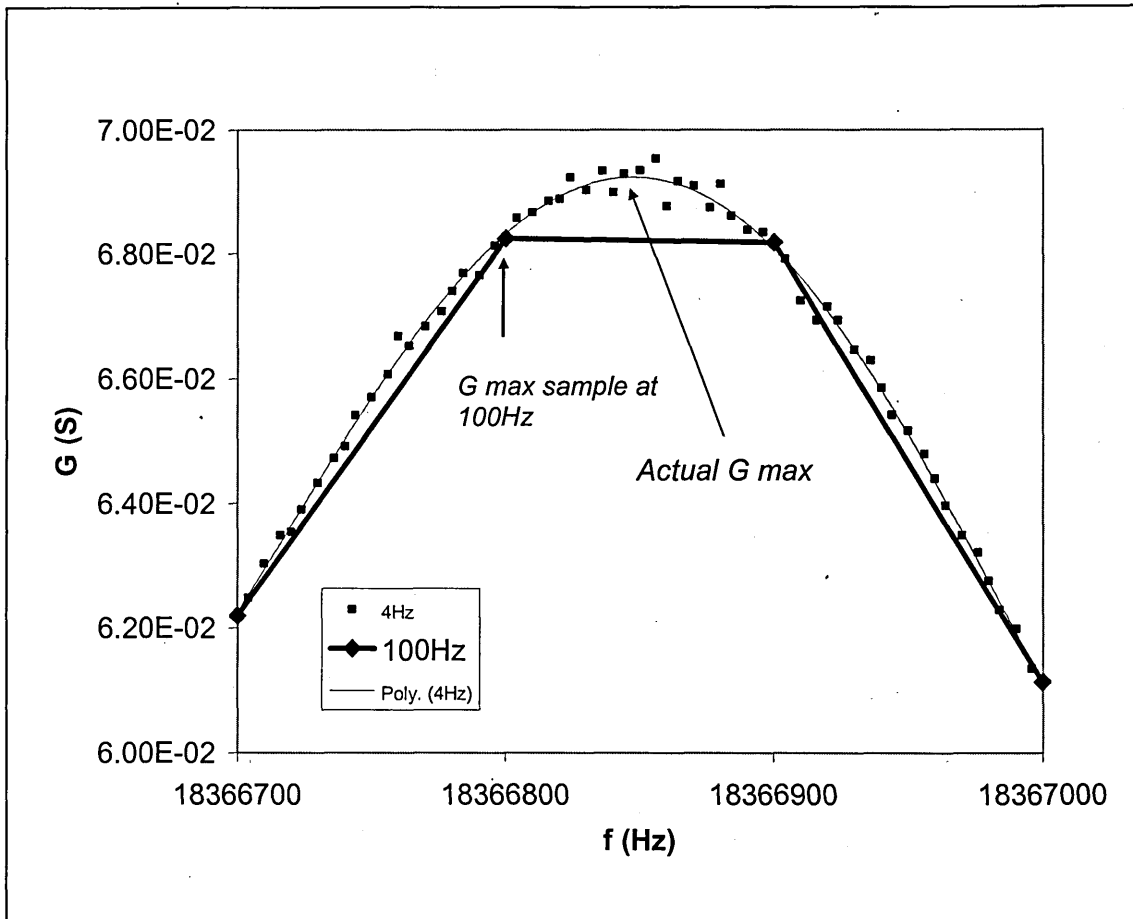


Figure 4.4. Peak of measured impedance sampled at 4Hz and 100Hz. A polynomial fit has been applied to the 4Hz spectra and shows excellent agreement with the experimental data points. The spectra highlights the need for either a high sampling frequency and or additional data fitting as applied in this case.

Repeatability of the experimental measurements is also critical, the impedance analysis technique is particularly sensitive to changes in signal path between the crystal and impedance analyser. An accurate compensation or null facility described in chapter 3.3.4 is required to cancel the loading effects caused by the connecting leads and the crystal test fixture. Figure 4.5a&b shows the admittance spectra of the same crystal measured on four separate occasions, between each of the measurements the crystal was removed from the test fixture. With careful experimental design and using the compensation procedures, almost identical results can be consistently reproduced within

the experimental error in either the frequency shift or the measured dissipation of the QCM.

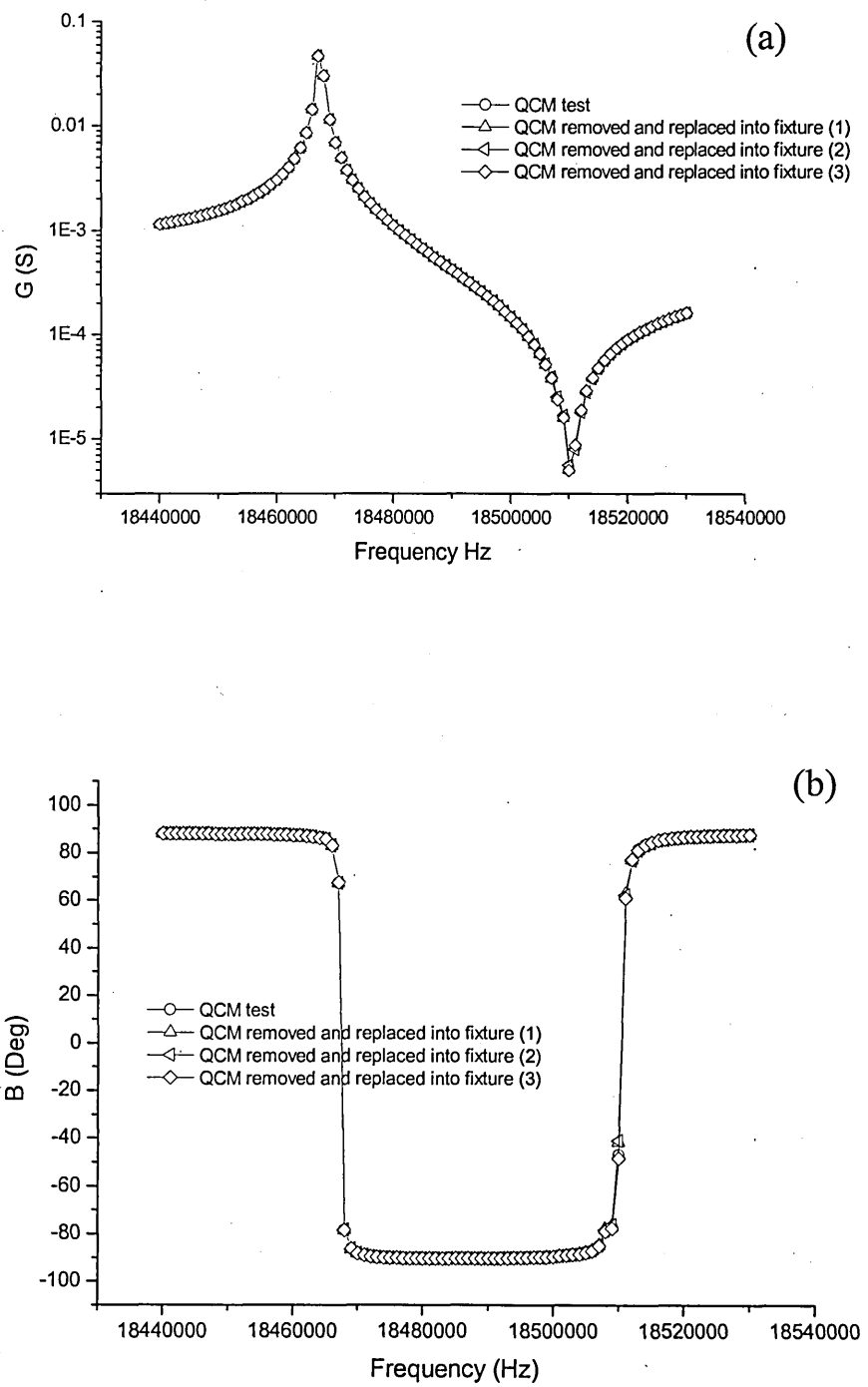


Figure 4.5 a&b. QCM admittance magnitude and phase respectively measured on four separate occasions used to validate the repeatability of the measurement procedure.

4.1.3 QCMD

Figure 4.6 shows a typical response obtained using the QCMD technique. The measured dissipation factor can be related to the resistance parameter of the BVD equivalent circuit model by equation (3.7). The accuracy and stability of the QCMD measurements are comparable to those achieved using the impedance analysis method. Although a slightly higher standard deviation is obtained, the speed of the technique allows larger number of measurements to be taken. After averaging and filtering of the obtained data, almost identical results to the impedance analysis method in terms of accuracy and stability are achieved.

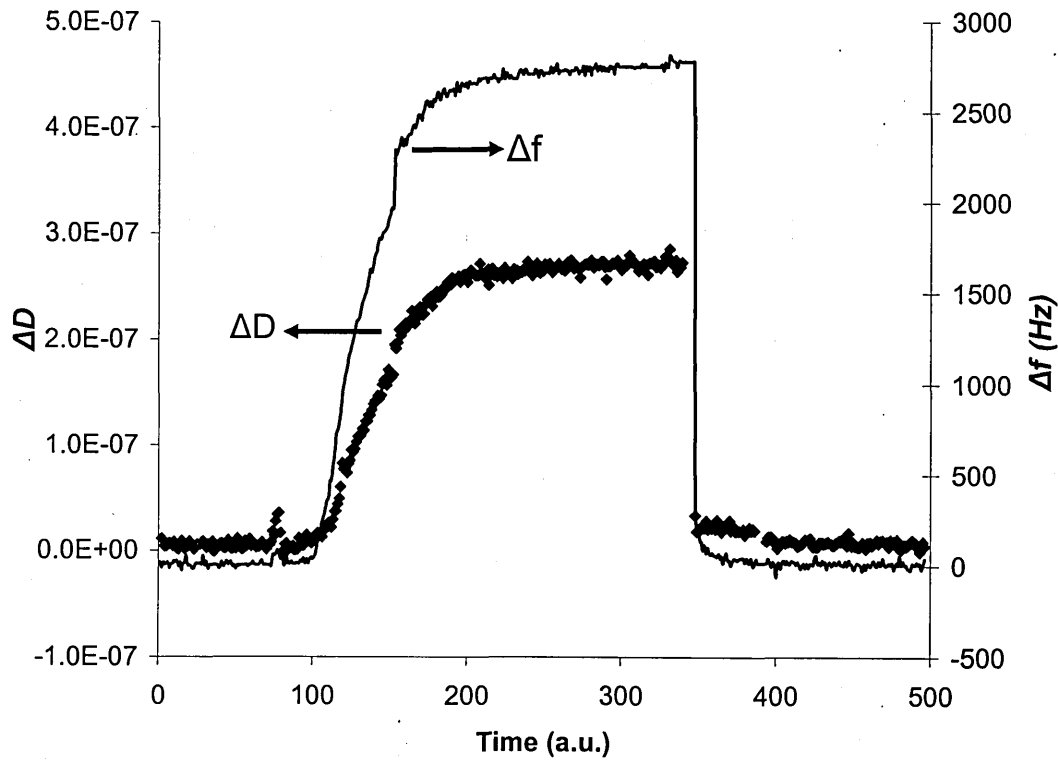


Figure 4.6. Kinetic measurement of Δf and ΔD obtained using the QCMD method.

4.2 Temperature measurements

The temperature stability of uncoated quartz crystals was tested and found to be in the range of $\pm 1\text{Hz}/^\circ\text{C}$, which is negligible in comparison to the frequency changes measured in our experiments. The effect of the moisture on QCM coated with LB C[4]RA films was studied earlier [3]. The effect of injection of saturated water vapours was unnoticeable because of extremely high hydrophobicity of calixarene coating. That is why in the present study no special measures were taken to control the humidity during measurements.

In contrast the effect of temperature on the coated crystal was found to be considerable. Figure 4.7 shows the change in the admittance spectra of a QCM coated with calix[4]resorcinarene ($\text{C}_{15}\text{H}_{31}$) at several temperatures between 25 to 85°C . With increasing temperature the frequency increases, at 85°C the frequency is over 1100Hz above the initial measured value at 25°C . This indicates a significant loss in the film mass. A value of $-1.4651\mu\text{g}/\text{cm}^2$ is obtained, using the Sauerbrey relationship given by equation (2.5) in Chapter 2.

A decrease in the resonance peak is also observed with a total resistance change of $+2.54\Omega$ over the measured temperature range. This indicates softening of the film. Extracted parameters f and R are shown in figure 4.8, a distinct correlation between the two parameters is clearly observed. A softening of the film and decrease in the mass is however unusual. The decrease in the mass may be attributed to the evaporation of residual solvent/water from within the C[4]RA matrix, such phenomena is however normally associated with a decrease in resistance (stiffening of the film).

The observed behaviour can be however understood from the fact that the solvent ethanol is used for the preparation of coating, the ethanol interacts mostly with the OH groups of C[4]RA molecules. As a result the main structure unit e.g. a dimer of C[4]RA molecules is broken by the incorporation of solvent molecules (see the schematic in figure 4.9a). After evaporation of ethanol molecules at elevated temperatures the dimer structure is restored (see figure 4.9b) and the films become much softer due to the formation of hydrogen bonding between C[4]RA molecules.

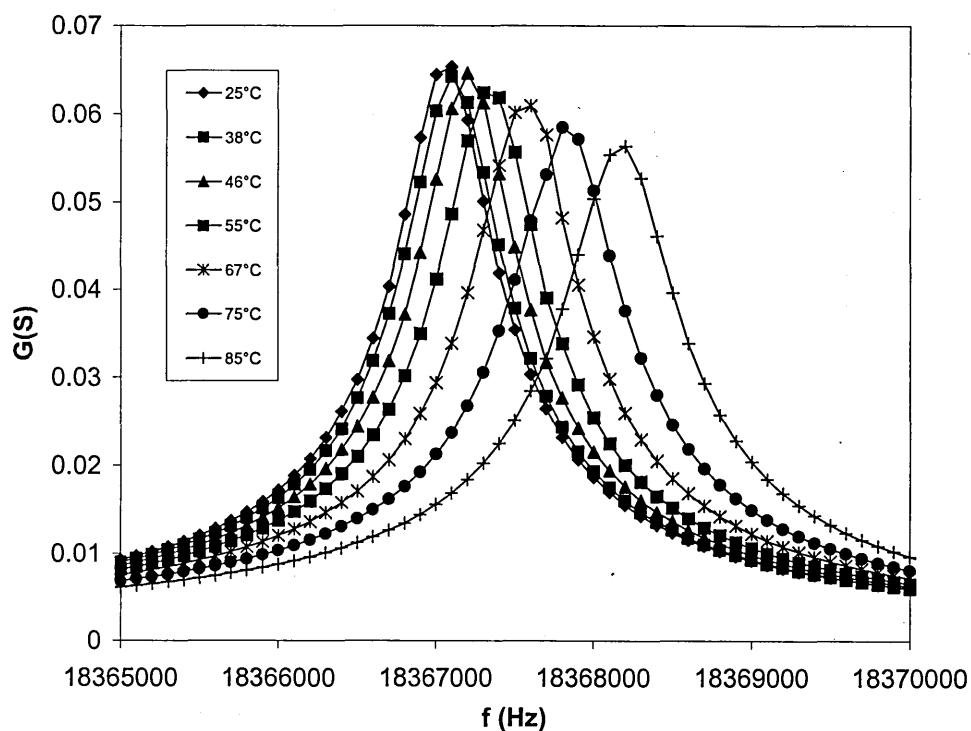


Figure 4.7. Measured Admittance spectra of a C[4]RA coated QCM at temperature ranging from 25°C to 85°C.

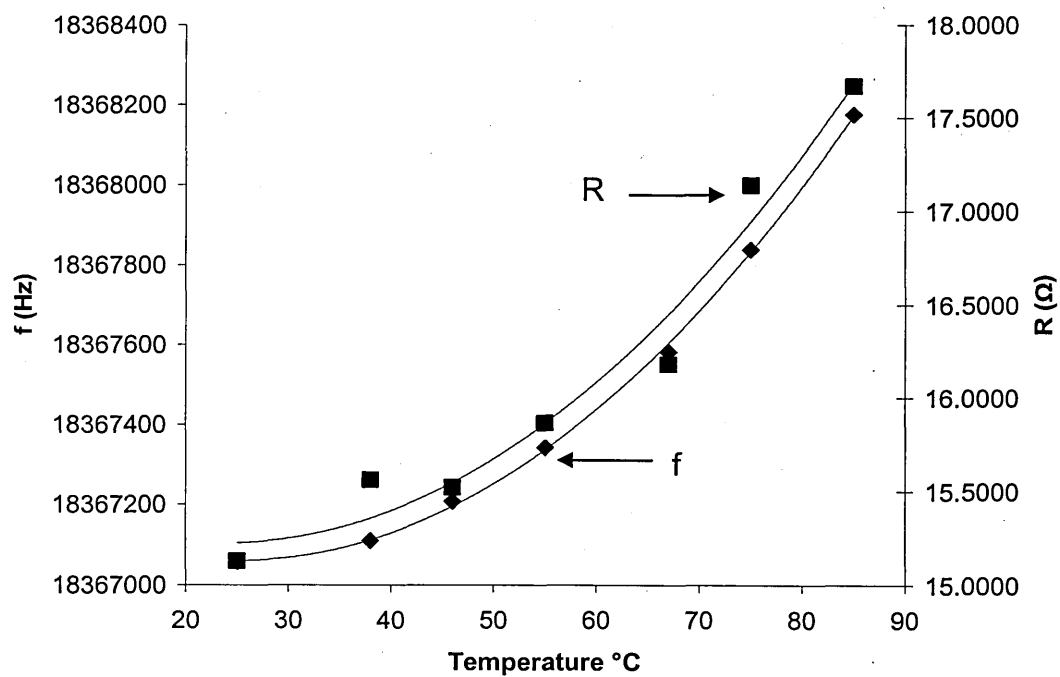


Figure 4.8. Extracted values f (Hz) and R (Ω) of a C[4]RA coated QCM at temperature ranging from 25°C to 85°C.

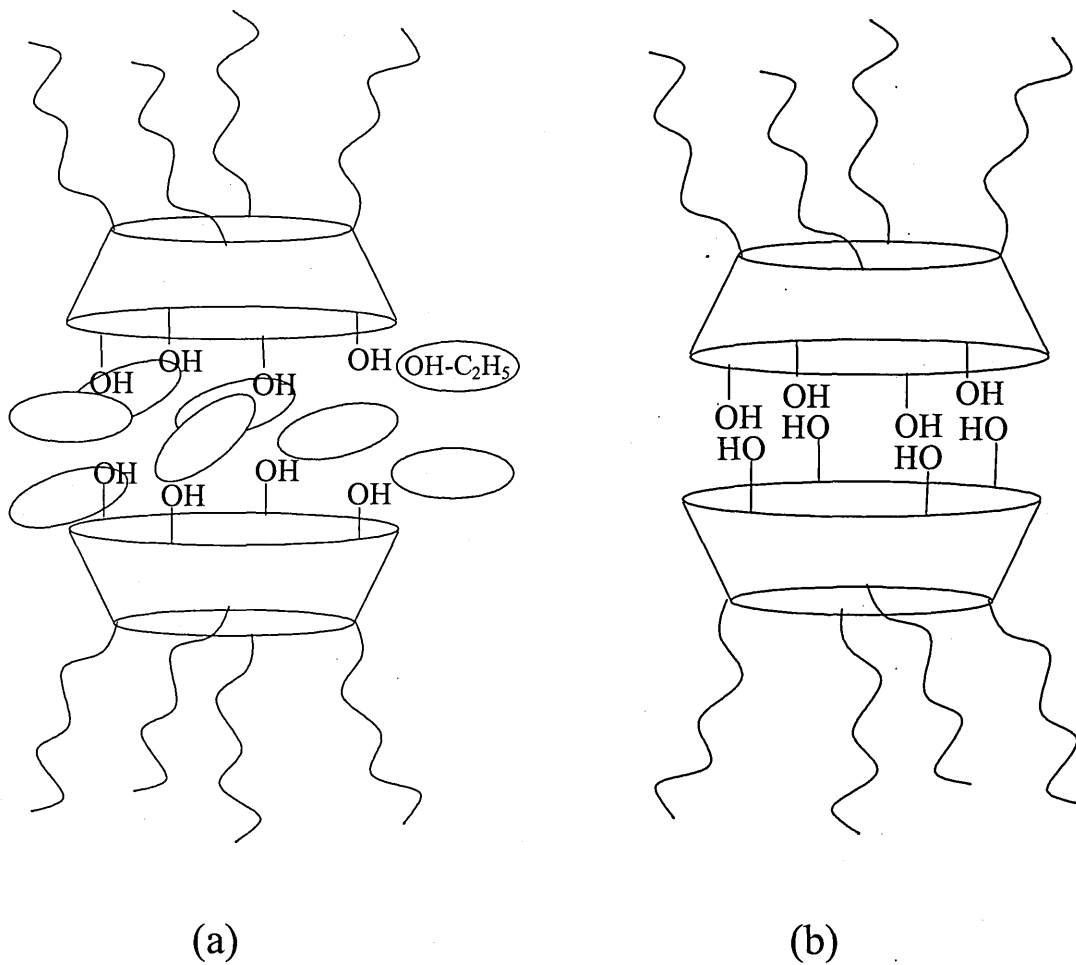


Figure 4.9. Schematic of the C[4]RA dimer structure a) Before and b) after the evaporation of ethanol molecules, caused by elevated temperatures.

4.3 Crystal properties and selection

Before the application of a sorbent coating all the crystals were measured using the impedance analysis technique. Each spectrum was fitted to the BVD equivalent circuit and the values of R, L, C and C_p were obtained. Figure 4.10 clearly shows the variation between admittance spectra of 18 uncoated crystals. The variation although large is within the stated manufactures tolerance. To compensate for this most of the results in this thesis are therefore given as difference values i.e. Δf or ΔR . This allows more genuine comparison between crystals. From the above test of 18 crystals, the maximum difference in frequency and resistance are 73000Hz and 27.11 Ω respectively. To compensate for the large variation, crystals were also grouped into batches of three, four or five with similar initial resonant frequencies. Table 5.3 shows a summary of the results obtained from this test.

	f (Hz)	R(Ω)
Mean	18453000.00	16.99
Max	18494000.00	27.11
Min	18421000.00	8.30
Std Deviation	23874.67	6.29
Max - Min	73000.00	18.81

Table 4.3. Summary of the results from the measurement and fitting of the 18 uncoated QCM spectra.

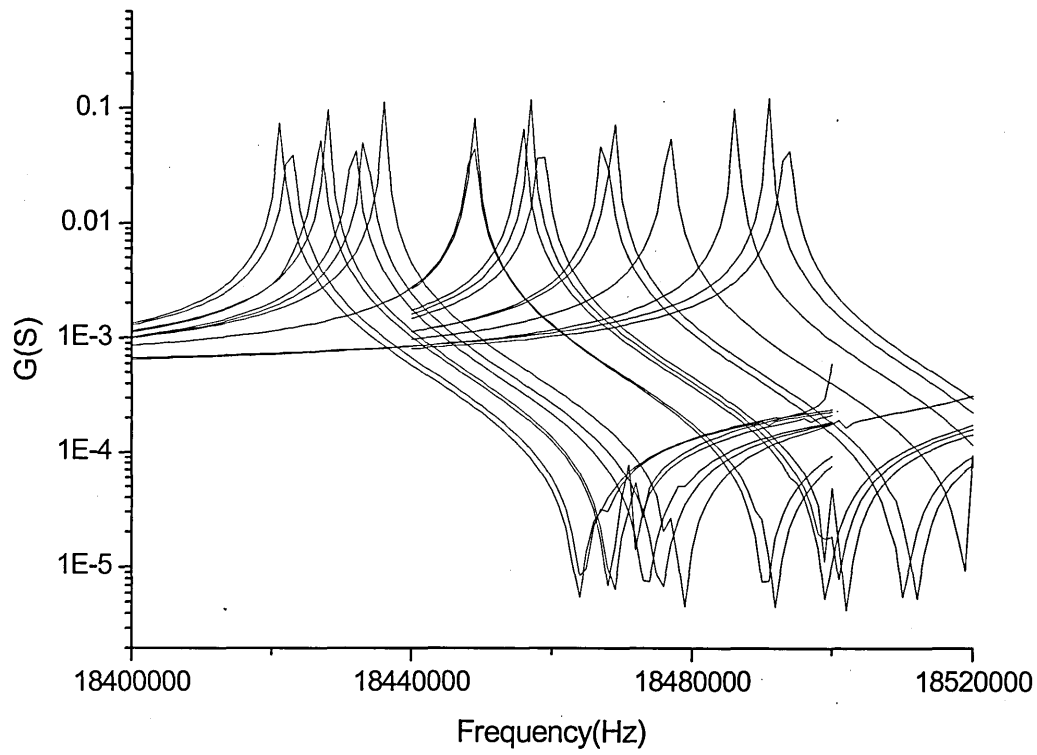


Figure 4.10. Admittance magnitude of 18 uncoated QCM.

4.4 Crystal Coating

To produce a suitably thick film a combination of the spin and LB coating processes described in Chapter 3 was used. Firstly a relatively thin film was applied using spin coating to provide a thin homogenous layer; secondly the LB technique was used to obtain a coating of suitable thickness. Figure 4.11 shows the resonant frequencies of four crystals coated in an identical process, the results are also summarised in table 4.4. The spin coating and LB techniques produce approximately the same frequency shifts of about 25 kHz between each stage.

The spin coating process produces relatively consistent results in terms of a frequency shift. Typically results as shown in this case show the frequency shift for each crystal fall within $\pm 5\%$ of the mean frequency shift. The LB process gave slightly higher deviation of frequency of approximately $\pm 10\%$ of the mean frequency. This may be caused by the inconsistent and non ideal transfer ratio of films produced by LB deposition. The deposited film thickness can be estimated from the mass load calculated from the Sauerbrey equation and equation (4.1) [4]. Assuming a density of 0.63 g/cm^3 taken from literature [5] a film thickness of approximately 400nm is obtained. The change in the resistance parameter is however not as consistent, with ΔR ranging from $2.73 - 4.67\Omega$ after LB deposition as shown in figure 4.12.

$$h_f = \frac{\Delta m}{\rho_f} \quad (4.1)$$

where ρ_f is the density of the film material in g/cm^3 , and Δm is the change in mass per unit area g/cm^2 calculated from equation 2.5.

After preliminary tests it was found that the spin coating procedure could be optimised to produce films of a comparable thickness to the LB technique. This was achieved by increasing the concentration of the dissolved calixarene and lowering the spin speed. Typical frequency shifts using the higher concentration spin coating solution are 35-45 kHz.

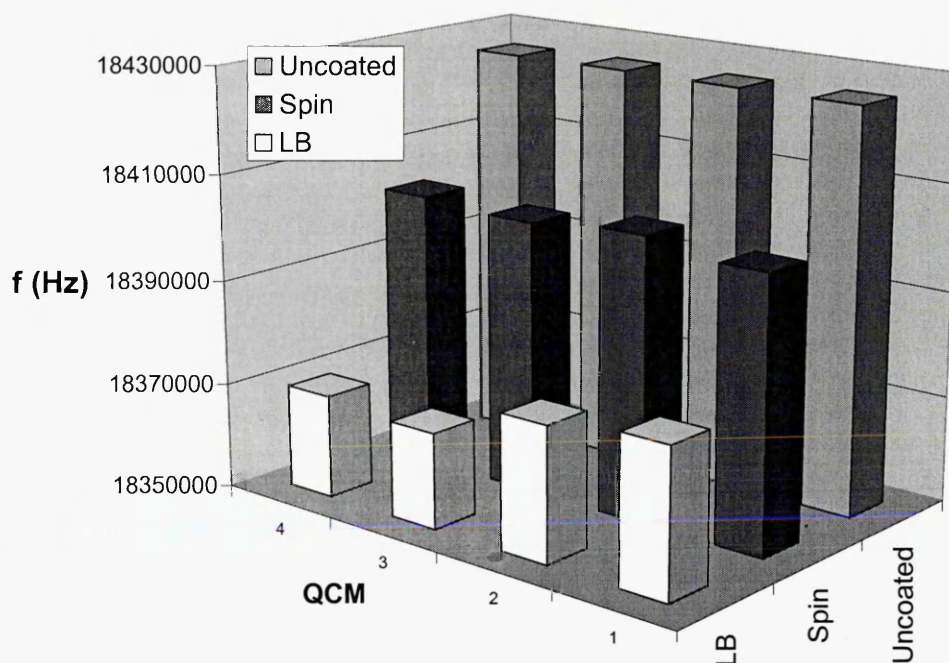


Figure 4.11. Resonant frequencies of four QCM coated with an identical C[4]RA compound.

		f (Hz)			
QCM	Uncoated	spin	LB	Δf (spin)	Δf (LB)
1	18425921	18401367	18377677.5	24554	48243.5
2	18425842	18403524	18375282.5	22318	50559.5
3	18425948	18401612	18367970	24336	57978
4	18425851	18402492.5	18369427.5	23358.5	56423.5
		R(Ω)			
QCM	Uncoated	spin	LB	ΔR (spin)	ΔR (LB)
1	16.13	18.79	20.8	2.66	4.67
2	12.41	16.23	16.39	3.82	3.98
3	9.18	9.44	12.87	0.26	3.69
4	10.43	11.23	13.16	0.8	2.73

Table 4.4. Resonant frequencies and resistances of four QCM coated with an identical C[4]RA compound .

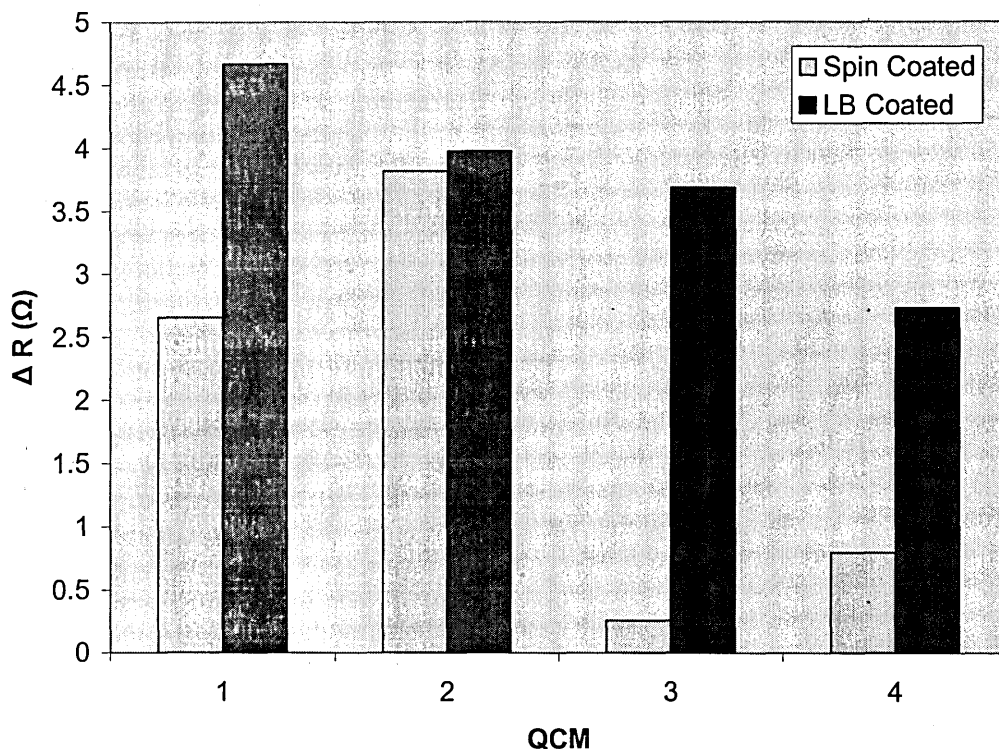


Figure 4.12. Change in resistance of four QCM coated with an identical C[4]RA compound.

The differences in resistance between the coated QCM (see figure 4.12) can be attributed to variation in several film parameters including surface roughness, homogeneity, film coverage and thickness.

Using the approximations proposed by Lucklum (equations (2.49a) and (2.49b)) the effect of the applied viscoelastic film on both the parameters f and R can be calculated. The deviation from a pure mass load has also been calculated and showed as an apparent 'extra mass' (see figure 4.13). The frequency difference between a rigid and viscoelastic film being approximately 250Hz for a thickness of 350nm equates to a perceived additional mass of 327 ng. This value is however relatively small (less than 1% of the total calculated mass). The deviation in the frequency shift between rigid and viscoelastic films is however a function of the film thickness, and it becomes significant

for thicker films as shown in figure 4.15. A film of 1000nm would produce an additional frequency shift of 5150Hz in comparison to a purely rigid film. Using a film density of 650 kg/m³ [6], shear modulus of $G' = 0.5 \times 10^8$ Pa and $G'' = 2 \times 10^6$ Pa and a resonant frequency of 18.4MHz. The shear moduli of the film were estimated using the fast three step method proposed by Lucklum et al [7]. Step 1: The acoustic load Z_L was calculated from the measured electrical admittance at the series resonant frequency using a rearrangement of equation (2.25), and is given in equation (4.2).

$$Z_L = jZ_{cq} \frac{(Y - j\omega C_p) \frac{\alpha}{K^2} - 2Y \tan \frac{\alpha}{2}}{Y - (Y - j\omega C_p) \frac{\alpha}{K^2} \cot \alpha} \quad (4.2)$$

Step 2: A series of approximations are used for the tan function in equation (4.3), these cover a range of acoustic phase shift φ between 0 and π (see appendix [F]). In this step a set of shear moduli were calculated, although not all values of G' and G'' can be simultaneously valid. The calculated shear moduli are then substituted back into equation (4.3) and the acoustic load Z_L recalculated. The calculated values of Z_L are compared with the measured value of Z_L and the best approximation of shear moduli was obtained. A MATLAB 6.0 program was written to perform the above calculations and can be found in appendix [E]. It must be noted this only gives very approximate values of film modulus and further iterative fitting is required to find precise values of shear modulus.

$$Z_L = j(\rho_f G_f)^{1/2} \tan \left(\omega \left(\frac{\rho_f}{G_f} \right)^{1/2} h_f \right) \quad (4.3) \text{ rpt of equation (2.44)}$$

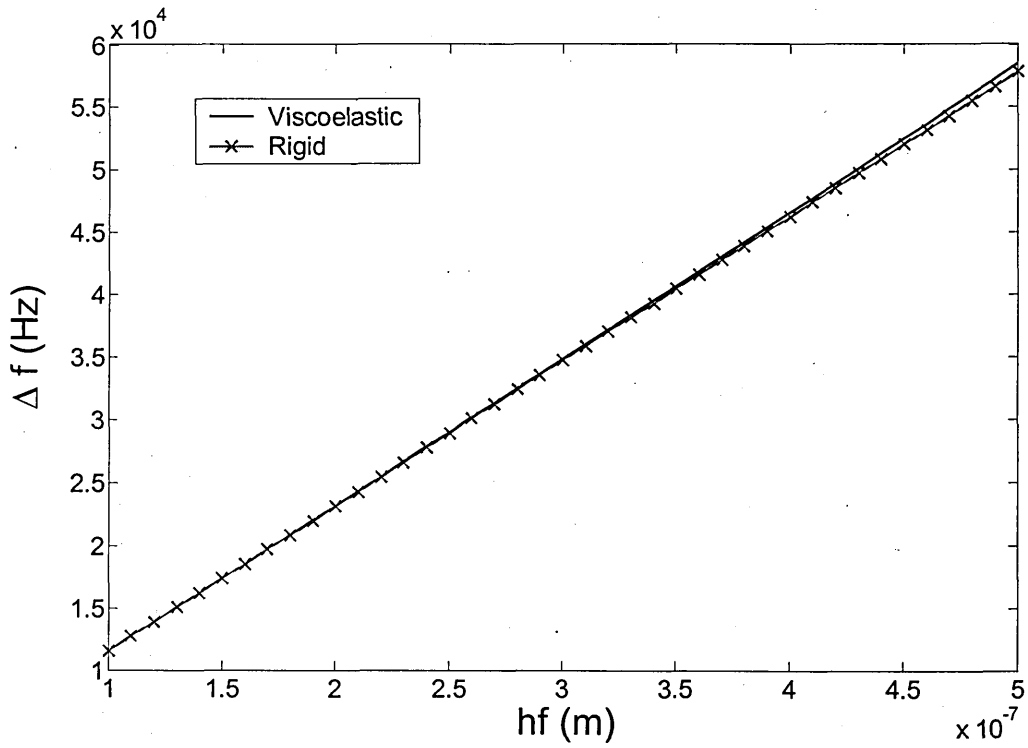


Figure 4.13 Δf for a rigid and viscoelastic film for increasing film thickness calculated using equation (2.49a).

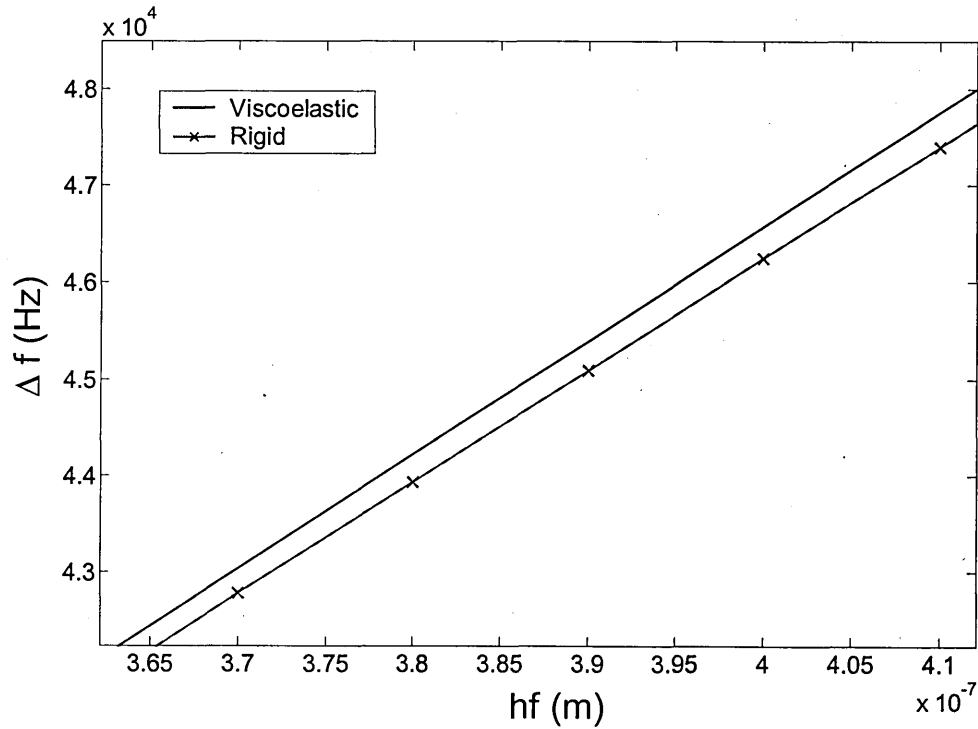


Figure 4.14. Magnified view of figure 4.13 shows Δf at values of thickness around anticipated film thickness of the films used.

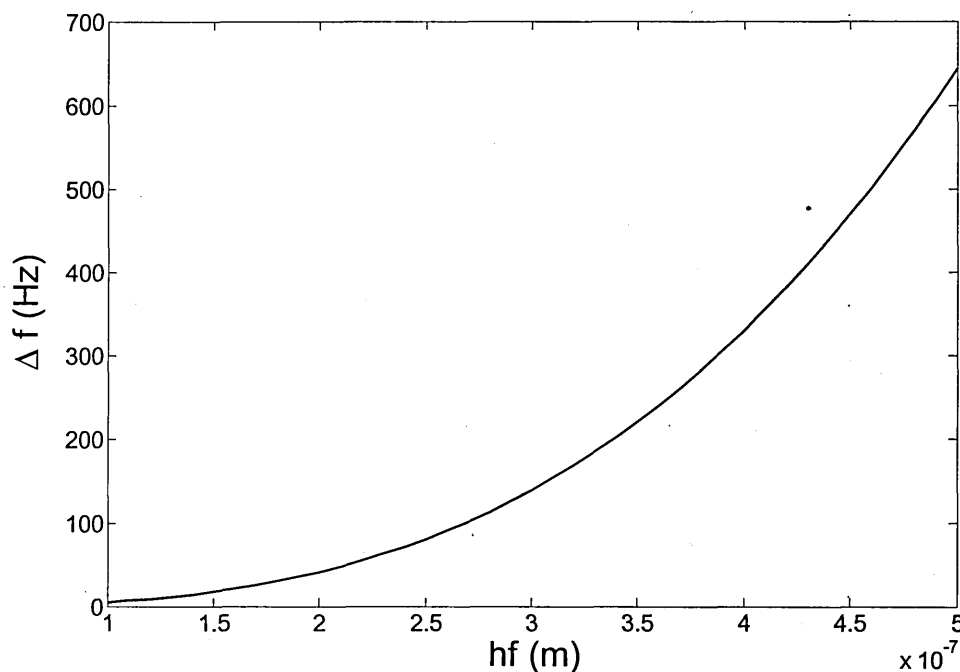


Figure 4.15. Calculated difference in frequency shift between a rigid and viscoelastic film.

The calculated resistance increase caused by the viscoelastic film is shown in figure 4.16. Again the calculated results are in acceptable agreement with the experimental data in Table 4.4. With a film thickness of 350nm a resistance change of approximately 6Ω . The resistance increase therefore indicates the film must be viscoelastic in nature, a purely rigid film would show no increase in resistance ($\Delta R=0$). Similarly to the frequency ΔR is proportional to the film thickness and quickly starts to rise as the film thickness increases; a 1000nm film giving a ΔR of above 50Ω as shown in figure 4.16 (inset). The increase in resistance is a resultant of the loss modulus G'' which is introduced with a viscoelastic film.

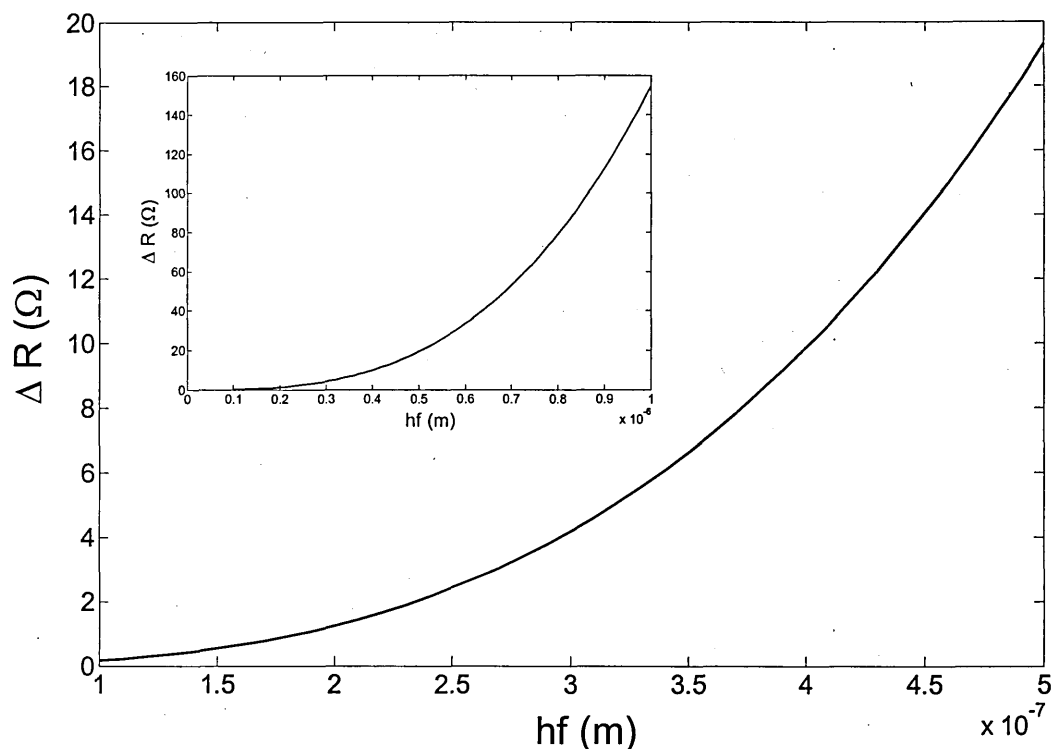


Figure 4.16. Change in resistance of viscoelastic film for increasing film thickness.

Inset shows increased film thickness to 1 μm .

4.5 Film properties/structure

The properties of the coating film such as uniformity, roughness and homogeneity also play an important part in the behaviour of a QCM. Although in depth investigation of such effects is out of the scope of this thesis, both AFM and ellipsometry have been used to determine the film thickness and give fundamental information on the morphology, surface roughness and homogeneity of C[4]RA films used.

4.5.1 Atomic Force Microscopy measurements

The samples were prepared on silicon wafers with the C[4]RA coatings listed in table 4.5. AFM tapping mode was used due to the soft composition of the organic samples. Figures 4.17 through 4.21 show selected images of the C[4]RA films. Most of the films

studied are similar in structure and surface roughness, with typical values of the maximum height variation in the range of 3-4nm. The calixarenes with the smallest of the hydrocarbon tails (CH₃) did however produced unexplained holes in the film (figure 4.20), and hence gave the largest standard deviation in the Z values.

C[4]RA	(RMS Rq) nm	(Ra) nm
C ₁₇ H ₃₅	0.563	0.448
C ₁₅ H ₃₁	0.37	0.29
C ₅ H ₁₁	0.554	0.407
C ₁ H ₃	0.891	0.403

Table 4.5. Surface roughness of C[4]RA films from the AFM study.

where the (RMS Rq) is the standard deviation of Z values and (Ra) is the Mean roughness calculated from the average of surface height deviations.

It is well known that a homogeneous structure of C[4]RA films is due to the interaction of hydrocarbon chains. Obviously the shortest CH₃ substitution groups do not provide such interaction and the films are less homogeneous as a result.

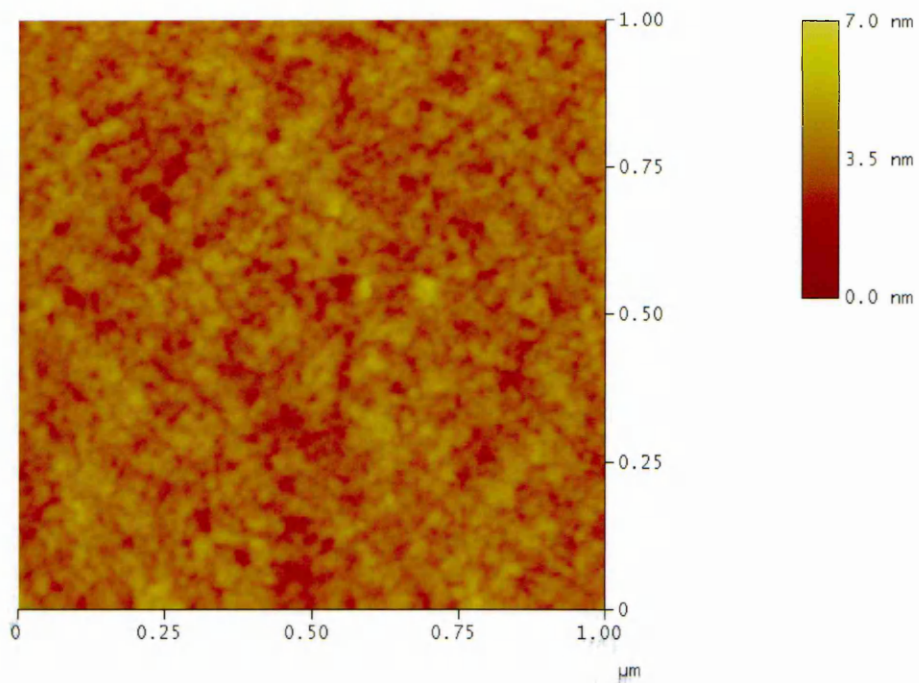


Figure 4.17. AFM image of C[4]RA C₁₇H₃₅ compound.

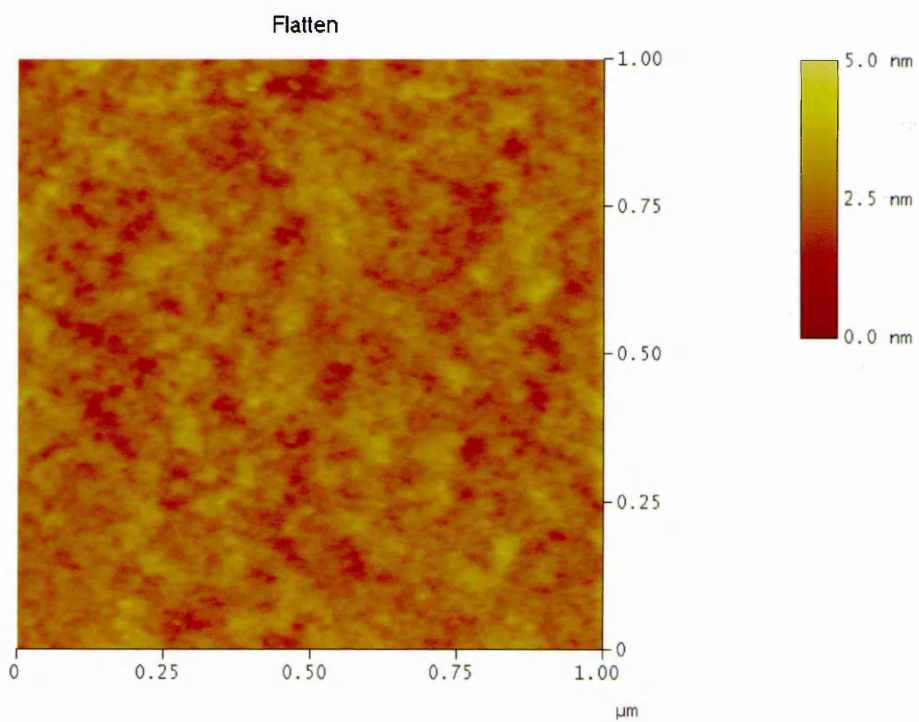


Figure 4.18. AFM image of C[4]RA C₁₅H₃₁ compound.



Figure 1: A 3D plot showing a rectangular prism with a grid on its top surface.

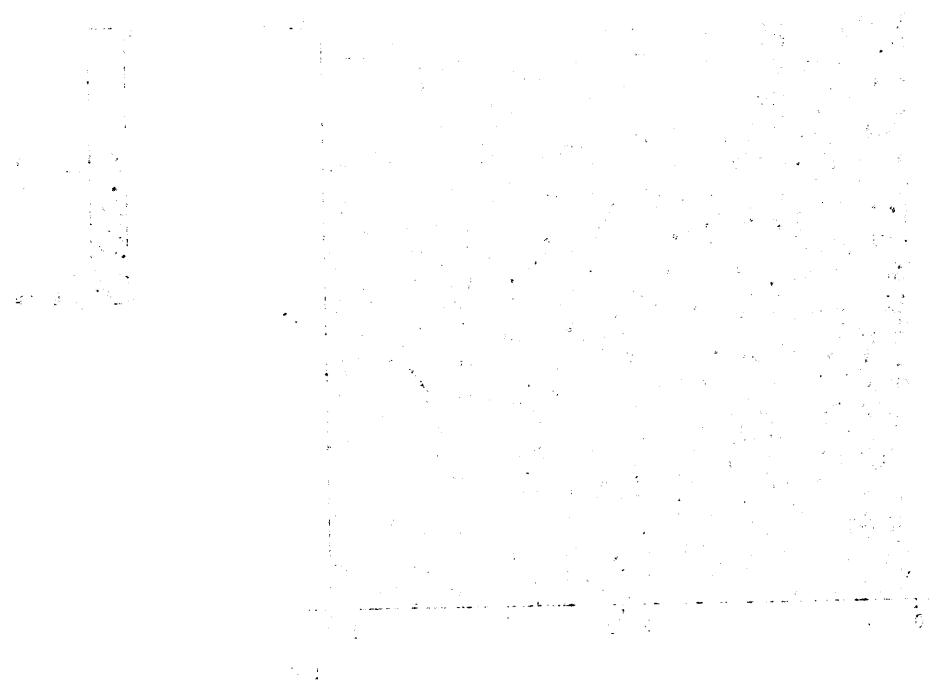


Figure 2: A 2D plot showing a rectangular prism with a grid on its top surface.

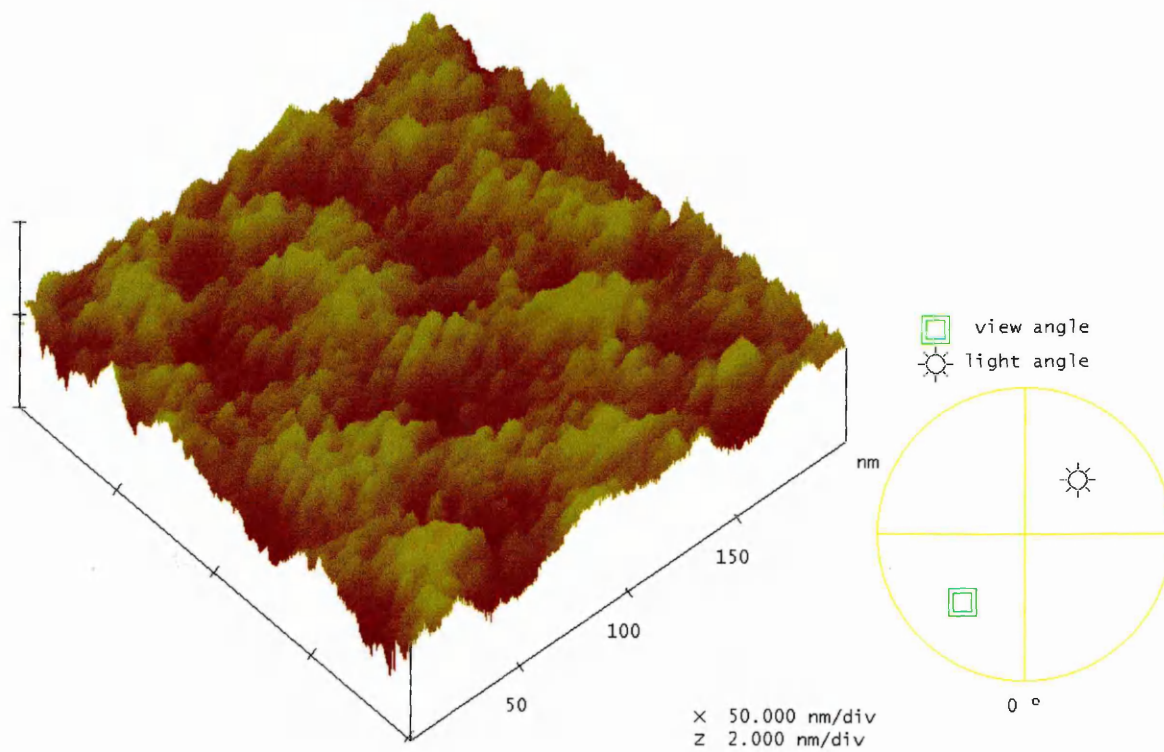


Figure 4.19. Pseudo 3D AFM image of C[4]RA C₁₅H₃₁ compound.

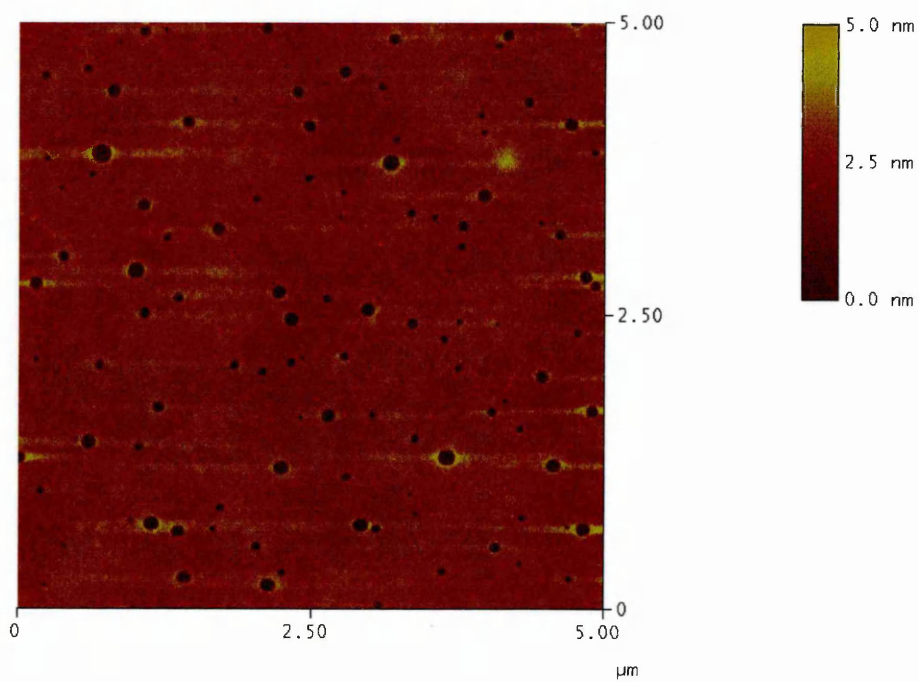


Figure 4.20. AFM image of C[4]RA C₁H₃ compound.

A crude but efficient AFM check of film thickness is carried out by simply scratching the surface of the sample with a fine tip. This leaves a groove on the surface of the film. The groove is clearly visible on the AFM image in figure 4.21 and shows large walls on either side where the coating material has been pushed aside. The film thickness has been estimated from the profile shown in figure 4.22 to be in the range of 300nm. This shows good correlation with results obtained from ellipsometry measurements.

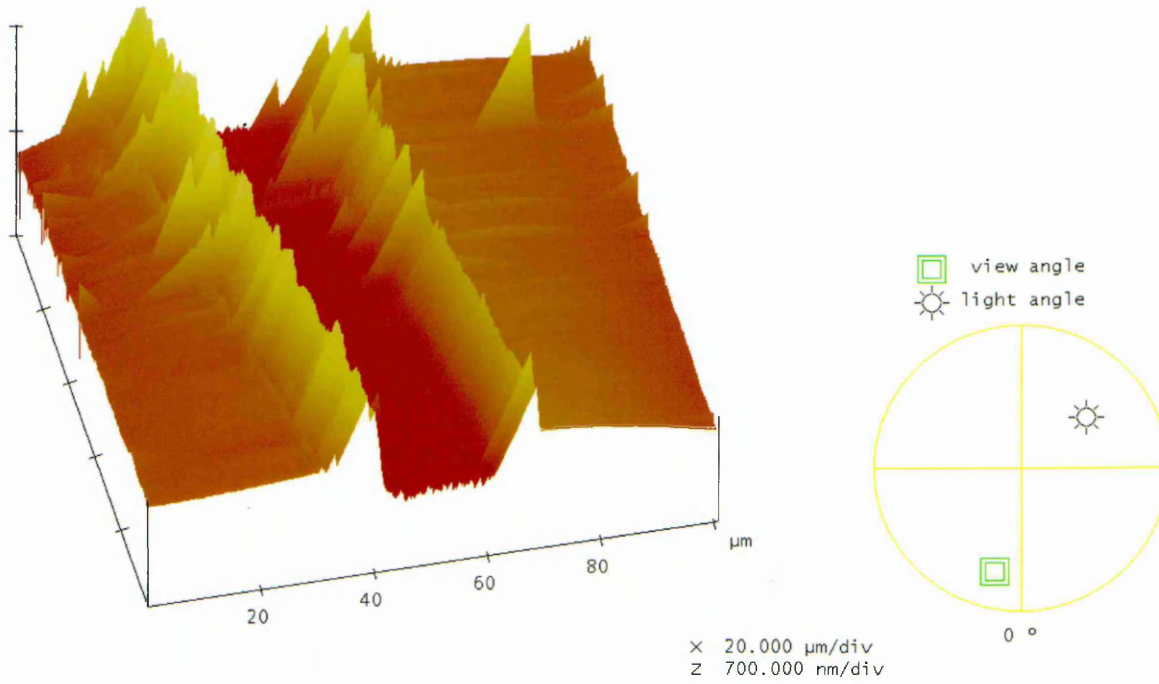


Figure 4.21. Pseudo 3D image of $\text{C}_{15}\text{H}_{35}$ compound with surface scratch.

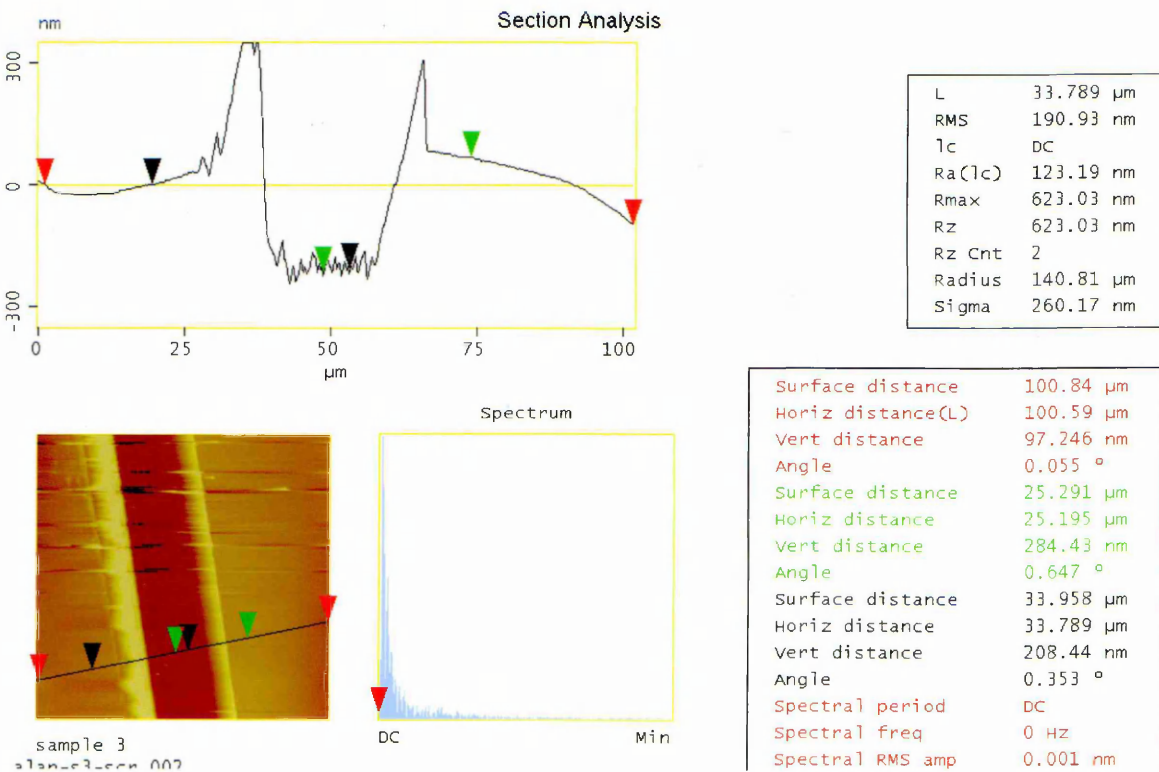


Figure 4.22. Screen capture of the AFM software showing the profile of the groove along the line drawn in the bottom left corner of the image.

4.5.2 Ellipsometry measurements

The same samples tested using AFM were also measured using ellipsometry to obtain values of film thickness. The experimental values of Ψ and Δ were first obtained for each of the C[4]RA films. A suitable optical model was then constructed which describes the sample structure as shown in figure 4.23. The C[4]RA film are represented by a cauchy layer. The dispersion of refractive index is given by equation (4.1). Theoretical data were then generated from the optical model. A least squares fit was then performed minimizing the error between experimental and the generated data adjusting the relevant parameters (film thickness and or optical constants), until a ‘best fit’ is achieved. The final parameters are then obtained from the best fit parameters. The values for parameters A, B, and C in equation (4.4) are given in table 4.6. The extinction coefficient k was fixed at zero value since the films are transparent in the visible range. All data fitting was performed using the WVASE32[®] software from J.A. Woollam Co., Inc. The values of film thickness were found to be in the range 300-350nm, the two C[4]RA C₁₅ H₃₅ compounds giving thicknesses of approximately 320nm which is in reasonable agreement with values estimated from QCM and AFM techniques.

$$n(\lambda) = A + \frac{B}{\lambda^2} + \frac{C}{\lambda^4} \quad (4.4)$$

A	B	C
1.3113	0.012009	-0.000047928

Table 4.6. Parameters of the dispersion model.

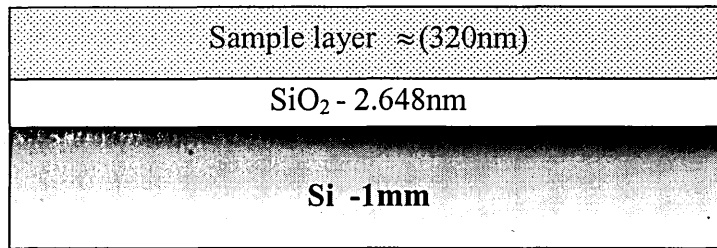


Figure 4.23. Optical model of the sample structure used in the ellipsometry fitting.

4.6 Conclusion

The QCM experimental techniques detailed in chapter 3 have been tested and verified. Limits of detection and repeatability for the three measurement techniques (Oscillator circuit, QCMD and impedance analysis) have been established. The additional polynomial fit used to interpolate additional data points has been shown to successfully increase the accuracy of the impedance analysis technique.

A large variation between uncoated QCM must however be noted and all further experiments were therefore undertaken using batches of similarly specified crystals. The results from the crystal coating process also show some variability. The LB technique gave the most consistent results, however spin coating was preferred based on the significantly decreased time scale required to deposit the sensing membranes. The effect of the deposited films has been estimated using the equations proposed by Lucklem et al, and approximations for the shear parameters of the film have been obtained using the fast three step method [6,7]. The calculated deviation from the Sauerbrey model caused by the viscoelastic film is relatively small, resulting in an additional frequency shift of 250Hz.

The deposited films have been probed using the AFM technique and found to be relatively flat and consistent. The coating thickness has also been obtained and estimated in the range of 300nm. This is in good agreement with the results from ellipsometry measurements and the calculated thickness based on the Sauerbrey equation.

REFERENCES

- [1] V. Bottom, "Introduction to Quartz Crystal Unit Design," Van Nostrand Reinhold, New York, 1982, pp. 82-83.
- [2] J.W. Gardner and P.N. Bartlett, "Electronic Noses Principles and Applications," pages 245, Oxford University Press, New York, 1999.
- [3] A. V. Nabok, N. V. Lavrik, Z. I. Kazantseva, B. A. Nesterenko, L. N. Markovskiy, V. I. Kalchenko, and A. N. Shivaniuk, "Complexing properties of calix[4]resorcinolarene LB films," *Thin Solid Films*, vol. 259, pp. 244-247, Apr. 1995.
- [4] Stanford research systems, "QCM100- Quartz Crystal Microbalance theory and calibration," 2003.
- [5] T. Wilkop, "Thin film calixresorcinarene membranes for chemical sensing," PhD Thesis, Sheffield Hallam University UK, 2001.
- [6] R. Lucklum and P. Hauptmann, "Transduction mechanism of acoustic-wave based chemical and biochemical sensors," *Measurement Science and Technology*, vol. 14, pp. 1854-1864, 2003.
- [7] R. Lucklum and P. Hauptmann, "Thin film shear modulus determination with quartz crystal resonators: A review," *IEEE International Frequency Control Symposium and PDA Exhibition*, pp. 480-417, Seattle, WA, USA, 2001.

Chapter 5

Results and discussion – Vapour exposure

5.0 Introduction

This chapter reports the results of from QCM measurements taken during vapour exposure. The three experimental techniques: (i) oscillator measurements, (ii) impedance analysis and (iii) QCMD have been used in conjunction with a series of calixarene based sensing membranes in order to detect and discriminate between a range of organic solvents. The sensor array technique has also been implemented with the use of artificial neural networks to perform the pattern recognition of solvent vapours and hence their classification. The measurements of multiple parameters (Δf and ΔR) from a single QCM, obtained with either impedance analysis or QCMD methods showed a novel approach method of solvent classification through unique changes in film parameters induced by the contacting solvents.

5.1 Vapour exposure – Frequency based measurements

The frequency based array measurements were performed using four QCM coated with different C[4]RA compounds and an uncoated reference QCM. Although several more variants of the C[4]RA compounds were available, only four compounds were chosen. Preliminary tests showed that the C[4]RA C₁₇H₃₅ compound produced results identical to the C₁₅H₃₁ compound. The C[4]RA compounds with small hydrocarbon chains (C₁H₃ and C₃H₅) proved to be unusable giving erratic oscillator frequency shifts during exposure, and were often highly unstable producing large amounts of baseline noise during measurements (see page 165 for details).

Figure 5.1 shows a typical kinetic frequency response of four QCM exposed to a hexane vapour. Two crystals were coated with identical C[4]RA C₁₅H₃₁ films and the other two with C[4]RA C₁₁H₂₃ and C[4]RA C₅H₁₁ films. As expected the response time is relatively fast in the order of a few seconds. The $|\Delta f|$ value for each concentration was estimated from the mean value of response at saturation (indicated in figure 5.1). The concentration ranges for the solvents were determined empirically by number of preliminary tests using each target vapour. The final concentration ranges were selected such that each solvent would produce values of $|\Delta f|$ spanning a similar frequency range. The obtained values for solvent vapour concentrations differ considerably when measured in absolute units of ppm, however when calculated as a function of their relative saturated vapour pressures (p/p_s), their correlation becomes apparent.

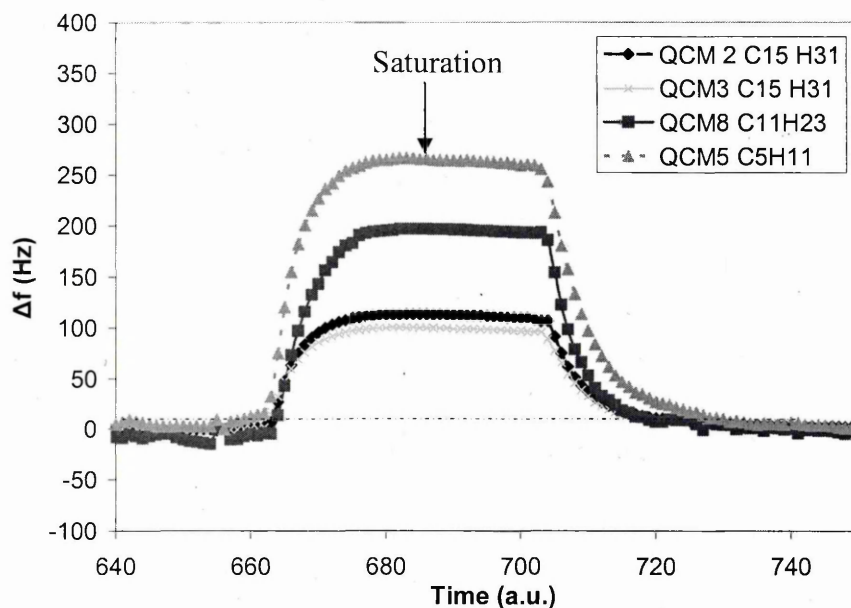


Figure 5.1. Kinetic frequency response of four QCM exposed to 8104ppm of hexane vapour.

The accuracy in the vapour concentration is principally related to the precision of the liquid solvent measured to be injected into the cell. To produce the required concentrations two syringes were used, 1 μl and 10 μl depending on the concentration required. Where high concentrations up to 15×10^3 ppm were necessary, as in the case of hexane, the 10 μl syringe would be used. In the case of toluene a maximum concentration of approximately 3.5×10^3 ppm is required, and hence a 1 μl syringe is suitable. The accuracies were estimated as 0.01 μl for the 1 μl syringe and 0.1 μl for the 10 μl syringe. The corresponding are experimental errors, 281ppm (0.00982p/ps) in absolute concentration for toluene and 2269ppm (0.013526 p/ps) for hexane using the 1 μl and 10 μl syringes respectively. It is assumed that the gas-cell is air-tight and no vapour leakage occurred during relatively short time (a few minutes) of vapour exposure.

Figure 5.2a shows the sensor response of a C[4]RA C_5H_{11} coated QCM to four organic solvent vapours. The order of sensitivity corresponds to the relative vapour pressure of

the analytes at a given temperature. Hexane having a saturated vapour pressure (SVP) of 17kPa, exhibiting the lowest sensitivity, while the highest sensitivity is observed for m-xylene with a SVP of 0.8kPa (see table 5.1).. The responses in the given concentration range appear to be linear, so the sensitivity levels can be estimated from the gradient values of the respective curves. Table 5.2 gives a summary of the sensitivity levels and limits of detection observed for the C[4]RA C₅H₁₁ membrane. The latter parameter was calculated from the concentration needed to produce a frequency shift of twice the baseline noise. The values of detection limit quoted are however substantially lower than levels at which vapour discrimination can be achieved. Table 5.3 gives the Lower Explosion Limit (LEL) and Upper Explosion Limit (UEL) in % for a range of organic solvents. Figure 5.2b shows the slope of the curves from figure 5.2a plotted against the boiling point of each respective vapour. This Confirms the relationship of sensitivity against the and boiling point which is directly related to the saturated vapour pressure of the vapour (higher vapour pressure = lower boiling point).

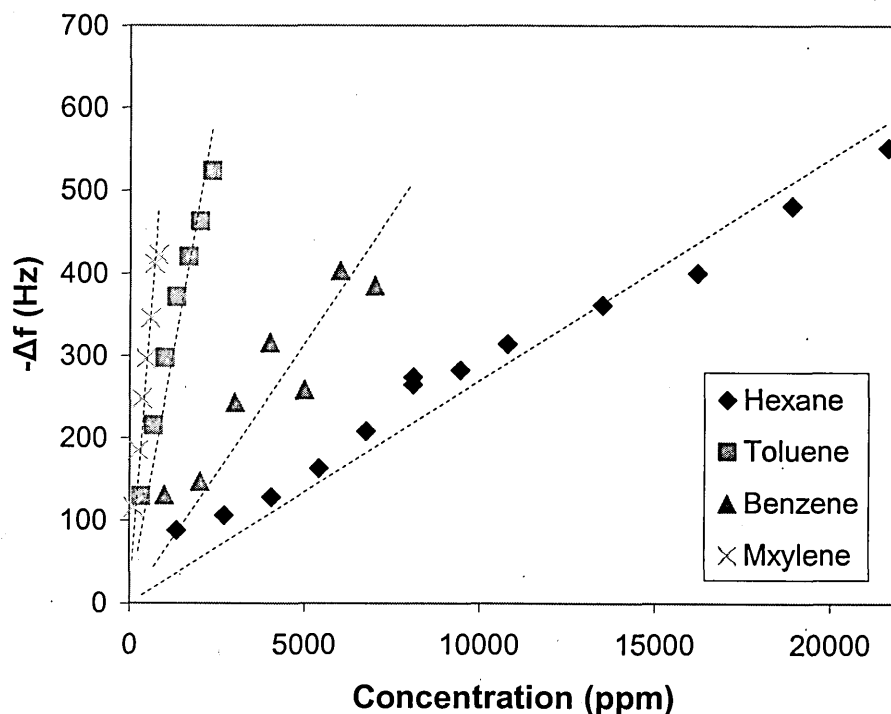


Figure 5.2a. Frequency shift (Hz) against concentration (ppm) for a C[4]RA C₅H₁₁ membrane exposed to a range of organic solvents.

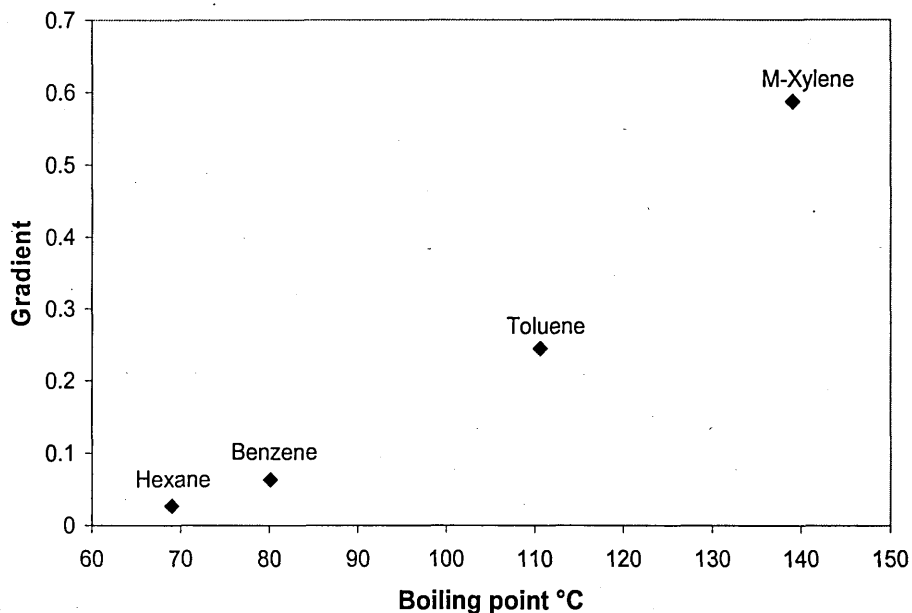


Figure 5.2b. Gradient of curves from figure 5.2a plotted against boiling point of the respective vapour.

Compound	Molecular weight	Vapour pressure (kPa)
Benzene	78.11	10
Hexane	86.2	17
Toluene	92.1	2.9
M xylene	106.2	0.8
Acetone	58.1	24
Cyclohexane	84.16	12.7

Table 5.1. Molecular weight and vapour pressures the target organic solvent.

Vapour	Sensitivity Hz/ppm	Sensitivity ppm/Hz	2×SD Baseline	Detection limit (ppm)
Hexane	0.0272	36.7647	0.5844	21.4864
Benzene	0.063	15.8730	0.5844	9.2767
Toluene	0.2448	4.0850	0.5844	2.3873
M Xylene	0.5871	1.7033	0.5844	0.9954

Table 5.2. Sensitivity levels and detection limits of C[4]RA C₅H₁₁ membrane calculated from linear fitting of the experimental data.

Compound	LEL-HEL
Hexane	1.2% – 7.7%
Benzene	1.3 % - 8 %
Toluene	1% - 7%
xylene	1.1 – 7%
cyclohexane	1.3% - 8.4%
m xylene	1.1 % - 7 %

Table 5.3. Lower and Higher explosion limits for a selected set of volatile organic solvents as a volume percentage of air.

Reproducibility between coated crystals is acceptable as shown in figure 5.3a. The graph shows two identically coated QCM (a&b) exposed to hexane and toluene vapours within the same chamber. In terms of absolute frequency shifts, the two QCM produce distinguishably different responses, the relative frequency changes are however almost identical for both vapours. This is demonstrated by plotting the data normalised between 0 and 1 with respect to the largest shift frequency produced by each QCM and is shown in figure 5.3b. The normalised frequency shifts for each coating when exposed to hexane to toluene vapours are nearly undistinguishable.

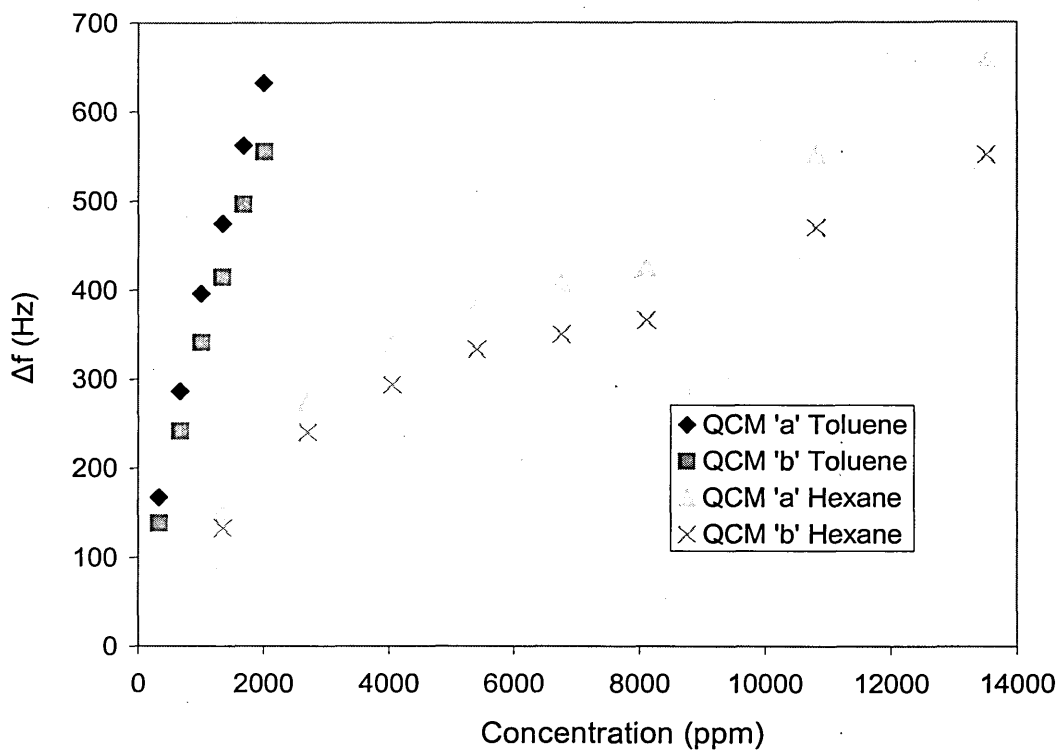


Figure 5.3a. Frequency response of two identically coated QCM exposed to several concentrations of hexane and toluene vapours.

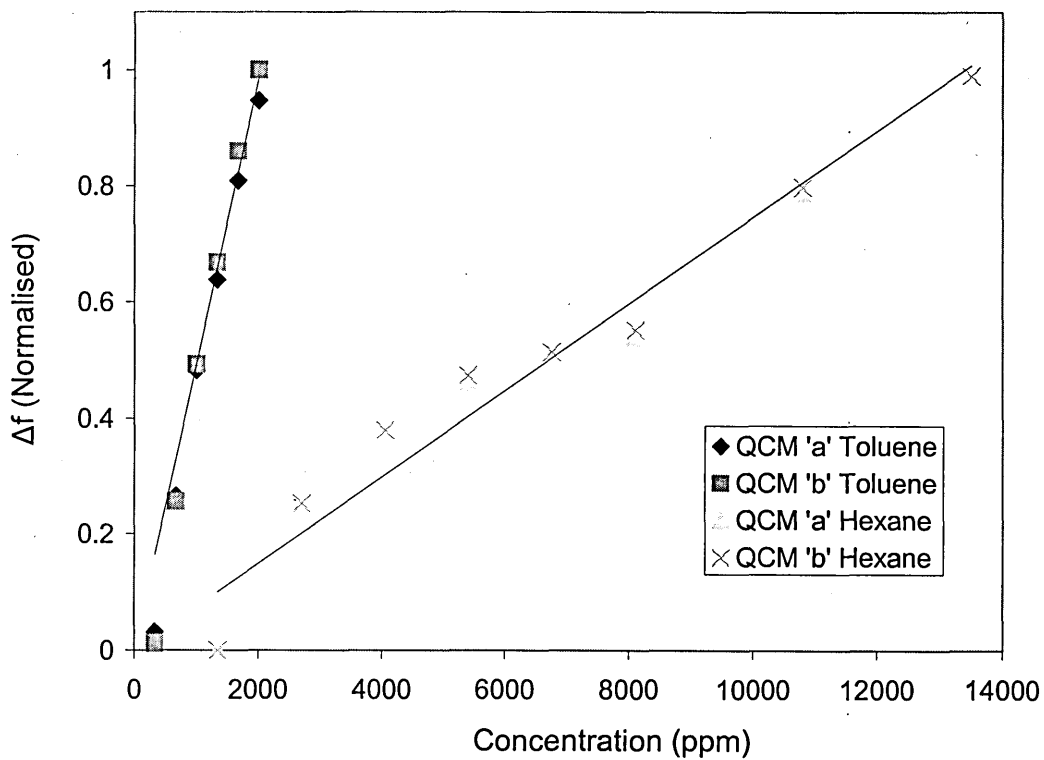


Figure 5.3b. Normalised Frequency response of two identically coated QCM (a&b) exposed to several concentrations of hexane and toluene vapours.

The response patterns for all C[4]RA compounds tested are show the same order of sensitivity based on the levels of SVP for the respective solvent vapours as described previously. It must be however noted that the frequency shifts are discernibly different for each compound, making the C[4]RA coatings tested suitable for an array based sensor approach. Figure 5.4 shows a three dimensional plot of absolute frequency shifts of three QCM exposed to several concentrations of hexane and m-xylene vapours (only two vapours are shown for clarity). The pseudo 3D plot response pattern of the sensors shows clear separation between the two solvents. With such a limited amount of data (2 vapours 3 sensors), analysis is relatively straightforward; however increasing the array size and the number of test vapours quickly makes such simple analysis impossible and thus requires additional more sophisticated techniques.

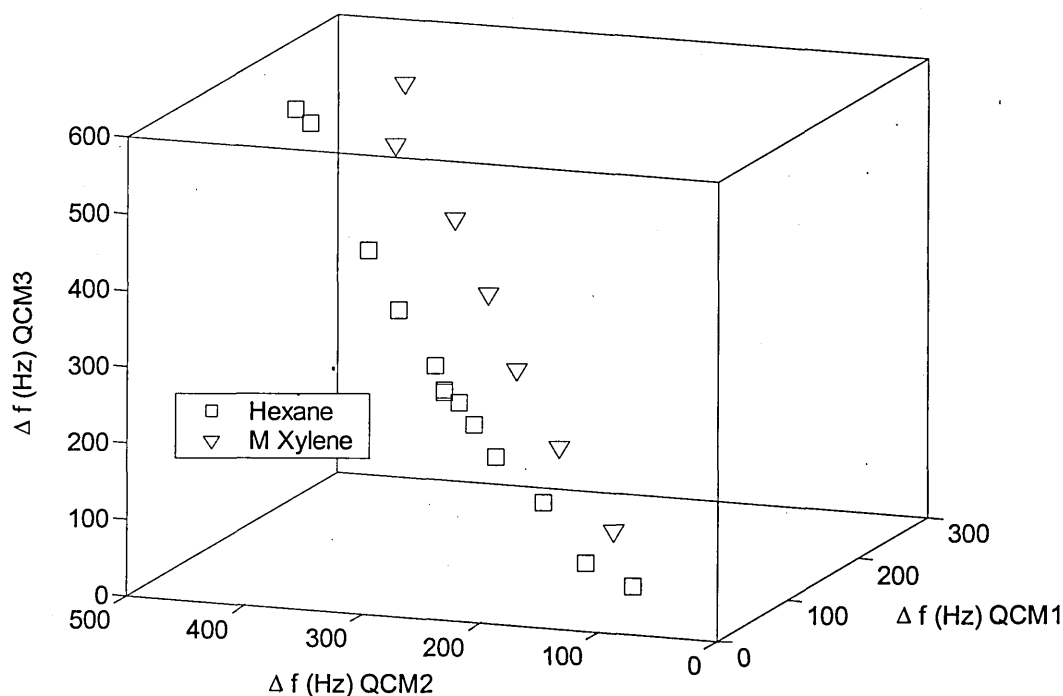


Figure 5.4. Sensor responses of three QCM from within an array to a sequence of increasing concentrations of hexane and m-xylene vapours.

5.2 Analysis of the QCM array using Artificial Neural Network (ANN)

With the experimental data clearly showing distinct sensor patterns (see figure 5.4) additional analysis in order to classify and quantify the analytes is possible. Several techniques are available such as Principle Component Analysis (PCA), Partial Least Squares (PLS), fuzzy logic and Artificial Neural Networks to name a few.

The ANN has been used extensively for the classification of data produced from electronic noses [1-13]. Applications vary widely ranging from the identification of paper quality [5], tea quality prediction [2], through to the detection of hazardous organic vapours [4] as in this case. The following section gives an overview of the ANN, the description and format of the equations are taken from Gardner et al [14]. The ANN consists of an interconnected group of processing elements called neurons. The neurons are connected to each other in a specific way known as the network architecture, with the strength of the interconnections known as the synaptic weights. The input at each neuron (a) is the sum of the input values (x_i) multiplied by its associated weight (w_i).

$$a_h^1 = \sum_{i=1}^n (w_{hi}^{(1)} x_i - w_{h0}^{(1)}) \quad (5.1)$$

where, h signifies a hidden layer, 1 refers the first of the hidden layers, w_{h0} is the neuron bias. This value is then transferred to an activation function (F) (usually non linear) which produces the final neuron output (z).

$$z_h = a_h^1 F \quad (5.2)$$

The most commonly used ANN for analysis of electronic nose data is the Multilayer Perceptron (MLP). The MLP consists of three layers: input, hidden layer and output.

The input layer represents the input from each of the (n) sensor inputs. A fully connected MLP neural network is shown schematically in figure 5.5.

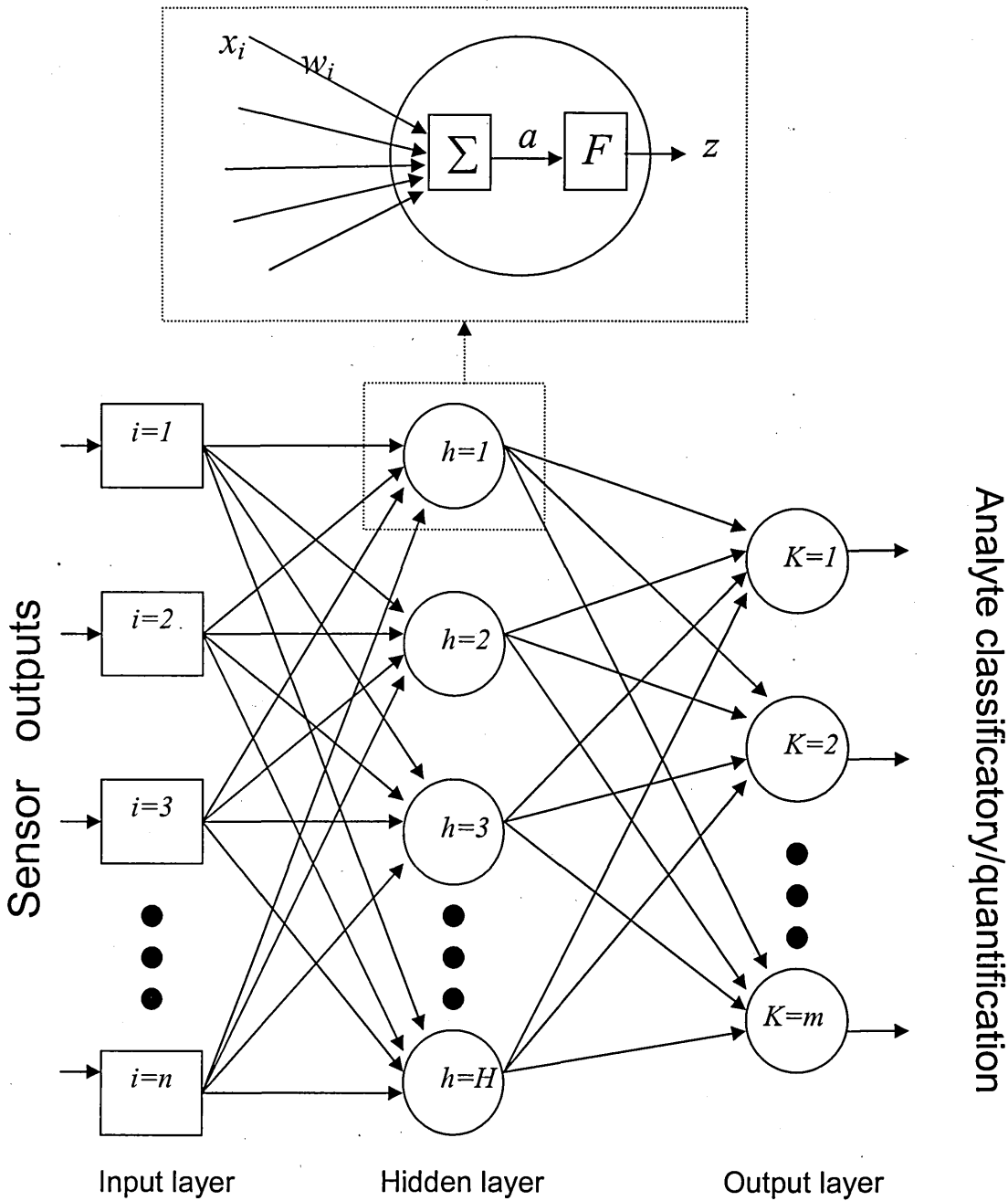


Figure 5.5. A typical multilayer perceptron arrangement consisting of three layers. i is the input layer, h the hidden layer and k the output layer.

The activation functions used in this work was the tan sigmoid and log sigmoid. The final neuron output for the log sigmoid function is given by equation (5.3).

$$z_h = \left(\frac{1}{1 + \exp^{-a_h}} \right) \quad (5.3)$$

The same calculation is performed by each neuron in the hidden layer, the output value is then fed forward into the next layer of the network. The value into neuron k in the output layer is given by equation (5.4), where H is the total number of neurons in the hidden layer.

$$a_k = \sum_{h=1}^H (w_{kh}^{(1)} z_h - w_{k0}^{(1)}) \quad (5.4)$$

The final output vector o_k and is defined as:

$$o_k = (f(a_1), f(a_2), \dots, f(a_m)) \quad (5.4)$$

where m is the final neuron in the output layer.

The network is trained by comparing the values of the output neurones o_k with the target outputs (t_j) for the analyte data set (the difference vector). The difference vector value is then used to modify the weights which are then fed back into into the network (often referred to as backpropagation). The training process iteratively adjusts the weights of the network to minimize the error between the network outputs and the target values until convergence on a solution, usually a specified minimum error is achieved.

There are many variations of the backpropagation algorithm. The simplest implementation of backpropagation learning updates the network weights and biases in the direction in which the performance function decreases most [15].

The performance of the neural network is measured through the the total sum of the square errors εTSS given by equation (5.5).

$$\varepsilon TSS = \Sigma \left[\sum_{k=1}^n (\delta_{jk}^2) \right] \quad (5.5)$$

where δ is the difference vector calculated from equation (5.6).

$$\delta_{jk} = (t_j - o_k)(1 - o_k) \quad (5.6)$$

For this application the Neural Network was implemented using MATLAB software (version 6.0, Mathworks, Natick, MA) and using the supplied functions and algorithms within the MATLAB Neural networking Toolobox (version 4.0, Mathworks, Natick, MA).

The network architecture chosen consisted of 4 inputs (one per sensor), a single hidden layer of 8 neurons and output layer of three neurons giving 96 weights to for the network to learn. The number of neurons in the hidden layer was optimized through an empirical process in order to find the minimum number of neurons which are still able to achieve the desired network performance. Prior to the training process the sensor data were divided into training and validation data sets. Due to the limited amount of data available, extra data points were interpolated using the lines of best fit from the sensor response graphs (see figure 5.2). In total 120 vectors were used to train the network. The Levenberg Marquadt back propagation algorithm was chosen for the network training because of its stated superior speed at achieving convergence [15]. The training was performed over 20000 epochs (iterations) or until the desired error performance goal of 1×10^{-10} was achieved. Figure 5.5 shows a plot of network performance against the number of epochs for a typical training run. The target values for the output neurons are binary combinations representing each of the target analytes.

The NN was trained by experimental and interpolated data results from the four measured QCM and five target vapours (hexane, toluene, benzene, cyclohexane and m-xylene).

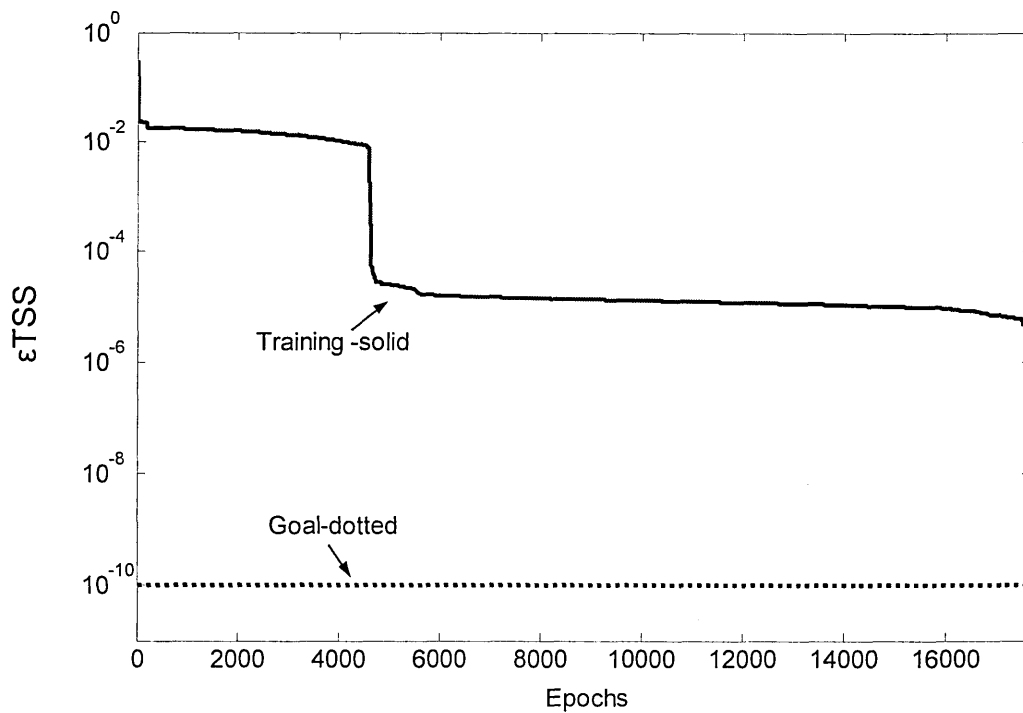


Figure 5.5. Total sum of the squared error output ϵTTS during network training. After 17642 epochs the desired network performance has been achieved and training is stopped.

To evaluate the network performance the validation data set were entered into the network and the values at the output neurons measured. Once again due to the limited amounts of data additional interpolated data points were used. These were obtained from the lines of best fit of the original data (see figure 5.2) with added random noise (ranging from \pm the maximum measured baseline noise). A program was written in MATLAB to read the data file of test input vectors, simulate the network response, and record the neuron output values.

At concentrations over 1000ppm over 98% of the test data was classified correctly. It is also evident from figure 5.4 that the separation between the vapours is proportional to solvent concentration. This was confirmed with the ANN results where higher

concentrations gave rise to increased performance to almost 100% certainty in vapour classification. Although in this case the QCM sensing and ANN analysis were performed independently, the incorporation of both functions into a single software/hardware package is easily achieved. The resultant sensor would allow real time detection and discrimination to a range of VOC's.

5.3 Results QCM Impedance measurement

The C[4]RA $C_{15}H_{31}$ compound was initially selected for the impedance measurements because of a large cavity formed by the long hydrocarbon chains. This was considered to be optimal for organic vapour detection and may induce specific host guest interactions within the membrane. Figure 5.6 shows a typical response of QCM coated with C[4]RA film exposed to several concentrations of toluene vapours in the range of $0 - 2 \times 10^4$ ppm. Both the decrease in resonant frequency and damping of the admittance peak are taking place on course of vapour adsorption. The second effect is believed to be caused by capillary condensation of hexane vapours in the C[4]RA film bulk [16]. A purely rigid film results in only a shift of the admittance curve to a lower frequency, with no changes in the peak amplitude and shape. The change in admittance the magnitude is related directly to the resistance (R_1) of the equivalent circuit model, and can be easily evaluated by fitting the experimental admittance spectra to the BVD equivalent circuit, as described in Chapter 3.

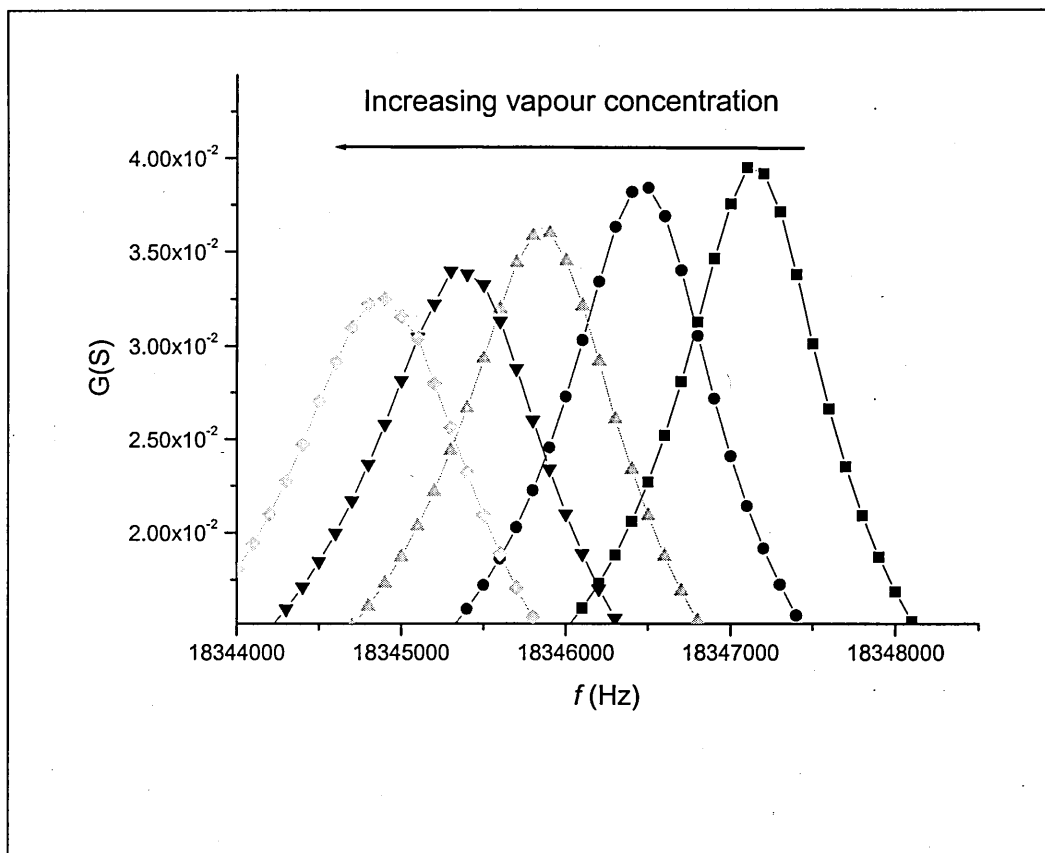


Figure 5.6. Typical set of admittance spectra measured at different concentrations of toluene vapours.

The equivalent circuit model parameters R , L , C and C_p were first fitted to the admittance spectra of uncoated crystals. This allowed us to obtain the values for the non-variable parameters C (the mechanical elasticity of the quartz) and C_p (the capacitance of the quartz between the electrodes and the parasitic capacitance of the crystal fixture). C_p remaining constant in gas phase applications. Table 5.1 shows typical values of the equivalent circuit parameters for uncoated crystals. On exposure to the target analytes, parameters C and C_p were kept constant, while R_1 and L_1 were obtained from the difference between uncoated values of R and L and measured values obtained during vapour exposure.

Figure 5.7a shows changes in the resonant frequency against concentration for both hexane and toluene. As expected, the resonant frequency decreased in an approximately linear fashion with increasing analyte concentration. When the vapour concentration is given in absolute units of ppm (figure 5.7a), the two types of solvent vapours yield different frequency shift according to their relative vapour pressures. From this graph alone it is not possible to solve a reverse problem of evaluation of the vapour concentration from the frequency shift because of a multiple solution. Moreover, these vapours have become completely indistinguishable, if the concentration is presented in the units of a relative vapour pressure in respect to the saturated vapour pressure (p/p_s) at a given temperature, and two dependencies fall almost into the same line (see figure 5.7b). The latter fact is in a good agreement with the results of our previous study of adsorption of organic vapours using QCM and Surface Plasmon Resonance (SPR) techniques [16].

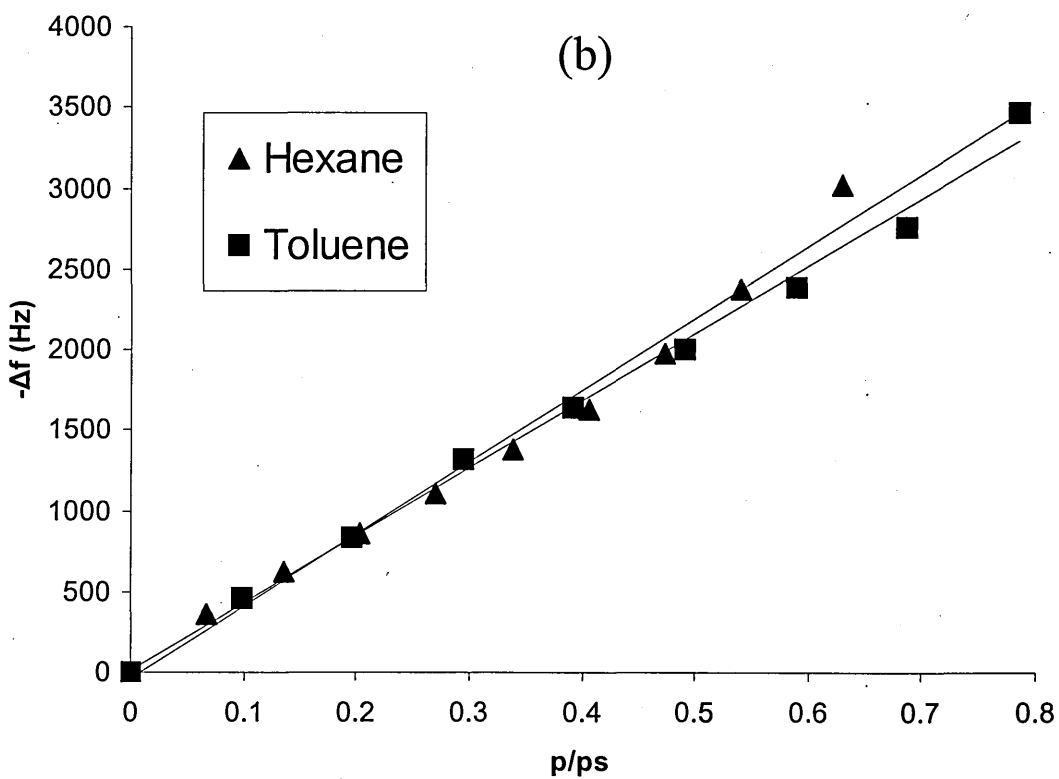
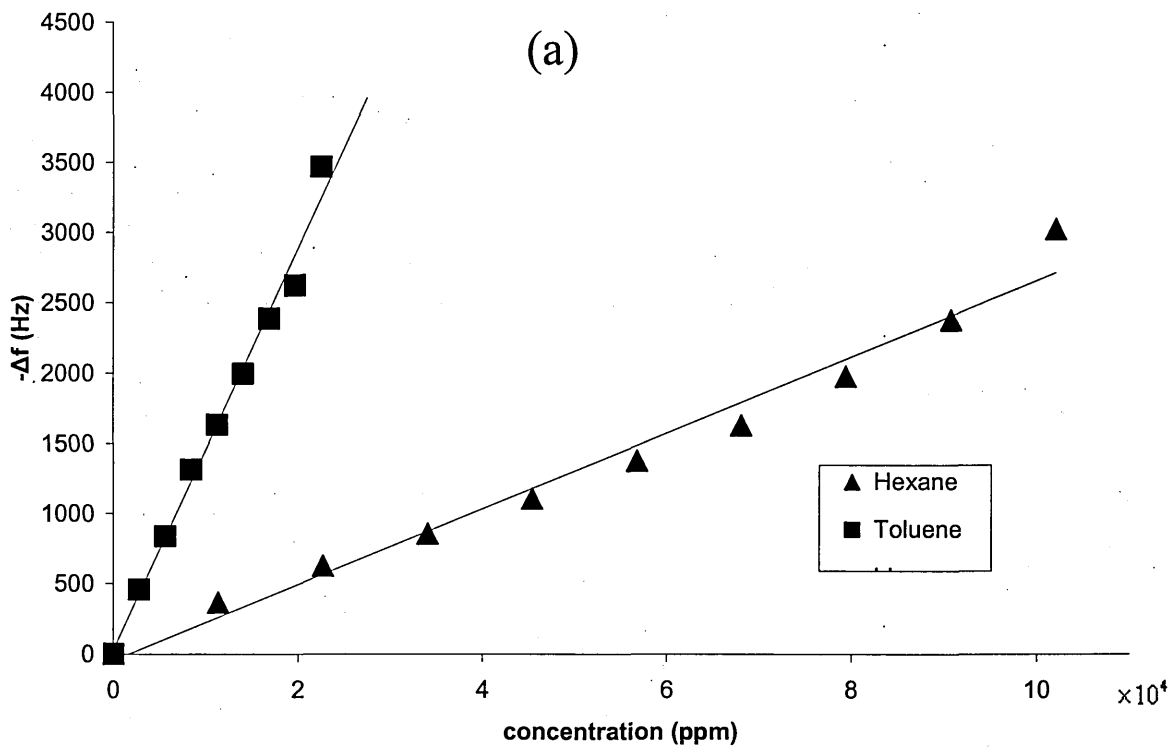


Figure 5.7. The dependence of Δf against vapour concentration measured in absolute ppm units (a) and relative vapour pressure units (p/p_s) (b).

The changes in resistance against the concentration/relative vapour pressure for the two selected analytes are shown in figure 5.8. Firstly, the curves for hexane and toluene curves, presented in both ppm (figure. 5.8a) and p/p_s (figure. 5.8b) units are well distinguished. The responses appear exponential which is confirmed from plotting ΔR on a logarithmic scale (inset figure. 5.8a) and (inset figure. 5.8b). The increase in the resistance (R_1) value, which represents viscoelastic film properties, is believed to be associated with the film softening. Such behaviour is expected from the mechanism of capillary condensation of organic vapours of high concentrations in the range of a few percent of saturated vapour pressure [16]. The two curves in figure 5.8b are very close at low pressures, but separated at high pressures. This trend is clearly seen when the results presented in semi-logarithmic scale on the inset to figure 5.8b. The pressure value of about 0.1 p/p_s , where the two curves met, corresponds to the characteristic pressure (p_{cc}) for capillary condensation governed by the Kelvin's formula 5.7 [17]:

$$p_{cc} = p_s \exp\left(-\frac{2V\gamma}{rRT} \cos\theta\right) \quad (5.7)$$

where V and γ are respectively the molar volume and surface tension of liquid adsorbate, r is the radius of cylindrical capillary, and θ is the wetting angle in the capillary. This approach was successfully implemented in [16] for nano-porous calixarene films, and the pore size in the range of 1 nm was estimated.

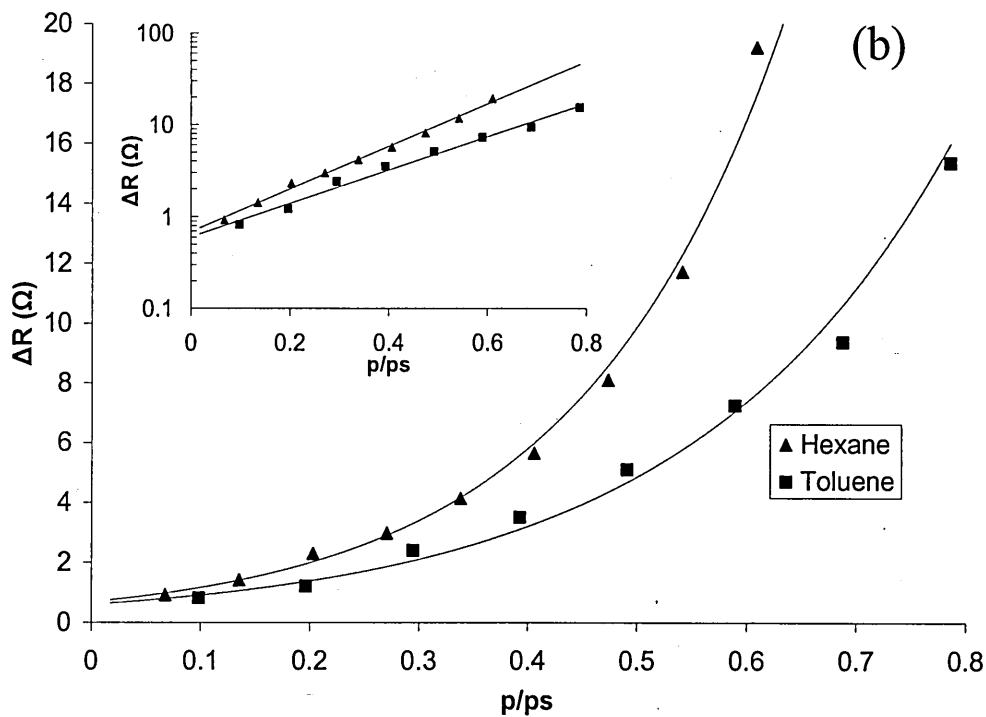
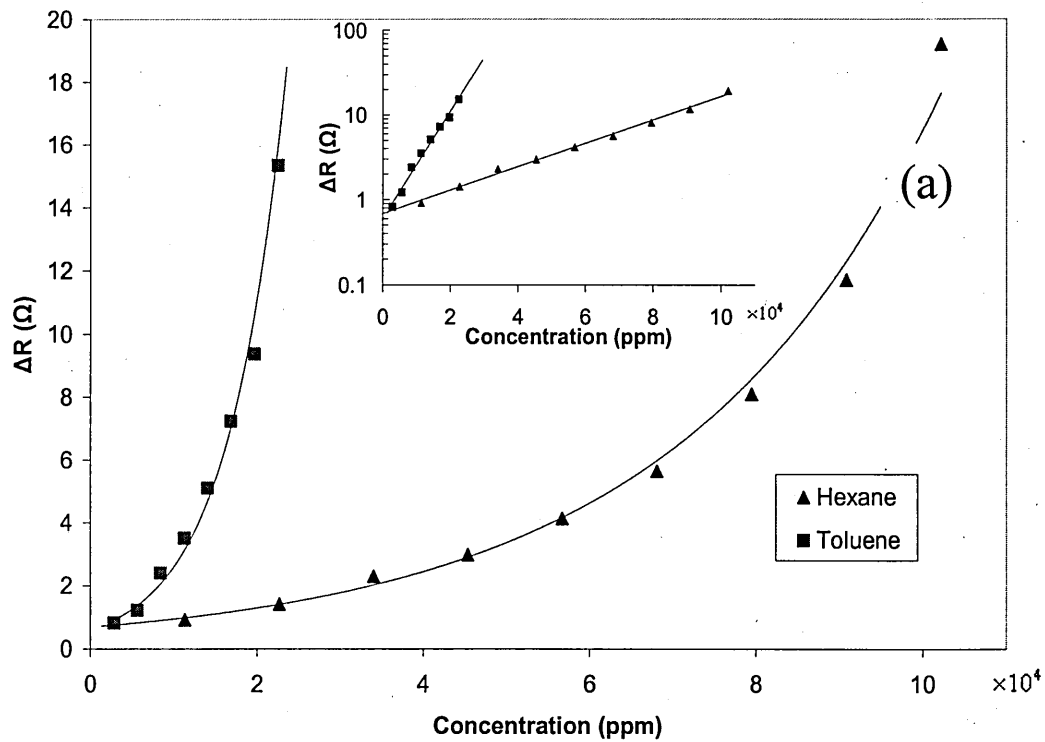


Figure 5.8. The dependence of ΔR against vapour concentration measured in absolute ppm units (a) and relative vapour pressure units (p/p_s) (b). Inset (a) and (b) ΔR represented on a logarithmic scale.

To determine the type of solvent and its relative concentration figure 5.7a and 5.8a can be cross referenced and presented as a plot of Δf (change in resonant frequency) against ΔR (change in resistance). This has been done in figure 5.9, which gives an unambiguous indication that each analyte tested affects the viscoelasticity of C[4]RA film in a unique way. It also shows that damping effects produced each vapour are not directly proportional to the change in resonant frequency and have been estimated to follow an exponential trend as shown in figure 5.9.

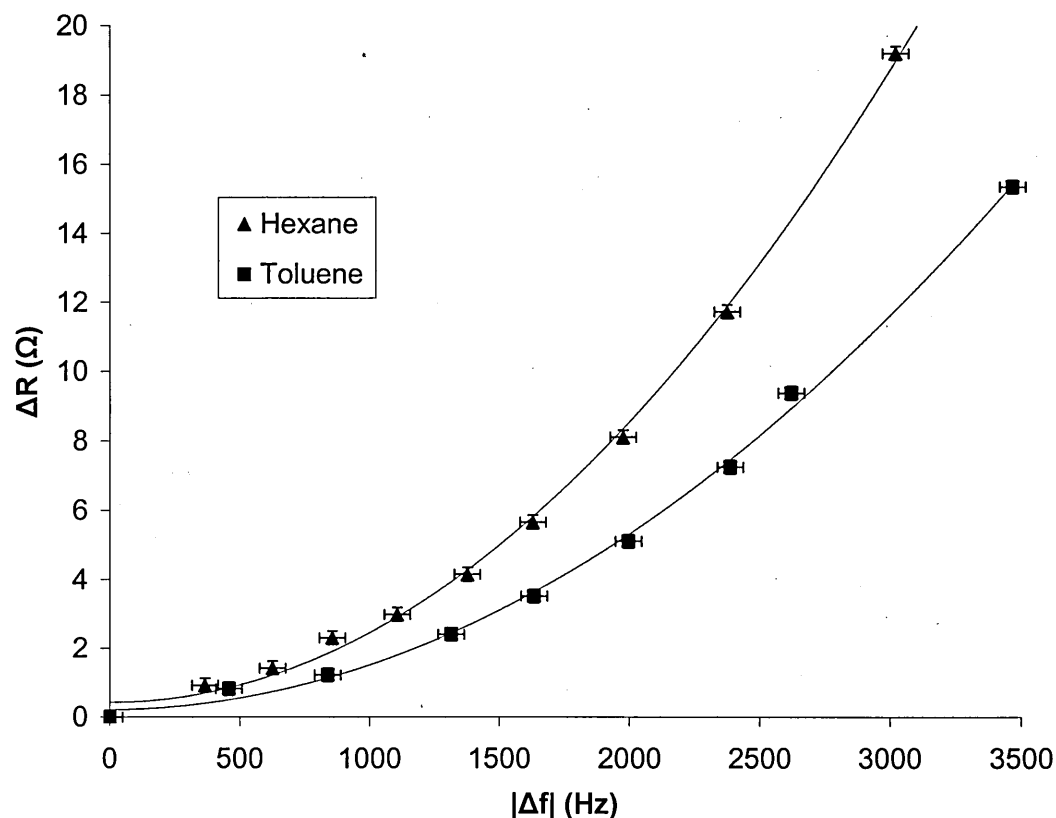


Figure 5.9. The dependence of ΔR against Δf for hexane and toluene vapours.

The experimental error of the admittance analysis is approximately $\pm 5\text{Hz}$ for the frequency measurements and within $\pm 0.1\Omega$ for the resistance. Figure 5.10(a) and (b) shows typical kinetics of changes in Δf and ΔR respectively, extracted by fitting of admittance spectra measurements, as a response to exposure to hexane vapour of

different concentration. The time scale here is given in arbitrary units, which is equal to about 20 sec and determined by the duration of admittance spectra measurements. The response is fast and reproducible, and full recovery was observed after flushing the gas cell with fresh air, the facts typically observed for adsorption of organic vapours of high concentration in calixarene films [18,19]. The slightly longer time of response of about 12 a.u.(240 sec) compared to recovery of 4 a.u. (80 sec) is most likely caused by the extra time required for evaporation of injected liquid solvent and vapour diffusion inside the gas-cell.

Also the two stage impedance measurements procedure seems to be optimal in a sense of a number of experimental spectra points measured and therefore yields reasonable accuracy in evaluation of Δf and ΔR and at the same time allows *in-situ* tests of vapour exposure to be performed.

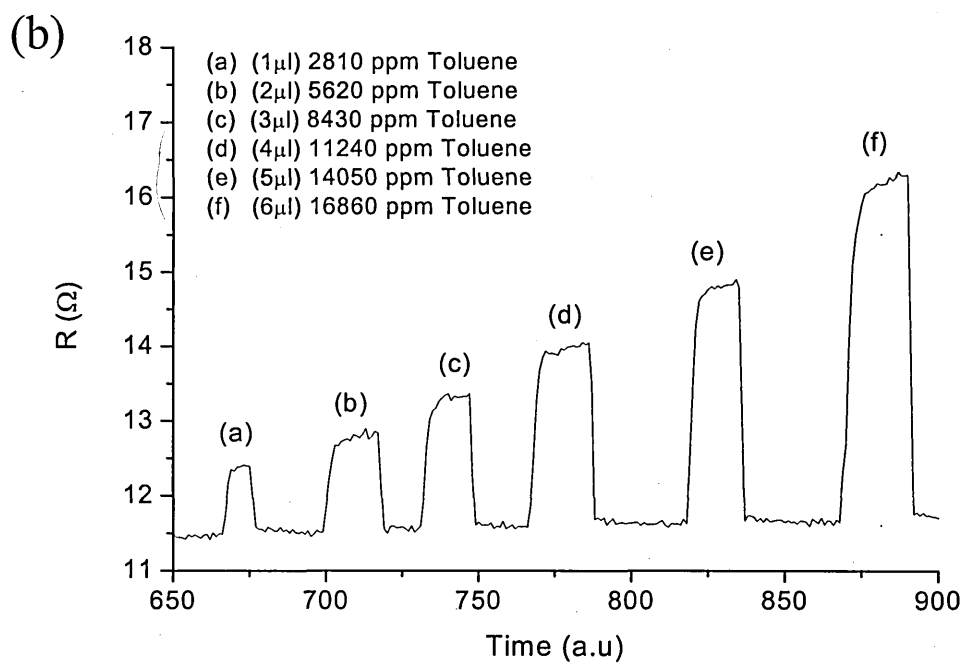
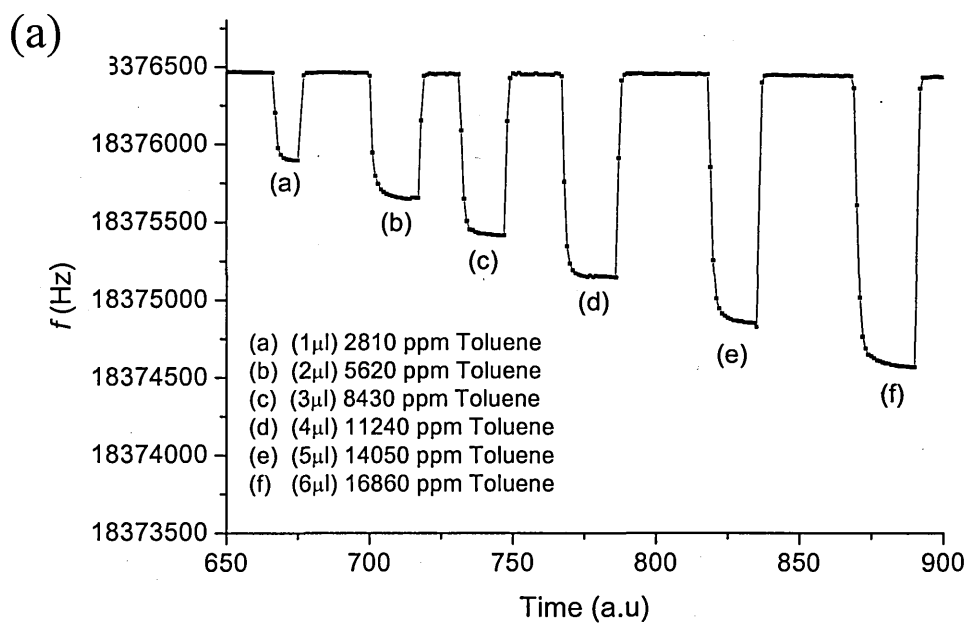


Figure 5.10. Typical time dependence of the resonance frequency (a) and the resistance R (b) during a sequence of exposures to hexane vapours of different concentrations and intermediate flushing with air.

The effect of analyte adsorption into a viscoelastic film has been predicted by Lucklum and coworkers [20]. The values Δf_v and ΔR_v represent the frequency shift and resistance change caused by sorption of a small amount of analyte into the viscoelastic film and are given by equations 5.8 and 5.9 respectively.

$$\Delta f_v \propto M_v \left(1 + \frac{G'}{\rho |G|^2} M^2 \right) \quad (5.8)$$

$$\Delta R_v \propto M_v \left(1 + \frac{G''}{\rho |G|^2} M^2 \right) \quad (5.9)$$

where M_v is a further increase in mass factor caused by analyte adsorption and relates directly to the Sauerbrey relationship as described in section 2.42.

With no change in film parameters (G' or G'') a mass increase caused by any analyte would give identical values of ΔR for the observed changes in Δf . It is therefore believed that the sorption of hexane and toluene vapours showing unique values of $\frac{\Delta R}{\Delta f}$ indicates changes in viscosity (G' & G'') are unique to either vapour. The above phenomenon is not necessarily observed in all membranes. Figure 5.11 shows the $\frac{\Delta R}{\Delta f}$ sensor response of a polyurethane based polymer with calix[4]arene unit incorporated in the main chain (PU-C[4]A) exposed to hexane, toluene and benzene vapours. All three vapours fall into the same line, indicating no unique change in shear moduli (G' or G''). It is also worth noting a large variation in sensitivity levels between the (PU-C[4]A) and C[4]RA compounds (see figure 5.12). Although the (PU-C[4]A) shows no discrimination from measuring Δf and ΔR of a single sensor, the difference in vapour sensitivity compared to the C[4]RA films makes it suitable for a QCM array.

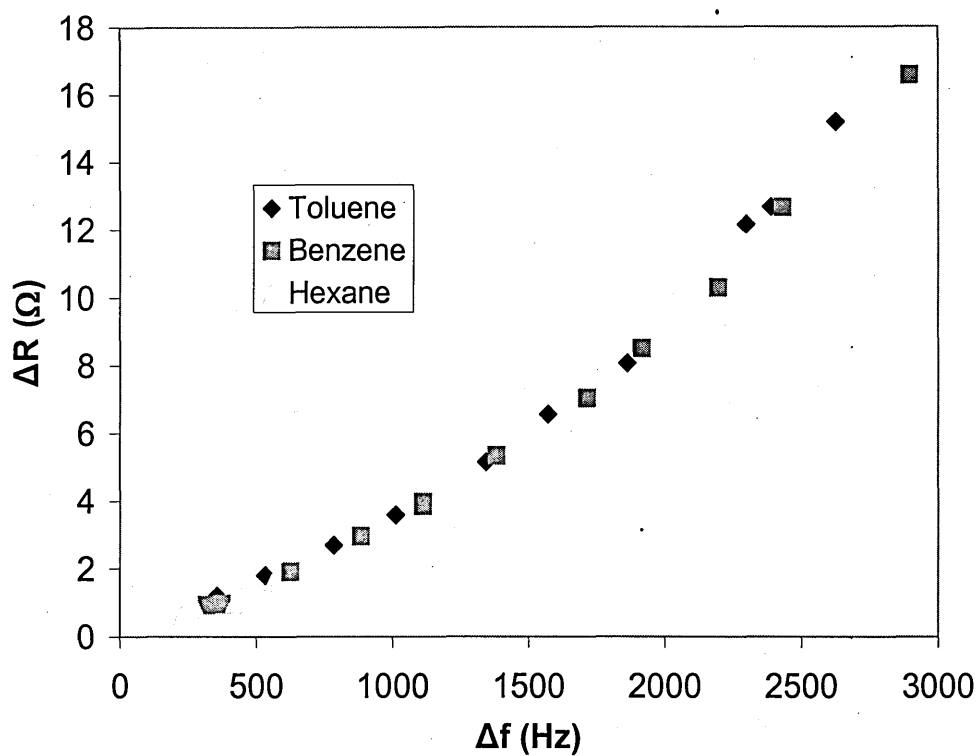


Figure 5.11. $\Delta R/\Delta f$ response of a (PU-C[4]A) coated QCM to hexane, toluene and benzene vapours.

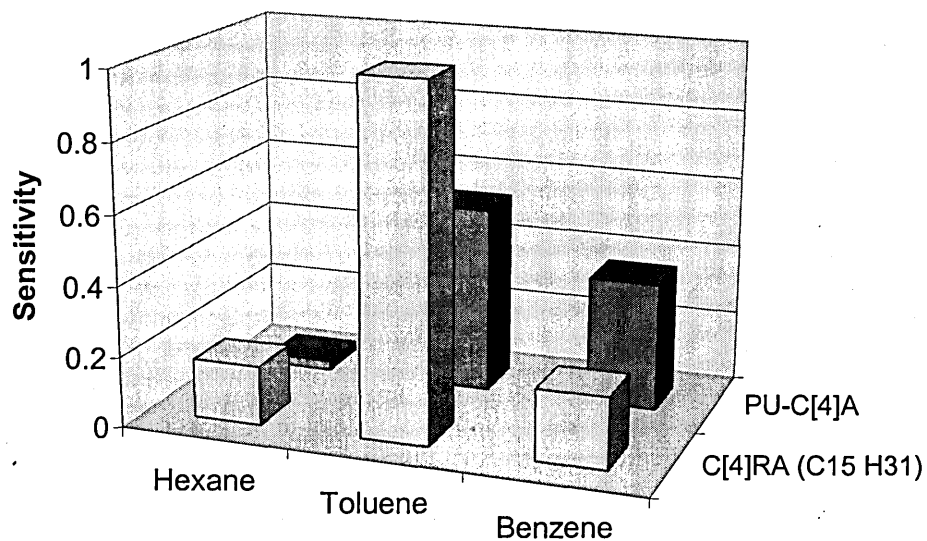


Figure 5.12. Normalised sensitivity chart for C[4]RA C₁₅H₃₁ and (PU-C[4]A) coatings to hexane, toluene and benzene vapours.

The detection limits using the impedance analysis technique are summarised in table 5.4 based on the extracted frequency parameter. The values were established from linear fits

of the experimental data as shown in figure 5.7a. The detection limits for hexane and toluene vapours are 120.5ppm and 22ppm, respectively, making the sensitivity to toluene (in absolute units of ppm) 5.5 times greater than that of hexane.

	Sensitivity Hz/ppm	Sensitivity ppm/Hz	2xSD	LOD
Hexane	0.0264	37.8787	3.1806	120.4765
Toluene	0.1447	6.9109	3.1806	21.9805

Table 5.4. Sensitivity levels and detection limits of C[4]RA C₁₅H₃₁ membrane calculated from linear fitting of the experimental data (impedance analysis technique).

The sensitivity of the resistance parameters ΔR (or R_1 of the BVD equivalent circuit) is slightly more complicated as the increase is not linear with concentration and follows an exponential trend (figure 5.8). From fitting the experimental data, the change in ΔR for increasing concentration in ppm is given by equation (5.10).

$$\Delta R = a \exp^b \quad (5.10)$$

where values of a and b for hexane and toluene vapours are given in the table table 5.5 below.

	a	b
Hexane	6.86935×10-01	3.17908E×10-5
Toluene	6.04560×10-01	1.45644E×10-4

Table 5.5. Coefficients of equation (5.10) from hexane and toluene vapours obtained from fitting of experimental data (see figure 5.8).

The limit of discrimination between the two vapours has been estimated at the point where the difference between the ΔR values for each vapour is greater than 2×SD of the baseline noise (see table 5.4). From equations (5.10) the value has been calculated as 1704ppm. Although this value seems moderately high, it is still well below the LEL for

either of the vapours, and hence suitable for the application as a pre-explosive alarm devices.

	Hexane	Toluene	$\Delta R_{\text{ToI}} - \Delta R_{\text{Hex}}$
Concentration (ppm)	$\Delta R \ \Omega$		$R \ \Omega$
1704	0.72517	0.77486	0.049683157 (>0.04966)

Table 5.3. Values of ΔR for hexane and toluene vapours at which discrimination is achieved.

5.4 QCMD Results

Identical tests to those performed using impedance analysis (section 5.4) were completed using the QCMD method. The dissipation factor (D) measured directly with the experimental setup described in Chapter 3.3.2 has been converted into an equivalent circuit resistance using equation (3.7). The value of L obtained from previous impedance measurements and fitting was used. Figure 5.13a shows the frequency change Δf (Hz) against concentration (ppm) for hexane and toluene vapours, the results are effectively identical to those shown previously in figure 5.7a for QCM impedance measurements. The good agreement between the two methods continues for both frequency shifts Δf and resistance changes ΔR as shown in figures 5.13 though 5.15,. Table 5.4 gives the Δf sensitivity levels for hexane and toluene using impedance analysis and the QCMD method based on the C[4]RA C₁₅ H₃₁ crystal coating. A high degree of correlation in sensitivity levels obtained with the two techniques is evident.

	Impedance Analysis		QCMD	
	Sensitivity	ppm/Hz	Sensitivity	ppm/Hz
Hexane	0.024	41.66666667	0.0264	37.87878788
Toluene	0.1437	6.958942241	0.1447	6.910850035

Table 5.4. The Δf sensitivities of hexane and toluene vapours using the Impedance analysis and QCMD methods.

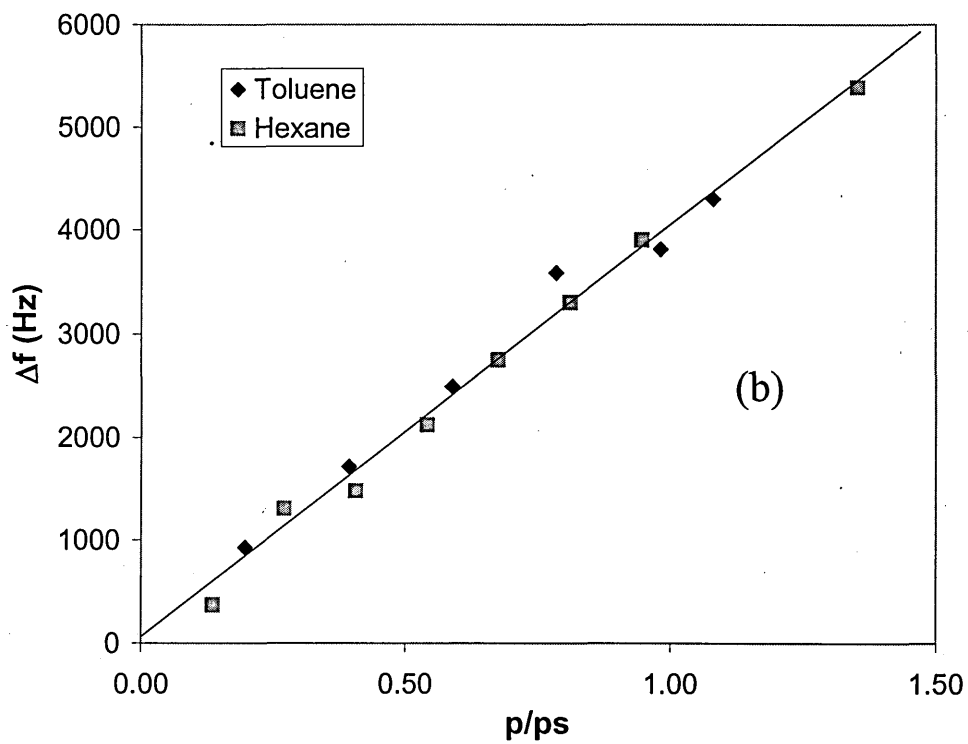
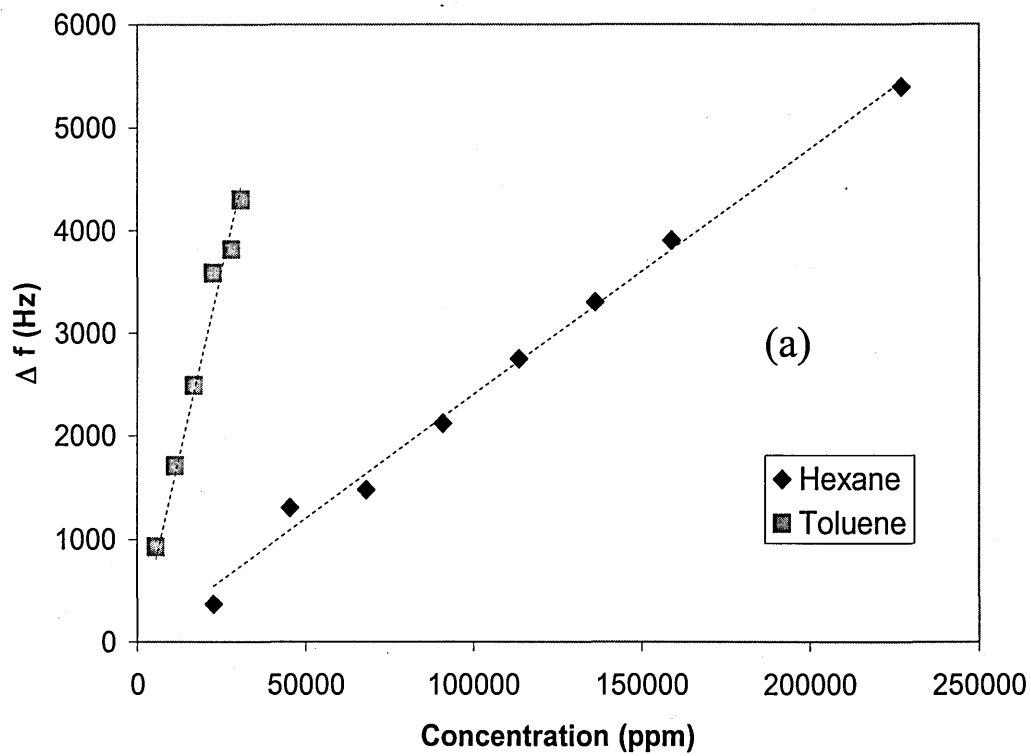


Figure 5.13. The dependence of Δf against vapour concentration measured in absolute ppm units (a) and relative vapour pressure units (p/p_s) (b).

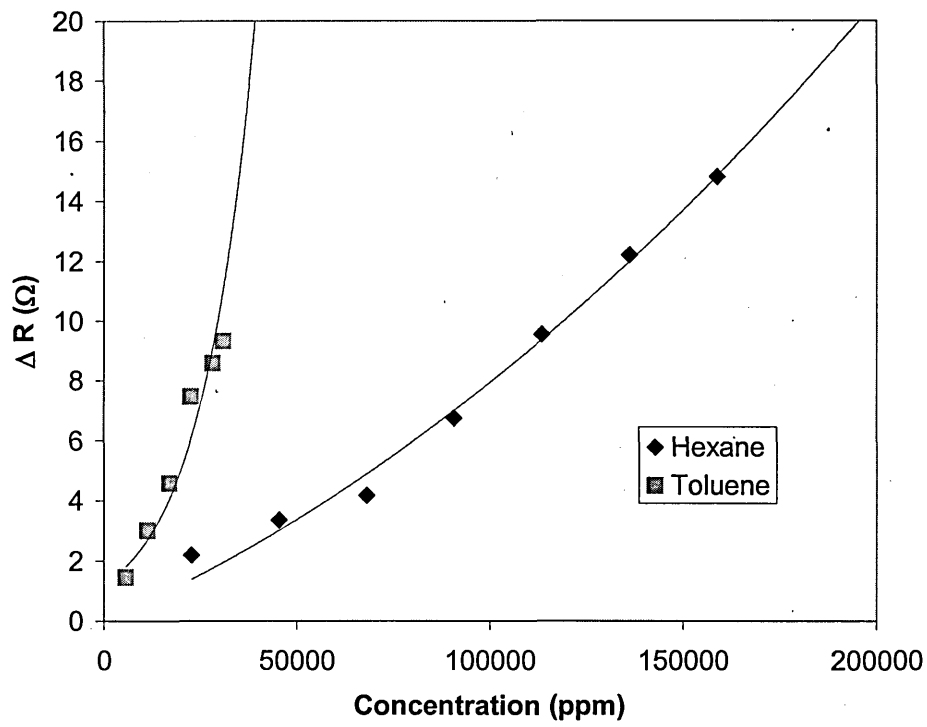


Figure 5.14. The dependence of ΔR against vapour concentration measured in absolute ppm units.

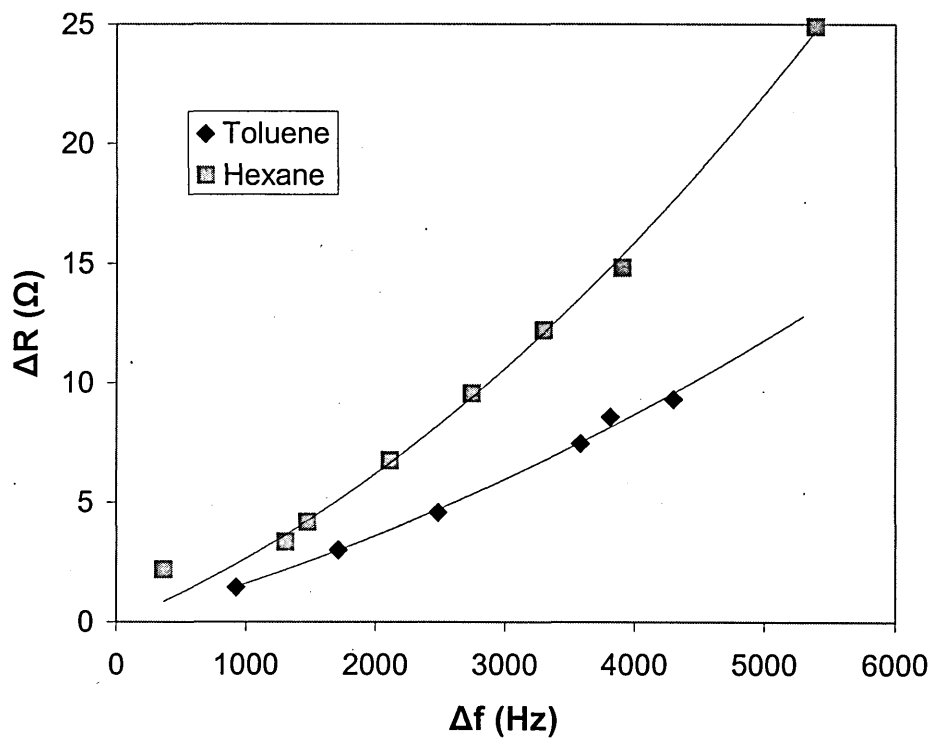


Figure 5.15. The dependence of ΔR against Δf for hexane and toluene vapours.

5.5 Vapour sensing – impedance analysis/QCMD

measurements for an array based sensor

The following sections describe the collection of data by the impedance analysis/QCMD methods for the implementation within a sensor array. The advantages of obtaining an additional parameter ΔR extracted from the measurements of a QCM coated with a viscoelastic films have been shown in the previous sections and proposed by several research groups [20-29]. In this work the extraction of multiple parameters has shown that the detection and discrimination of contacting hexane and toluene vapours is possible using even a single sensor. Further tests have therefore been undertaken with more target analytes and several of the C[4]RA compounds used previously in the QCM sensor array.

Figure 5.17a shows the frequency response of the C[4]RA C₁H₃ (the calix[4]resorcinarene with smallest hydrocarbon tail length) exposed to hexane, toluene, benzene, m-xylene and cyclohexane vapours. Similar to previous measurements taken using the oscillator based QCM array, responses are erratic and very random, with no clear trends emerging (see figures 5.16 and 5.17). The poor response pattern is believed to be caused by the lack of basket shaped cavities which are created by the calix[4]resorcinarenes with longer hydrocarbon chain lengths.

In contrast to the frequency, the value ΔR appears to follow definite trends for each vapour and even more unexpectedly, a negative ΔR value is obtained. Figure 5.16 shows the kinetic frequency and resistance responses during a sequence of increasing benzene exposures. The decrease in resistance ($-R$) is not predicted or explained by equations 5.8 and 5.9 for an increasing mass. The decrease in resistance suggests an increase in film stiffness [27] which may be attributed to the incorporation of solvent

(benzene) molecules into the film, and therefore improving the links between the C[4]RA baskets. The largest change in ΔR is produced by hexane vapours, the long hydrocarbon hexane molecule displaying the best interlinking properties and therefore gives most rigidity to the C₁H₃ C[4]RA structure. It must also be noted that cyclohexane does not follow the same pattern as hexane and is closer to the aromatic hydrocarbons (benzene, toluene, m-xylene).

The erratic variations in frequency may be due to statistical adsorption/desorption processes, however the exact cause is unknown and further investigation is required.

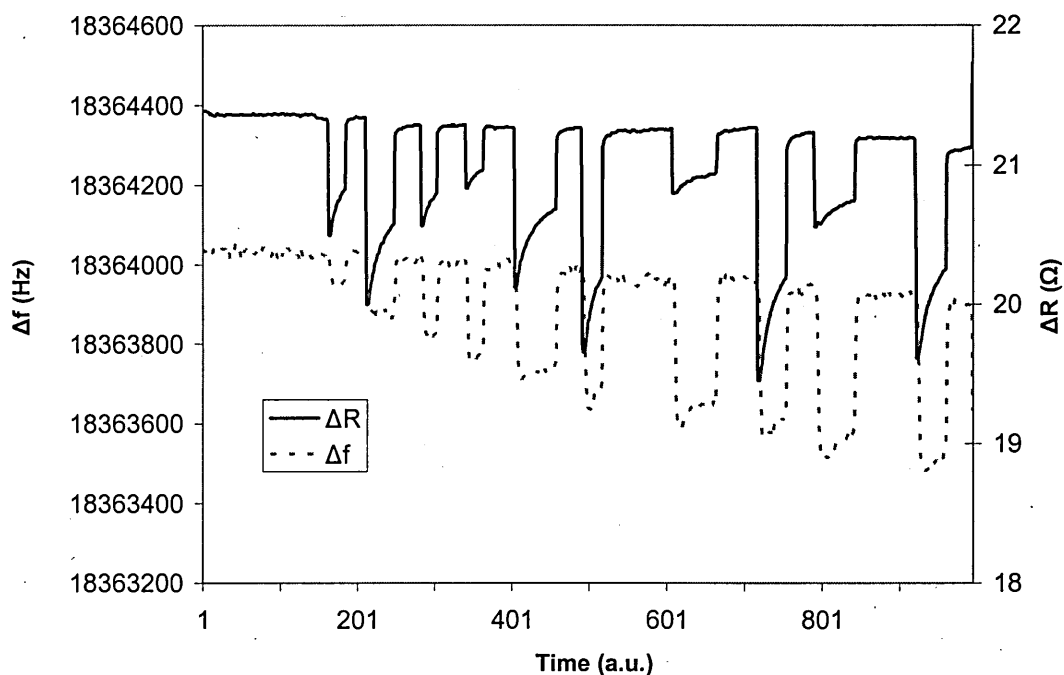


Figure 5.16. Typical time dependence of the resonance frequency (f) and the resistance (R) during a sequence of exposures to benzene vapours of different concentration and intermediate flushing with air.

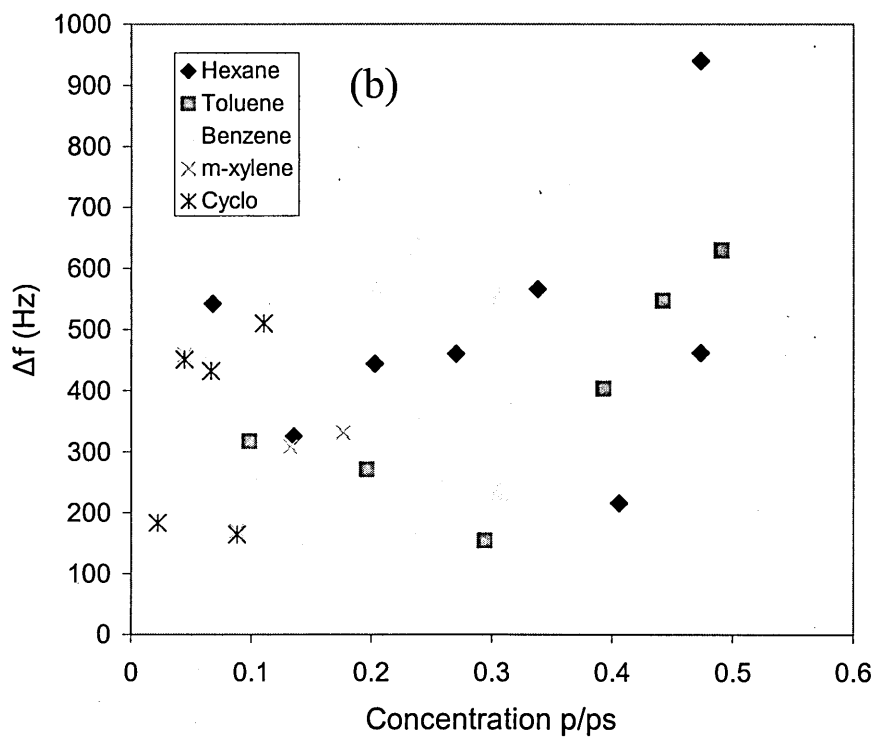
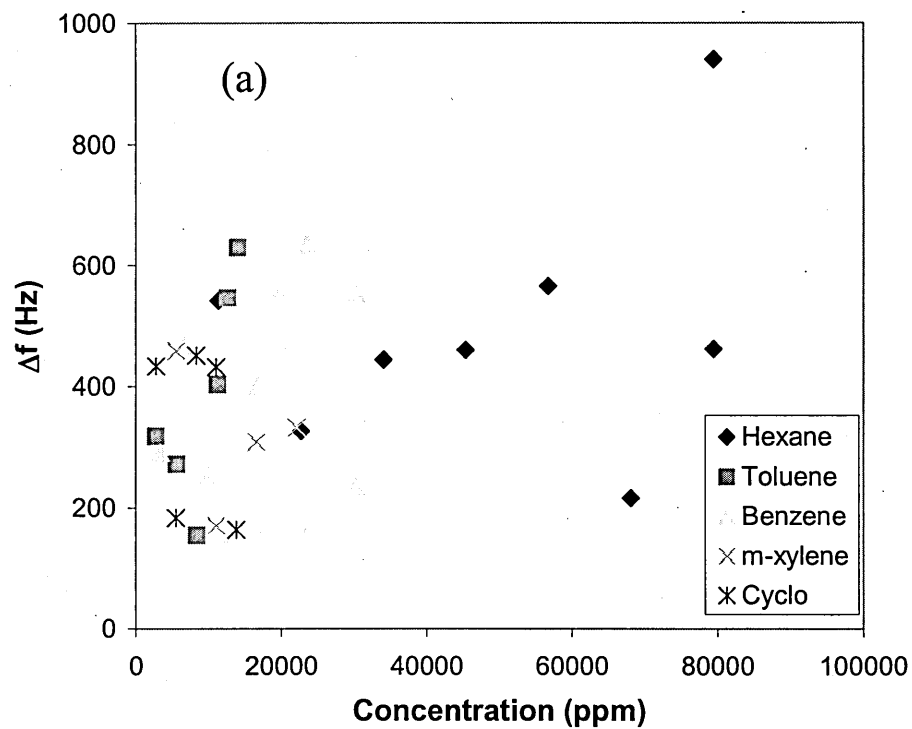


Figure 5.17. The dependence of Δf against vapour concentration measured in (a) absolute ppm units (b) and relative vapour pressure units (p/p_s) for a C[4]RA C_1H_3 sensing membrane.

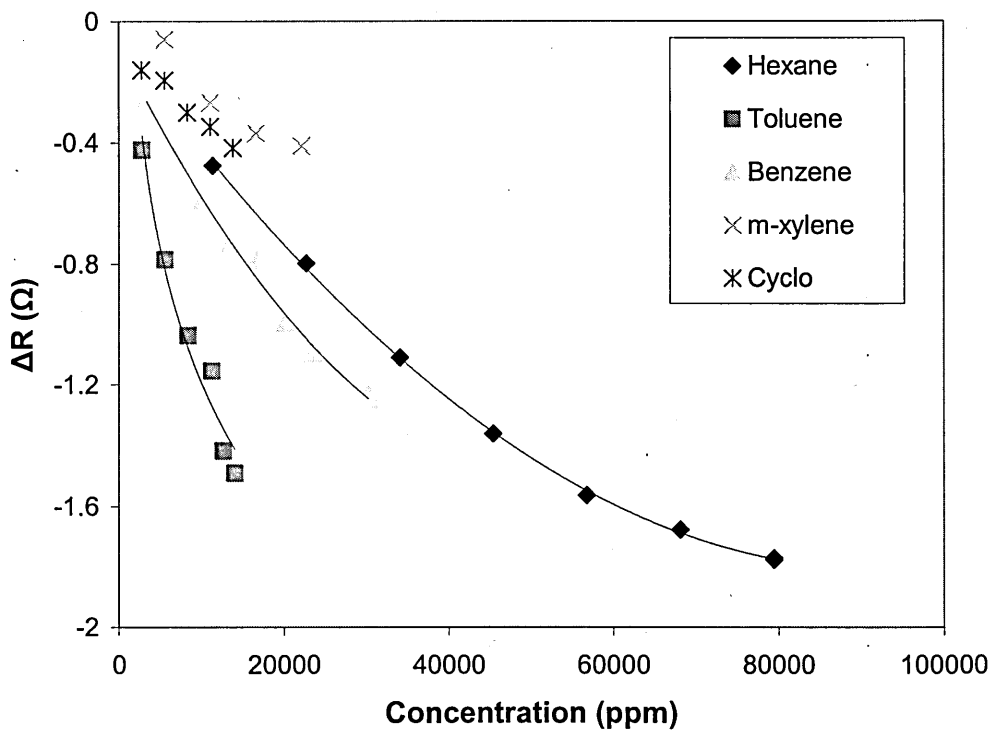


Figure 5.18. The dependence of ΔR against vapour concentration measured in absolute ppm units for a C[4]RA C₁H₃ sensing membrane. The decrease in resistance suggests a hardening of the film.

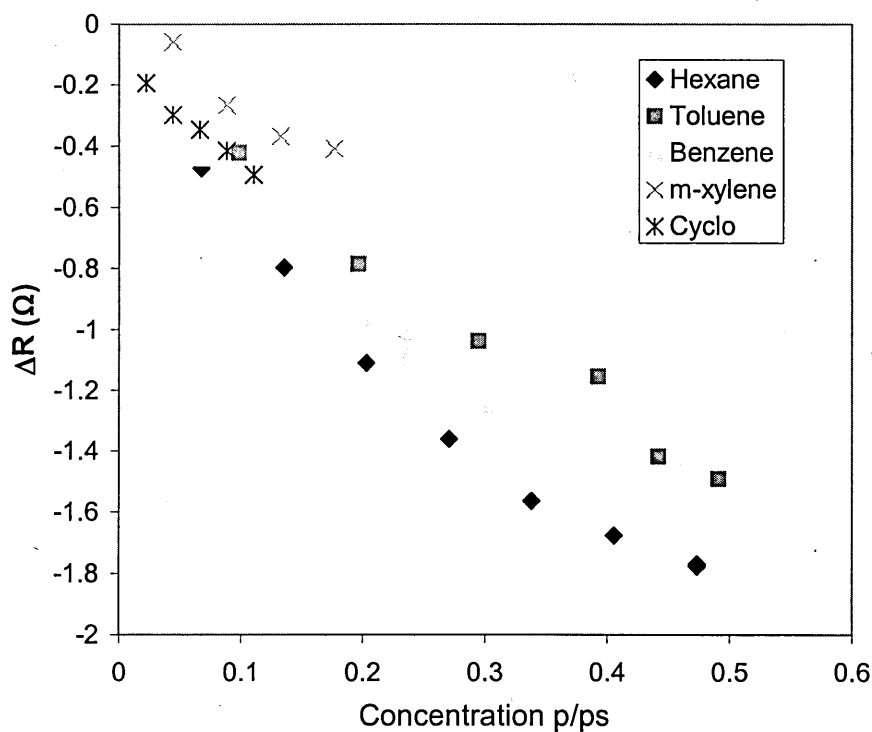


Figure 5.19. The dependence of ΔR against vapour concentration measured in units of relative vapour pressure $\frac{p}{ps}$ units for a C[4]RA C₁H₃ sensing membrane.

The next compound tested was C[4]RA C₅H₁₁. Figure 5.20a shows the frequency sensorgram for the C[4]RA C₅H₁₁ compound in ppm units. The responses show a definite logarithmic trend, with high sensitivity levels at lower concentrations. Over the larger concentration range tested here the C₅H₁₁ membrane shows decreasing sensitivity with increasing vapour concentration. This indicates the high sensitivity levels obtained previously using QCM oscillator measurements are only applicable at low organic vapour concentrations, when using the C[4]RA C₅H₁₁ compound. The general trend appears to follow typical Langmuir (equation 5.11) or BET (at low concentration) adsorption isotherms, with a large number of adsorption sites at low vapour pressure giving the high sensitivity (see figures 5.20a and 5.20b). The Langmuir constant calculated from equation 5.11 for each respective vapour is given table 5.5. It is however believed that the adsorption process is not purely Langmuir and solvation of the vapour into the film may also occur. The small response displayed by m-xylene vapours (see figure 5.20b) has been observed previously [16] and has been attributed to the fact that m-xylene is a larger molecule and permeation into the membrane is therefore more difficult. The responses are believed not to be an effect associated with transient behaviour as the samples were taken when sensor(s) had fully settled (see figure 5.1).

$$\theta = \frac{bP}{1 + bP} \quad (5.11)$$

where θ is the surface coverage P is the pressure and b is the equilibrium constant.

Vapour	Langmuir Constant
Hexane	7.597
Toluene	6.302
Benzene	6.782
M-xylene	2.026
Cyclo hexane	4.983

Table 5.5 Fitted Langmuir constants obtained from figures 5.20.

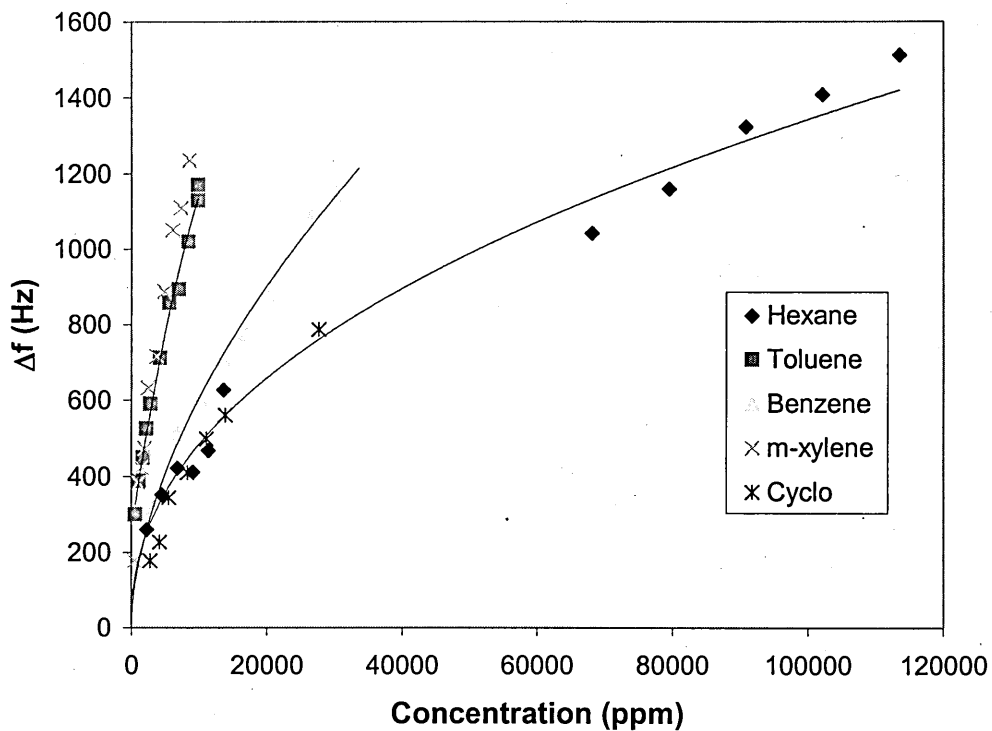


Figure 5.20a. The dependence of Δf against vapour concentration measured in absolute ppm units for a C[4]RA C_5H_{11} sensing membrane.

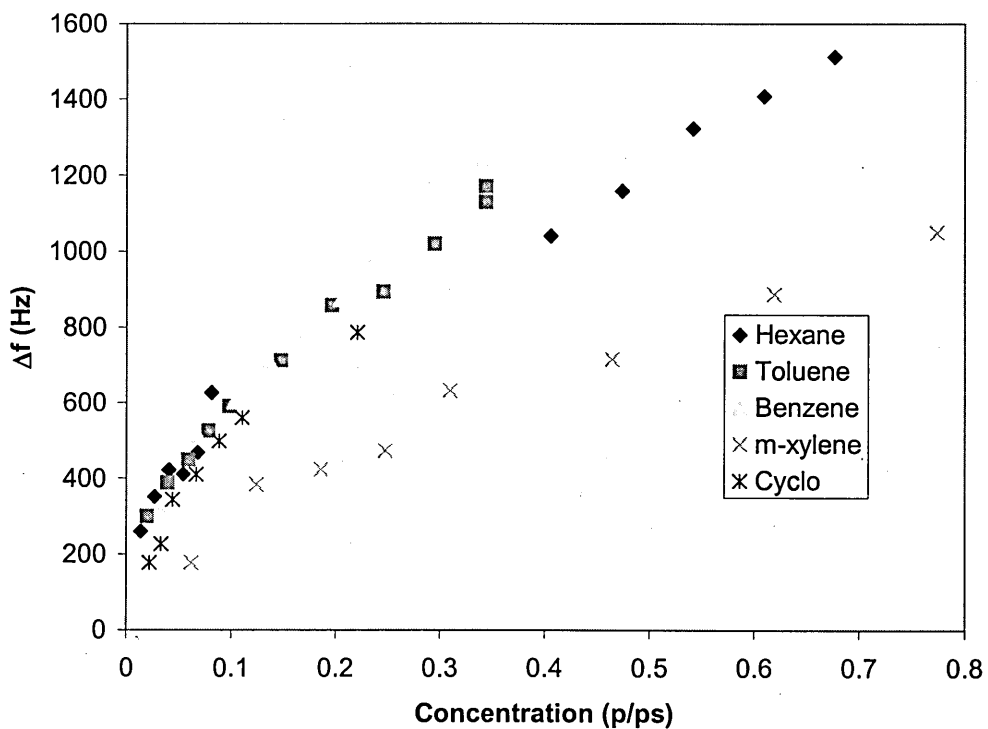


Figure 5.20b. The dependence of Δf against vapour concentration measured in relative vapour pressure units (p/p_s) for a C[4]RA C_5H_{11} sensing membrane.

Figure 5.21 shows the frequency sensorgram for a further increase in hydrocarbon tail length C[4]RA C₁₁H₂₃. The response appears very similar to the C[4]RA C₁₅H₃₁, showing an approximately linear frequency responses to increases in vapour concentration. It is believed that the linear responses seen for the longer chain C[4]RA compounds, corresponds to the early stages of a typical Langmuir or BET adsorption isotherm. The smaller chain length C[4]RA compounds begin to saturate much earlier with less adsorption capabilities, compared with the longer tail C[4]RA compounds.

The changes in the resistance parameter for both C[4]RA C₅H₁₁ and C[4]RA C₁₁H₂₃ parameters are however not in agreement with results obtained from C[4]RA C₁₅H₃₁. At lower concentrations a negative ΔR is observed (figure 5.22), this decrease in resistance continues until a 'negative saturation' is reached. With further increases in vapour concentration the resistance shows an abrupt increase, quickly becoming positive again and rises sharply to above 4 Ω at the highest concentrations tested. The point of polarity change for the ΔR parameter when plotted against units of absolute ppm (figure 5.22a) shows the familiar series of vapour pressure values, hexane (lowest) through to mxylene (highest) (see table 5.1). Plotting as a function of saturated vapour pressure p/p_s also yields no further information (see figure 5.23b), with no particular point of vapour pressure signifying the change in polarity of ΔR , the approximate values range from 0.2-0.8 p/p_s . In this case it is believed that at lower concentrations interlinking between solvents and the C[4]RA structures takes place as observed previously for the C[4]RA C₁H₃ compound. This suggests a stiffening of the film. However, further increases in concentration leads to a maxima in the interlinking between the solvents and C[4]RA films. After this point the sharp increase in resistance (film softening) is seen and is believed to be a result of capillary condensation as observed within the C[4]RA C₁₅H₃₁ film matrix.

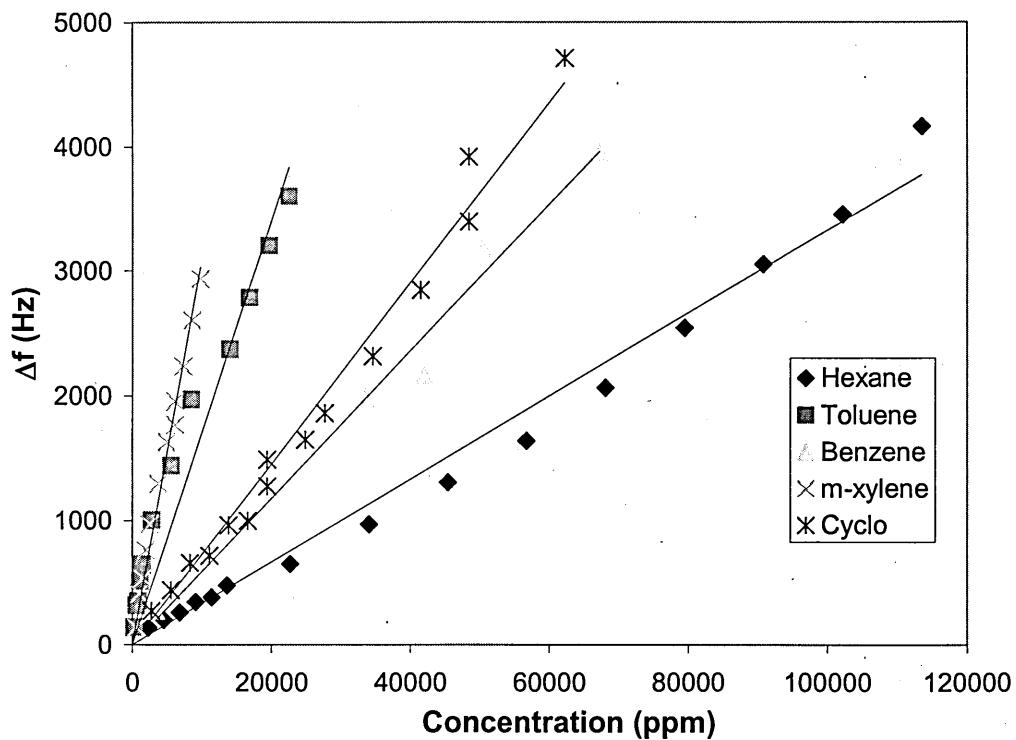


Figure 5.21. The dependence of Δf against vapour concentration measured in absolute ppm units for a C[4]RA $C_{11}H_{23}$ sensing membrane.

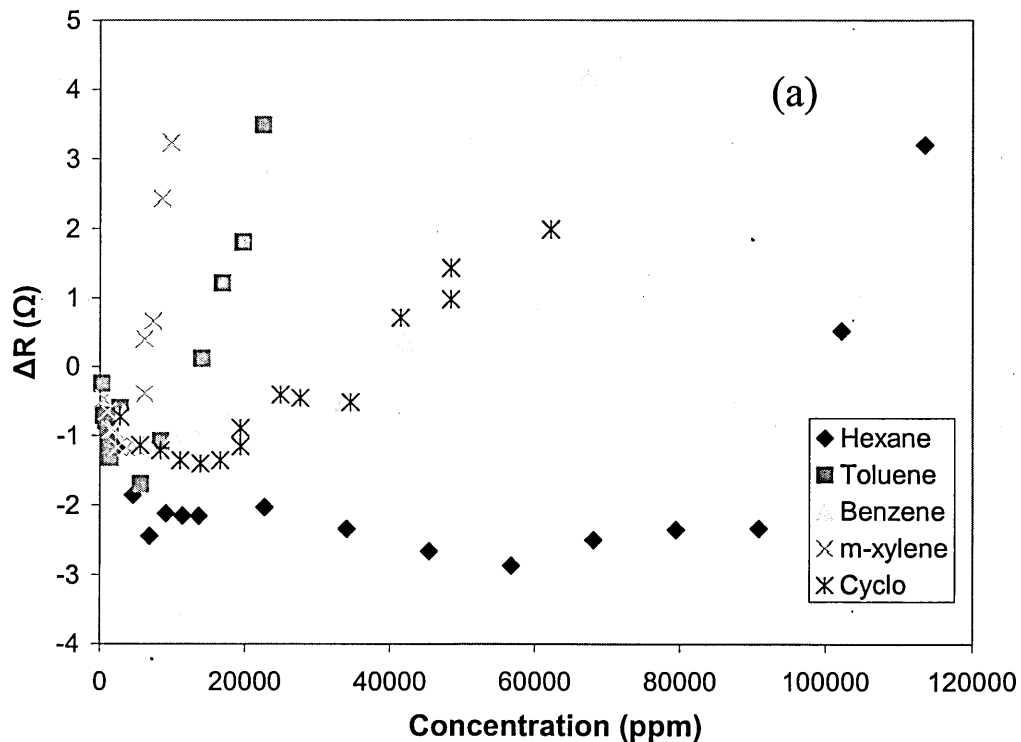


Figure 5.22a. Typical dependence of ΔR against vapour concentration measured in absolute ppm units.

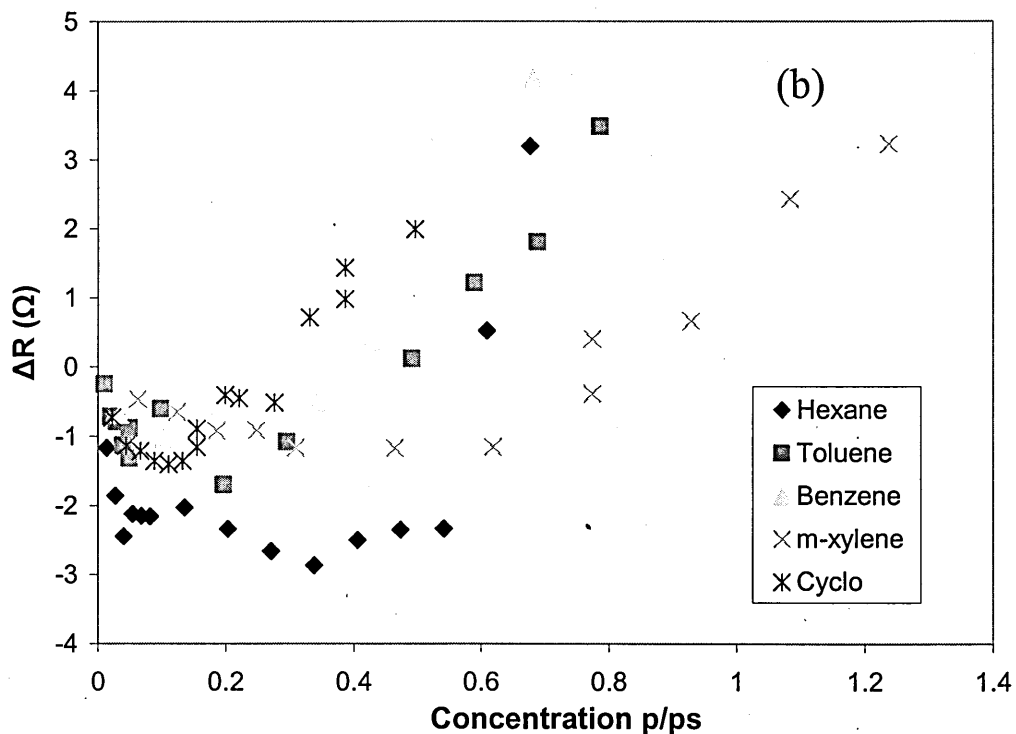


Figure 5.22b. Typical dependence of ΔR against vapour concentration measured in relative vapour pressure units (p/p_s) for either a C[4]RA C_5H_{11} or $C_{11}H_{23}$ sensing membrane.

The C[4]RA $C_{15}H_{31}$ compound as before produced good reproducible results as shown in figures 5.23 through 5.26. Once again the frequency response when plotted as a function of saturated vapour pressure shows all the vapours lying on approximately the same line (figure 5.25), indicating the mass increase is purely related to p/p_s ratio. Figure 5.26 shows the $\Delta R/\Delta f$ response for the four vapours, a clear separation between the hexane and toluene vapours is apparent. The benzene follows the same trend but lies approximately between the hexane and benzene vapours. M-xylene as before (see figure 5.20b) shows an unusual deviation from the other vapours.

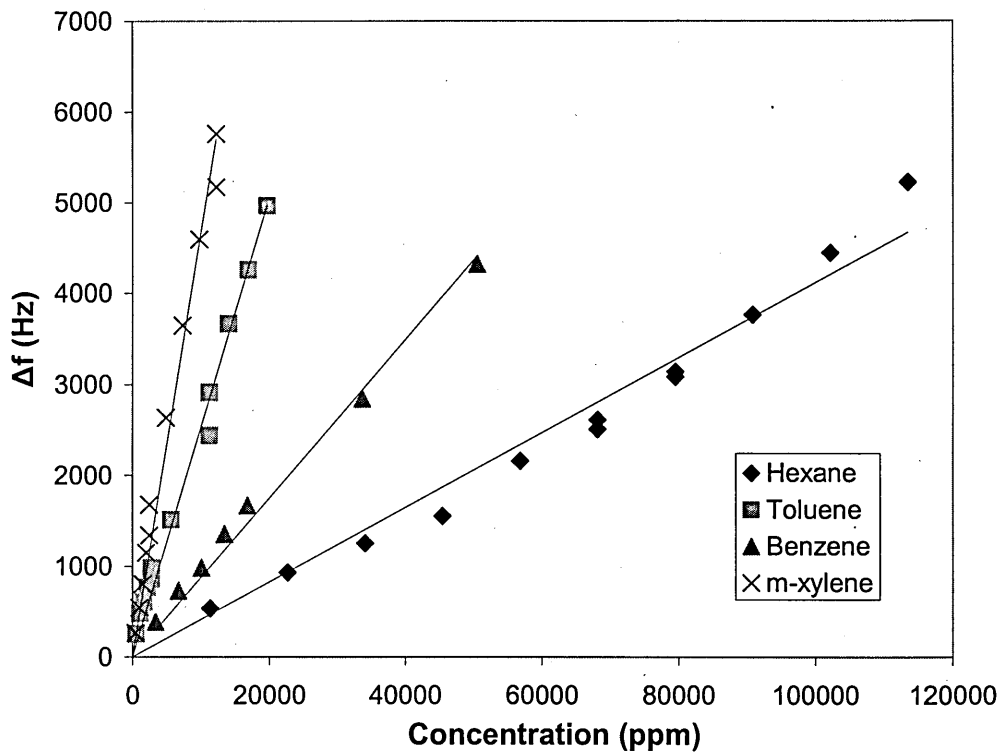


Figure 5.23. The dependence of Δf against vapour concentration measured in absolute ppm units.

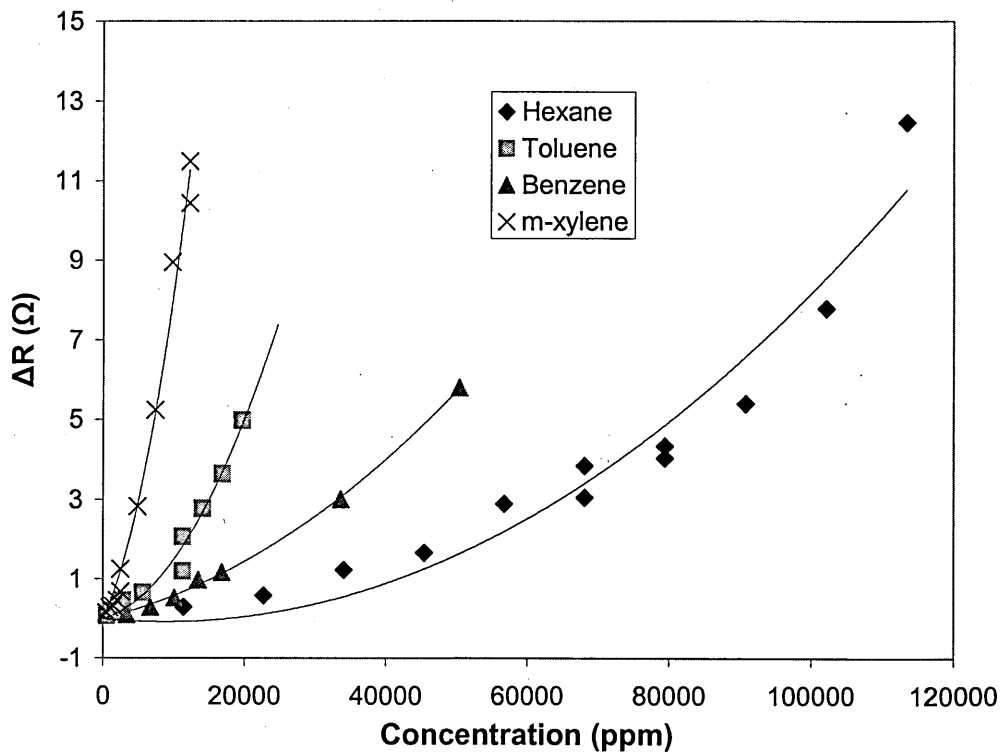


Figure 5.24. The dependence of ΔR against vapour concentration measured in absolute ppm units.

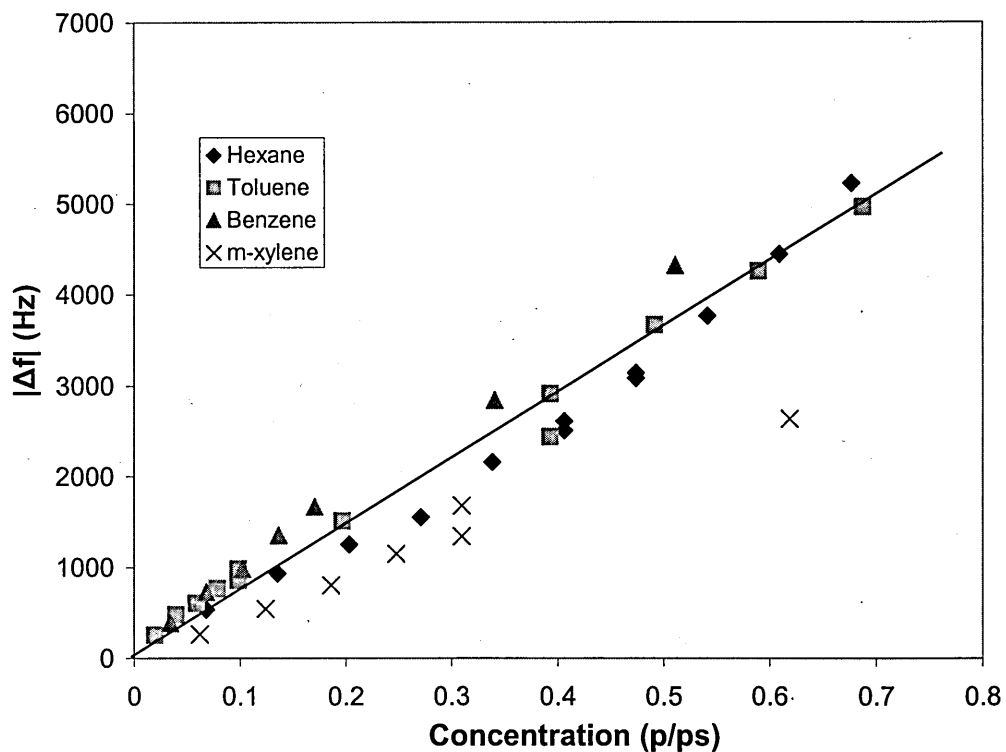


Figure 5.25. The dependence of Δf against vapour concentration measured in relative vapour pressure units (p/p_s).

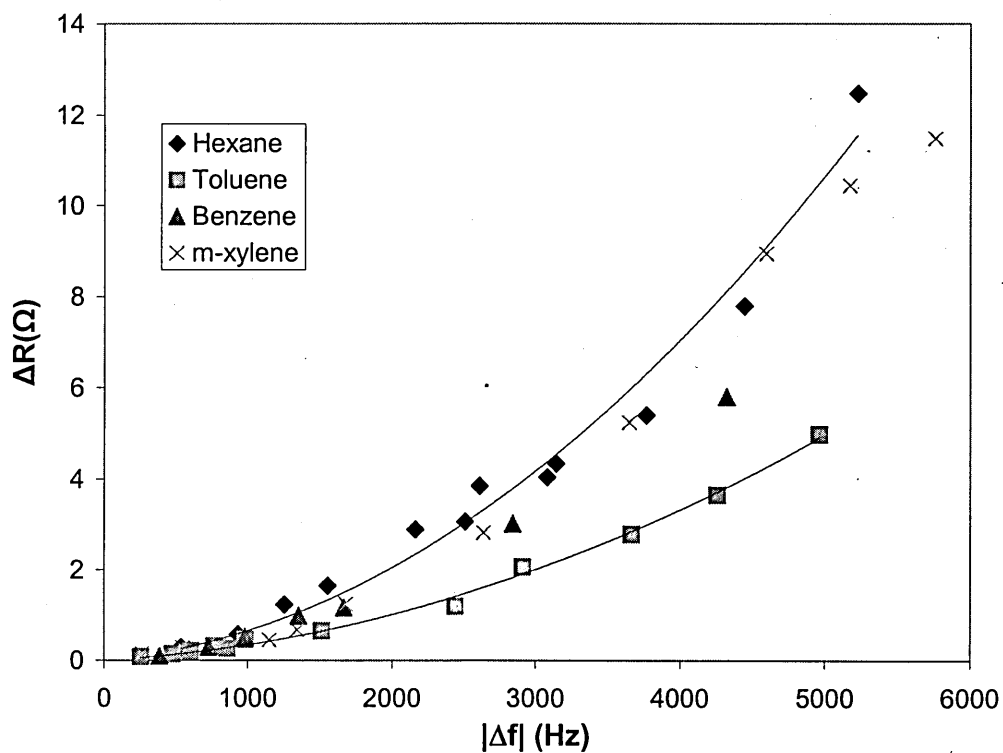


Figure 5.26. The dependence of ΔR against Δf for hexane, toluene, benzene and m-xylene vapours.

From the results obtained using the series of C[4]RA compounds a speculative model may be suggested relating the hydrocarbon chain length of C[4]RA compounds, to the observed responses from organic solvents. The C[4]RA compounds may be broadly classified into three categories:

(i) Small chain lengths (C_1H_3), in this case the short CH_3 chains provide reduced cavity sizes and only a small number of molecules are required to saturate (fill) the available adsorption sites. Once this threshold is reached statistical adsorption/desorption occurs and erratic results, as demonstrated in figures 5.16 and 5.17 are observed. The decrease in the resistance (film stiffening) is a result of interlinking solvents, with hexane itself a long hydrocarbon chain structure and produces the largest decrease in resistance.

(ii) Medium chain lengths (C_5H_{11} and $C_{11}H_{23}$). The chain length now provides sufficient adsorption properties for the solvents. The smaller C[4]RA C_5H_{11} chain reaching saturation earlier and shows a typical Langmuir or early stages of BET adsorption dependence (see figure 5.20). The C[4]RA $C_{11}H_{23}$ exhibits linear responses over the tested vapour concentration range. It is believed that the increase in chain length further enhances adsorption capabilities, and the linear responses correspond to the first stages of a typical Langmuir isotherm. The change in resistance for this group of C[4]RA compounds show an initial decrease in resistance which corresponds to a stiffening of the film. At lower concentrations the film undergoes the same interlinking mechanism seen in the C[4]RA C_1H_3 . The stiffening effect continues until the onset of capillary condensation at increased values of vapour pressure /concentration. After this point a rapid softening of the film (increase in resistance) is observed which is accompanied by swelling of the film.

(iii) Long chain lengths ($C_{15}H_{31}$ and $C_{17}H_{35}$). Of all the C[4]RA compounds tested this group produce the most stable and repeatable sensor responses. The large basket cavities formed by the long hydrocarbon chains already provide sufficient interlinking and no decrease in resistance is observed. Vapours exposure causes a significant softening of the film which is the effect normally associated with adsorption of an analyte into a viscoelastic membrane [20,27,30]. The frequency response appears be linear neglecting minimal contributions which may be caused by the viscoelastic membrane (see Chapter 4.4).

5.6 Coating stability

Interesting results have also been obtained from freshly prepared samples of the C[4]RA $C_{15}H_{31}$ compound. If samples are measured directly after the coating process has taken place (within 24 hours), an unexpected negative ΔR is observed at low concentrations, as shown in figure 5.27. The resistance decrease is also initially seen at the start of exposure at higher concentrations but after a small number of sample points (a short time) the resistance rises dramatically (indicated in figure 5.29). The frequency shift however shows no altered response and decreases consistently with the increasing vapour concentration (figure 5.28). This feature has only been observed with freshly coated samples of the C[4]RA $C_{15}H_{31}$ compound. After the coated QCM have been exposed to the natural environment for an undetermined period (24 hours in the case of these samples), the response of the resistance parameter behaves as previously tested with increases in R as expected for vapour adsorption as described in section 5.4. Baking of the freshly prepared samples at $100^{\circ}C$ for several hours also results in a normal behaviour of ΔR during further experiments. Figure 5.30 shows $\Delta R/\Delta f$ plot for a

newly prepared film at low concentrations, the negative resistance is clearly observed. After ΔR passes zero, identical results to 'normal' C[4]RA C₁₅H₃₁ films are obtained. This phenomenon is believed to be a special case for newly prepared films. Initially after coating the films may contain large quantities of ethanol molecules making the films softer than anticipated. Adsorption of non polar molecules gives additional rigidity to the structure at lower concentrations, until the mechanism of capillary condensation becomes predominant and increases in resistance are observed. After an undetermined period of exposure to air the majority of ethanol molecules evaporate from within the film matrix. Further vapour adsorption therefore only shows increases in resistance related to film softening. Baking of the samples has resulted in the evaporation of residual ethanol molecules, and thus normal adsorption behaviour is observed.

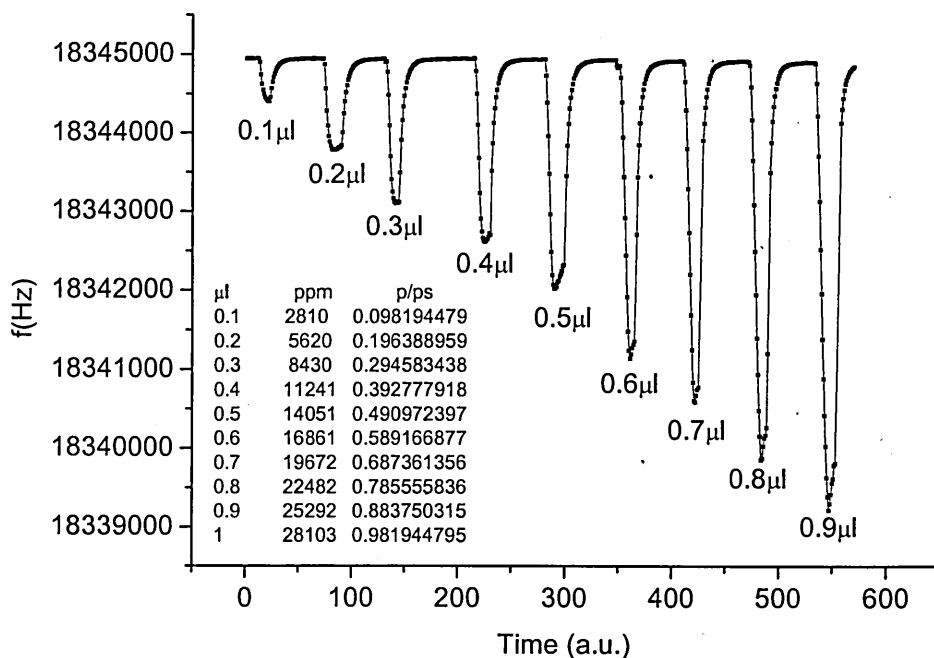


Figure 5.27. Time dependence of the resonance frequency during a sequence of exposures to toluene vapours of different concentration and intermediate flushing with air on a freshly prepared C[4]RA C₁₅H₃₁ sensing membrane.

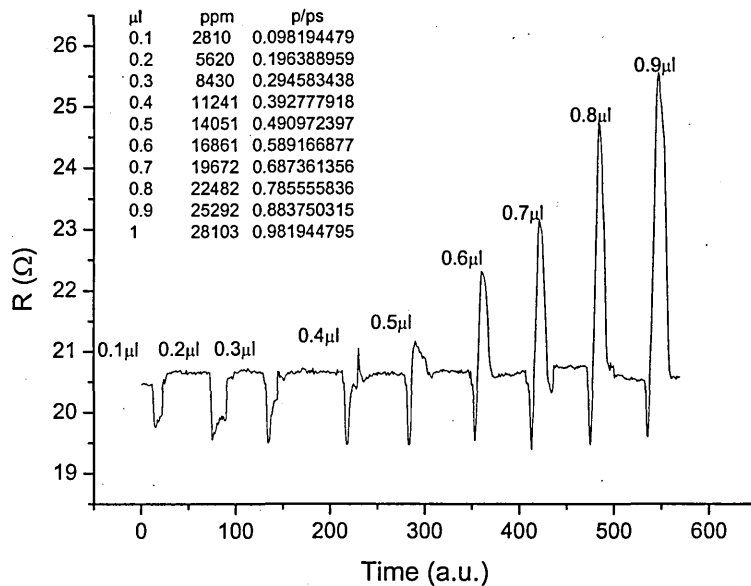


Figure 5.28. Time dependence of the extracted resistance during a sequence of exposures to toluene vapours of different concentration and intermediate flushing with air on a freshly prepared C[4]RA C₁₅H₃₁ sensing membrane.

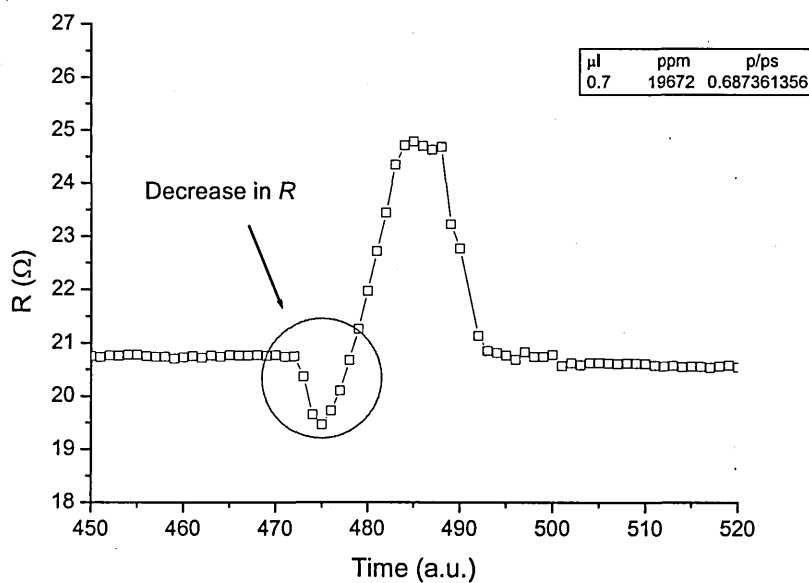


Figure 5.29. Enlarged section of figure 5.28 with the decrease in resistance circled at the onset of the exposure. Several samples later the resistance rises rapidly until reaching a maxima corresponding to the exposed vapour concentration.

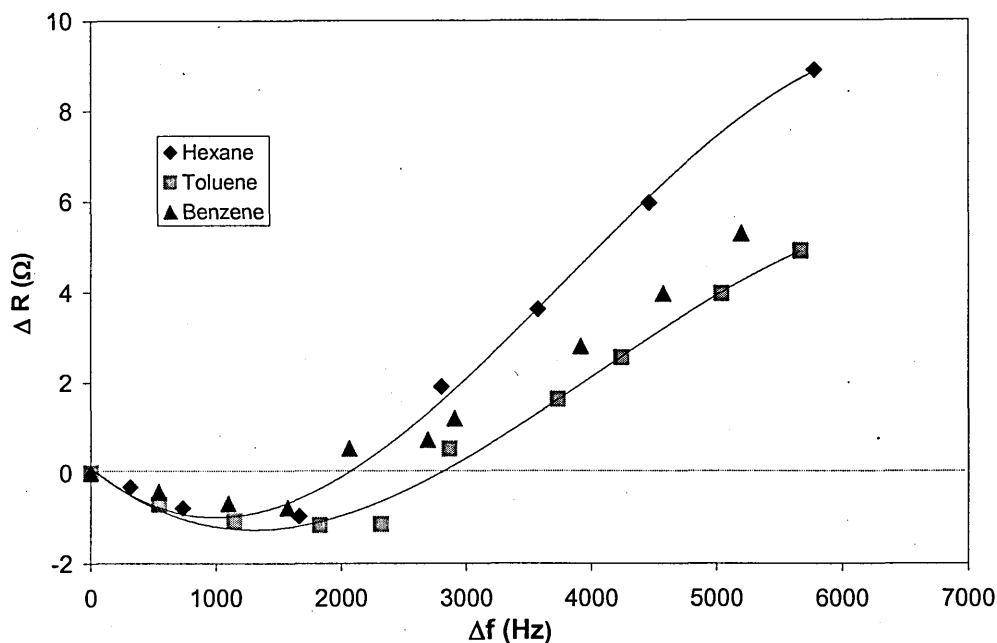


Figure 5.30. $\Delta R/\Delta f$ plot for a newly prepared film on vapour exposure.

5.7 Summary

The three QCM measurement techniques: (i) oscillator circuits, (ii) impedance analysis and (iii) QCMD in combination with C[4]RA sensitive membranes have been successfully exploited as VOC sensors. The oscillator based frequency only measurements when used in an array of sensors allows both sensor discrimination and quantification for all the organic solvents tested.

The additional resistance/dissipation parameter obtained from impedance analysis and QCMD is a measure of the mechanical properties (viscoelasticity) of the sensing membrane. Through acquiring both changes in the mass and in film properties, it has been possible to detect and discriminate a selected number of VOC's using only a single sensing element. The unique combination of mass loading and changes in film viscosity caused by vapour adsorption shows a novel method for classification of VOC's. The

possibility of combining multi-parameter QCM measurements with array techniques has been investigated using a series C[4]RA compounds, with different hydrocarbon chain lengths as sensing membranes. The results show some unexpected responses from the C[4]RA compounds with smaller hydrocarbon chains, primarily an increase in the film stiffness is observed on vapour adsorption. This behaviour does not correspond with previous literature where analyte adsorption into a viscoelastic film is accompanied by film softening. A speculative model has been put forward explaining the phenomena, however further research is required and currently underway to fully understand the adsorption mechanisms and resultant effects on the film properties.

REFERENCES

- [1] J. Auge, P. Hauptmann, J. Hartmann, S. Rosler, and R. Lucklum, "Versatile microcontrolled gas sensor array system using the quartz microbalance principle and pattern recognition methods," *Sensors and Actuators B: Chemical*, vol. 26, pp. 181-186, May 1995.
- [2] R. Dutta, E. L. Hines, J. W. Gardner, K. R. Kashwan, and M. Bhuyan, "Tea quality prediction using a tin oxide-based electronic nose: an artificial intelligence approach," *Sensors and Actuators B: Chemical*, vol. 94, pp. 228-237, Sept. 2003.
- [3] J. W. Gardner, E. L. Hines, and H. C. Tang, "Detection of vapours and odours from a multisensor array using pattern-recognition techniques Part 2. Artificial neural networks," *Sensors and Actuators B: Chemical*, vol. 9, pp. 9-15, July 1992.
- [4] A. Hierlemann, U. Weimar, G. Kraus, M. Schweizer-Berberich, and W. Gopel, "Polymer-based sensor arrays and multicomponent analysis for the detection of hazardous organic vapours in the environment," *Sensors and Actuators B: Chemical*, vol. 26, pp. 126-134, May 1995.
- [5] M. Holmberg, F. Winquist, I. Lundstrom, J. W. Gardner, and E. L. Hines, "Identification of paper quality using a hybrid electronic nose," *Sensors and Actuators B: Chemical*, vol. 27, pp. 246-249, June 1995.
- [6] S. W. Moore, J. W. Gardner, E. L. Hines, W. Gopel, and U. Weimar, "A modified multilayer perceptron model for gas mixture analysis," *Sensors and Actuators B: Chemical*, vol. 16, pp. 344-348, Oct. 1993.
- [7] T. Nakamoto, S. Hanaki, and T. Moriizumi, "Artificial odor-recognition system using neural network for estimating sensory quantities of blended fragrance," *Sensors and Actuators A: Physical*, vol. 57, pp. 65-71, Oct. 1996.
- [8] T. Nakamoto and H. Hiramatsu, "Study of odor recorder for dynamical change of odor using QCM sensors and neural network," *Sensors and Actuators B: Chemical*, vol. 85, pp. 263-269, July 2002.
- [9] R. Polikar, R. Shinar, L. Udpa, and M. D. Porter, "Artificial intelligence methods for selection of an optimized sensor array for identification of volatile organic compounds," *Sensors and Actuators B: Chemical*, vol. 80, pp. 243-254, Dec. 2001.
- [10] A. M. Reznik, A. A. Galinskaya, O. K. Dekhtyarenko, and D. W. Nowicki, "Preprocessing of matrix QCM sensors data for the classification by means of neural network," *Sensors and Actuators B: Chemical*, vol. 106, pp. 158-63, 2005.
- [11] H. Shinichi, N. Takamichi, and M. Toyosaka, "Artificial odor-recognition system using neural network for estimating sensory quantities of blended fragrance," *Sensors and Actuators A: Physical*, vol. 57, pp. 65-71, Oct. 1996.
- [12] L. X. Sun and T. Okada, "Simultaneous determination of the concentration of methanol and relative humidity based on a single Nafion(Ag)-coated quartz crystal microbalance," *Analytica Chimica Acta*, vol. 421, pp. 83-92, Sept. 2000.

- [13] T. Nakamoto and H. Hiramatsu, "Study of odor recorder for dynamical change of odor using QCM sensors and neural network," *Sensors and Actuators B: Chemical*, vol. 85, pp. 263-269, July 2002.
- [14] J. W. Gardner, and P. N. Bartlett, "Electronic Noses Principles and Applications", pages 245, Oxford University Press, New York, 1999.
- [15] H. Demuth, and M. Beale, "Neural Network Toolbox User's Guide Version 4," The MathWorks, Inc.
http://www.mathworks.com/access/helpdesk/help/pdf_doc/nnet/nnet.pdf
- [16] A. V. Nabok, A. K. Hassan, and A. K. Ray, "Condensation of organic vapours within nanoporous calixerene thin films," *Journal of materials chemistry*, vol. 10, pp. 189-194, June 1999.
- [17] S. J. Greg, and K. S. W. Sing, "Adsorption, surface area and porosity," Academic press, New York, 1982.
- [18] A. K. Hassan, A. K. Ray, A. V. Nabok, and T. Wilkop, "Kinetic studies of BTEX vapour adsorption onto surfaces of calix-4-resorcinarene films," *Applied Surface Science*, vol. 182, pp. 49-54, Oct. 2001.
- [19] A. V. Nabok, N. V. Lavrik, Z. I. Kazantseva, B. A. Nesterenko, L. N. Markovskiy, V. I. Kalchenko, and A. N. Shivaniuk, "Complexing properties of calix[4]resorcinolarene LB films," *Thin Solid Films*, vol. 259, pp. 244-247, Apr. 1995.
- [20] R. Lucklum and P. Hauptmann, "Transduction mechanism of acoustic-wave based chemical and biochemical sensors," *Measurement Science and Technology*, vol. 14, pp. 1854-1864, 2003.
- [21] A. F. Holloway, A. Nabok, M. Thompson, A. K. Ray, and T. Wilkop, "Impedance analysis of the thickness shear mode resonator for organic vapour sensing," *Sensors and Actuators B: Chemical*, vol. 99, pp. 355-360, Feb. 2004.
- [22] R. Lucklum, C. Behling, P. Hauptmann, S. J. Martin, and R. W. Cernosek, "Error analysis of material parameter determination with quartz-crystal resonators," *Sensors and Actuators A: Physical*, vol. 66, pp. 184-192, Apr. 1998.
- [23] R. Lucklum, C. Behling, and P. Hauptmann, "Signal amplification with multilayer arrangements on chemical quartz crystal resonators," 1999 Joint Meeting EFTF - IEEE IFCS, pp. 987-990, 1999.
- [24] R. Lucklum, C. Behling, R. W. Cernosek, and S. J. Martin, "Determination of complex shear modulus with thickness shear mode resonators," *Journal of Physics D: Applied Physics*, vol. 30, pp. 346-356, 1997.
- [25] R. Lucklum and P. Hauptmann, "The quartz crystal microbalance: mass sensitivity, viscoelasticity and acoustic amplification," *Sensors and Actuators B: Chemical*, vol. 70, pp. 30-36, Nov. 2000.
- [26] R. Lucklum and P. Hauptmann, "The $[\Delta]f$ - $[\Delta]R$ QCM technique: an approach to an advanced sensor signal interpretation," *Electrochimica Acta*, vol. 45, pp. 3907-3916, July 2000.

- [27] R. Lucklum, C. Behling, and P. Hauptmann, "Gravimetric and non-gravimetric chemical quartz crystal resonators," *Sensors and Actuators B: Chemical*, vol. 65, pp. 277-283, June 2000.
- [28] S. J. Martin, "Interactions of acoustic waves with thin films and interfaces - Closing remarks," *Faraday Discussions*, vol. 107, pp. 463-476, 1997.
- [29] S. J. Martin, H. L. Bandey, R. W. Cernosek, A. R. Hillman, and M. J. Brown, "Equivalent-circuit model for the thickness-shear mode resonator with a viscoelastic film near film resonance," *Analytical Chemistry*, vol. 72, pp. 141-149, Jan. 2000.
- [30] D. S. Ballatine, R. M. White, S. J. Martin, A. J. Ricco, G. C. Fryre, E. T. Zellers, and H. Wohltjen, "Acoustic Wave Sensors Theory, Design and Physico chemical applications," Academic press, New York, 1997.

Chapter 6

6.0 Conclusions and Recommendations

The development of a QCM sensor for in situ monitoring of volatile organic solvents in the pre-explosive vapour range has been investigated in this thesis. Several QCM measurement techniques have been exploited ranging from the standard oscillator circuits to impedance analysis and QCMD methods, where multiple parameters can be obtained from a single crystal. The latter two methods have a distinct advantage through acquiring the resistance/dissipation parameter, which gives a further insight into the adsorption of the analyte into the film. The measurement of dissipation within the film becomes increasingly important with the use of viscoelastic membranes, such as calixarene films used in this thesis (described in chapter 2). The adsorption of an analyte into a viscoelastic film in most cases does not follow the simple linear relation described by Sauerbrey, unless strict conditions of film thickness and rigidity are met.

The measurement of the impedance is typically performed using a laboratory based impedance analyser as demonstrated within this work. The technique allows all the resonance properties of the crystal to be measured and gives most information of the QCM measurement techniques available. The equipment for impedance analysis is however bulky, expensive and complex. Further fitting of the spectra to an equivalent circuit is also quite complicated and required a specifically designed software program. A suitable alternative was found in the use of the QCMD measurement technique proposed by Rodahl et al [1,2]. An experimental test setup based on the QCMD system was built in house, and was found to give levels of performance comparable to that

achieved using the impedance analyser. Further improvements were made to the design through additional multiplexing circuitry. This allowed the measurements of multiple parameters from several crystals in pseudo real time, making the system suitable for array applications.

Simple oscillator measurements are still however suitable for many applications if changes in viscoelastic properties are of little or no concern. As shown in Chapter 4.4 the contribution to the frequency shift caused by a viscoelastic load is minimal when using films with small thicknesses (negligible acoustic phase shift). In such cases the viscoelastic effects may be insignificant.

In this work a small array of QCM oscillators has been utilized for the classification of several VOCs. Using the array technique and a suitable ANN, accurate classification and quantification of a number of organic solvents has been achieved at concentrations above 5% of LEL for the tested vapours. A series of calix[4]resorcinarene compounds were used as sensing membranes, showing suitably different sensitivity levels from one another to facilitate odour classification. It is believed the levels of sensitivity are related to their respective substituent alkyl chain length, and hence the cavity size formed by the calix[4]resorcinarene compounds. The compounds having shorter alkyl chains (C_1H_3 & C_3H_7) show poor sensitivity and unpredictable frequency shifts. The highest sensitivity is seen when using the mid length calix[4]resorcinarene alkyls in (C_5H_{11} & $C_{11}H_{23}$), with vapour detection in some cases below 1 ppm. While the longer alkyl chains prove to be the most stable and provide approximately linear responses over the concentration ranges tested.

The method of impedance analysis/QCMD was first applied to the C[4]RA C₁₅H₃₁ sensing membrane. It is well documented that adsorption of an analyte into a sensing membrane may cause changes in its mechanical properties[3-7]. This principle was therefore exploited for the selective detection of several organic solvent vapours using a single QCM. Through monitoring changes in both the mass and the viscoelastic properties of the C[4]RA C₁₅H₃₁ film, classification was made possible by the unique changes in film properties and mass load caused by some target analytes.

The effect of dissipation in a viscoelastic can be related to the mechanical properties of the film through equations (5.8) and (5.9). Adsorption of a vapour into the membrane causing no change in the mechanical film properties (G' and G'') would therefore be indistinguishable. All vapours would produce an identical resistance change for a specified frequency shift $\left(\frac{\Delta R}{\Delta f}\right)$, as demonstrated by PU-C[4]A compound shown in figures 5.1. In the case of the C[4]RA compound it is believed that the capillary condensation of the solvent occurs at concentrations well below saturated vapour pressure (see chapter 5.4). The effect of condensation within the film matrix gives rise to the unique changes in the films mechanical properties for certain organic solvents. Calixarene membranes represent a unique combination of rigidity and nano-porosity of the film structure, in which the adsorption and condensation of organic vapours takes place. This constitutes the main advantage of calixarenes over the other amphiphilic compounds.

It has to be mentioned that the organic vapour adsorption in C[4]RA C₁₅H₃₅ films is fast (a few seconds), and a full recovery of QCM sensors was observed. All the facts mentioned above make the proposed sensor very much suitable for the detection of high (pre-explosive) concentrations of organic solvent vapours.

The success of the oscillator array and impedance analysis/QCMD techniques motivated the development of a system combining the two methods. Further investigation using impedance analysis was undertaken into a series of C[4]RA membranes used previously for simple oscillator measurements. The results showed a remarkable uncharacteristic decrease in resistance (film stiffening). Such an effect is abnormal as adsorption of a vapour into a viscoelastic membrane in most cases is accompanied with film softening, and is not predicted by equations (5.8) and (5.9). The peculiar behaviour continues into the mid chain length of C[4]RA compounds. In this instance a negative resistance change is only seen at lower concentrations. A speculative model for the C[4]RA series of compounds has been proposed in Chapter 5 which accounts for this phenomena. However, to fully characterise and understand the adsorption mechanism and resultant changes in film properties much further investigation is required.

The work in this thesis constitutes the basis for multi parameter QCM array measurements. The measurement of viscoelastic properties of the film in addition to the mass accumulation gives an additional parameter to aid the classification and in some cases allows a single QCM to discriminate between vapours. The calix[4]resorcinarene coatings do not provide high specificity for the any particular individual or group of organic solvent vapours. However, when combined with array techniques and/or multiple parameter QCM measurements, the discrimination between vapours can be achieved within and in some cases below the range of LEL and HEL, thus making the sensor a valuable tool for the detection of explosive organic vapours.

Further work on the study of different analytes, vapour mixtures (including cross-sensitivity study of inorganic gases) in a wide range of concentrations and using

different sensitive membranes as well as long term stability of QCM sensors is currently underway.

6.1 Recommendations for future work

The work in this thesis gives promising results for the further development of a pre explosive vapour alarm using QCM techniques. A combination of multiple parameter measurements and electronic nose techniques is proposed to provide both the detection and quantification of target VOC's. Although a considerable amounts of work has been done during the study of this thesis, further investigation and new designs are required in order to implement a final prototype sensor. The following list contains recommendations for future work proposed by the author.

- 1.) The study of an increased number of organic solvent vapours building a database of sensor responses for further classification of all compounds possible.
- 2.) The study of exposure of the all the C[4]RA compounds to a mixture of organic vapours, building a database of sensor responses for the classification between mixtures of solvent vapour in the air.
- 3.) Further investigation into the increases in film stiffness seen in small chain length C[4]RA compounds. Further verification of the model relating C[4]RA chain length to the sensor responses.
- 4.) Integration of the complete experimental setup into a single hardware/software package including the ANN/pattern recognition algorithm.
- 5.) Testing of the sensors in non laboratory conditions. Studying the effects of vapour flow, and natural environment.

6.) Investigation of recent oscillator circuit designs which allow frequency and dissipation measurements. Evaluation of the resolution and stability of such circuits for the sensor applications.

REFERENCES

- [1] M. Rodahl, F. Hook, A. krozer, P. Bzezinski, and B. Kasemo, "Quartz crystal microbalance setup for frequency and Q-factor measurements in gaseous and liquid environments," *Review of Scientific Instruments*, vol. 66, pp. 3924-3930, June 1995.
- [2] M. Rodahl and B. Kasemo, "A simple setup to simultaneously measure the resonant frequency and the absolute dissipation factor of a quartz crystal microbalance," *Review of Scientific Instruments*, vol. 67, pp. 3238-3241, Aug. 1996.
- [3] D. S. Ballatine, R. M. White, S.J. Martin, A.J. Ricco, G.C. Fryre, E.T. Zellers, and H. Wohltjen, "Acoustic Wave Sensors Theory, Design and Physico chemical applications," Academic press, New York, 1997.
- [4] R. Lucklum and P. Hauptmann, "The $[\Delta]f$ - $[\Delta]R$ QCM technique: an approach to an advanced sensor signal interpretation," *Electrochimica Acta*, vol. 45, pp. 3907-3916, July 2000.
- [5] R. Lucklum, C. Behling, and P. Hauptmann, "Gravimetric and non-gravimetric chemical quartz crystal resonators," *Sensors and Actuators B: Chemical*, vol. 65, pp. 277-283, June 2000.
- [6] R. Lucklum and P. Hauptmann, "Transduction mechanism of acoustic-wave based chemical and biochemical sensors," *Measurement Science and Technology*, vol. 14, pp. 1854-1864, 2003.
- [7] S. J. Martin, C Gregory, G. C Fryre, and S Senturia, "Dynamics and Response of Polymer-Coated Surface Acoustic Wave Devices: Effect of Viscoelastic Properties and Film Resonance," *Analytical Chemistry*, vol. 66, pp. 2201-2219, 1994.

Appendix [A]

1. Program to simulate the acoustic load over a range of shear modulus values.
Film thickness, density and the probing frequency must be known.
2. Program to calculate admittance spectra using the TLM model.
Uses physical properties of the quartz and contacting film.
3. Program to first calculate an admittance spectra from the TLM or experimental
Data, the fast 3 step method is then performed.
4. Program to calculate Δf and ΔR for known shear parameters over defined
thickness range.

Program 1

% Program to calculate and produce 3D plot the acoustic load
%for a range of shear moduli input parameters are
%film thickness , film density and probing frequency

```
clear all
p_film = 1000;      %film density kg m3 1100
hs = 1.0e-6;       %1E-6
```

```
y=4:0.05:9
x=4:0.05:9%Gdd
```

```
Gf_d = 10.^x;
Gf_dd = 10.^y;
```

```
%c = complex(a,b)
```

```
w = 2*pi*10e6; %10MHz
```

```
x=Gf_d;
y=Gf_dd;
[X Y]=meshgrid(x,y);
a_size=size(X)
```

```
for i=1:a_size(1)
    for j=1:a_size(1)
        Gf = complex(Gf_d(i),Gf_dd(j));
        ZLA = (((p_film*Gf)^0.5)*1i);
        ZLB = tan(w * (((p_film/Gf)^0.5)*hs));
        ZL(i,j)=ZLA*ZLB;
    end
end
```

```
ZL_real = real(ZL);
ZL_imag = -1*imag(ZL);
```

```
meshc(log10(Y),log10(X),ZL_imag);
%set(gca,'Xscale','log')
%zlim([-800000 500000])
%caxis([0000 150000])
rotate3d
```

```
xlabel({' log10 (G'')/Pa '});
Ylabel({' log10 (G''')/Pa '});
zlabel({' imaginary (Zl) '});
```

```
clear all
```

Program 2

%Program to generate sample admittance spectra from the
%TLM and values of known shear modulus

```
clear all
format long
size = 200
p_q = 2.651e3;      %density
ep_q = 3.982e-11;  %permittivity
e_q = 9.53e-2;     %piezoelectric constnt
n_q = 3.5e-4;      %viscosity
c_q = 2.947e10;    %piezo electric stiffened elastic constant
f_q = 18.44e6;     %resonant freq of my qcm
A = 28.3e-6;       %area of my qcm in m2

vs = (c_q/p_q)^0.5; %velocity
ko2 = e_q^2/(ep_q*c_q); %electromechanical coupling factor
h_q = vs/(2*f_q) %quartz thickness
Co = (ep_q*A)/h_q %static capacitance
%al_q = (w*h_q)/vs; %wave phase shift im quartz from luclum behling j phys d
%al_q = (w*h_q)*((p_q/c_q)^0.5) ;
zc_q = (p_q*c_q)^0.5;
i=1;

%calculate viscoelastic load
p_film = 650; %film density kg m3
hs = 0.5e-6; %from ellipsometry
w = 2*pi*f_q;

Gf_d=1e8;
Gf_dd=1e6;
Gf = complex(Gf_d,Gf_dd);
ZLA = (((p_film*Gf)^0.5)*1i);
ZLB = tan(w * (((p_film/Gf)^0.5)*hs));
ZL=ZLA*ZLB

load=ZL/zc_q;
%Z split into two parts of motional branch
for f=18.3e6:100:18.5e6

% Impedance of the motional branch
w=2*pi*f;
al_q = (w*h_q)/vs;
parta = 1/((w*Co)*1i);

front=(ko2/al_q);
topline= ((2*tan(al_q/2))-((load*1i)));
bottomline = (1-(((load)*1i)*cot(al_q)));
partb= 1-(front*(topline/bottomline));

zm_tot=parta*partb;
Ztotal(i)=zm_tot^-1;
freq(i)=f;
i=i+1;
end

%plot the data
```

```
zm_fs = abs(Ztotal); % get the magnitude
min=min(zm_fs)
semilogy(freq,zm_fs)
[Gmax,ind]=max(zm_fs)
R=1/Gmax
```

```
fs_approx=freq(ind)
Ztotal(ind)
```

Program 3

% Program to first calculate an admittance value using the full transmission line model
% and known values of shear modulus. (this can be replaced with a measured admittance value)
% The fast three step method is then implemented and (Lucklum 2001) and approximate values
% of shear parameters obtained
% for the measured/simulated admittance

```
clear all
format long
size = 200
p_q = 2.651e3;      %density
ep_q = 3.982e-11;  %permittivity
e_q = 9.53e-2;     %piezoelectric constant
n_q = 3.5e-4;      %viscosity
c_q = 2.947e10;    %piezo electric stiffened elastic constant
f_q = 18.44e6;     %resonant freq of my qcm
A = 28.3e-6;       %area of my qcm in m2

vs = (c_q/p_q)^0.5; %velocity
ko2 = e_q^2/(ep_q*c_q); %electromechanical coupling factor
h_q = vs/(2*f_q) %quartz thickness
Co = (ep_q*A)/h_q %static capacitance
%al_q = (w*h_q)/vs; %wave phase shift in quartz from lucklum behling j phys d
%al_q = (w*h_q)*((p_q/c_q)^0.5) ;
zc_q = (p_q*c_q)^0.5;
i=1;

%calculate viscoelastic load
p_film = 650; %film density kg m3
hs = 0.5e-6; %from ellipsometry
w = 2*pi*f_q;

Gf_d=1e6;
Gf_dd=1e6;
Gf = complex(Gf_d,Gf_dd);
ZLA = (((p_film*Gf)^0.5)*1i);
ZLB = tan(w * (((p_film/Gf)^0.5)*hs));
ZL=ZLA*ZLB

load=ZL/zc_q;

f=18.3e6

w=2*pi*f;
al_q = (w*h_q)/vs;
parta = 1/((w*Co)*1i);

front=(ko2/al_q);
topline= ((2*tan(al_q/2))-((load*1i)));
bottomline =(1-(((load)*1i)*cot(al_q)));
partb= 1-(front*(topline/bottomline));

zm_tot=parta*partb;
Ztotal=zm_tot^2-1;
impedance=Ztotal
```

ZL

%

```
bit =impedance-((w*Co)*1i);  
high=(bit*(al_q/ko2))-(2*impedance*(tan(al_q/2)));  
low=impedance-(bit)*((al_q/ko2)*cot(al_q));
```

```
Zl_calc=(zc_q*1i)*(high/low)
```

```
m=w*p_film*hs
```

```
p0=1/p_film*(((1/3)*m^3)/((Zl_calc/1i)-m))
```

```
p1=1/p_film*(((Zl_calc/1i)-(2*m))/(1-(pi/2)))^2
```

```
p2=1/p_film*((-(pi^2)/8)*(Zl_calc^2)-(m*Zl_calc/1i)+(pi/4)*Zl_calc*sqrt(((pi^2)/4)*(Zl_calc^2)-  
4*1i*m*Zl_calc))
```

```
p3=1/p_film*(((Zl_calc/1i)-(2*m))/(1+(pi*(3/2))))^2
```

```
p4=1/p_film*(((Zl_calc/1i)-(m))/(pi))^2
```

```
%substitute values back into equation for ZL
```

```
w = 2*pi*f_q;
```

```
ZL0= (((p_film*p0)^0.5)*1i)*tan(w * (((p_film/p0)^0.5)*hs))
```

```
ZL1= (((p_film*p1)^0.5)*1i)*tan(w * (((p_film/p1)^0.5)*hs))
```

```
ZL2= (((p_film*p2)^0.5)*1i)*tan(w * (((p_film/p2)^0.5)*hs))
```

```
ZL3= (((p_film*p3)^0.5)*1i)*tan(w * (((p_film/p3)^0.5)*hs))
```

```
ZL4= (((p_film*p4)^0.5)*1i)*tan(w * (((p_film/p4)^0.5)*hs))
```

```
%compare these values with measured ZL to obtain best approximation
```

Program 4

%Program to calculate df and dr of a viscoelastic film over a
%defined set of thickness values and known shear parameters

```
clear all
p_film = 630 ;      %film density kg m3
Gf_d = 0.5e8;
Gf_dd = 2e6;
w = 2*pi*18.4e6;

j=1;

for hf = 0.1e-6:0.01E-6:0.5E-6;

    Gf = complex(Gf_d,Gf_dd);
    ZLA = (((p_film*Gf)^0.5)*1i);
    ZLB = tan(w * (((p_film/Gf)^0.5)*hf));
    ZL=ZLA*ZLB;
    theta=(w *hf*(((p_film/Gf)^0.5)));
    M=w*p_film*hf;
    V=(tan(theta))/theta;

    df_visco(j)=M*(1+((1/3)*(Gf_d/(p_film*(abs(Gf)^2))))*M^2);
    dr_visco(j)=M*(((1/3)*(Gf_dd/(p_film*(abs(Gf)^2))))*M^2);

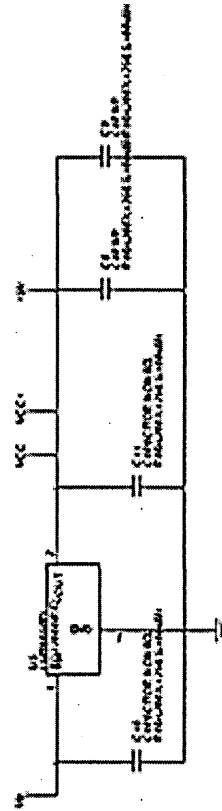
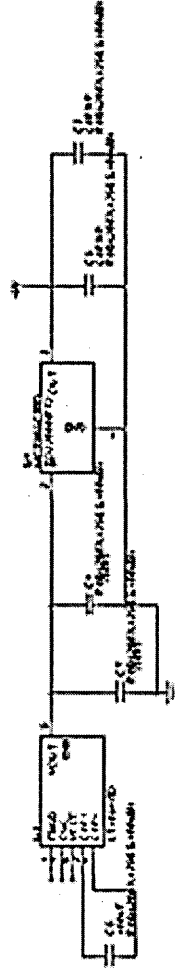
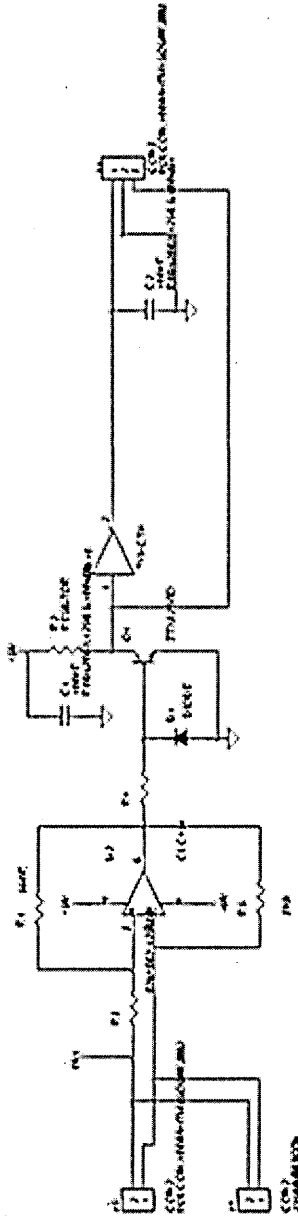
    hf_p(j)=hf;;
    M_p(j)=M;
    diff_freq(j)=df_visco(j)-M_p(j)
    j=j+1;

end

plot(hf_p,dr_visco)
%plot(hf_p,df_visco,hf_p,M_p,'x')
%plot(hf_p,diff_freq)
xlabel({' hf (m)';})
%Ylabel({' \Delta f (Hz)';})
Ylabel({' \Delta R (\Omega)';})
```

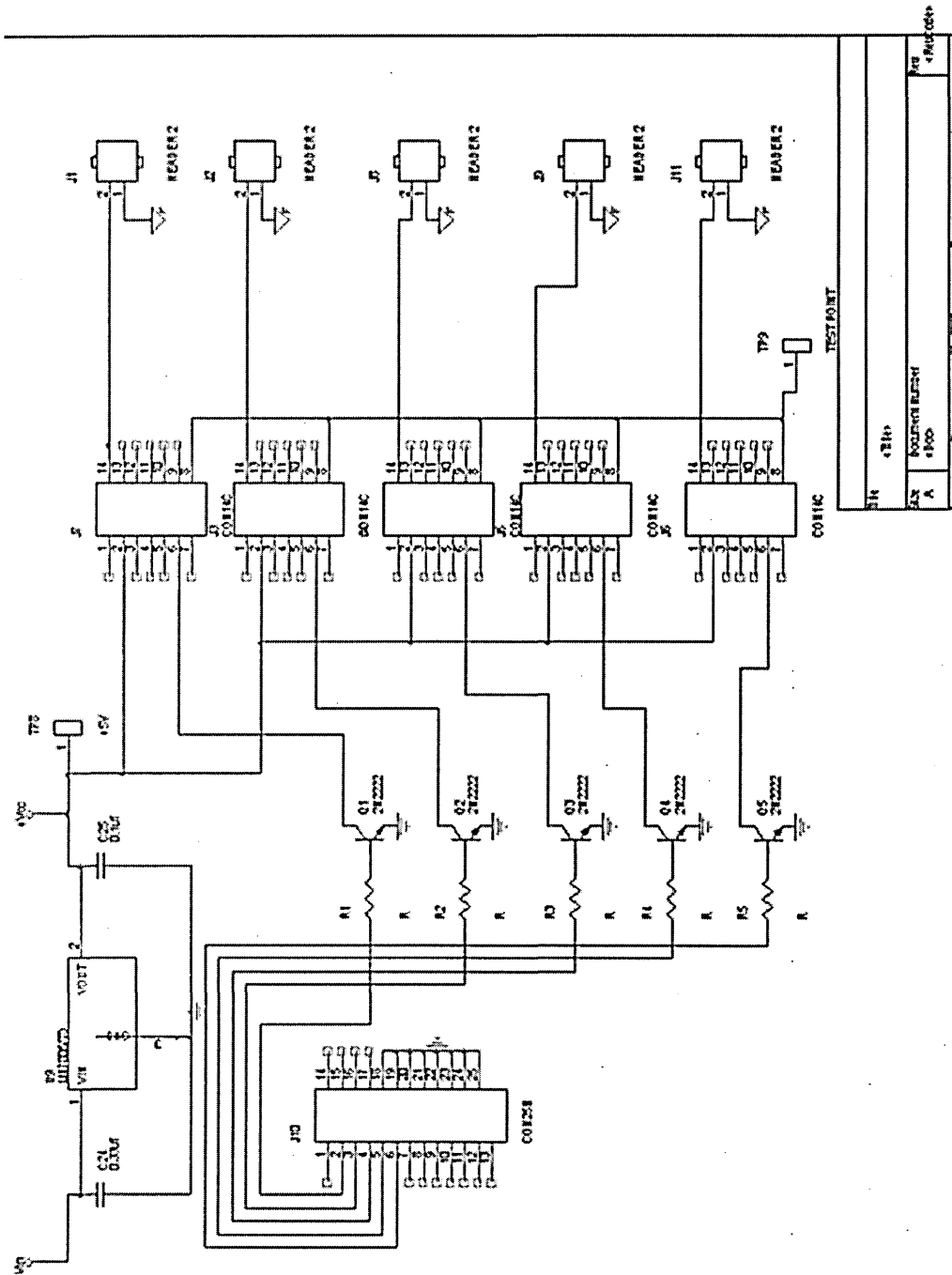
APPENDIX [B]

Single QCM oscillator



APPENDIX [B]

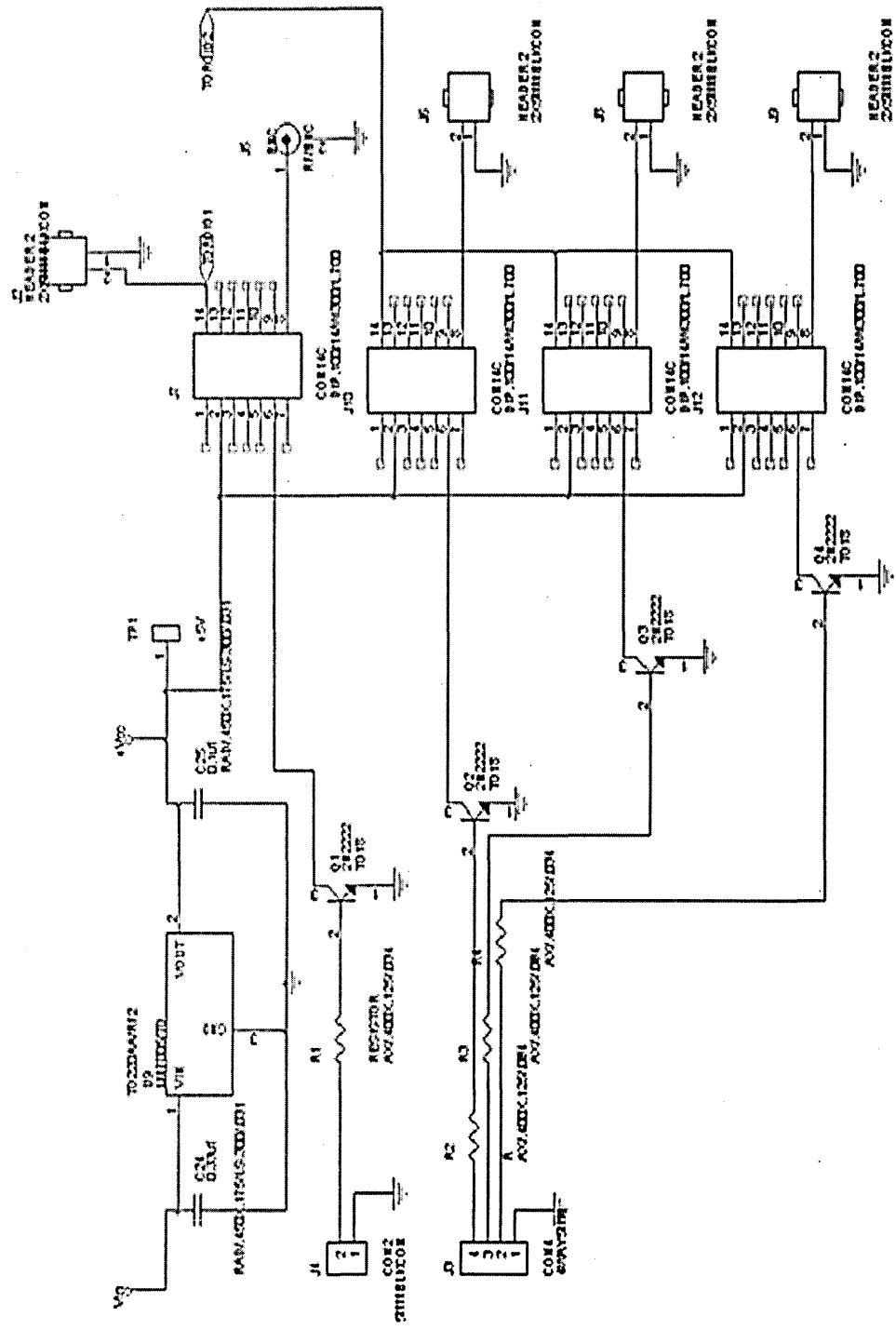
Multiplexer Circuit based around multiple reed relays



REV	DATE	BY	CHKD
1	10/1/70	W. J. B.	W. J. B.
2	10/1/70	W. J. B.	W. J. B.
3	10/1/70	W. J. B.	W. J. B.
4	10/1/70	W. J. B.	W. J. B.
5	10/1/70	W. J. B.	W. J. B.

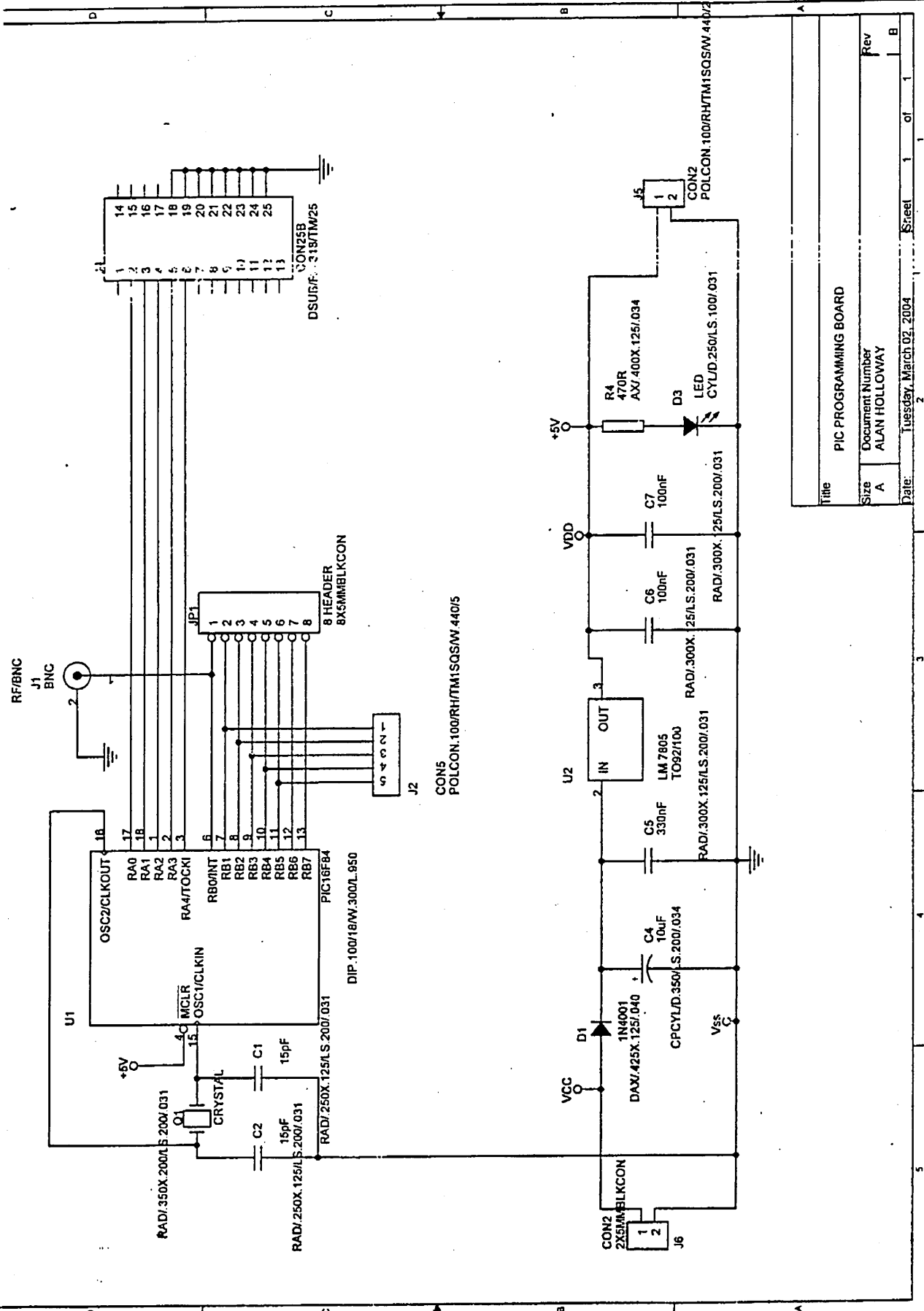
APPENDIX [C]

QCMD Main board



APPENDIX [C]

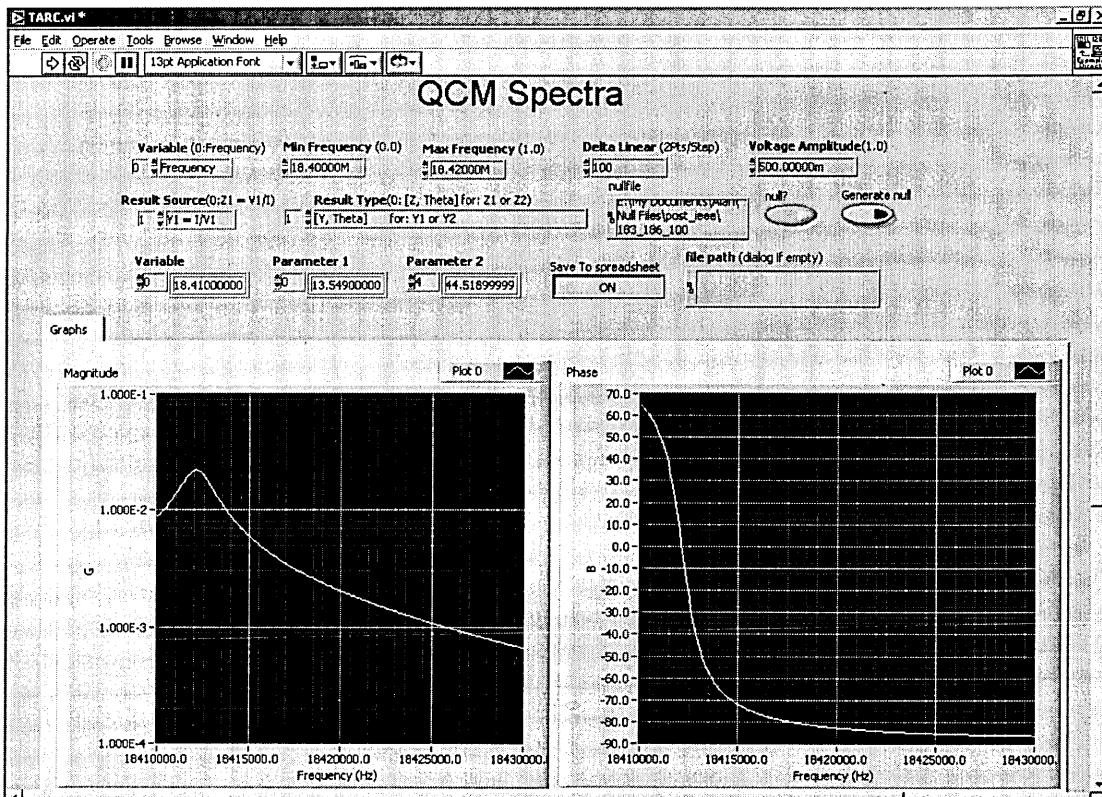
PIC Microcontroller schematic



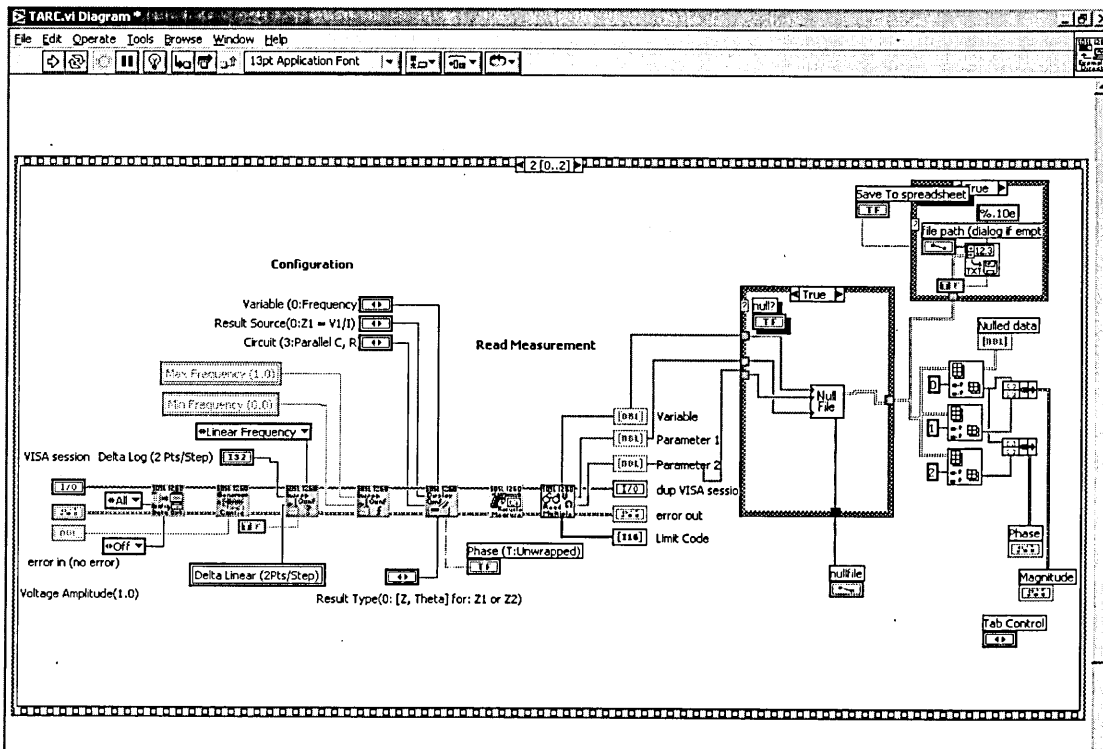
Title		PIC PROGRAMMING BOARD	
Size	Document Number	ALAN HOLLOWAY	
Rev	Date:	Tuesday, March 02, 2004	Sheet 1 of 1

APPENDIX [D]

Front panel of QCM spectra acquisition program.

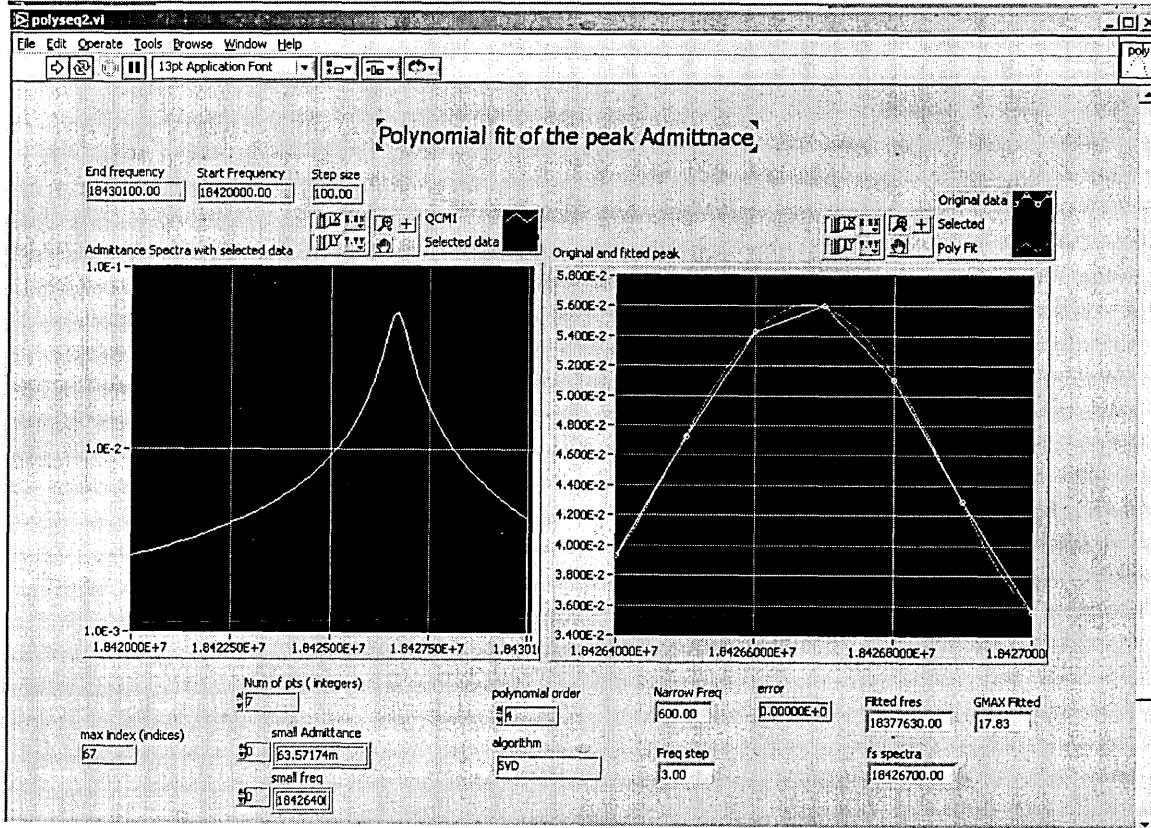


Main window of code from spectra acquisition program



Appendix [E]

Front panel of polynomial fit program



Appendix [F]

Approximations used for the tangent function when using the fast three step method proposed by Lucklum et al[1], and implementing MATLAB program.

name	φ	$\tan \varphi$	Shear modulus G
p0	≈ 0	$\approx \varphi + \frac{1}{3}\varphi^3$	$= \frac{\frac{1}{3}M^3}{\rho \frac{Z_L - M}{j}}$
p1	$\approx \frac{\pi}{4}$	$\approx 1 + \frac{\pi}{2} + 2\varphi$	$= \frac{1}{\rho} \left(\frac{\frac{Z_L - 2M}{j}}{1 - \frac{\pi}{2}} \right)^2$
p2	$\approx \frac{\pi}{2}$	$\approx \frac{1}{\frac{\pi}{2} - \varphi}$	$= \frac{1}{\rho} \left(-\frac{\pi^2}{8} Z_L^2 - M \frac{Z_L}{j} + \frac{\pi^2}{4} Z_L \sqrt{\frac{\pi^2}{4} Z_L^2 - 4jMZ_L} \right)$
p3	$\approx \frac{3}{4}\pi$	$\approx 1 - \frac{3}{2} + 2\varphi$	$= \frac{1}{\rho} \left(\frac{\frac{Z_L - 2M}{j}}{1 + \frac{3\pi}{2}} \right)^2$
p4	$\approx \pi$	$\approx -\pi + \varphi$	$= \frac{1}{\rho} \left(\frac{\frac{Z_L - M}{j}}{\pi} \right)^2$

REFERENCES

- [1] R. Lucklum and P. Hauptmann, "Thin film shear modulus determination with quartz crystal resonators: A review," IEEE International Frequency Control Symposium and PDA Exhibition, pp. 480-417, 2001.